NATIONAL AERONAUTICS AND SPACE ADMINISTRATION

Technical Report 32-1526

Volume VI

The Deep Space Network

Progress Report
For September and October 1971

JET PROPULSION LABORATORY
CALIFORNIA INSTITUTE OF TECHNOLOGY
PASADENA, CALIFORNIA

December 15, 1971

NATIONAL AERONAUTICS AND SPACE ADMINISTRATION

Technical Report 32-1526

Volume VI

The Deep Space Network

Progress Report
For September and October 1971

JET PROPULSION LABORATORY
CALIFORNIA INSTITUTE OF TECHNOLOGY
PASADENA, CALIFORNIA

December 15, 1971

Prepared Under Contract No. NAS 7-100
National Aeronautics and Space Administration

Preface

This report series presents progress on DSN supporting research and technology, advanced development and engineering, and implementation, and DSN operations which pertain to mission-independent or multiple-mission development as well as to support of flight projects. Each issue presents material in some, but not all, of the following categories in the order indicated.

Description of the DSN

Mission Support
- Interplanetary Flight Projects
- Planetary Flight Projects
- Manned Space Flight Project
- Radio Science Experiments
- Advanced Flight Projects

Advanced Engineering
- Tracking and Navigational Accuracy Analysis
- Communications Systems Research
- Communications Elements Research
- Supporting Research and Technology

Development and Implementation
- Space Flight Operations Facility Development
- Ground Communications Facility Development
- Deep Space Instrumentation Facility Development
- DSN Projects and Systems Development

Operations and Facilities
- DSN Operations
- Space Flight Operations Facility Operations
- Ground Communications Facility Operations
- Deep Space Instrumentation Facility Operations
- Facility Engineering

In each issue, the part entitled "Description of the DSN" describes the functions and facilities of the DSN and may report the current configuration of one of the six DSN systems (tracking, telemetry, command, monitoring, simulation, and operations control).

The work described in this report series is either performed or managed by the Tracking and Data Acquisition organization of JPL for NASA.

Page Intentionally Left Blank

Contents

Contents (contd)

Communications Systems Research

Communications Elements Research

Supporting Research and Technology

Contents (contd)

DEVELOPMENT AND IMPLEMENTATION

GCF Development

DSIF Development

OPERATIONS AND FACILITIES

DSN Operations

DSIF Operations

DSN Functions and Facilities

N. A. Renzetti
Mission Support Office

The objectives, functions, and organization of the Deep Space Network are summarized. The Deep Space Instrumentation Facility, the Ground Communications Facility, and the Space Flight Operations Facility are described.

The Deep Space Network (DSN), established by the NASA Office of Tracking and Data Acquisition under the system management and technical direction of JPL, is designed for two-way communications with unmanned spacecraft traveling approximately 16,000 km (10,000 mi) from Earth to planetary distances. It supports, or has supported, the following NASA deep space exploration projects: *Ranger, Surveyor, Mariner* Venus 1962, *Mariner* Mars 1964, *Mariner* Venus 67, *Mariner* Mars 1969, *Mariner* Mars 1971 (JPL); *Lunar Orbiter* and *Viking* (Langley Research Center); *Pioneer* (Ames Research Center); *Helios* (West Germany); and *Apollo* (Manned Spacecraft Center), to supplement the Manned Space Flight Network (MSFN).

The Deep Space Network is one of two NASA networks. The other, known as the Space Flight Tracking and Data Network, is under the system management and technical direction of the Goddard Space Flight Center. Its function is to support manned and unmanned Earth-orbiting and lunar scientific and communications satellites. Although the DSN was concerned with unmanned lunar spacecraft in its early years, its primary objective now and into the future is to continue its support of planetary and interplanetary flight projects. It has been a development objective that the network capability be kept at the state of the art of telecommunications and data handling and that it support as many flight projects as possible with a minimum of mission-dependent hardware and software. It provides direct support of each project through that project's tracking and data system. This management element, in concert with the telecommunications and mission operations personnel of the project, is responsible for the design and operation of the hardware and software which are required for the conduct of flight operation. The organization and procedures necessary to carry out these activities are described in Ref. 1.

The DSN function, in supporting a flight project by tracking the spacecraft, is characterized by six DSN systems:

(1) DSN Tracking System. Generates radio-metric data; i.e., angles, one- and two-way doppler and range.

(2) DSN Telemetry System. Receives, records, and retransmits engineering and scientific data generated in the spacecraft.

(3) DSN Command System. Sends coded signals to the spacecraft in order to initiate spacecraft functions in flight.

(4) DSN Monitor System. Instruments, transmits, records, and displays those parameters of the DSN that measure its performance.

(5) DSN Simulation System. Provides computer-based facilities in order to test and train network functions and assist the flight project in carrying out similar functions for its Mission Operations System.

(6) DSN Operations Control. Provides the hardware and software personnel, real-time and non-real-time operational direction of the network, and primary interface with the flight projects Mission Operations personnel.

The facilities needed to carry out these functions have evolved in three technical areas: (1) the deep space stations and the telecommunications interface through the RF link with the spacecraft is known as the Deep Space Instrumentation Facility (DSIF); (2) the Earth-based point-to-point voice and data communications from the stations to the control center is known as the Ground Communications Facility (GCF); (3) the control center, both for network control function and mission control support, is known as the Space Flight Operations Facility (SFOF).

I. Deep Space Instrumentation Facility

A. Tracking and Data Acquisition Facilities

A world-wide set of deep space stations (DSSs) with large antennas, low-noise phase-lock receiving systems, and high-power transmitters provide radio communications with spacecraft. The DSSs and the deep space communications complexes (DSCCs) they comprise are given in Table 1.

Radio contact with a spacecraft usually begins when the spacecraft is on the launch vehicle at Cape Kennedy, and it is maintained throughout the mission. The early part of the trajectory is covered by selected network stations of the Air Force Eastern Test Range (AFETR) and the MSFN of the Goddard Space Flight Center,[1] Normally, two-way communications are established between the spacecraft and the DSN within 30 min after the spacecraft has been injected into lunar, planetary, or interplanetary flight. A compatibility test station at Cape Kennedy (discussed later) monitors the spacecraft continuously during the launch phase until it passes over the local horizon. The deep space phase begins with acquisition by either DSS 51, 41, or 42. These and the remaining DSSs given in Table 1 provide radio communications to the end of the flight.

To enable continuous radio contact with spacecraft, the DSSs are located approximately 120 deg apart in longitude; thus, a spacecraft in deep space flight is always within the field-of-view of at least one DSS, and for several hours each day may be seen by two DSSs. Furthermore, since most spacecraft on deep space missions travel within 30 deg of the equatorial plane, the DSSs are located within latitudes of 45 deg north or south of the equator. All DSSs operate at S-band frequencies: 2110–2120 MHz for Earth-to-spacecraft transmission and 2290–2300 MHz for spacecraft-to-Earth transmission.

To provide sufficient tracking capability to enable useful data returns from around the planets and from the edge of the solar system, a 64-m (210-ft) diam antenna network will be required. Two additional 64-m (210-ft) diam antenna DSSs are under construction at Madrid and Canberra, which will operate in conjunction with DSS 14 to provide this capability. These stations are scheduled to be operational by the middle of 1973.

B. Compatibility Test Facilities

In 1959, a mobile L-band compatibility test station was established at Cape Kennedy to verify flight–spacecraft–DSN compatibility prior to the launch of the *Ranger* and *Mariner* Venus 1962 spacecraft. Experience revealed the need for a permanent facility at Cape Kennedy for this function. An S-band compatibility test station with a 1.2-m (4-ft) diam antenna became operational in 1965. In addition to supporting the preflight compatibility tests, this station monitors the spacecraft continuously during the launch phase until it passes over the local horizon.

Spacecraft telecommunications compatibility in the design and prototype development phases was formerly verified by tests at the Goldstone DSCC. To provide a more economical means for conducting such work and because of the increasing use of multiple-mission telemetry and command equipment by the DSN, a compatibility test area (CTA) was established at JPL in 1968. In all essential characteristics, the configuration of this facility is identical to that of the 26-m (85-ft) and 64-m (210-ft) diam antenna stations.

The JPL CTA is used during spacecraft system tests to establish the compatibility with the DSN of the proof test

[1]The 9-m (30-ft) diam antenna station established by the DSN on Ascension Island during 1965 to act in conjunction with the MSFN orbital support 9-m (30-ft) diam antenna station was transferred to the MSFN in July 1968.

model and development models of spacecraft, and the Cape Kennedy compatibility test station is used for final flight spacecraft compatibility validation testing prior to launch.

II. Ground Communications Facility

The GCF provides voice, high-speed data, wideband data, and teletype communications between the SFOF and the DSSs. In providing these capabilities, the GCF uses the facilities of the worldwide NASA Communications Network (NASCOM)[2] for all long distance circuits, except those between the SFOF and the Goldstone DSCC. Communications between the Goldstone DSCC and the SFOF are provided by a microwave link directly leased by the DSN from a common carrier.

Early missions were supported by voice and teletype circuits only, but increased data rates necessitated the use of high-speed circuits for all DSSs, plus wideband circuits for some stations.

[2]Managed and directed by the Goddard Space Flight Center.

III. Space Flight Operations Facility

Network and mission control functions are performed at the SFOF at JPL. The SFOF receives data from all DSSs and processes that information required by the flight project to conduct mission operations. The following functions are carried out: (1) real-time processing and display of radio metric data; (2) real-time and non-real-time processing and display of telemetry data; (3) simulation of flight operations; (4) near-real-time evaluation of DSN performance; (5) operations control, and status and operational data display; and (6) general support such as internal communications by telephone, intercom, public address, closed-circuit TV, documentation, and reproduction of data packages. Master data records of science data received from spacecraft are generated. Technical areas are provided for flight project personnel who analyze spacecraft performance, trajectories, and generation of commands.

Reference

1. *The Deep Space Network*, Space Programs Summary 37-50, Vol. II, pp. 15–17. Jet Propulsion Laboratory, Pasadena, Calif., Mar. 31, 1968.

Table 1. Tracking and data acquisition stations of the DSN

DSCC	Location	DSS	DSS serial designation	Antenna		Year of initial operation
				Diameter, m (ft)	Type of mounting	
Goldstone	California	Pioneer	11	26 (85)	Polar	1958
		Echo	12	26 (85)	Polar	1962
		(Venus)[a]	13	26 (85)	Az-El	1962
		Mars	14	64 (210)	Az-El	1966
—	Australia	Woomera	41	26 (85)	Polar	1960
Tidbinbilla	*Australia*	*Weemala* (formerly Tidbinbilla)	42	26 (85)	Polar	1965
		Ballima (formerly Booroomba)	43	64 (210)	Az-El	Under construction
—	South Africa	Johannesburg	51	26 (85)	Polar	1961
Madrid	Spain	Robledo	61	26 (85)	Polar	1965
		Cebreros	62	26 (85)	Polar	1967
		Robledo	63	64 (210)	Az-El	Under construction

[a]A research-and-development facility used to demonstrate the feasibility of new equipment and methods to be integrated into the operational network. Besides the 26-m (85-ft) diam az–el-mounted antenna, DSS 13 has a 9-m (30-ft) diam az–el-mounted antenna that is used for testing the design of new equipment and support of ground-based radio science.

DSN Simulation System

H. C. Thorman
DSN Engineering and Operations Office

This article describes the upgrading of the DSN simulation system which was accomplished to provide support of DSN development, testing, and training activities in 1970 and 1971.

I. Introduction

The DSN simulation system provides real-time insertion of simulated tracking, telemetry, command, monitor and operations control systems data into the DSN. Data flows originating from the simulation system are used extensively in testing and training activities to prepare the DSN and its users for coverage of planned missions.

Functional design of the DSN simulation system for the 1970 to 1971 era, and the baseline configuration of the system for *Mariner* Mars 1971 test support, were described in Refs. 1 and 2. The system requirements outlined therein have since been implemented, and the system has been utilized by the DSN and by Mission Operations for MM'71 pre-launch and pre-orbital testing and training activities. Simulation support of *Pioneer F* pre-flight activities has recently begun.

II. System Description

The DSN simulation system consists of the DSN simulation center (SIMCEN) at JPL and the DSIF simulation conversion assemblies (SCA) at the deep space stations. The GCF provides communications among the elements of the system. A functional diagram of the system is shown in Fig. 1.

The system is designed to operate in any or all of the following three basic modes:

(1) *Short-loop mode, SIMCEN/SFOF.* The SIMCEN receives high-speed data from the SFOF and sends simulated DSIF teletype, high-speed, and wideband data to the SFOF; SIMCEN operators provide simulated DSS voice information to the DSN Operations Center.

(2) *Long-loop mode, SIMCEN/DSIF/SFOF.* The SIMCEN sends simulated spacecraft data via GCF high-speed and wideband circuits to one or more SCAs for conversion and insertion into DSS receptacles; SIMCEN also sends SCA control and text messages via high-speed circuits. SIMCEN receives high-speed data from the DSS and extracts information needed for responsive simulation. SIMCEN and DSS-simulation operations are coordinated by voice or teletype messages.

(3) *SCA stand-alone mode, SCA/DSS.* The SCA provides on-site simulation of spacecraft signal characteristics and fixed-pattern data for insertion into DSS receptacles.

III. System Implementation

Figure 2 shows a schematic summary of the system capabilities resulting from hardware and software improvements outlined below.

A. Hardware

The following items of new equipment were added to the DSN simulation system in 1970:

(1) Ten complete simulation conversion assemblies (SCA) in the DSIF, utilizing existing XDS 910 computers. Each SCA is equipped with two input-communications buffers, four output bit-stream generators, two block encoders, one convolutional encoder, four subcarrier modulators, two mixing subassemblies, and two carrier attenuation controllers.

(2) Ten RF-carrier simulation assemblies. Each assembly has two S-band-frequency test transmitters to feed the DSS receivers with carriers modulated by the SCA output. The assembly also includes signal-level attenuators, which are remotely controlled by the SCA.

(3) Additional GCF multiplexing, transmitting, receiving and demultiplexing equipment throughout the DSN, permitting communications between SIMCEN and DSIF or SFOF via three full-duplex high-speed data (HSD) channels and one half-duplex wideband data (WBD) channel simultaneously.

(4) Additional bit stream generators and receivers for interfacing EMR 6050 input/output channels to the GCF HSD and WBD communication terminals.

(5) Additional core units for the EMR 6050 in SIMCEN to increase the computer memory capacity to 32,000 words.

(6) Seven interactive television (IATV) units and two printers in the SIMCEN operations areas, and associated interface equipment at the EMR 6050 computer, to provide real-time control and display.

(7) Interface equipment connecting the Univac 1108 computers in the JPL Scientific Computing Facility (SCF) to the EMR 6050 computer in SIMCEN (50,000-bps capacity).

B. Software

The following new computer programs were designed and developed to implement the 1970 to 1971 simulation system functional requirements:

(1) *SCA Program.* The Data Routing Operations Program for the XDS 910 computer of the SCA provides:

(a) Generation and/or storage of test-data patterns for SCA stand-alone operating mode.

(b) Detection and input processing of data blocks received on up to two HSD or one HSD and one WBD communication channels.

(c) Extraction of data from specified portions of HSD message blocks and routing of data to ouput buffers.

(d) Output of data on up to four independent channels at controlled rates.

(e) Computer control of signal-conditioning simulation devices for data encoding, subcarrier frequency modulation and mixing, and carrier attenuation.

(f) Execution of SCA control functions in response to HSD messages or local entries.

(g) Printout of status and alarm messages and HSD text messages on local typewriter.

(2) *SIMCEN Programs.* Programs written for the EMR 6050 computer include:

(a) Executive system routines to provide formatting and distribution of data from two simulated spacecraft to three HSD and one WBD output channels.

(b) Executive system routines to provide drum-to-core overlay of subprograms for real-time simulation of tracking, telemetry, command, and monitor data.

(c) Tracking data subprogram to simulate DSIF output for two spacecraft, 3 DSSs.

(d) Telemetry data subprogram to generate controllable data patterns for two spacecraft, 3 DSSs.

(e) Command system subprogram to simulate DSIF receiving of command messages from SFOF and outputting verification, confirmation, abort and alarm messages by up to 3 DSSs with two command processors each.

(f) Station data subprogram to provide modeling of 3 DSSs, with real-time output of simulated monitor status/performance data and monitor summary data.

(g) Interface program for EMR 6050 to accommodate Project-supplied dynamic spacecraft math model data from SCF Univac 1108 computer and to input commands from the DSN to the spacecraft model.

References

1. Thorman, H. C., "Simulation System," in *The Deep Space Network*, Space Programs Summary 37-61, Vol. II, pp. 3–7. Jet Propulsion Laboratory, Pasadena, Calif., January 31, 1970.

2. Laeser, R. P., "*Mariner* Mars 1971 Mission Support," in *The Deep Space Network*, Space Programs Summary 37-61, Vol. II, pp. 18–22. Jet Propulsion Laboratory, Pasadena, Calif., January 31, 1970.

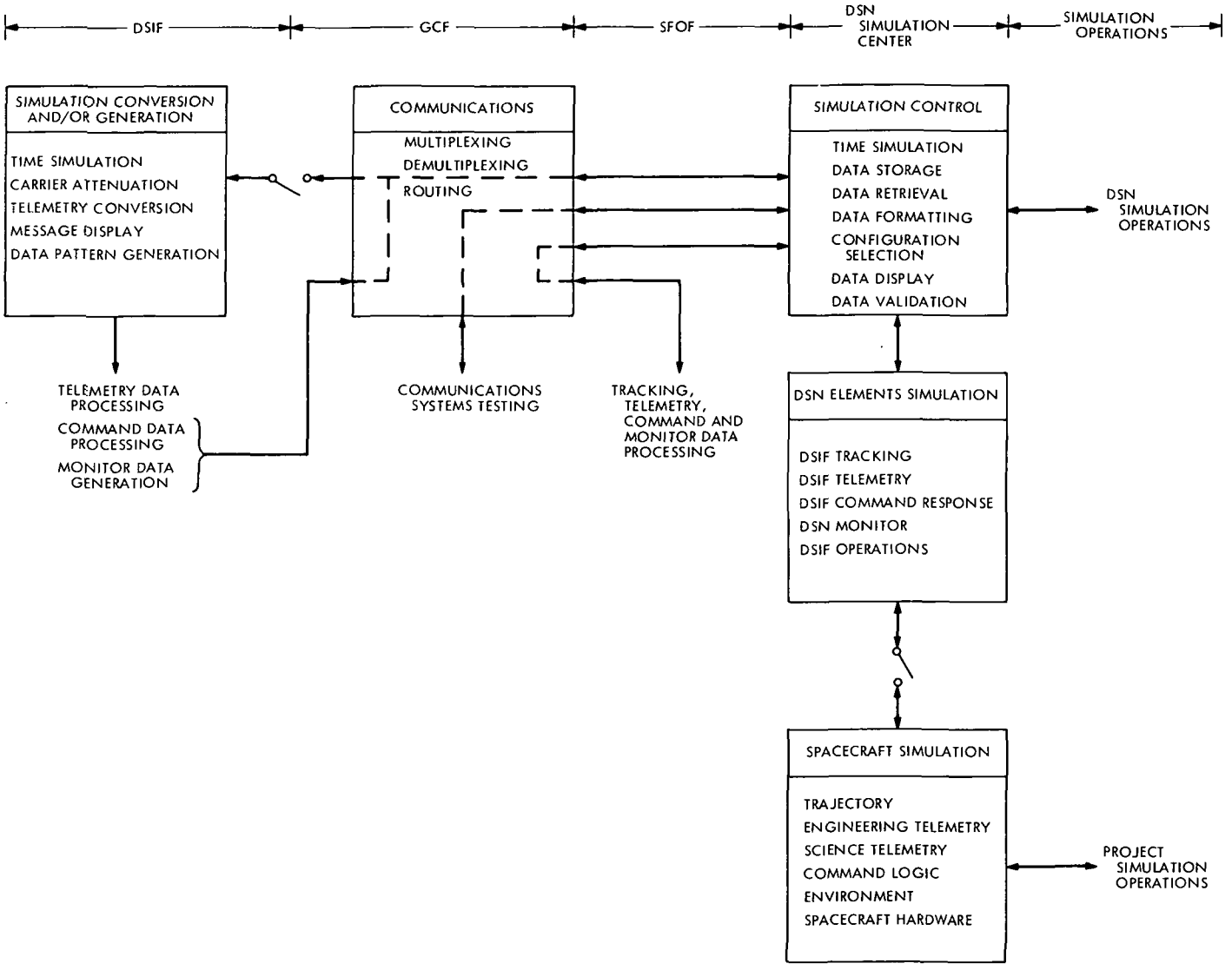

Fig. 1. Functional diagram of DSN simulation system for 1970–1971 era

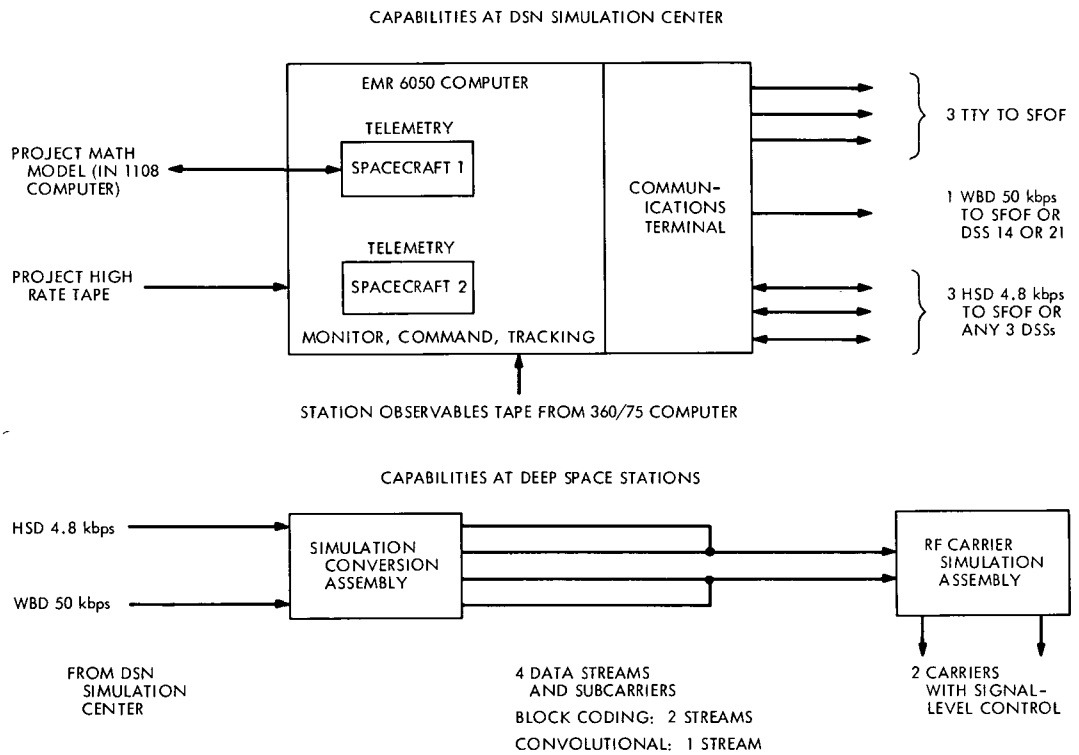

Fig. 2. DSN simulation system capabilities

DSN Telemetry System Tests

W. J. Kinder and R. S. Basset
DSN Engineering and Operations Office

The overall DSN System test plan, as edited for the DSN multi-mission Telemetry System, is briefly described. Specific results, with delivered Mariner Mars 1971 telemetry software, are presented in relation to this test plan. Recommendations are included for future system demonstration, specifically as to system documentation and training.

I. Introduction

As stated in the DSN Standard Test Plan, the purpose of the DSN system tests is to verify that DSN capabilities meet multi-mission design/operational standards and that systems can be transferred to DSN Operations. Particular DSN telemetry system tests and their objectives are shown in Table 1. With the arrival of *Mariner* Mars 1971 DSIF/SFOF software and GCF's HS/WB system, the DSN inaugurated its system test activity.

Since both the DSIF and SFOF telemetry software were being delivered in phases or models, DSN telemetry test procedures were written for scheduled delivered capabilities, progressing toward a completed system in support of *Mariner* Mars 1971 orbital operations.

II. Test Activity

During December 1970 and January 1971, DSN system tests to verify interfaces and data flow were conducted with SFOF, GCF, and CTA 21 elements of the DSN Telemetry System. Throughput of 8⅓- and 33⅓-bps engineering data was attempted. Serious problems were encountered, namely, the inability to process complemented telemetry data, abnormal number of missing data blocks, and the high failure rate of the 360/75 computers. Testing was further hampered by lack of any user guide information, lack of available telemetry formats, and the competition for computer time between system test activity and facility development. During the latter phases of these tests, DSSs were scheduled for support with mixed results. In summary, 8⅓- and 33⅓-bps simulated spacecraft engineering data were processed through the DSS telemetry system.

Early in March 1971, with delivery of the SFOF model 2 and the DSIF phase 2 software, DSN multimission and performance testing began. Building upon previous DSN tests, the telemetry system demonstrated processing of simulated spacecraft 8⅓- and 33⅓-bps engineering data for output and display on TTY, line printer, and digital TV devices. Telemetry system standard processors, i.e., engineering unit conversion, alarm limits, and data range suppression, were exercised.

In the beginning of the test activity, the 360/75 computer experienced excessive backlogging of the engineering data being output to display devices. Also, data backlogging was observed when large background processes, other than the operational telemetry program, were concurrently operating in the same 360/75 computer. Telemetry data recall from the DSIF's original digital data record and from the SFOF's digital system data record was accomplished. However, if the 360/75 computer should fail, there is no file protection for the system data record. On April 23, 1971 this test activity culminated in a four-station, four-spacecraft stream combination telemetry system test without noting any serious data backlogging.

A third round of DSN telemetry system testing began with the delivery of the SFOF model 4 and the DSIF phase 4 software in late August 1971. Simulated spacecraft 50-bps science and 8⅓- and 33⅓-bps engineering data were throughput to the DSN telemetry system. No failures of the SFOF 360/75 processor occurred as a result of data backlogging. One- and two-kbps science data were also received from the DSIF by the 360/75 and logged. The DSN Telemetry Analysis Group assisted in isolating simulation problems with the new DSIF simulation conversion assemblies. Another new telemetry feature, the automatic data stream selection routine, was found to function properly. This allows the selection of the best telemetry stream for comprehensive processing and display, from two separate DSSs tracking the same spacecraft. Background sequential operation of the user analysis program along with the operational telemetry program in the same 360/75 caused no interference. The *Mariner* Mars 1971 Project Mission and Test Computer confirmed medium (1–2 kbps) and high (8–16 kbps) rate data flow through the system. Demonstration of data recall from the system data record and better control of the DSN telemetry system elements due to better visibility with added new television formats was witnessed by the DSN Telemetry Analysis Group.

III. Conclusion

These tests have confirmed the basic soundness of the DSN test plan and ensuing procedures. Complete multimission test objectives of the test plan will have to wait until the delivery of the DSIF and SFOF *Pioneer F* software to operate in the same DSN telemetry processors. These tests are scheduled for December 1971. In retrospect, it is hoped that the facilities schedule will allow adequate test time to be better prepared for the system level tests that follow. Operator training was also deficient due to the stringent test schedule and competition for resources. It would help considerably if even the preliminary facility documentation was available for system testing. DSN system transfer agreements between development and operational interests were executed for *Mariner* Mars 1971 launch support capabilities. Presently, transfer agreements are being pursued for *Mariner* Mars 1971 delivered orbital capabilities.

Table 1. Telemetry system tests

Test and objectives	Description	Prerequisites	Standards	Resources	Participants
1. DSN system test: Verifies interfaces, data flow.	Repetitive frames of S/C data are generated by SIMCEN, routed via an HSD to a DSS, where SCA and MM test set transform them to RF signals. These are acquired, demodulated, data is extracted and formatted and transmitted via HSD to the SFOF. Data is decommutated, routed and displayed by the 360/75 to the telemetry analysis area where the tests are conducted and results are analyzed.	Applicable facility systems have been tested and transferred to operations.	820-2 Latest edition Section III.	1 DSS: TCD, receiver/exciter, simulation conversion assembly, multimission test set GCF: 1 HSD, 1 TTY, 1 VOICE SFOF: 360/75, Telemetry Analysis Area SIMCEN SOFTWARE: TCD/MMT S/W, SCA S/W, MMT S/W, TCD/MMT diagnostics, MDR/EDR S/W, General Purpose Commutation, Simulation Center S/W for 2 S/C with up to 4 subcarriers.	Test Supervisor: DSN S.E. Test Conductor: DSN Ops Chiefs. Test Associate: Contemporary P.E. DSIF Facility Engineer. SFOF Facility Engineer. DSN Telemetry Analysis Supervisor. Telemetry Analysis Group and supporting facility personnel.
2. DSN system multiple-mission test: Verifies system integrity, multiple-mission capability.	Following additions to test 1: Generation of configuration and standard and limits messages by the telemetry analysis group relayed to and executed by the facilities. Periodic generation of TM system status messages relayed to Ops control. Demonstration of generation within 24 h of telemetry system data record.	Completion of DSN system test (telemetry).	820-2 Latest edition Section IIB.	Same as above.	Same as above.
3. DSN system performance test: Measures system parameters (bit rates, subcarrier frequencies) and modes of operation.	Following additions to test 2: With SIMCEN exercising telemetry system, bit rates are varied and telemetry modes are demonstrated. Tracking and command systems are operated simultaneously. This test is conducted under conditions simulating a typical planetary mission profile. Sharing of processors with the other DSN systems, on a non-interference basis, is demonstrated. This includes real-time changes to the telemetry system.	Completion of multiple-mission tests of telemetry and command systems and completion of all tracking system tests.	820-2 Latest edition Sections IID and IV.	Same as above plus command plus tracking resources.	Same as above plus command plus tracking test participants.

Pioneer Mission Support

A. J. Siegmeth
Mission Support Office

The DSN plans to use the Mark III system configuration for the tracking and data acquisition support for the Pioneer F and G mission. As a continuation of the description of the network systems, the configurations of the simulation, monitoring, and operations control systems are given. Block diagrams show the planned functions, data flow methodology and the interfaces between the subsystems and the three DSN facilities.

I. Introduction

Continuous reports published in previous issues of the DSN Progress Report (Refs. 1–4) contained a description of the *Pioneer F* and *G* mission profile, spacecraft, conical scanning system (CONSCAN), and the specific objectives of the scientific instrumentation. Special emphasis was given on the elaboration of mission characteristics which interface with the tracking and data acquisition functions.

The functional configuration, data flow methodology, and interfaces of the simulation, monitoring, and operational control systems of the Mark III DSN are presented.

II. DSN Simulation System

The purpose of the DSN simulation system is to create realistic simulation of expected operational environments for testing and training to prepare the DSN and its users for support of planned missions. This system also provides a capability for DSN and spacecraft failure mode isolation. The DSN simulation system is described in Fig. 1.

III. DSN Monitor System

This system provides the capability for sensing strategic characteristics of the various elements of the DSN, processing, displaying the data for use by DSN operations personnel, and for storing data for later analysis or reference. Monitor data are used for determining DSN status and configurations, for guidance in the direction of operations, for furnishing alarms of nonstandard conditions, and for analysis of the quantity and quality of data provided to the flight project.

The DSN monitor system as it will exist at the SFOF, GCF, and DSSs 12, 14, 41, 51, and 62 is described in Fig. 2. This implementation plan utilizes the DIS II (16-K core) of the DSIF. Figure 3 presents the DSN monitoring system configuration as planned for the SFOF, GCF, and DSSs 11, 42, and 61.

IV. DSN Operations Control System

This system is the mechanism necessary for directing the operations of the DSN facilities and systems in support of flight projects. The functions of operations control are affected by both the DSN operations chief and the facility chiefs. Plans and procedures assure coordination and provide real-time direction in the event of anomalous conditions so that optimum support to flight projects is provided. The operations control functions are: operating the network, scheduling, discrepancy reporting, sequence-of-events generation, master data records production, and operational document control. The DSN operations control system is described in Fig. 4.

References

1. Siegmeth, A. J., "*Pioneer* Mission Support," in *The Deep Space Network Progress Report*, Technical Report 32-1526, Vol. II, pp. 6–17. Jet Propulsion Laboratory, Pasadena, Calif., April 15, 1971.
2. Siegmeth, A. J., "*Pioneer* Mission Support," in *The Deep Space Network Progress Report*, Technical Report 32-1526, Vol. III, pp. 7–19. Jet Propulsion Laboratory, Pasadena, Calif., June 15, 1971.
3. Siegmeth, A. J., "*Pioneer* Mission Support," in *The Deep Space Network Progress Report*, Technical Report 32-1526, Vol. IV, pp. 13–21. Jet Propulsion Laboratory, Pasadena, Calif., Aug. 15, 1971.
4. Siegmeth, A. J., "*Pioneer* Mission Support," in *The Deep Space Network Progress Report*, Technical Report 32-1526, Vol. V, pp. 4–16. Jet Propulsion Laboratory, Pasadena, Calif., Oct. 15, 1971.

Table 1. DSN Simulation system (Fig. 1)

EQUIPMENT/SUBSYSTEM CAPABILITIES

Ⓐ High-speed data line is full duplex, one per DSS

SOFTWARE CAPABILITIES

ⓐ *DSS Simulation Conversion Assembly (SCA), 910 Real-Time Program (Control from DSN Simulation Center)*

A. *Input Processing*

1. Input process message blocks from one high-speed data (HSD) line, with contents listed in ①

B. *Output Processing*

1. Output process simulated Pioneer telemetry on Channel No. 1. Encoding to be switched in as required by control message. (Three additional output channels available as alternates, but only for uncoded data.)
2. Output process bit rate control, subcarrier frequency control, modulation index control, and carrier attenuation control.

ⓑ *DSS SCA 910 Data Generation Program (Local Control)*

A. *Input Processing*

Input process operator controls and initialization

B. *Internal Processing*

Generate telemetry data patterns and attenuation control data according to operator controls and initialization

C. *Output Processing*

1. Output process telemetry data stream
2. Output process bit rate control, subcarrier frequency control, modulation index control, and attenuation control according to operator inputs

ⓒ *6050 Computer Program (DSN supplied)*

A. *Input Processing*

Input process:

1. Spacecraft math model data from the 1108
2. Spacecraft position as a function of time, in terms of station centered angles, range rates, and range from phi-factor tape obtained from 360/75 PREDICTS Program
3. DSS parameters which can be affected by the spacecraft condition. (Used for transmission to SCA in long-loop and to vary Monitor data in short-loop)
4. All HSD from up to three DSSs, when in long-loop mode, discarding all but command data, monitor data, and SCA display messages
5. All HSD to three (maximum) DSSs from SFOF, disregarding all but command system and standards and limits traffic (short-loop mode only)
6. Processing control messages for 6050 or 1108 and display-control messages

B. *Output Processing*

Output process and format:

1. HSD as listed in ① and ② for up to three DSSs
2. TTY tracking data as listed in ④
3. Displays of system status and selected data
4. Processing control messages to 1108
5. Anticipated and actual commands to 1108

C. *Internal Processing*

1. Generate telemetry data streams (any rate) correctly formatted (frame sync words, etc.), but with controllable-pattern data values
2. Store the decommutated telemetry data received from the 1108 for construction of HSDA message blocks
3. Generate tracking data, based upon PREDICTS phi-factor tape input, for up to three DSSs. Effect a maneuver response in the data under input control of maneuver parameters
4. Generate DSS responses, in terms of command and monitor system data, when in the short-loop mode
5. Generate DSS parameters which may vary with change in spacecraft or DSS conditions

ⓓ *1108 Program (Project-supplied)*

A. *Input Processing*

Input Process:

1. Program control (including initialization and inputting of constants) from 6050 or 1108 I/O console
2. Anticipated or actual commands from 6050

B. *Output Processing*

Output process:

1. Spacecraft commutated telemetry output
2. Spacecraft parameters which affect DSS status
3. Spacecraft parameters which affect tracking data

C. *Internal Processing*

1. Generate with math models command responsive telemetry at any Pioneer data rate

Table 2. DSN monitoring system (Fig. 2)

EQUIPMENT/SUBSYSTEM CAPABILITIES

Ⓐ Located in DSN Operations Area of SFOF

Ⓑ One 4800-bps full-duplex line, per DSS, shared by all systems; 1200-bit block size

SOFTWARE CAPABILITIES

ⓐ *DSIF Monitor System Phase II Program*

A. *Input Processing*

Input process:

1. Tracking parameter values and indicator settings from TDH-1[a] for one spacecraft consisting of the following:
   (a) Hour angle and declination angle
   (b) Doppler counts from counter
   (c) Range units
   (d) Exciter voltage-controlled oscillator (VCO) reference frequency
   (e) Doppler resolver time
   (f) Tracking data sample rate
   (g) Doppler, angle, and range data condition codes
   (h) Station ID
   (i) Spacecraft ID
   (j) Pass number
2. Input process DSS telemetry system monitor data from all TCP computers via the 24-bit parallel registers.
3. Parameter values and indicator settings associated with station hardware configuration for one or two spacecraft:
   (a) SDA parameters and indicators
   (b) Receiver parameters and indicators including doppler and range indicators
   (c) Cassegrain and acquisition aid, right or left circular polarization indicators
   (d) Antenna servo modes
4. DSS command system monitor data from all TCP computer via the 24-bit parallel registers.
5. Instrumentation parameter values consisting of:
   (a) Ground AGC and SPE values
   (b) Transmitter power
6. Time for labeling
7. Predicts and operations data received via HSDL from SFOF
8. Operator messages
9. Servo angle error values, antenna pointing subsystem (APS) modes and status, and angle data condition from APS computer program
10. Selected GCF HSD monitor data from DSS Comm equipment subsystem

B. *Output Processing*

Output process and format:

1. Parameter values and indicator settings (full DSS status) into HSD blocks for transmission to the SFOF 360/75s every 5 s
2. Selected monitor parameters and alarms to the station manager console area on a DTV display
3. Digital instrumentation subsystem (DIS) operator control messages to a page printer
4. Digital recording of monitor HSD blocks; capable of replay, postpass.
5. Page prints of predicts and operations data
6. Magpak recording of predicts

C. *Internal Processing*

1. The following calculations are made for the tracking system:
   (a) Compute doppler measurement in counts per time unit
   (b) Compute doppler residuals using predicts and compute mean and standard deviation of the residuals
   (c) For alarm purposes, compare criteria data with selected tracking data, and compute mean and standard deviation for angle residuals
   (d) Calculate doppler alarm limits from least squares or Lagrangian extrapolation, and perform blunder point alarm calculation using supplied limits
   (e) Calculate range residual, range mean and standard deviation
   (f) Calculate noise detection range parameter for range rejection
2. The following calculations are made for the monitor system:
   (a) Convert DSS static phase error (SPE) from volts to degrees
   (b) Convert RF angle errors from volts to degrees when angle channels have been calibrated
   (c) Convert transmitter power from volts to kilowatts
   (d) Register GCF (station comm) alarm occurrence; reset after each HSDA block output to DSN Monitor in SFOF

ⓑ *Communication Processor Program, Monitor portion*

In addition to its primary function of automatic message switching for TTY circuits, the following monitor functions are performed by the CP program:

A. *Input Processing*

Input process:

1. Operator Commands which control and direct HSD Line monitoring
2. Parameters which are received for each HSDA line being monitored. The signals are generated by GCF error detection decoders on the HSD Lines and are passed to a teletype character generator which outputs TTY characters to the GCF communications processor (CP).

B. *Output Processing*

Output process and format:

1. Data blocks to each active 360/75 comprised of the following:
   (a) The on-line CP and its busy rate
   (b) The mode of the off-line CP
   (c) Accounting information and status on each HSDA line monitored
2. Data to the digital TV for each HSDA line being monitored
3. Advisory messages to the CP operator when the carrier ON/OFF status changes for a HSD line being monitored
4. Account blocks for each HSDA line to the CP log tape and to the 360/75 on termination of a monitoring period

Table 2 (contd)

C. *Internal Processing*

1. The CP calculates the time it is actively processing data as a percentage of time available for such processing in a given period (busy rate)
2. The following internal calculations are performed by each HSD line monitored:
   (a) Error rate
   (b) Total amount of carrier off time
   (c) Number of null sample periods
   (d) Total number of sample periods

© *The 360/75 DSN Monitor Real Time (RT) Software*
Part I—Collection and Processing of Monitor Data for Real-Time Display

A. *Input Processing*

Input process:

1. HSD blocks containing DSIF and station command monitor data: Parameter values, and indicator settings every 5 seconds, summary data every 30 seconds
2. GCF monitor messages from SFOF communications terminal subsystem via normal input lines from the CP
3. Operator messages input from the DSN monitor area
4. MCD set generation, modification and storage (see following Part III)

B. *Output Processing*

1. *Output process DSN Monitor SDR*

   All input data shall be logged on magnetic tape in a format suitable for playback on the 360/75, or for use as input to the 360/75 post-processor program

2. *Output process digital TV displays*

   DTV displays will be available over computer-driven channels, allowing, for example, simultaneously, display of the same information for several tracking stations. Many of the displays have more than one selectable format, allowing the grouping of display parameters as subsets. The displays fall into three basic groups:
   (a) DSN operations
   (b) Facility operations
   (c) System operations

   Each contains a spectrum of displays and format, ranging from gross status and alarming to detailed status and performance data for troubleshooting. By procedurally controlling the assignment of displays to the DTV channels, the number of tracking stations that are simultaneously monitored is selectable to all DSN stations with digital instrumentation system (DIS II) monitor capability.

3. *Output Process Monitor Alarms*

   All monitor alarms are printed on TTY character printers in the DSN area of the SFOF. Alarms are also displayed on DTV adjacent to the anomalous parameter

C. *Internal Processing*

Internal processing of monitor data is restricted to:

1. Display definition
2. Formatting for displays
3. Routing of display data
4. Conversion of monitor input parameters for display purposes
5. *Comparison of real-time data with MCD sets to yield alarms* (see Part III)

Part II—360/75 Processors for Other Systems

The mission-dependent processor supplies to the mission-independent system accounting and status information on all telemetry tracking and command streams currently being processed or logged.

Part III—Monitor Criteria Data Control Program

The purpose of monitor criteria data (MCD) sets is to provide facility configuration and tolerance masks against which subsystem configuration and performance can be compared. Configurations different from the one defined by the MCD set, or parameter variations larger than the tolerances in the MCD set cause an alarm.

Part IV—Data Summaries

This part of the program uses a monitor data file as input and generates summary reports.

1. *Input Processing*
   (a) Input process the data from file
   (b) Input process control cards via magnetic tape
2. *Output Processing*
   Output process on to 1443 line printer in DSN Operations Area and into Ops control output router for transmission to DSS

Part V—DSN Status MDR

This part of the program accepts and time-merges replayed monitor data from the facilities on to the monitor SDR. When all available data have been merged, the monitor SDR becomes the DSN status MDR.

[a]Does not apply to prototype DSIF Tracking System DTS at DSS 14.

Table 3. DSN operations control system (Fig. 4)

EQUIPMENT CAPABILITIES

A GCF HSD Lines: one-half of full duplex 4800 bps line with 1200-bit data blocks

B DSIF Processor for Operations Control Messages: shared computer with other DSS functions

C SFOF/DSN real time and nonreal-time processor: redundant IBM 360/75's shared with other system processing and project processing

D Non-real Time Processor: single Univac 1108 in scientific computer facility (SCF), controlled by DSN; project analysis software and DSN Simulation System software only

E Project MSA: except as noted for display of DSN status (data flow paths ⑦ and ㉙), applies to both local and remote MSAs. (Systems Development Laboratory is defined as local MSA.)

F DSN simulation subsystem: shown for reference only. (See simulation system description for capabilities.)

SOFTWARE CAPABILITIES

a Telemetry Predicts: (For MM'71, obtained from project analysis program[a] and transferred to 360 via tape)

A. *Output Process*

1. Predicted downlink AGC as a function of time
2. Predicted subcarrier SNRs as a function of time
3. Items 2 and 3 are functions of spacecraft data mode
4. Other parameters are contained in TPAP output (such as uplink AGC) but are not extracted by DSN

ⓑ SFOF General Purpose Program in Master Control and User Interface Subsystem to Format Outbound Blocks

A. *Input Processing*

1. Tracking predicts from tracking system software
2. Telemetry predicts from telemetry predicts analysis program (TPAP) (MM'71 only[a])
3. DSN MCD sets from DSN monitor real-time software
4. DSN seven-day schedule software output
5. DSN SOE software output

B. *Internal Processing*

1. Accept data in formats defined by data source
2. Format HSD blocks in formats defined by Document 820-13

C. *Output Processing*

Route HSD blocks to SFOF Comm Terminal

ⓒ DSN Seven-Day Schedule Program

A. *Input Processing*

1. Accept midrange schedule as base schedule
2. Accept real-time change requests

B. *Internal Processing*

1. Modify seven-day schedule in accordance with approved real-time change requests
2. Tabulate listing of DSN resources committed at any point in time
3. Tabulate status of uncommitted resources at any point in time
4. Tabulate history of real-time changes to Seven-Day Schedule for selectable intervals

C. *Output Processing*

1. Transfer Seven-Day Schedule to Master Control and User Interface Subsystem (Program *b* above) for transmission to remote sites
2. Output items ⓒ to DTV for display to DSN operation via closed-circuit Television
3. Transfer seven-day schedule to DSN sequence of events (SOE) program for use as constraints (see ⓓ below)
4. Create historical file (tape) of DSN SOE resources as actually used

ⓓ DSN SOE PROGRAM[b]

A. *Input Processing*

1. Accept all supported projects' SOEs in machine language
2. Accept card and manual inputs to build or modify sequences
3. Accept card, manual, and machine language inputs (e.g., Tracking predicts to build or modify a subsequence library)
4. Accept card, manual and machine language inputs (e.g., seven-day schedule in ⓒ B. 3. above) to build or modify a constraints library
5. Accept card and manual inputs to define or modify format of outputs

B. *Internal Processing*

1. Identify all events which are keyed as "triggers" and insert subsequence(s) appropriate for each such event
2. Insert event time for each event in a subsequence; fixed delta-T if so defined, or use round-trip light time (RTLT), obtained via interface with tracking predicts if delta-T is trajectory dependent
3. Sort and time-order resulting master multimission sequence
4. Check resulting master multimission sequence against library of constraints (e.g., seven-day schedule for simultaneous mutually exclusive events)

C. *Output Processing*

1. Real-time alarms to SOE program operator of constraints violations
2. Uniquely identify each production run so that the "most recently produced" SOE for a given period of support operations can be easily and clearly recognized.
3. Output to 1443's in DSN Operations Area in SFOF and via master control and user interface subsystem (MCUIS) and HSDL to remote sites
4. Tailor outputs to individual users by suppressing predefined unwanted data from master multimission sequence
5. Output a predefined format to digital television system for display to DSN Operations via CCTV
6. Create historical file (tape) of each SOE production run

ⓔ DSIF Page Prints of Operations Control Information

A. *Input Processing*

1. Accept incoming HSD blocks
2. Check for blocks in errors by means of GCF error code
3. Check for mission blocks by consecutiveness of HSD block serial numbers

Table 3 (contd)

B. *Internal Processing* 1. Format for output to 132-column-line printer C. *Output Processing* 1. Produce page prints 2. Flag received lines suspected of errors 3. Insert dummy lines flagging suspected missing lines	B. *Internal Processing* 1. Create master data bank 2. Update individual discrepancy report entries if new data is input relative to that discrepancy report 3. Invoke security measures to protect discrepancy report data C. *Output Processing* 1. Output periodic reports to predefined recipients in predefined formats 2. Output special reports in a format which is determined by recipient in near-real time 3. Create historical tape file of data no longer needed in the active data bank
(f) *DSN discrepancy report (DR) Data Bank (Off-line Process with SCF Software)* A. *Input Processing* 1. Accept (DR) data manually transferred from discrepancy report forms to IBM cards 2. Accept instructions on format of output	

[a]To be replaced by DSN multimission telemetry predicts program prior to *Pioneer F* support operations

[b]This program is multimission. It is used by supported projects in data files assigned to them.

Page intentionally left blank

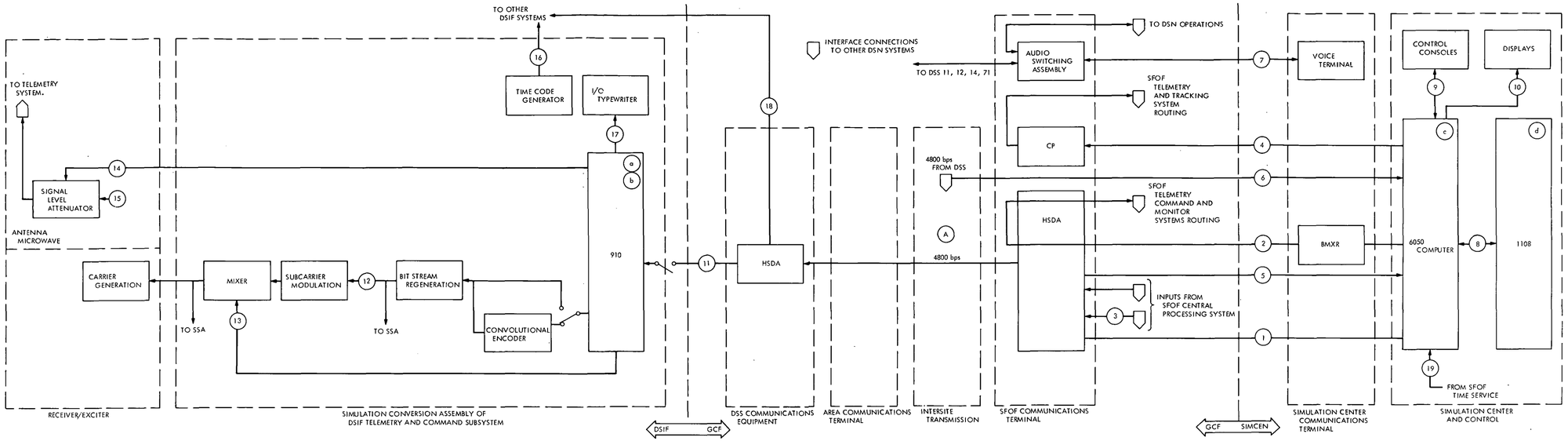

DATA FLOW PATHS

(1) SIMULATED DATA FORMATTED FOR HSDA TRANSMISSION, TO ANY DSS (LONG-LOOP MODE), AND CONSISTING OF THE FOLLOWING:
- a. TELEMETRY DATA BLOCKS (16 TO 2048 bps DATA RATES)
- b. BIT RATE, SUBCARRIER FREQUENCY, ATTENUATION AND MODULATION INDEX CONTROL INFORMATION
- c. SIMULATION INSTRUCTIONS

NOTE: DUPLICATED AT ANY GIVEN TIME FOR TWO OTHER DSSs (INCLUDING CTA 21, DSS 71) OR MSFN

(2) SIMULATED DATA FORMATTED FOR HSDA TRANSMISSION, SIMULATING OUTPUT OF ONE DSS TO SFOF (SHORT-LOOP MODE), AND CONSISTING OF THE FOLLOWING:
- a. TELEMETRY DATA BLOCKS (16 TO 2048 bps DATA RATES)
- b. MONITOR DATA
- c. COMMAND TRAFFIC
- d. PARTIAL STATUS AND SUPPLEMENTAL DATA
- e. HIGH-SPEED TRACKING DATA (DSSs 11, 14, 42, 61 SIMULATION ONLY)

NOTE: DUPLICATED FOR TWO OTHER DSS

(3) SFOF MESSAGES TO DSIF SYSTEMS MULTIPLEXED ON TO HIGH-SPEED DATA LINE

(4) TTY FORMATTED SIMULATED TRACKING DATA REPRESENTING UP TO THREE DSSs

(5) COMMAND AND STANDARD AND LIMITS RECEIVED FROM SFOF WHEN SIMULATION SYSTEM IS SIMULATING DSS

NOTE: DUPLICATED FOR TWO OTHER DSSs

(6) COMMAND AND MONITOR TRAFFIC FROM DSS, ALSO SCA DISPLAY (IF FROM DSS 11, 42, OR 61) PARALLEL-ROUTED TO 6050 (DUPLICATED FOR TWO OTHER DSSs)

(7) VOICE TRAFFIC TO DSIF FOR TEST COORDINATION AND TO DSN OPERATIONS FOR SIMULATION OF VARIOUS DSS OPERATING POSITIONS

(8) DATA TRANSFER FROM 1108 MATH MODEL TO 6050, AND CONTROL INFORMATION IN BOTH DIRECTIONS

(9) PROCESSING CONTROL INFORMATION

(10) SELECTED DATA AND SYSTEM STATUS

(11) HIGH-SPEED DATA BLOCKS CONTAINING DATA TYPES LISTED, NOTE (1), ITEMS a, b, c.

(12) CODED (32 TO 4096 sps) OR UNCODED (16 TO 2048 bps) TELEMETRY DATA STREAM

(13) MIXING RATIO (MODULATION INDEX) CONTROL

(14) S-BAND CARRIER ATTENUATION CONTROL

(15) S-BAND EQUIVALENT OF ONE SPACECRAFT DOWNLINK (WITHOUT DOPPLER)

(16) BINARY-CODED DECIMAL TIME CODE FOR USE THROUGHOUT DSS

(17) SIMULATION INSTRUCTIONS AND SIMULATION CONVERSION ASSEMBLY CONTROL AND DISPLAY

(18) COMMANDS TO TCP, MONITOR STANDARDS AND LIMITS TO DIS, AND TRAFFIC TO OTHER DSIF SYSTEMS FROM SFOF

(19) SIMULATED GMT AND INTERVAL TIMING INTERRUPT

(A) AND (a) TO (d) DEFINED IN TABLE 1

Fig. 1. DSN simulation system for *Pioneers* F and G at the 26- and 64-m antenna stations

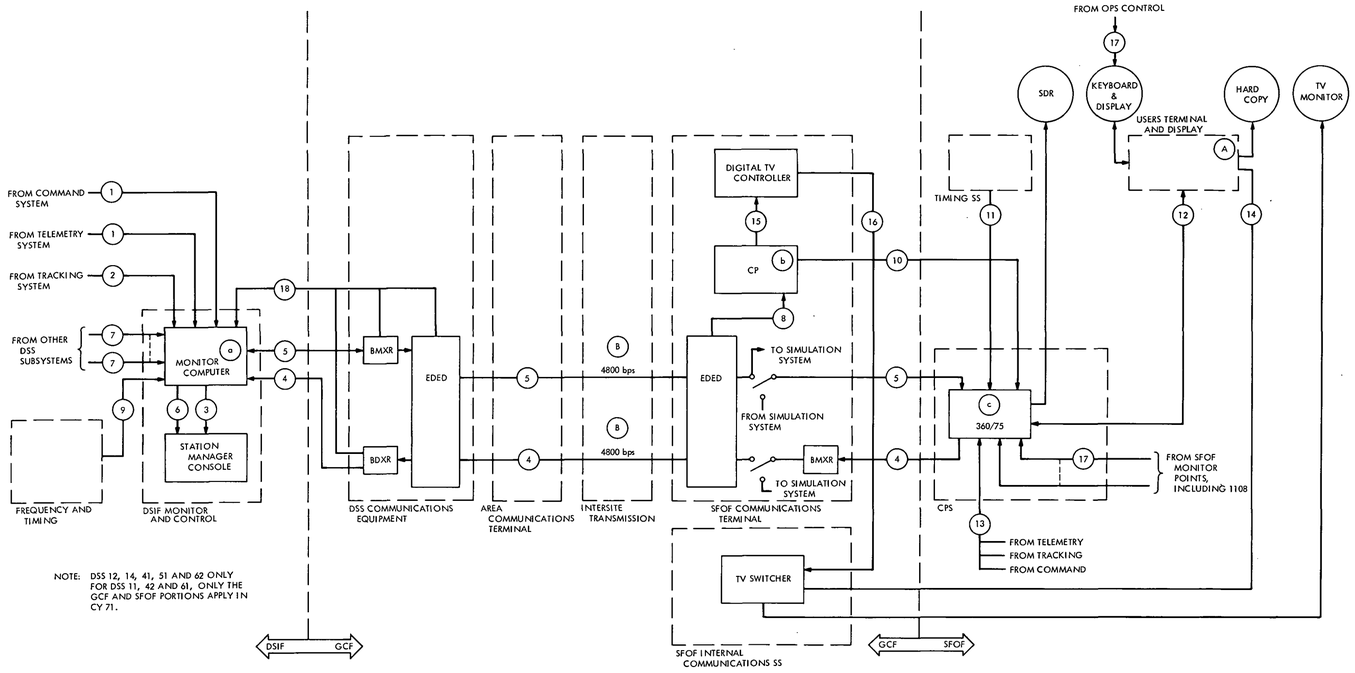

NOTE: DSS 12, 14, 41, 51 AND 62 ONLY FOR DSS 11, 42 AND 61, ONLY THE GCF AND SFOF PORTIONS APPLY IN CY 71.

DATA FLOW PATHS

(1) DSIF TELEMETRY SYSTEM AND COMMAND SYSTEM ALARMS AND STATUS (DOES NOT INCLUDE DECOMMUTATED SPACECRAFT DATA)
(2) DSIF TRACKING SYSTEM DATA, STATUS, AND ALARMS
(3) DSIF ALARMS FOR CORRECTIVE ACTION BY STATION MANAGER (NO GCF STATUS DATA OR ALARMS)
(4) DSS INSTRUMENT STANDARDS AND LIMITS (PREDICTS)
(5) DSS STATUS DATA; INCLUDES ALL DATA PROCESSED BY DSS MONITOR COMPUTER EXCEPT ALARMS FROM DSS INSTRUMENT STANDARDS AND LIMITS
(6) DSS TRACKING SYSTEM ALARMS FROM TRACKING ERROR DETECTION FUNCTION LOCATED IN MONITOR COMPUTER
(7) INSTRUMENT STATUS FROM OTHER DSS SUBSYSTEMS
(8) GCF HSD INSTRUMENT ALARMS FOR ALL HIGH-SPEED TRAFFIC INBOUND TO SFOF
(9) TIME
(10) GCF INSTRUMENT STATUS AND DATA STATUS TO 360/75
(11) TIME
(12) MONITOR PROGRAM/OPERATOR INTERPLAY, PLUS STATUS DISPLAYS
(13) DATA ALARMS GENERATED WITHIN SFOF, TRACKING, TELEMETRY, AND COMMAND SYSTEMS, AND PERIODIC PROCESSING STATUS MESSAGES. INCLUDES DECOMMUTATED S/C TELEMETRY.
(14) VIDEO IMAGES OF DIGITAL DISPLAYS
(15) GCF INSTRUMENT ALARMS FORMATTED FOR GCF CONTROL TV DISPLAY
(16) GCF ALARM DISPLAY FOR CORRECTIVE ACTION BY GCF CONTROL
(17) SFOF MONITOR DATA, BOTH 360/75 AND 1108
(18) SELECTED GCF STATION HSDA TERMINAL MONITOR DATA FOR RETURN TO SFOF

(A) AND (B) AND (a) TO (c) ARE DEFINED IN TABLE 2

Fig. 2. DSN monitoring system for *Pioneers* F and G at SFOF, GCF, and DSSs 12, 14, 41, 51, and 62

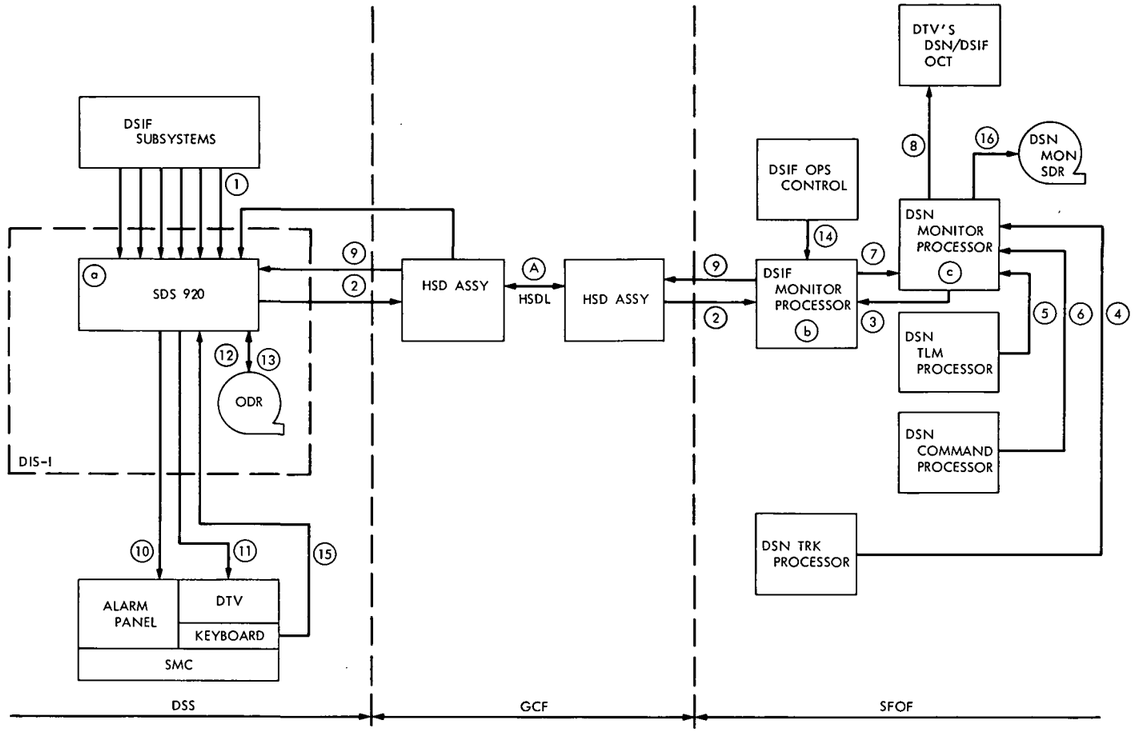

DATA FLOW PATHS

(1) RAW MONITOR DATA INPUTS
(2) RAW MONITOR DATA HSD BLOCKS
(3) SELECTED DSN MONITOR; INCLUDES PSEUDO-RESIDUALS, DECOMMUTED TELEMETRY
(4) PROCESSED TRACKING DATA AND ALARMS
(5) TELEMETRY SYSTEM MONITOR MESSAGES
(6) COMMAND SYSTEM MONITOR MESSAGES
(7) PROCESSED DSIF MONITOR DATA AND ALARMS
(8) MONITOR DTV DISPLAYS FOR DSIF/DSN OCT
(9) PROCESSED DSIF MONITOR DATA TO ORIGINATING DSS; INCLUDES DATA IN (3)
(10) ALARM SIGNALS TO STATION MONITOR AND CONTROL CONSOLE (SMC) ALARM PANEL
(11) DTV DISPLAYS
(12) NON-REAL TIME DUMP OF DSIF MONITOR ODR
(13) RAW MONITOR DATA TO LOG TAPE (ODR)
(14) OPERATION CONTROL OF DSIF PROCESSOR IN 360/75
(15) STATION MONITOR CONTROL FROM KEYBOARD
(16) DSN MONITOR SDR

EQUIPMENT/SUBSYSTEM CAPABILITIES

(A) ONE 4800-bps FULL-DUPLEX LINE PER DSS, SHARED BY ALL SYSTEMS; 1200-BIT BLOCK SIZE

SOFTWARE CAPABILITIES

(a) DSIF MONITOR BACKFEED DIS PROGRAM (TO BE ADDED)
(b) DSIF MONITOR PROGRAM IN 360/75 (TO BE ADDED)
(c) DSN MONITOR PROGRAM
A. THIS PROGRAM IS THE SAME AS THAT WHICH DESCRIBED SOFTWARE CAPABILITY, ITEM (c), OF THE MONITOR SYSTEM, AS CONFIGURED FOR DSSs 12, 14, ETC, BUT WITH THE ADDITION OF THE FOLLOWING:
1. OUTPUT PROCESS SELECTED DSN MONITOR DATA TO THE DSIF PROCESSOR IN THE 360/75. THIS DATA WILL INCLUDE PSEUDO-RESIDUALS AND SELECTED DECOMMUTATED S/C TELEMETRY.
2. INPUT PROCESS DSIF MONITOR DATA BLOCKS FROM THE DSIF MONITOR PROCESSOR IN THE 360/75. BLOCK FORMAT AND RATE ARE IDENTICAL TO THOSE RECEIVED VIA HSDA LINE FROM DSS 12, 14, ETC.

Fig. 3. DSN monitoring system for *Pioneers F and G* at SFOF, GCF, and DSSs 11, 42, and 61

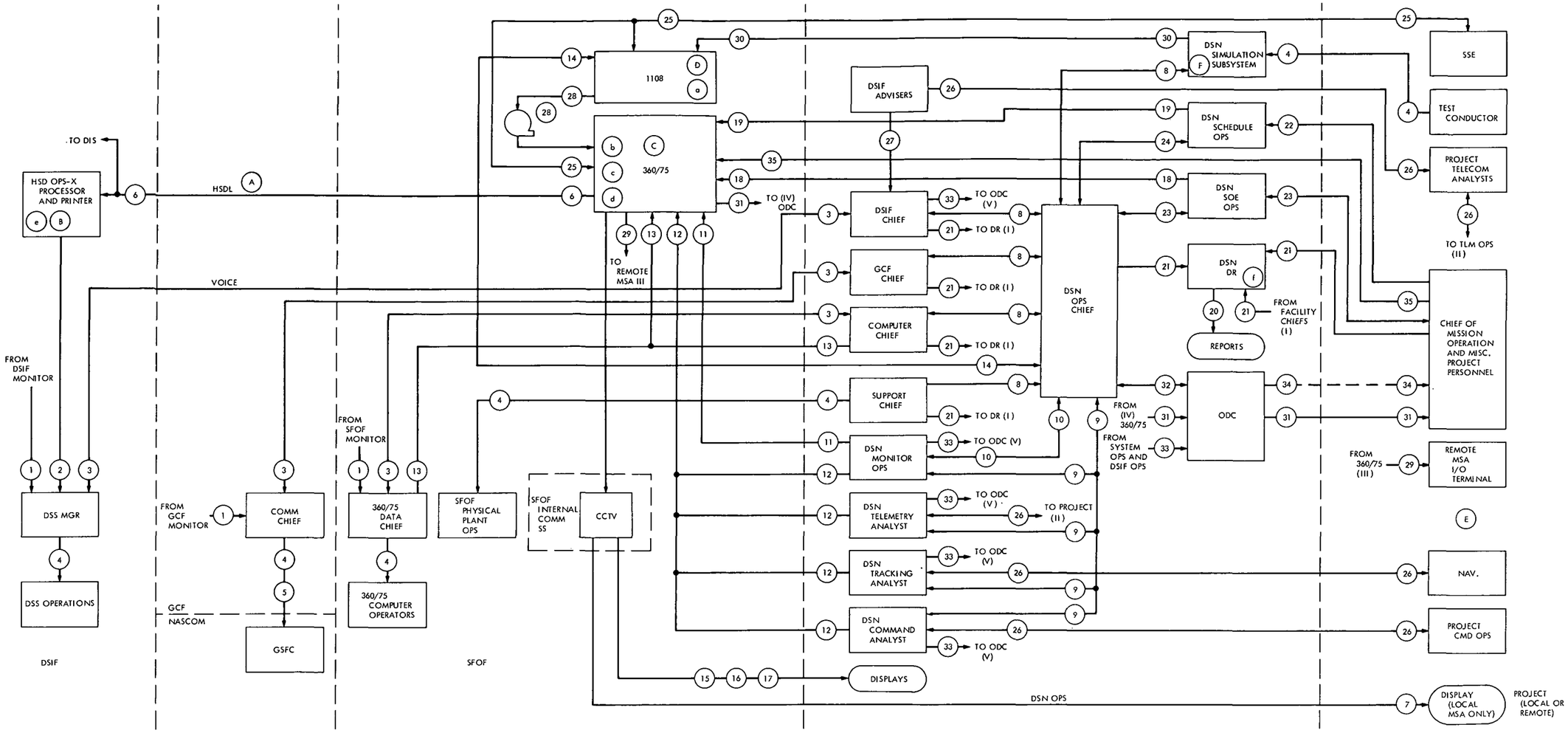

DATA FLOW PATHS

1. FACILITY STATUS AND ALARMS FOR ACTION AT FACILITY OPERATION SUPERVISOR'S INITIATIVE
2. PAGE PRINTS OF DSIF OPERATION CONTROL DATA, e.g., SEQUENCE OF EVENTS (SOE), DSIF (S AND L)
3. FACILITY INTERNAL ACTIVITY COORDINATION
4. OPERATIONAL DIRECTION
5. RESOURCE REQUIREMENTS AND COMMITMENTS
6. HSDA BLOCKS OF DSIF OPERATIONS CONTROL DATA AND DSIF S AND L, e.g., SOE, PREDICTS
7. DSN MONITOR DISPLAY FOR DSN OPERATION OF "DSN STATUS INFORMATION FOR PROJECT" (LOCAL MSA ONLY)
8. FACILITY INTERFACE ACTIVITY COORDINATION
9. SYSTEM DATA STATUS, TROUBLESHOOTING ADVICE, DATA RECALL REQUIREMENTS
10. COORDINATION OF NETWORK S AND L
11. REAL-TIME CONTROL OF NETWORK S AND L (LIMITED TO DSIF IN CY 71 AND 72
12. CONTROL OF EACH SYSTEM DATA PROCESSOR, INCLUDING MDR
13. CONTROL OF 360/75
14. COORDINATION OF 1108 CONTROL
15. DSN MONITOR DISPLAYS FOR DSN OPERATION
16. DSN MONITOR DISPLAYS FOR FACILITY OPERATION
17. DSN MONITOR DISPLAYS FOR SYSTEMS OPERATION
18. CONTROL OF SOE SOFTWARE
19. CONTROL OF SCHEDULING SOFTWARE (SKED S/W)
20. REPORTS ON DISCREPANCY REPORT (DR) DATA VIA OFFLINE PROCESSING FOR MANAGEMENT, DSN OPERATION, FACILITY OPERATION, SYSTEMS OPERATION
21. REPORTING OF RECOVERY OPERATIONS
22. PROJECT RESOURCE AND SUPPORT REQUIREMENTS
23. COORDINATION OF SEQUENCE PLANNING
24. COORDINATION OF REAL-TIME CHANGES OF SUPPORT REQUIREMENTS
25. CONTROL OF PROJECT ANALYSIS PROGRAMS IN 1108 AND 360/75
26. TECHNICAL INFORMATION EXCHANGE
27. SPECIALIZED ADVISORY SUPPORT (NOT OPERATIONAL DIRECTION)
28. TELEMETRY PREDICTS FROM TELEMETRY PREDICTS ANALYSIS PROGRAM (TRAP[a]), VIA TAPE INTERFACE
29. SAME DSN MONITOR DATA AS 7, BUT FORMATTED FOR ROUTING TO REMOTE MSA I/O TERMINAL IN MACHINE LANGUAGE
30. CONTROL OF DSN SIMULATION SOFTWARE IN 1108
31. TRACKING, TELEMETRY AND COMMAND MDRs
32. COORDINATION OF PHYSICAL TRANSFER OF MDRs TO PROJECT
33. INPUTS TO DSN PASS FOLDERS
34. PASS FOLDERS AVAILABLE (ORIGINAL FOR CURRENT DAY, MICROFILM FOR HISTORICAL FOLDERS) FOR PROJECT PERUSAL. MAY SEND TO PROJECT IF SO NEGOTIATED AS INTERFACE.
35. CONTROL OF SOE GENERATION PROGRAM IN 360/75 BY PROJECT

(A) TO (F) AND (a) TO (f) ARE DEFINED IN TABLE 3

[a] SEE NOTES ON (a) AND (b) IN "SOFTWARE CAPABILITIES"

Fig. 4. DSN operations control system for *Pioneers F and G*

Helios Mission Support

P. S. Goodwin
Mission Support Office

Project Helios, a joint endeavor between the United States and West Germany, will place two unmanned spacecraft into heliocentric orbits whose perihelion distance will come closer to the Sun than any previous or presently planned free world deep space undertaking. The first spacecraft is expected to be launched in mid-1974 and the second in late 1975. Prior volumes of this series describe the history and objectives of this program, the contemplated spacecraft configuration, and the spacecraft's radio system. This article deals with the capabilities of the telecommunications link between the spacecraft and the Deep Space Network.

I. Introduction

This is the fifth of a series of articles pertaining to Project *Helios*. The previous article (Ref. 1) completed a detailed description of the *Helios* spacecraft radio system. Specifically, it covered the operation of the spacecraft's command system and its compatibility with the Deep Space Network (DSN). Reference 1, and the several articles that preceded it, provides the necessary background for a discussion of the various telecommunications links between the *Helios* spacecraft and the DSN, which are treated in this article.

II. Telecommunications Link Design

A. Required Communications Links

As might be surmised from previous articles (Refs. 1–4), there is a multitude of telecommunications link combinations between the *Helios* Spacecraft and the DSN and/or West German ground stations. For instance, there are three different spacecraft antennas (low, medium, and high gain) available for use, three different spacecraft RF power output levels (0.5, 10, and 20 W), and six different spacecraft telemetry modes which can be transmitted at ten separate bit/symbol rates, in communication with either the 26-m or 64-m-diameter antenna stations within the Deep Space Network or with the West German 100-m antenna at Effelsberg. Since the number of such combinations far exceeds that needed to accomplish mission objectives, the *Helios* Project Office has chosen to restrict their nominal mission design to the 21 combinations listed in Table 1. While this does not imply that other combinations cannot be used under abnormal or emergency conditions, these 21 preselected telecommunications links should provide ample flexibility to accomplish mission objectives while at the same time not impose undue constraints upon the spacecraft from a thermal, electrical power, or attitude control system

viewpoint. Therefore, this article will confine its discussion to those links listed in Table 1.

B. Telecommunications Analytic Model

The performance of any telecommunications link is obviously dependent upon the amount of power transmitted, the gain of the transmitting and receiving antennas, the distance (i.e., loss) between the transmitter and receiver, and, of course, the information bandwidth to be transmitted. In addition, there are losses internal to the transmitter and receivers themselves. Many of these parameters are usually either pre-established or represent the desired solution from an analytical calculation of telecommunications link performance. For instance, the transmitter/receiver losses associated with the Deep Space Network Stations are well known from prior experience and may be found in such documents as DSN Standard Practice 810-5. In contrast, the losses associated with the spacecraft transmitter/receiver are not usually known accurately until at least a working model of the spacecraft has been fabricated. To compensate, an early analytical model of the spacecraft, together with stringent specifications concerning its telecommunications design performance, are needed prior to the actual fabrication of spacecraft hardware. These are developed to insure that the actual spacecraft design can be made to meet its mission objectives. The analytic model used for the *Helios* telecommunication subsystem losses is depicted in Fig. 1. The values used in computing these losses for the various links depicted in Table 1 were taken from the Project Office's specifications to the spacecraft prime contractor, and as such represent the best data currently available.

C. Uplink Considerations

The DSN has been requested to provide continuous coverage to the *Helios* spacecraft from initial acquisition through completion of the primary mission (i.e., first solar occultation). The spacecraft design goal is for this coverage to be provided by the DSN 26-m sub-network with occasional coverage being provided by the DSN 64-m sub-network for mission enhancement purposes. For a 0.25-AU *Helios* trajectory, first solar occultation occurs at a range of 1.5 AU from Earth (see Fig. 3, p. 28, in Ref. 3). If the mission is nominal, the spacecraft will be oriented such that after the first DSN Goldstone pass its medium-gain antenna pattern will be directed toward Earth from that time onward through perihelion and solar occultations to the end of the spacecraft's lifetime. If such is the case, the uplink performance from the DSN to the spacecraft will be as depicted in Fig. 2 of this article. If not, the uplink signal will have to be received by the spacecraft's low-gain (omni) antenna whose performance is depicted in Fig. 3 of this article. In the latter case, the transmission of commands via the 26-m links becomes somewhat questionable at a range of 1.5 AU. However, two alternatives are possible: (1) transmit the command via a 26-m station that has 20-kW power output capability, or (2) transmit the commands via the DSN 64-m sub-network. Since either of these represents reasonable alternative solutions to a situation that would only occur during a nonstandard mission, the performance of the link between a DSN 26-m antenna and the spacecraft low-gain antenna at a 1.5-AU range from Earth is not considered a serious problem at this time. In contrast, the performance of the uplink for a standard mission, as shown in Fig. 2 of this article, appears comfortably adequate to meet all primary objective missions.

D. Downlink Power Modes

As mentioned above, the *Helios* spacecraft has several downlink power output levels that can be chosen via ground command. In addition, the spacecraft telecommunications system has redundant channels for generating the downlink signal in order to provide reliability through redundancy. These are shown in Fig. 4 of this article. Obviously, the circuit losses associated with these various paths will differ—even for the same nominal power output level. However, the exact value of these losses will have to await the construction of actual spacecraft hardware. For the purposes of the present discussion, it will be assumed that the path loss for any given spacecraft power output level will be the same regardless of which channel is in use at a particular time.

E. Downlink Performance

The *Helios* downlink contains spacecraft telemetry and, upon occasion, also a turnaround ranging signal. Since the latter is used infrequently (see Table 1), it will be discussed separately. A reasonable measure of the performance of the telemetry portion of the downlink is the maximum information bit rate that can be transmitted over a given distance from the spacecraft to Earth. Since the bit rate from the spacecraft can only be changed in steps of a factor of two, a plot of the maximum bit rate versus spacecraft distance from Earth will appear to be a stair step drawing. Further, multiple stair steps can be drawn depicting the adverse, nominal, and

favorable tolerances associated with the individual entries within the telecommunications link analysis calculations.

1. Performance to a 26-m network. The *Helios* downlink telemetry performance to a DSN 26-m network is shown in Figs. 5 and 6 of this article. Figure 5 depicts the link via the spacecraft medium-gain antenna, while Fig. 6 depicts the link via the spacecraft high-gain antenna. Both figures are for the spacecraft high-power (i.e., 20 W) mode; however, a conversion factor is provided for the medium-power (i.e., 10 W) mode. From these figures it can be seen that if the spacecraft's despun high-gain antenna is working properly and the spacecraft is capable of transmitting in its high-power mode, bit rates of 256 bps are possible out to 1.5 AU from Earth. However, if either the medium-gain antenna or the medium-power mode has to be used, the telemetry performance from perihelion (i.e., 1.0 AU) is marginal.

2. Telemetry performance to 64-m network. The *Helios* telemetry performance at perihelion (1.0 AU) and again at first solar occultation (1.5 AU) improves considerably with the use of the DSN 64-m network, as can be seen from Figs. 7 and 8. For a completely standard mission, it is theoretically possible to receive 4096-bps telemetry from perihelion and 2048 bps up to first solar occultation (Fig. 8). However, if a failure occurs in the spacecraft's high-gain antenna, these telemetry bit rates would be reduced to 32 bps at perihelion and 16 bps at first solar occultation for the case of adverse tolerance (Fig. 7).

3. Telemetry performance to 100-m antenna. A representative case of the *Helios* telemetry performance to the West German 100-m antenna located at Effelsberg is shown in Fig. 9. Since this is for the spacecraft medium-gain antenna case, the maximum bit rates at perihelion and first solar occultation are 256 bps and 32 bps, respectively.

4. Ranging performance. The DSN Planetary Ranging System in the 64-m network will be used around each solar occultation of the *Helios* spacecraft to provide data for the celestial mechanics experiment. The uplink range code will be transmitted by the 64-m stations to the spacecraft's medium-gain antenna and then to the transponder in the turnaround ranging mode for retransmission back via the spacecraft's high-gain antenna to the originating 64-m station where the received code will be correlated with the transmitted code. The principal criterion for the performance of the ranging loop is the time required for the 64-m stations to acquire and correlate the received code with the transmitted code. This time, which is in addition to the round trip light-time for the RF signal to travel from the station to the spacecraft and return to the station, is plotted in Fig. 10. Of particular interest is the region between 1.0 and 2.0 AU from Earth, since the *Helios* solar occultations occur at 1.5 and 2.0 AU from Earth. Under the most favorable conditions, this acquisition time is between 1 and 2 min, while under the most adverse conditions the acquisition time can be in the region of 40 to 80 min. Nonetheless, range code acquisition times of 1 h will still permit several unique range measurements to be made during any one 64-m antenna station's available view period for the *Helios* spacecraft. Therefore, the predicted performance of the ranging loop appears to satisfy mission requirements.

III. Conclusions

From the foregoing discussion and figures, one may conclude that *Helios* can meet its mission objectives via these telecommunications links—*providing, of course, that the specifications for the radio system are met and that the spacecraft flies a nominal mission.* However, to achieve certain objectives, support will be required from the DSN 64-m and/or Effelsberg 100-m antennas when the range exceeds 1 AU, i.e., beyond perihelion. The greatest uncertainty in achieving mission objectives lies in the assumption of a "nominal mission." For instance, an unexpected failure of the mechanically despun high-gain antenna would significantly reduce the amount of telemetry (data rate) and/or ranging data (celestial mechanics experiment) that can be obtained at perihelion (1 AU) and beyond. Nonetheless, a meaningful mission can be accomplished using only the spacecraft's medium-gain antenna system, which is practically free of such potential mechanical failures.

Another conclusion that can be drawn is that the telecommunications link performance is dependent upon having proper spacecraft attitude orientation. For instance, an attitude control system failure that would preclude the spacecraft's medium-gain antenna pattern from impinging upon Earth (or doing so only intermittently) would also preclude the high-gain antenna from being directed toward Earth. Such a situation would force the use of the spacecraft's omni-directional antenna system which would greatly reduce the maximum distance from Earth that one could communicate with the spacecraft, even at the lowest data rates. However, even under such a situation, some telemetry data should still be received at perihelion or even from first solar occultation, using the 64-m or 100-m ground antennas.

The foregoing two examples are considered the most serious sources of potential failure in the telecommunications link design, because most of the electronics in the spacecraft's radio system has been redundantly designed (Fig. 4).

In summary, one may, therefore, conclude that, barring a catastrophic failure in the spacecraft's attitude control system, the calculated *Helios* telecommunications link design provides ample optional modes for a meaningful mission.

References

1. Goodwin, P. S., "*Helios* Mission Support," in *The Deep Space Network Progress Report*, Technical Report 32-1526, Vol. V, pp. 17–21. Jet Propulsion Laboratory, Pasadena, Calif., Oct. 15, 1971.
2. Goodwin, P. S., "*Helios* Mission Support," in *The Deep Space Network Progress Report*, Technical Report 32-1526, Vol. II, pp. 18–27. Jet Propulsion Laboratory, Pasadena, Calif., Apr. 15, 1971.
3. Goodwin, P. S., "*Helios* Mission Support," in *The Deep Space Network Progress Report*, Technical Report 32-1526, Vol. III, pp. 20–28. Jet Propulsion Laboratory, Pasadena, Calif., June 15, 1971.
4. Goodwin, P. S., "*Helios* Mission Support," in *The Deep Space Network Progress Report*, Technical Report 32-1526, Vol. IV, pp. 22–31. Jet Propulsion Laboratory, Pasadena, Calif., Aug. 15, 1971.

Table 1. Required *Helios* communication links

Link number	Ground station	Spacecraft antenna	Maximum range, AU	Channel bit rate, bps	Command capability	Ranging capability
1	26 m	Low	0.1	64	Yes	—
2	26 m	High	0.4	2048	Yes	—
3	26 m	High	1.3	128	Yes	—
4	26 m	High	1.6	64	Yes	—
5	26 m	High	2.0	8	Yes	—
6	64 m	High	0.4	2048	Yes	Yes
7	64 m	High	1.3	128	Yes	Yes
8	64 m	High	1.6	64	Yes	Yes
9	64 m	High	2.0	8	Yes	Yes
10	100 m	High	1.6	2048	Yes	—
11	64 m	Low	2.0	—	Yes	—
12	26 m	Medium	0.1	2048	Yes	—
13	26 m	Medium	0.3	128	Yes	—
14	26 m	Medium	0.4	64	Yes	—
15	26 m	Medium	0.8	8	Yes	—
16	64 m	Medium	2.0	8	Yes	—
17	100 m	Medium	0.3	2048	Yes	—
18	100 m	Medium	1.3	128	Yes	—
19	100 m	Medium	1.5	64	Yes	—
20	100 m	Medium	2.0	8	Yes	—
21	64 m	High	1.0	4096	Yes	—
22	Near Earth			64	Yes	—

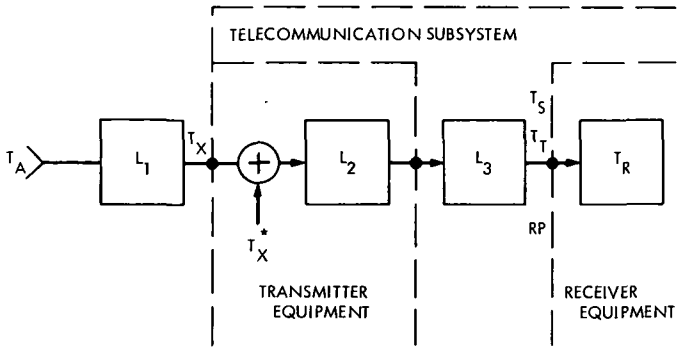

$$T_S = T_R + T_0 \frac{L_3 - 1}{L_3} + T_0 \frac{L_2 - 1}{L_2 L_3} + \frac{T_X^*}{L_2 L_3} + T_0 \frac{L_1 - 1}{L_1 L_2 L_3} + \frac{T_A}{L_1 L_2 L_3}$$

L_1 LOSSES (>1) OF ANTENNA CABLING

L_2 LOSSES (>1) OF DIPLEXER

L_3 LOSSES (>1) OF CONNECTION CABLING BETWEEN TRANSMITTER AND RECEIVER EQUIPMENT

RP REFERENCE POINT

T_A ANTENNA NOISE TEMPERATURE

T_R RECEIVER EQUIPMENT NOISE TEMPERATURE

T_S SYSTEM NOISE TEMPERATURE

T_T TELECOMMUNICATION SUBSYSTEM NOISE TEMPERATURE

T_X TRANSMITTER EQUIPMENT NOISE TEMPERATURE

T_X^* NOISE FROM TRANSMITTER POWER STAGES AFTER NOTCH FILTERS

Fig. 1. *Helios* spacecraft analytic model

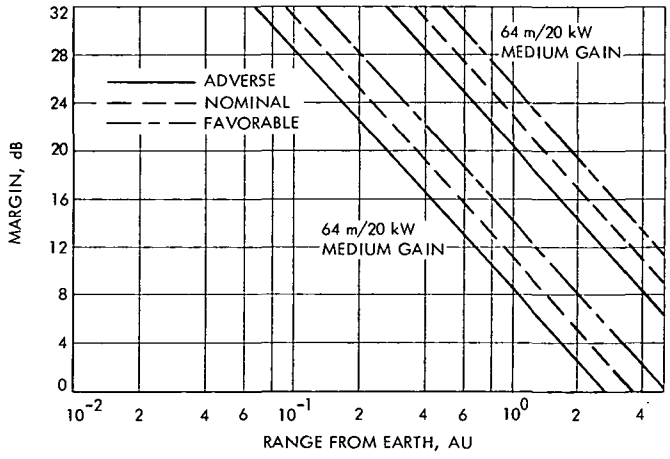

Fig. 2. *Helios* spacecraft medium-gain antenna uplink performance margin

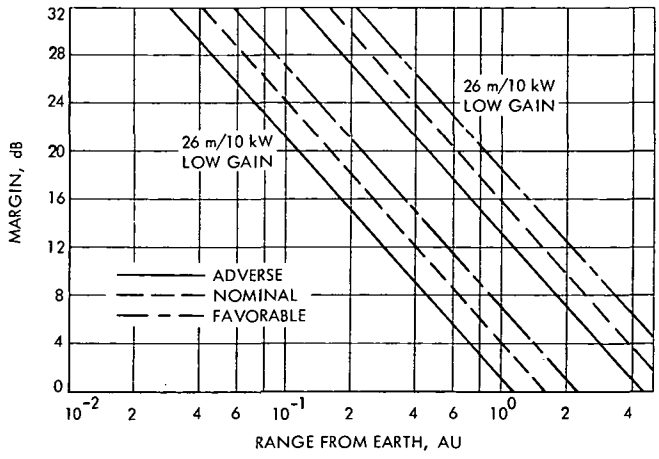

Fig. 3. *Helios* spacecraft low-gain antenna uplink performance margin

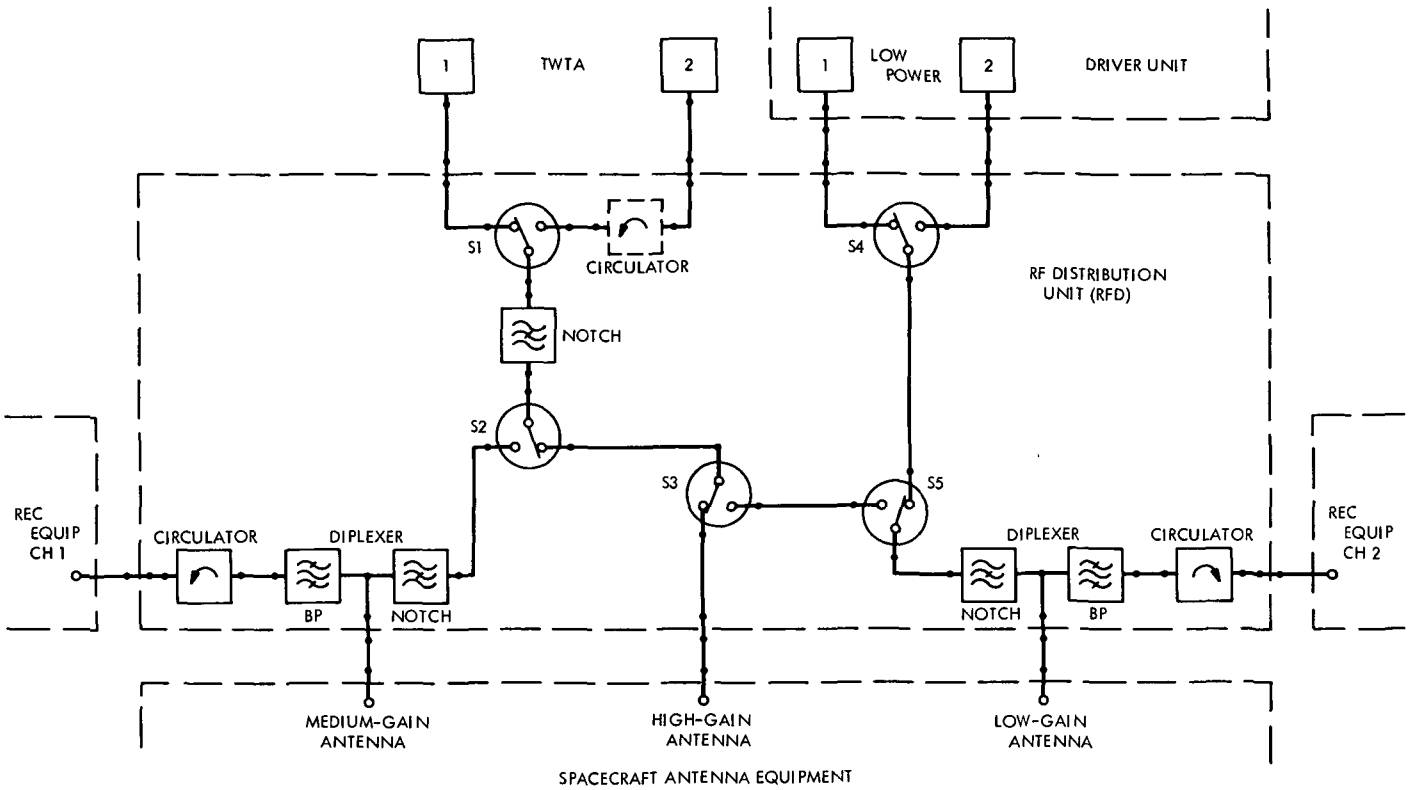

Fig. 4. *Helios* RF signal distribution block diagram

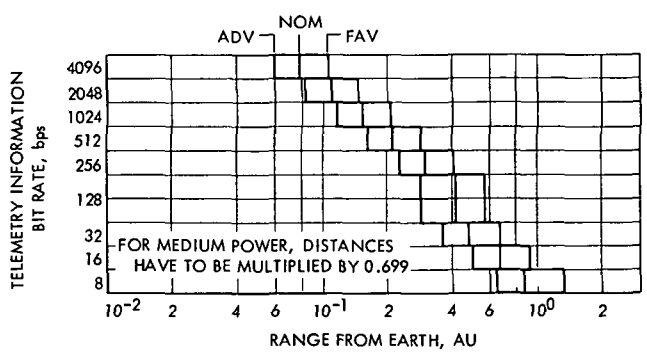

Fig. 5. *Helios* spacecraft medium-gain antenna (high-power mode) downlink to 26-m antenna

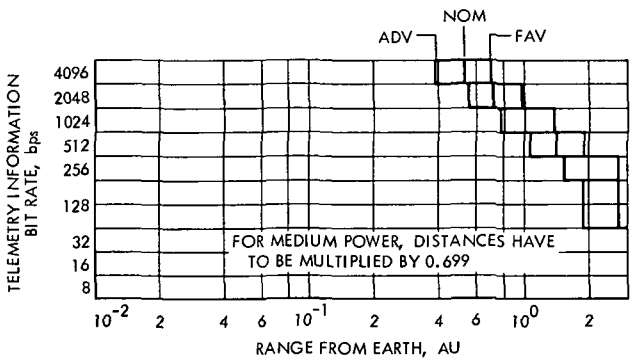

Fig. 6. *Helios* spacecraft high-gain antenna (high-power mode) downlink to 26-m antenna

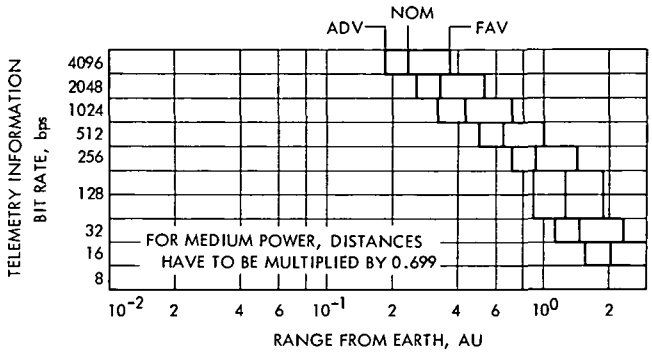

Fig. 7. *Helios* spacecraft medium-gain antenna (high-power mode) downlink to 64-m antenna

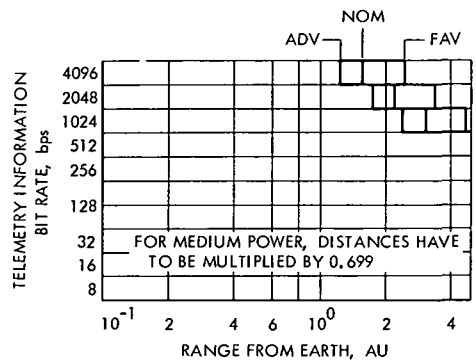

Fig. 8. *Helios* spacecraft high-gain antenna (high-power mode) downlink to 64-m antenna

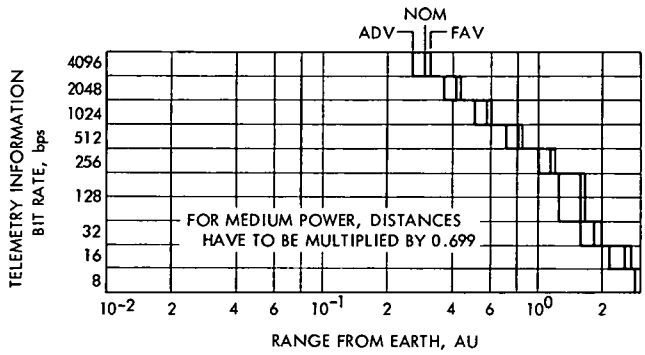

Fig. 9. *Helios* spacecraft medium-gain antenna (high-power mode) downlink to 100-m antenna

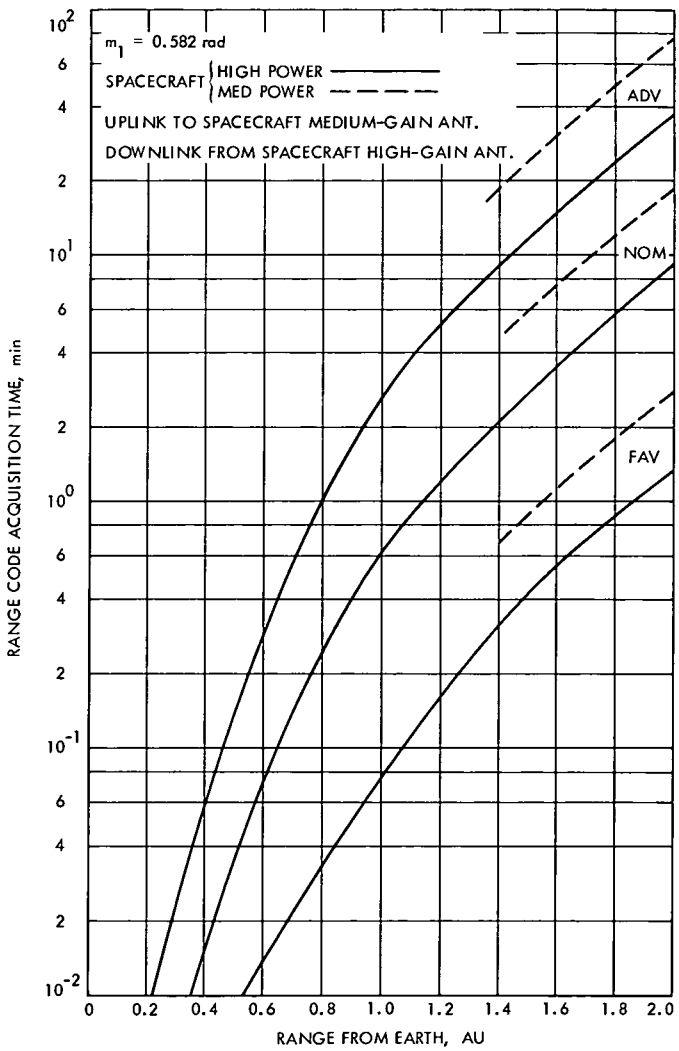

Fig. 10. 64-m/20-kW Tau Ranging System

Mariner Mars 1971 Mission Support

R. P. Laeser
Mission Support Office

This article completes and updates the description of the planned DSN configuration for support of Mariner 9 orbit insertion and orbit operations. Specifically covered are the S-band occultation experiment data handling, planetary ranging configuration, and the simulation configuration.

I. Introduction

Previous articles in this series described the configuration of the six DSN Systems for support of the *Mariner* Mars 1971 mission. Because of their unique nature and because of changes since their original description, several capabilities applicable to support of the Mars orbital mission need to be described to make this series of articles complete. These capabilities are:

(1) Occultation data handling.

(2) Planetary ranging configuration.

(3) Final simulation configuration.

II. Occultation Data Handling

The occultation experimenter is interested in two types of data: open-loop data and closed-loop data. The configuration for providing these data to the experimenter is shown in Fig. 1. The on-site instrumentation for acquisition of the open-loop data is described in Ref. 1. The instrumentation at CTA 21 for digitization of the analog tapes is described in Ref. 2. The TDH punched paper tape in excess of that transmittable to the SFOF in real time will be allowed to back up at DSSs 12, 41, and 62 and to catch up during the remainder of the pass, or immediately after pass if necessary.

The occultation experimenter originally required the open-loop data from DSS 14 within 6 hours of the occultation. Negotiations have since extended this time to noon of the following day, about 15 hours, on only six days of the week. This enables use of the daily flights to Goldstone and the scheduling of only one special flight per weekend. The experimenter plans to accomplish two day's processing on each Monday.

III. Planetary Ranging Configuration

A set of circumstances, some of them differing from the original plan, have caused a modification in the

strategy for provision of a planetary ranging capability for *Mariner* Mars 1971. The circumstances are:

(1) Tau ranging threshold[1] at DSS 14, *with* command modulation:

	20 kW	*100–400 kW*
Nominal:	Mar. 12, 1972	No significant extension
Worst case:	Feb. 14, 1972	

(2) Tau ranging threshold (Footnote 1) at DSS 14, *without* command modulation:

	20 kW	*100 kW*	*400 kW and LGA*
Nominal:	Mar. 17, 1972	Mar. 21, 1972	No significant extension after March 21
Worst case:	Feb. 23, 1972	Mar. 9, 1972	

(3) Mu ranging threshold (Footnote 1) at DSS 12, *with* command modulation:

Nominal: Dec. 9, 1971 (10-kW transmitter)

(4) Mu ranging threshold (Footnote 1) at DSS 12, *without* command modulation:

Nominal: Late Feb. 1972 (10-kW transmitter)

Worst case: Early Feb. 1972 (10-kW transmitter)

(5) Mu ranging threshold (Footnote 1) at DSS 14:

Nominal: Threshold not exceeded at 20 kW

(6) As a result of the loss of *Mariner 8*, two, rather than three, TCP 920 computers will be available at DSS 14, and two at DSS 12. Mu ranging requires the use of one TCP 920 computer. Until the DSIF tracking subsystem (DTS) is available, Tau ranging requires the use of one TCP 920 computer.

(7) The DTS–Tau ranging capability will be delivered too late for use at the start of orbit operations.

Considering these circumstances, the following was concluded:

(1) For the first part of the orbital mission, a 920 computer must be used for range data processing.

(2) Between DSSs 12 and 14 there are four TCP 920 computers, one is required for high-rate telemetry, one for low-rate telemetry and command, and a third for range data processing until the DTS is available. It seems reasonable to provide the most readily available backup, the fourth 920, to the high-rate telemetry function. In most cases range data processing can be sacrificed if its computer fails. Short delays can be tolerated in low-rate telemetry/command processing.

(3) Considering the various thresholds, it appears that the Extended Mission planetary ranging requirement can only be satisfied by the Mu system located at DSS 14.

(4) When the time is reached that all necessary processing can be performed at DSS 14, there is no justification to also use DSS 12 for *Mariner* Mars 1971 support.

Therefore, the following plan has been adopted:

(1) During the pre-orbit insertion period, when no high-rate telemetry is involved:

(a) During regularly scheduled DSS 14 tracks, use Tau ranging with TCP 920 range data processing. The other TCP 920 will be used to support low-rate telemetry and command. DSS 12 will not be scheduled. Sacrifice ranging if only one 920 is available.

(b) During regularly scheduled DSS 12 tracks, use Mu ranging with TCP 920 range data processing. The second TCP 920 will be used to support low-rate telemetry and command. DSS 14 will not be scheduled. Sacrifice ranging if only one 920 is available.

(2) Pre-orbital science through approximately mid-December and also prior to pre-orbital science activity when high-rate telemetry is involved:

(a) Both DSSs 12 and 14 will be scheduled. Use Mu ranging at DSS 12 with TCP 920 range data processing and with second TCP 920 used for command and low-rate telemetry. DSS 14 used for high-rate telemetry processing only, with second 920 in a backup role. If only one TCP is available at DSS 12, Project has option of sacrificing ranging or using Tau ranging at DSS 14 without high-rate telemetry backup or command capability.

(b) Off-spacecraft checkout of Tau/DTS will be accomplished during this period.

[1]Assumes high power, best high-gain antenna position, 180-min maximum acquisition, high-rate telemetry, 25-deg elevation, 9-dB (Tau) or 3-dB (Mu) range suppression.

(3) Mid-December through end of nominal mission: Use Tau–DTS ranging, with one TCP 920 on high-rate telemetry, second on low-rate telemetry/command. DSS 12 on one hour or less callup to cover DSS 14 920 failures.

(4) Extended Mission: Shift Mu ranging system to DSS 14 and use.

IV. Simulation System Configuration

Reference 3 provided a thorough description of the Simulation System for support of *Mariner* Mars 1971 and should be reviewed to understand this discussion. The Simulation Center design has not met expectations since it was implemented. The major problems have been:

(1) 6050 computer reliability. There is only one 6050, and when it fails, the flow of simulated data stops.

(2) 1108 response failures. When the 6050 needs data to feed the data lines, it asks the 1108 computer, which must respond within a fixed period of time; if it does not, everything comes to an abrupt halt.

Nothing much could be done about the first problem. However, the second problem led to much experimentation with the mode of operation in the 6050 and 1108; the actual configuration as described in Ref. 3 remained the same.

Initial efforts were aimed at running the simulation mathematical model in the same 1108 as the navigation software, with the aim of eliminating the response failures by placing controls on the level of input/output activity of the navigation programs. This obviously could not be done with simulation co-existing with all other general-purpose computing in the second 1108. The result of this experiment was the slowing down of the navigation programs to an unacceptable level.

The second approach was to limit the amount of other activity on the second 1108 by limiting the number of communications ports and to raise the priority of simulation activity through various system program modifications. None of these attempts worked—the response failures continued.

Finally, for the last three days of need for simulated data, all stops were pulled. Navigation was run on 1108B and simulation on 1108A, all by itself. It worked. Unfortunately, the cost to the DSN of this type of operation is overwhelming. In addition, this precluded the availability of the 1108 to the other users.

References

1. Laeser, R. P., "*Mariner* Mars 1971 Mission," in *The Deep Space Network*, Space Programs Summary 37-63, Vol. II, pp. 11–14. Jet Propulsion Laboratory, Pasadena, Calif., May 31, 1970.

2. Laeser, R. P., "*Mariner* Mars 1971 Mission Support," in *The Deep Space Network Progress Report*, Technical Report 32-1526, Vol. I, pp. 4–6. Jet Propulsion Laboratory, Pasadena, Calif., Feb. 15, 1971.

3. Laeser, R. P., "*Mariner* Mars 1971 Mission Support," in *The Deep Space Network*, Space Programs Summary 37-61, Vol. II, pp. 18–22. Jet Propulsion Laboratory, Pasadena, Calif., Jan. 31, 1970.

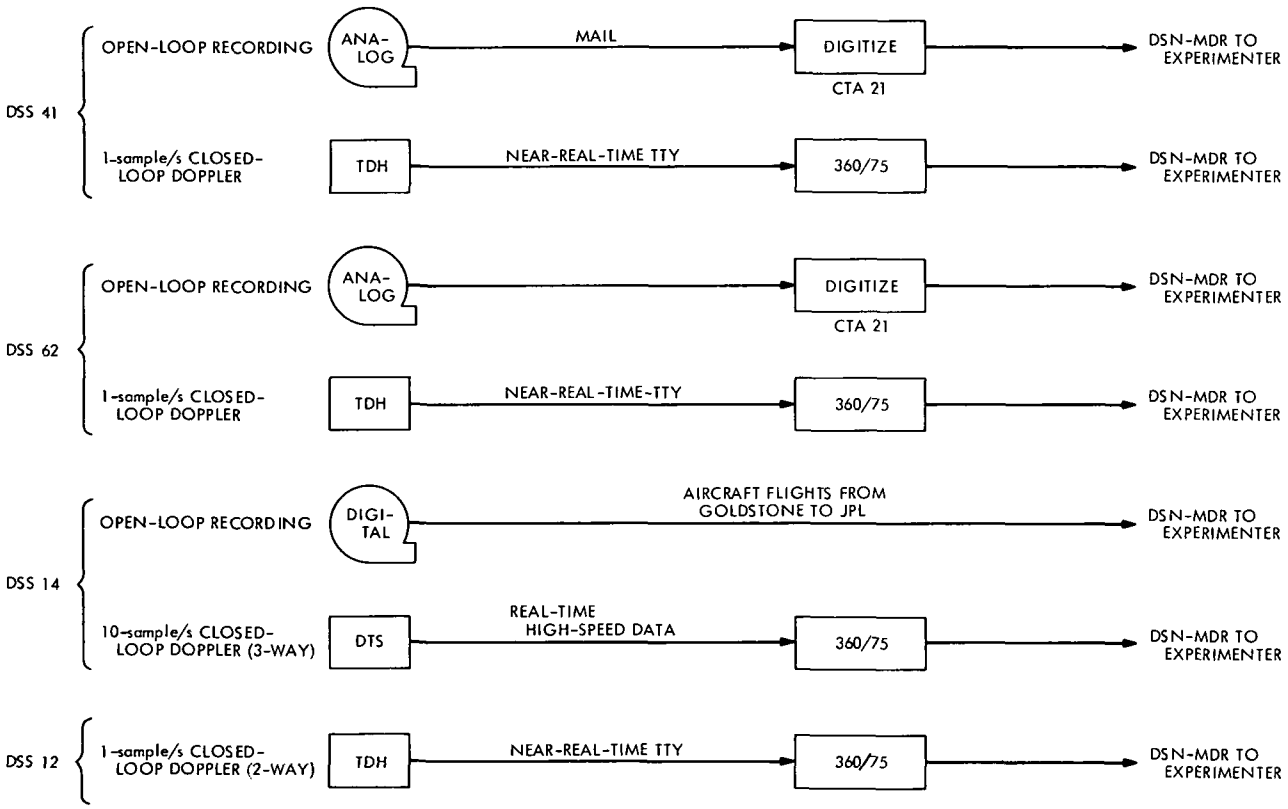

Fig. 1. DSN/*Mariner* Mars 1971 occultation configuration

Viking Mission Support

D. J. Mudgway
Mission Support Office

A functional specification for the Viking mission and a NASA support plan have been completed. A complex scheduling problem, created by the Viking Project request for mission design verification tests in late 1974 and early 1975 has been solved by reworking early agreements on responsibility for software development.

The Viking Project poses the problem of simultaneous multiple RF links to the DSN for the first time. Consequently, it has been necessary to introduce multiple-link requirements into the current DSN techniques for single-link RF compatibility testing. The effect of these new requirements, with particular reference to Viking, is discussed in this article.

I. Introduction

DSN support for the *Viking* Project continues to move forward with the completion of the TDS Functional Specification and the development of the NASA Support Plan (NSP). Both of these documents are required to establish the framework for the *Viking* Capabilities Planning Team (CPT) to begin work on designing the configuration of each of the DSN systems for *Viking*.

In addition, both documents provide a formal response to the requirements levied on the TDS by the *Viking* Project in the Project Specifications and the Support Instrumentation Requirements Document (SIRD), respectively.

Considerable impact to the DSN long-term planning resulted from a recent Project requirement for DSN support for additional mission demonstration tests covering the period December 1974 through March 1975. The DSN response was complicated by the potential conflicts with the *Mariner* Venus/Mercury encounters in early 1974, *Helios A* launch in mid-1974, and *Pioneer G* encounter late in 1974.

A simplified version of the schedule finally negotiated is shown in Fig. 1. Two key assumptions in the agreement are:

(1) That *Viking* and *Pioneer G* are able to share mission support areas in late 1974 and early 1975.

(2) That all software which runs in the 360/75 is developed at JPL.

(3) That all software developed by the Martin-Marietta Corporation for the *Viking* Project will run in the 1108.

After final review and agreement, this schedule will replace the existing TDS level 3 schedule as the formal top level Project/TDS commitment.

For some time now, attention has been directed toward the unique problems of RF compatibility testing posed by the multiple RF links of the *Viking* Project. Reference 1 described the *Viking* mission design, showing that during Mars Operations the DSN is required to provide two simultaneous uplinks for command and tracking and three simultaneous downlinks for telemetry and tracking. Hitherto, DSN practice in RF compatibility testing has been limited to one uplink or downlink at a time, and a significant increase in the scope of the existing standard practice has been necessary to accommodate the *Viking* conditions and ensure the integrity of the links both individually and collectively.

The following section summarizes the new techniques in multiple-link RF testing. Complete details of the test procedures and the rationale for each of the tests are presented in Refs. 2 and 3.

II. *Viking* RF Link Compatibility Testing (Single Link)

Reference 3 explains how RF compatibility testing is conducted in three phases as follows:

Phase I: Subsystem design starting with initial assembly of prototype/flight-model subsystems.

Phase II: System design following assembly of the flight-model (or equivalent) spacecraft.

Phase III: System verification of all flight-model spacecraft before launch.

The objectives of the subsystem design tests are to demonstrate design compatibility between the spacecraft telecommunications subsystems and the DSN as represented by the special test stations, CTA 21 and DSS 71. Design compatibility of equipment, preliminary mission-dependent software, and operational procedures are demonstrated during these tests.

The subsystem design compatibility tests are performed at CTA 21 as early as practicable in the RF equipment development program. Details of the CTA 21 and DSS 71 capabilities are found in JPL Document 801-2, Addendum 1 and Addendum 2, respectively.

CTA 21 will be configured with applicable equipment and software to perform subsystem testing. The Spacecraft Telecommunications System for each test may be represented by a single subsystem or by a group of subsystems, and may consist of engineering-model equipment.

Subsystem design tests are as follows:

(1) RF tests
   (a) Transponder maximum sweep and acquisition rate measurements.
   (b) S-band spectrum tests.
   (c) Transponder rest frequency determination.
   (d) Transponder subcarrier and carrier threshold.
   (e) Transponder carrier phase jitter.
   (f) Ground receiver carrier and subcarrier threshold.
   (g) Ranging delay calibrations.

(2) Command tests
   (a) Command performance with and without doppler.

(3) Telemetry tests
   (a) Bit error rates (block coded and uncoded modes).
   (b) Subcarrier phase jitter.
   (c) Carrier doppler effects on telemetry.
   (d) Telemetry bit rates and acquisition times.
   (e) Telemetry modulation index measurement.

The objectives of the system design tests are to demonstrate that the DSIF/Spacecraft Telecommunications System design is mutually compatible. Equipment, mission-dependent software, and operational procedures are tested for compatibility.

System design compatibility tests involve the first fully assembled spacecraft, and may be supported by CTA 21 or DSS 71. The station configuration will be operationally representative of a Deep Space Station (DSS) as required

for mission support. Typically, these tests are performed at CTA 21 using a calibrated RF link and hardline function for telemetry bit error rate tests.

This phase of compatibility demonstration repeats most of the subsystem design tests and includes the following additional tests:

(1) RF tests
   (a) Multiple S-band carrier operation (interchannel interference resulting from simultaneous transmission of more than one S-band downlink carrier).
   (b) Ranging probability of acquisition (verify probability of correct ranging correlation vs signal level, RF and telemetry modes).
   (c) Dynamic doppler simulation.
   (d) Two-way phase jitter vs signal level.

(2) Telemetry and command tests
   (a) End-to-end tests with SFOF using mission-dependent and multi-mission software.

The objectives of the system verification tests, typically performed at Cape Kennedy, are to verify that design compatibility, established during Phase II tests, is maintained for each flight-model spacecraft. If flight spacecraft system compatibility tests are not previously performed at CTA 21, the compatibility tests performed at Cape Kennedy become system design tests.

The system verification or system design tests involve the flight-model spacecraft, DSS 71, GCF, and SFOF. Both the spacecraft and the DSN must be in a mission-ready status to meet the test objectives.

The system verification or system design tests follow the same outline and use the same test procedures as Phase II testing. Maximum use will be made of the DSS 71 semi-automated test capabilities for measuring and recording test data. Spacecraft status and response will be determined from spacecraft telemetry received at DSS 71 via a calibrated RF link.

For *Viking* purposes each orbiter and each lander will proceed individually through each of these three phases. Under various configurations of exciters, receivers, antennas, and TWTs, the following classes of tests will be made:

(1) Downlink threshold, one-way.

(2) Uplink threshold.

(3) Receiver pull-in range.

(4) Tracking range and rate.

(5) Transmitter phase jitter.

(6) Best lock frequency.

(7) Auxiliary oscillator frequency.

(8) Telemetry bit error rate with ranging.

(9) Subcarrier phase jitter.

(10) Command polarity and acquisition.

(11) Ranging acquisition and delay.

(12) Downlink spectral analysis.

At this point, it will have been established that, individually, each orbiter and each lander is RF-compatible with the DSN. It now remains to be proved that two orbiters and one lander are simultaneously compatible with the DSN. This is accomplished in the next section.

III. *Viking* RF Link Compatibility Testing (Multiple Link)

For convenience in conducting the multiple-link tests, two orbiters and one lander will be set up in a fixed configuration of exciters, TWT, and low-gain antenna. The conditions of telemetry data rates listed in Table 1, with and without doppler and ranging, will then be established and a spectrum analysis and bit error rate check will be made under each condition for comparison with the results obtained previously under single-link conditions.

The objective of the test is to detect the presence of any interfering carrier or subcarrier cross products which may fall within the receiver pass band and cause degradation in the telemetry or tracking functions of the DSS receivers. The test configuration for the multiple S-band carrier tests is shown in Fig. 2.

Simultaneous acquisition of the three downlink carriers is possible by this configuration with any two of the links being also in a two-way coherent mode. Computer control of the RF attenuators in the downlink paths allows all S-band carriers to be set to the desired power levels.

The discrete Fourier transform technique described in Ref. 3 is used to analyze the RF spectrum around each carrier.

In addition, telemetry from each orbiter and lander will be processed and evaluated for interference using the standard bit error rate tests.

References

1. Mudgway, D. J., "*Viking* Mission Support," in *The Deep Space Network Progress Report*, Technical Report 32-1526, Vol. II, pp. 28–32. Jet Propulsion Laboratory, Pasadena, Calif., Apr. 15, 1971.
2. *Viking Project Master Integrated Test Plan; TDS Compatibility Test Plan*, PL-3701037. Martin-Marietta Corp., Denver, Colo.
3. *DSN Standard Practice, Deep Space Network/Flight Project Interface Compatibility Test Design Handbook*, Document 810-8, Rev. A, Oct. 1, 1971 (JPL internal document).

Table 1. *Viking* multiple-carrier telemetry conditions[a]

Orbiter 1	Orbiter 2	Lander
33⅓; 1w	33⅓; 1w	8⅓; 1w
33⅓; 1w	8⅓ and 16.2 k; 2w; R	8⅓; 1w
33⅓; 1w	8⅓ and 16.2 k; 2w; R	8⅓; 1w
33⅓; 1w	8⅓ and 16.2 k; 2w; R	1000; 2w
33⅓; 1w	8⅓ and 16.2 k; 2w; R	1000; 2w; R
8⅓ and 16.2 k; 1w	8⅓ and 16.2 k; 2w; R	1000; 2w; R
8⅓ and 16.2 k; 2w; R	8⅓ and 16.2 k; 2w; R	1000; 2w; R
8⅓ and 16.2 k; 2w; R	133⅓; 2w	1000; 2w; R
8⅓ and 16.2 k; 2w; R	2000; 2w	1000; 2w; R
8⅓ and 16.2 k; 2w; R	2000; 2w; R	1000; 2w; R
8⅓ and 16.2 k; 2w; R	2000; 2w; R	1000; 2w; R
8⅓ and 16.2 k; 2w; R	8⅓ and 16.2 k; 2w; R	1000; 2w; R
8⅓ and 16.2 k; 2w; R	8⅓ and 16.2 k; 2w; R	1000; 2w; R
8⅓ and 16.2 k; 2w; R	8⅓ and 16.2 k; 2w; R	1000; 2w; R
8⅓ and 16.2 k; 2w; R	8⅓ and 16.2 k; 2w; R	1000; 2w; R

[a]33⅓; 2w; R = 33⅓ bits/second in two-way RF lock with ranging modulation applied.

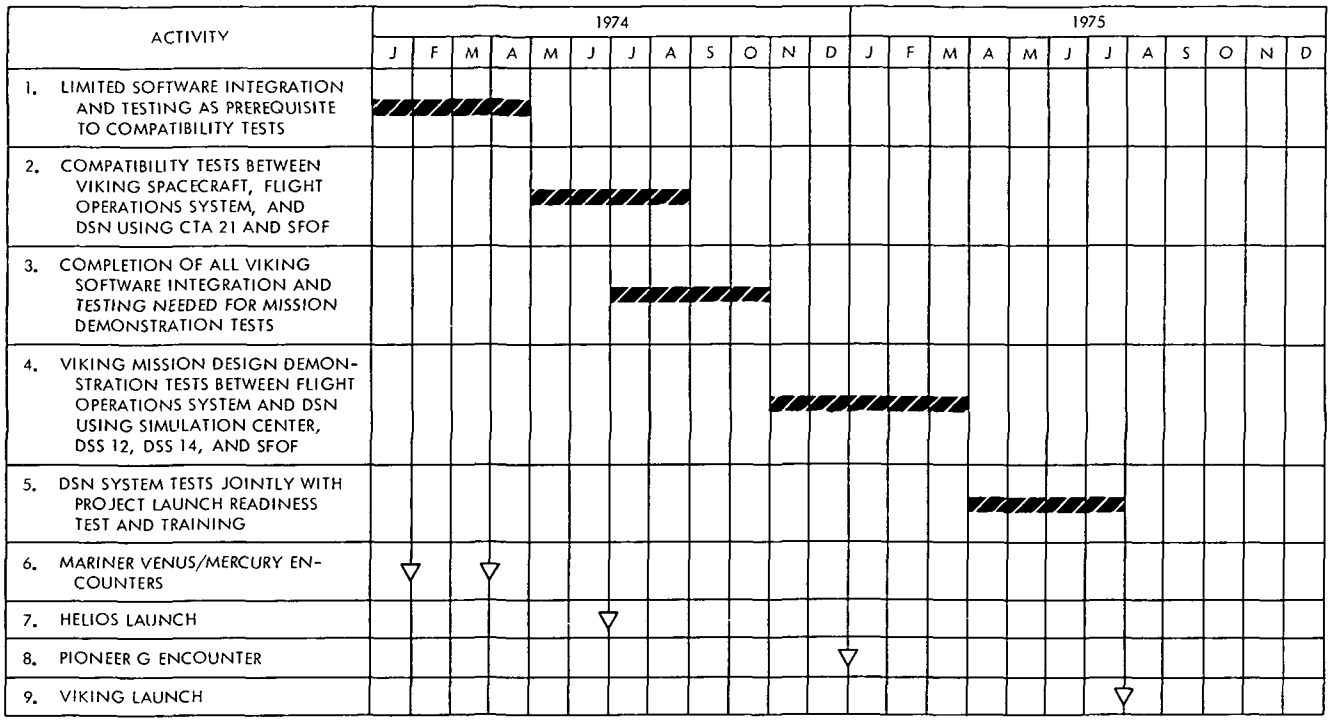

Fig. 1. Basic TDS schedule for support of *Viking* compatibility and mission design verification tests

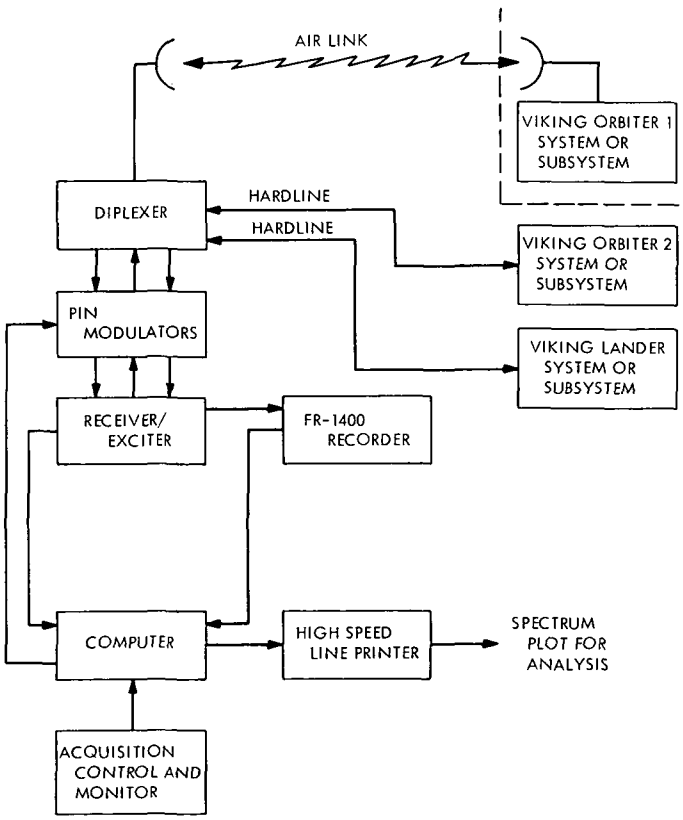

Fig. 2. Configuration for *Viking* multiple-link *spectrum tests*

Radio Science Support

K. W. Linnes
Mission Support Office

Since 1967, radio scientists have used the DSN 26- and 64-m antenna stations to investigate pulsars, to study the effects of solar corona on radio signals, and to observe radio emissions from X-ray sources. More recently, very long baseline interferometry (VLBI) techniques have been used for high-resolution studies of quasars. During the reporting period, VLBI observations were made in support of investigations of quasars and the application of VLBI techniques to Earth Physics problems. Support was also provided for preliminary investigation of the mapping of spiral galaxies.

I. Introduction

The 26- and 64-m antenna stations of the DSN have been used for several years to support radio science experiments. NASA, JPL, and university scientists have used key DSN facilities whose particular and unique capabilities were required for the performance of the experiments. In order to formalize the method of selecting experiments and experimenters, a Radio Astronomy Experiment Selection (RAES) Panel was formed in 1969. Notice of availability of these facilities was placed in professional journals to inform the scientific community that they were available for limited use by qualified radio scientists (Ref. 1). No charge is made for use of the standard DSN facilities and equipment; special equipment, however, must be provided by the experimenters. A summary of all experiments conducted through April 1971 was reported in Ref. 2. Activities through June 1971 are reported in Ref. 3.

II. Radio Science Operations

Table 1 shows experiments supported in September and October 1971. The X-band very long baseline interferometry (VLBI) observations continued the investigation of the structure of the quasars 3C273 and 3C279. In addition, it took advantage of the solar occultation of 3C279 to investigate further the relativistic effects first sought in October 1970.

Initial investigations of spiral galaxy mapping were conducted by H. Arp, using the 26-m antenna at 13 cm. This preliminary work confirmed that the goals can be

attained by use of the 64-m antenna and will require its use for the necessary resolution and sensitivity. Several new sources may also have been found.

III. RAES Panel Activities

The RAES Panel approved the proposal for the experiment shown in Table 2. The experiment makes use of the 64-m antenna, X-band maser, and noise-adding radiometer.

IV. OSSA Program Support

The DSN also provides support and use of the facilities for NASA programs of the Office of Space Sciences and Applications (OSSA). Initial support of a feasibility demonstration for application to Earth Physics of VLBI techniques was provided in January of 1971 (Ref. 4). In this demonstration two Goldstone tracking stations, the 26-m Echo Station and the 64-m Mars Station, were equipped with JPL hydrogen maser frequency systems and operated in electrically independent, although coordinated, observing modes. Using the short baseline, the feasibility of potential application to Earth Physics problems of position location was demonstrated. On September 1, 5, 10, and 22, DSN support was provided for Earth Physics VLBI observations using the 64-m antenna at Goldstone and the 26-m antenna at DSS 62 in Spain. These observations were of a number of celestial radio sources. The feasibility of using a spacecraft for source was demonstrated on October 17 using *Mariner* 9, while observing it from the Mars and Echo Stations simultaneously to obtain VLBI data.

References

1. *Bull. Amer. Astronom. Soc.*, Vol. 2, No. 1, p. 177, 1970.
2. Linnes, K. W., Sato, T., and Spitzmesser, D., "Radio Science Support," in *The Deep Space Network Progress Report*, Technical Report 32-1526, Vol. III, pp. 46–51. Jet Propulsion Laboratory, Pasadena, Calif., June 15, 1971.
3. Linnes, K. W., "Radio Science Support," in *The Deep Space Network Progress Report*, Technical Report 32-1526, Vol. V, pp. 42–44. Jet Propulsion Laboratory, Pasadena, Calif., Oct. 15, 1971.
4. Fanselow, J. L., et al., "The Goldstone Interferometer for Earth Physics," in *The Deep Space Network Progress Report*, Technical Report 32-1526, Vol. V, pp. 45–57. Jet Propulsion Laboratory, Pasadena, Calif., Oct. 15, 1971.

Table 1. Radio science experiments involving 64- and 26-m antenna facilities

Experiment	Purpose	Experimenter	DSN facility	Date
Quasar structure by X-band VLBI	To monitor time variations and fine structure and apparent position of quasars.	T. Clark (GSFC) R. Goldstein (JPL) H. Hinteregger (MIT) C. Knight (MIT) G. Marandino (University of Maryland) A. Rogers (MIT Haystack Observatory) I. Shapiro (MIT) D. Spitzmesser (JPL) A. Whitney (MIT)	DSS 14 (and MIT Haystack antenna)	June 9, 19, 1971 Sept. 19, 1971 Oct. 2–4, 10, 17, 1971
Spiral galaxy mapping	To study galaxies with anomalous red shifts and their possible association with radio sources.	H. Arp (Caltech)	DSS 13 (26 m)	Oct. 4, 7, 13, 20, 27, 1971

Table 2. Recent experiments approved by the RAES Panel

Experiment	Purpose	Experimenter	DSN facility
Small scale variations in cosmic background radiation.	Search for small-scale spatial variations in the 2.7°K cosmic background radiation at 3.5 cm.	R. Carpenter (Calif. State College at Los Angeles) S. Gulkis (JPL) T. Sato (JPL)	DSS 14

Analysis of Dual-Frequency Calibration for Spacecraft VLBI

O. H. von Roos
Tracking and Orbit Determination Section

In this article a feasibility study is undertaken and a detailed analysis is made of a wide-band very long baseline interferometer (VLBI) for the purpose of ranging and tracking a spacecraft. The system works on two frequencies (S- and X-band). By a new correlation technique, it is shown that it is possible to extract information on the total electron content with a rather high degree of accuracy, an accuracy certainly impossible to achieve with tracking modes currently in use. The total electron content and its time variation are valuable quantities on their own; they give important information on the solar wind. It is also shown that at the same time, potentially, the determination of the declination and right ascension of a spacecraft can be made much more accurately than by existing procedures.

I. Introduction

The ever increasing complexity of future unmanned space missions engenders an ever increasing need for higher accuracy with respect to tracking and ranging a spacecraft. Accordingly, here at JPL, a number of new tracking modes are currently under investigation. Before delving into this, let us first comment on the customary methods employed as of this writing. The range ρ (the distance between the spacecraft and an earthbound observer) is simply measured by measuring the round trip time between the observer and the spacecraft. This is achieved by transmitting a range code (a particular type of modulation of the S-band carrier) and comparing the received range code transmitted back from the spacecraft with the internally generated range code carefully calibrated with an internal clock (usually a Rb-standard, but recently H-masers, which are two orders of magnitude more accurate, are more and more the vogue). This round trip time, when corrected for tropospheric, ionospheric, and other influences on the electromagnetic radiation, is a direct measure of the range. On the other hand, the range rate $\dot{\rho}$ is determined by measuring the doppler shift, in other words by measuring the carrier frequency as a function of time. Again, corrections have to be made for time variations of electron densities, etc. Currently the inherent accuracy of the ranging system[1] is 7 m and the inherent accuracy of the tracking (doppler) system[1] is 1.3 m/12 h (Ref. 1).

Now, the range ρ depends, of course, on the orbital elements of the spacecraft: R the distance from the center of the earth, δ the declination, and α the right ascension, as well as on the station location in a certain way (for details see below). The problem then is to extract information about R, δ, and α from the measured values of ρ and $\dot{\rho}$ (the observables). An error analysis has shown two things (Ref. 2): (1) an accurate determination of the declination near $\delta \approx 0$ is very difficult, and (2) the process noise

[1]This does not take charged-particle or tropospheric calibrations into account.

(random forces due to jet leakage, solar pressure, etc.) is most severely affecting R and this error propagates "downstream" and degrades the determination of δ. If the geocentric range R could somehow be removed, a determination of δ, particularly at low δ, would principally be much more accurate. This can indeed be achieved by tracking and ranging from *two different* stations widely separated and *differencing* their respective topocentric ranges, for then R, being the same for both stations, cancels and we are left with a tidy expression containing only α, δ, and the station locations.

The differencing just described can be realized by a number of possibilities. Here we list the major ones now under active investigation:

(1) *Alternate ranging.* In this mode the two stations range separately and alternately, each for about 30 min during the overlap time, i.e., the time both stations can see the spacecraft simultaneously. The individual measurements are subsequently differenced. A simultaneous ranging is not possible since the two existing ranging machines (τ and μ) are quite different (different range codes, etc.).

(2) *Simultaneous tracking (2–3 way).* Here a signal is transmitted from one station and received at both stations. The received range and doppler cycles at the station which does not transmit are referenced to a synchronized clock. The independent measurements are subsequently differenced and yield the differenced range and range rate.

(3) *Coherent switching between the spacecraft and a radio star.* This is a true very long baseline interferometric (VLBI) mode. The idea is that two stations are receiving simultaneously a noise signal from a radio star and then switching the antennas so that the spacecraft's signal can be received alternately. The interference fringes in both cases give the relative position of the spacecraft against a background of radio stars, and if in turn their positions are known relative to the sky, the angular parameters of the spacecraft are determined.

(4) *Spacecraft VLBI.* In this mode the two stations listen simultaneously to a signal emanating from the spacecraft. This is the mode we are going to analyze in detail in the following.

All modes described here, as all tracking and ranging methods, have to be calibrated for charged particles and the troposphere. Because of the dispersion of the dielectric constant, as far as the interaction of the electromagnetic waves with the plasma is concerned, transmission and (or) reception of signals at two different frequencies will determine the total electron content (see *Section III*) and therefore calibrate for charged particles. The method we are going to analyze subsequently will determine *separately* the differenced range, the differenced range rate, and the total electron content within the ray path.

In *Section II* a VLBI correlation analysis is presented. In *Section III* this analysis is extended to determine the charged-particle effects and a correlation analysis is proposed and analyzed, which allows for a separate determination of the total electron content.

With the notation of Fig. 1 one readily establishes that the vectors from the center of the earth to station 1 or 2 on the surface of the earth are given by

$$\mathbf{r}_1 = r_s^{(1)}(\cos \Omega t\, \mathbf{e}_x + \sin \Omega t\, \mathbf{e}_y) + r_s^{(1)} \tan \epsilon_1\, \mathbf{e}_z \tag{1}$$

and

$$\mathbf{r}_2 = r_s^{(2)}(\cos (\Omega t + L)\, \mathbf{e}_x + \sin (\Omega t + L)\, \mathbf{e}_y) + r_s^{(2)} \tan \epsilon_2\, \mathbf{e}_z \tag{2}$$

where Ω is the angular speed of the earth, L the difference in longitude of the two antennas, and ϵ_1, ϵ_2 their respective latitudes. $\mathbf{e}_x$, $\mathbf{e}_y$, and $\mathbf{e}_z$, finally, are unit vectors conveniently placed in such a way that the longitude of station 1 coincides with the direction of the x axis, which we take to be the vernal equinox, again for convenience. The angle α of Fig. 1 is then the right ascension of the spacecraft. If these conveniences do not apply, an appropriate time translation has to be performed, a consideration which is immaterial for this analysis.

From Fig. 1 it is clear that

$$\mathbf{r}_1 + \boldsymbol{\rho}_1 = \mathbf{r}_2 + \boldsymbol{\rho}_2 = \mathbf{R} \tag{3}$$

where $\mathbf{R}$ is the geocentric range and $\boldsymbol{\rho}$ the topocentric range of the spacecraft. Representing $\mathbf{R}$ by

$$\mathbf{R} = R\{\sin \delta \mathbf{e}_z + \cos \delta\, (\cos \alpha \mathbf{e}_x + \sin \alpha \mathbf{e}_y)\} \tag{4}$$

where δ is the declination and α the right ascension of the spacecraft, and assuming $R >> r_s^{(1)} \approx r_s^{(2)}$, we obtain

$$|\boldsymbol{\rho}_1| = R - r_s^{(1)}\, (\cos \delta \cos (\Omega t - \alpha) + \sin \delta \tan \epsilon_1) \tag{5a}$$

and

$$|\boldsymbol{\rho}_2| = R - r_s^{(2)}\, (\cos \delta \cos (\Omega t + L - \alpha) + \sin \delta \tan \epsilon_2) \tag{5b}$$

One readily establishes that the time delay between the reception of a signal at station 1 and the reception of the same signal at station 2 is given by

$$T_g = \frac{1}{c}[|\rho_1| - |\rho_2|] = \frac{1}{c}\{D\cos\delta\cos(\Omega t - B) - (r_s^{(1)}\tan\epsilon_1 - r_s^{(2)}\tan\epsilon_2)\sin\delta\} \quad (6a)$$

$$\dot{T}_g = \frac{D}{c}[(\Omega - \dot{\alpha})\cos\delta\sin(\Omega t - B) + \dot{\delta}\sin\delta\cos(\Omega t - B)] - \frac{\dot{\delta}}{c}(r_s^{(1)}\tan\epsilon_1 - r_s^{(2)}\tan\epsilon_2)\cos\delta \quad (6b)$$

with

$$D = [(r_s^{(1)})^2 + (r_s^{(2)})^2 - 2r_s^{(1)}r_s^{(2)}\cos L]^{1/2} \quad (7)$$

$$\tan B = \frac{r_s^{(1)}\sin\alpha + r_s^{(2)}\sin(L-\alpha)}{r_s^{(1)}\cos\alpha - r_s^{(2)}\cos(L-\alpha)} \quad (8)$$

α and δ in Eq. (6) are the time-dependent quantities of greatest interest and can be determined more accurately with a VLBI technique than with existing methods, as will be shown on the following pages.

II. Development of the Analysis of the VLBI Technique

Since we are interested in ranging measurements, we are dealing with a *modulated* (wide-band) signal rather than a monochromatic (narrow-band) signal as in doppler.[2] If $F(\omega)$ is the Fourier spectrum of the signal we may represent the voltages at the output of the two RF amplifiers of the two stations relative to each other by

$$V_1 = \int d\omega\, F(\omega)\cos\omega t \quad (9a)$$

$$V_2 = \int d\omega\, F(\omega)\cos[\omega(t + T_g)] \quad (9b)$$

where T_g is given by Eq. (6) and the time t must be synchronous for the two stations. Since the frequency ω is usually very high (the modulation F is centered at the carrier frequency $\omega_0 \approx 10^{10}$ sec^{-1}), the signals (9a) and (9b) must be heterodyned to obtain a usable intermediate frequency. Let the local oscillators have frequencies ω_1 and $\omega_2 \approx \omega_1$. After mixing and filtering out the high-frequency component at each site, there results a signal which we may express as

$$V_1^{(if)} \sim \int d\omega\, F(\omega)\cos[(\omega_1 - \omega)t + \phi_1(t)] \quad (10a)$$

$$V_2^{(if)} \sim \int d\omega\, F(\omega)\cos[(\omega_2 - \omega)t + \omega T_g + \phi_2(t)] \quad (10b)$$

The phase errors ϕ_1 and ϕ_2 are introduced by the time standards and the electronic equipment. Both $\omega_1 - \omega$ and $\omega_2 - \omega$ are sufficiently slowly varying so that $V_1^{(if)}$ and $V_2^{(if)}$ can be recorded with ease (on tape for instance).

After recording the data (Eqs. 10a and 10b), which introduces additional phase errors ϕ_1^r and ϕ_2^r that we lump together with the previous phase errors, we obtain the cross correlation $C(\tau)$:

$$C(\tau) = \frac{1}{2\delta}\int_{-\delta}^{\delta} dt\, V_1^{(if)}(t)\, V_2^{(if)}(t+\tau) = \frac{1}{2\delta}\int_{-\delta}^{\delta} dt \int d\omega\, d\omega'\, F(\omega)\, F(\omega') \times \cos[(\omega_1 - \omega)t + \phi_1(t)] \times \cos[(\omega_2 - \omega')(t+\tau) + \omega' T_g(t+\tau) + \phi_2(t+\tau)] \quad (11)$$

For the noise pulse spectrum $F(\omega)$, we take the following as a simple analytical model which is, however, general enough to be quite adequate:

$$F(\omega) = \frac{1}{\sqrt{\pi}\,\omega_b}\sum_{i=-\infty}^{+\infty} R_i\cos[(\omega - \omega_0)T_i]\exp\left(-\frac{(\omega-\omega_0)^2}{\omega_b^2}\right) \quad (12)$$

Here R_i and T_i are random variables. R_i is the amplitude with zero mean and T_i the inverse repetition rate or the time elapsed between two pulses, itself a random variable with (possibly) a Poisson distribution. We will see presently that the underlying probability distribution for both R_i and T_i need not be known.[3] ω_0 is the carrier frequency and ω_b is essentially the bandwidth. For mathematical convenience we choose a Gaussian pulse shape. From Eqs. (12) and (10) we obtain in the time domain:

[2]The first part of the following analysis is similar to one given by P. S. Callahan (Ref. 3). Even so, this analysis is far more detailed. On the other hand, the only other paper in the open literature addressing itself to the same subject is by G. W. Swenson and N. C. Mathur (Ref. 4). That paper, however, does not address itself to a charged-particle calibration, which is the central theme of this article.

[3]The bandwidth ω_b could also be made a random variable erratically changing from noise pulse to noise pulse. The outcome of the analysis would be exactly the same.

$$V_1^{(i/)}(t) \sim \frac{1}{2}\sum_i R_i \cos\left[(\omega_1 - \omega_0)t + \phi_1(t)\right]$$

$$\times\left\{\exp\left[-\frac{\omega_b^2}{4}(t - T_i)^2\right] + \exp\left[-\frac{\omega_b^2}{4}(t + T_i)^2\right]\right\} \tag{13a}$$

$$V_2^{(i/)}(t) \sim \frac{1}{2}\sum_i R_i \cos\left[(\omega_2 - \omega_0)t + \phi_2(t) + \omega_0 T(t)\right]$$

$$\times\left\{\exp\left[-\frac{\omega_b^2}{4}(t - T_g - T_i)^2\right]\right.$$

$$\left.+ \exp\left[-\frac{\omega_b^2}{4}(t - T_g + T_i)^2\right]\right\} \tag{13b}$$

To evaluate the cross correlation we have to multiply the two voltages (13a) and (13b) together and integrate over time. Assuming that the integration time is only a few minutes and that the delay time T and the phases ϕ are slowly varying functions of time, we put

$$\phi_1 = \phi_{10} + \dot{\phi}_{10}t; \qquad \phi_2 = \phi_{20} + \dot{\phi}_{20}t \tag{14}$$

and

$$T_g = T_0 + \dot{T}_0 t \tag{15a}$$

as well as

$$\tau = \tau_0 + \dot{\tau}_0 t \tag{15b}$$

We also filter out the high-frequency component of the product (13a) times (13b). Because of the sharpness of the peaks in amplitude, the integration can safely be extended to infinity. Also, since we are only interested in positive times (the experiment starts at $t = 0$), the second terms in the braces of Eq. (13) may be discarded. Taking advantage of the fact that the R_j are random with zero mean so that the expectation $E(R_i R_j) = \delta_{ij} R_j^2$, we obtain for the cross correlation the following expression:

$$C(\tau) = \frac{\sqrt{\pi}}{8\omega_b \delta\sqrt{\beta}}\sum_j R_j^2 \cos\left(\dot{\alpha}\sqrt{\frac{B_j}{\beta}} + \gamma\right)$$

$$\times \exp\left\{-\frac{\alpha^2}{\omega_b^2\beta} - \frac{\omega_b^2}{4}(A_j - B_j)\right\} \tag{16}$$

where

$$\dot{\alpha} = \omega_2 - \omega_1 + \dot{\phi}_{20} - \dot{\phi}_{10} + \omega_0\dot{T}_0 + (\omega_2 - \omega_1)\dot{\tau}_0 \tag{17a}$$

$$\beta = 1 + (1 + \dot{\tau}_0 - \dot{T}_0)^2 \tag{17b}$$

$$\gamma = \phi_{20} - \phi_{10} + \dot{\phi}_{20}\tau_0 + \omega_0 T_0 + \omega_0\dot{T}_0\tau_0 + (\omega_2 - \omega_0)\tau_0 \tag{17c}$$

$$A_j = T_j^2 + (\tau_0 - T_j - T_0 - \dot{T}_0\tau_0)^2 \tag{17d}$$

$$B_j = \beta^{-1}\left[(1 + \dot{\tau}_0 - \dot{T}_0)(\tau_0 - T_j - T_0 - \dot{T}_0\tau_0) - T_j\right]^2 \tag{17e}$$

and 2δ is the integration time normalizing the summation over j. If we neglect $\dot{T}_0$ for a moment and set $\dot{\tau} = 0$ (constant time offset) and $\dot{\alpha} \approx 0$, we obtain from Eq. (16):

$$C(\tau) = \sqrt{\frac{\pi}{2}}\frac{1}{8}\cos\gamma \exp\left(-\frac{\omega_b^2}{8}(\tau - T_0)^2\right)\frac{1}{\omega_b\delta}\Sigma R_j^2 \tag{18}$$

The cross correlation $C(\tau)$ has a sharp maximum at $\tau = T_0$ and can, therefore, be measured accurately.[4] However, $\dot{T}_0$ is not zero. Disregarding the motion of the spacecraft relative to the earth, the order of magnitude of $\dot{T}_0$ is approximately given by $\dot{T}_0 \approx \Omega D/c$, where Ω is the angular velocity of the earth and D is the baseline of the VLBI. For $D = 7000$ km and $\Omega = 7.3\,10^{-5}$, $\dot{T}_0 \approx 10^{-6} << 1$. In this case a *constant* offset time τ_0 would not give any information about T_0 in contradistinction to the case considered in Eq. (18). The offset time τ must be changed with time at the same rate as T_0 changes with time. Since $\dot{T}_0 << 0$, it suffices to consider only linear terms in $\dot{T}_0$ (or $\dot{\tau}_0$).

Care must be taken here if large integration times are contemplated. For we have, conservatively speaking,

$$T \approx T_0 + \frac{\Omega}{c}Dt + \frac{1}{2}\frac{\Omega^2}{c}Dt^2 \cdots$$

In the following analysis we only keep the linear term. But if integration times are of the order of 10 min, the term quadratic in time will give a contribution of $2 \cdot 10^{-5}$ at the end of the integration interval. Reducing the integration time to 1 min reduces the quadratic correction to $2 \cdot 10^{-7}$, which is acceptable since the range is then accurate to the 30-cm level. On the other hand, a shorter integration time is quite adequate in the case of spacecraft VLBI for the simple reason that the spacecraft puts out a larger flux than the faint and distant radio stars. For instance the proposed (proposed for the grand tour) spacecraft transponder of 10 W at S-band yields 60 flux units under the assumption that the noise fills the whole 1-MHz band (1 flux unit = 10^{-26} W/m^2-Hz), whereas the 4-W X-band

[4]The accuracy of the measurement depends strongly, of course, on the bandwidth ω_b and the possibility of digitizing the information at a high bit rate.

transmitter yields approximately 1000 flux units at a distance of 1 AU. Compared to that a distant radio source emits about 1 flux unit. An integration time of 1 min is sufficient and the linear approximation is valid.

It turns out that the function $F_j(\tau) = A_j - B_j$ of Eq. (16) has a minimum at

$$\tau = \tau_j = T_0(1 + \dot{T}_0) + T_j(\dot{T}_0 - \dot{\tau}_0) \tag{19}$$

which is independent of j if $\dot{\tau}_0$ is set equal to $\dot{T}_0$. The value of $F_j(\tau)$ at the minimum with this choice for $\dot{\tau}_0$ is now

$$F_j(\tau = T_0[1 + \dot{T}_0]) = 0 \tag{20}$$

again independent of j. The cross correlation (16) will exhibit a sharp maximum at[5] $\tau_0 = T_0(1 + \dot{T}_0)$ provided that the offset time τ is given by

$$\tau = \tau_0 + \dot{T}_0 t = T_0(1 + \dot{T}_0) + \dot{T}_0 t \tag{21}$$

Neglecting $\dot{\alpha}/\omega_b$ we now have for $C(\tau)$:

$$C(\tau) = \sqrt{\frac{\pi}{2}}\frac{1}{8}\exp\left\{-\frac{\omega_b^2}{8}(\tau - \tau_0)^2\right\} \times \frac{1}{\omega_b \delta}\sum_j R_j^2 \cos\left[\gamma + (\omega_1 - \omega_2 + \dot{\phi}_{10} - \dot{\phi}_{20} - \omega_2\dot{T}_0)T_j\right] \tag{22}$$

where τ_0 is given by Eq. (21). The expression (22) is valid, after neglecting insignificant higher order terms, in the neighborhood of $\tau = \tau_0$ and exhibits again a very sharp maximum at $\tau = \tau_0$ if the cos terms in the series of Eq. (22) are slowly varying throughout the integration time 2δ. But this is assured if

$$2\delta(\omega_1 - \omega_2 + \dot{\phi}_{10} - \dot{\phi}_{20} - \omega_2\dot{T}_0) < \pi \text{ rad} \tag{23}$$

A conservative number for the fringe rate $\dot{T}_0$ is 10^{-6} assuming that $\dot{T}_0$ is solely given by $\dot{T}_0 = \Omega D/c$ with Ω the angular velocity of the earth and D the baseline of 7000 km. Neglecting the phase drifts in Eq. (23) and assuming an integration time of 1 min, the requirement (23) becomes

$$\omega_1 - \omega_2 - 10^{-6}\omega_2 < 10^{-2} \text{ Hz} \tag{24}$$

[5]The reason for the odd expression $\tau_0 = T_0(1 + \dot{T}_0)$ rather than $\tau_0 = T_0$ as in Eq. (11) is "retardation." The signal which reaches antenna 1 at time t does not reach antenna 2 at $t + T(t)$ but at $t + T(t + \tau) = t + \tau$ so that $T(t) + \tau\dot{T}(t) = \tau$ or $\tau = T(1 + \dot{T})$ in first order.

a condition which can easily be met. Since the drift rates $\dot{\phi}_0$ are unpredictable, they should not be allowed to exceed 10% of the 10^{-2} Hz just quoted or translated into frequency stability requirements; the fractional frequency deviation should be better than 5×10^{-14}, a requirement only a hydrogen maser can meet to date.

In principle it is, therefore, possible to measure with a high degree of accuracy both the fringe (the time delay or differenced topocentric range Eq. 6) and the fringe rate (the time rate of change of the time delay) by means of a wide-band VLBI. Obviously the accuracy becomes better the larger the bandwidth ω_b, since the maximum of the cross correlation at the correct offset time (Eq. 21) becomes more pronounced. There is no maximum if τ_0 is not chosen correctly, and there is only a weak maximum if $\dot{\tau}_0$ is chosen incorrectly. By varying τ and $\dot{\tau}$ around their expected values, the absolute maximum of $C(\tau)$, therefore, yields both T_0 and $\dot{T}_0$.

There are, however, two major contributors toward a degradation of the measurements. The first consists of the influence of the charged particles (the solar and ionospheric plasma) and the second consists of the influence of the troposphere. The tropospheric corrections must be made at each station separately, probably in the same manner as in the past. Radiosonde measurements, etc., are necessary for the determination of air density as a function of altitude, water vapor content, and so forth. The range corrections due to the troposphere vary typically from 2 to 100 m, depending on elevation angle, and will not be discussed further here.

III. Charged-Particle Corrections

The charged-particle corrections will keep us occupied for most of the remainder of this article. Taking into account the dispersive dielectric constant of the charged medium, it is easy to see (Ref. 5) that Eqs. (9) have to be replaced by

$$V_1 = \int d\omega\, F(\omega) \cos\left[\omega t - \frac{a}{\omega} I_1(t)\right] \tag{25a}$$

$$V_2 = \int d\omega\, F(\omega) \cos\left[\omega(t + T_g) - \frac{a}{\omega} I_2(t)\right] \tag{25b}$$

where $a = 2\pi e^2/mc$ and

$$I_j = \int_{\text{raypath}} dS\, N_j(S, t) \tag{26}$$

is the total electron content in the raypath between the spacecraft and station j ($j = 1, 2$). Following now exactly in the footsteps leading from Eq. (9) to Eq. (13), we obtain for the intermediate frequencies[6]

$$V_1^{(if)}(t) \sim \frac{1}{2}\sum_i R_i \cos\left[(\omega_1 - \omega_0)t + \phi_1(t) + \frac{a}{\omega_0} I_1(t)\right] \times \exp\left\{-\frac{\omega_0^2}{4}\left(t - \frac{a}{\omega_0^2} I_1 - T_i\right)^2\right\} \quad (27a)$$

$$V_2^{(if)}(t) \sim \frac{1}{2}\sum_i R_i \cos\left[(\omega_2 - \omega_0)t + \phi_2(t) + \frac{a}{\omega_0} I_2(t) + \omega_0 T_g(t)\right] \exp\left\{-\frac{\omega_b^2}{4}\left(t - T_g - \frac{a}{\omega_0^2} I_2 - T_i\right)^2\right\} \quad (27b)$$

and we see that the pulses are delayed by the interaction with the plasma (group velocity). In Eq. (27) we only took those terms into account for which the arrival time lies within the time interval $(0, 2\delta)$ in which the observations are actually made. Just as in Eqs. (14) and (15), we put:

$$I_1(t) = I_{10} + \dot{I}_{10} t \quad (28)$$

and similarly for I_2. Expansion (28) is again valid to a sufficient accuracy within the integration time 2δ, as it was the case with Eqs. (14) and (15). The analysis leading from Eqs. (13) to Eq. (16) can now be performed in complete analogy starting with Eqs. (27). After some tedious algebra, one is led to Eq. (16) again. Only the meaning of the parameters $\dot{\alpha}$, β, γ, A_j and B_j has changed. The result is the following: taking the charged-particle effects explicitly into account, the cross correlation is again given by Eq. (16), but the parameters (Eqs. 17) have to be replaced by

$$\dot{\alpha} \to \dot{\alpha}' = \omega_2 - \omega_1 + \dot{\phi}_{20} - \dot{\phi}_{10} + \omega_0 \dot{T}_0 + (\omega_2 - \omega_0)\dot{\tau}_0 + \frac{a}{\omega_0}(\dot{I}_{20} - \dot{I}_{10}) + \frac{a}{\omega_0^2}(\omega_2 - \omega_1)\dot{I}_{10} \quad (29a)$$

$$\beta \to \beta' = 1 + \left[1 + \dot{\tau}_0 - \dot{T}_0 + \frac{a}{\omega_0^2}(\dot{I}_{10} - \dot{I}_{20})\right]^2 \quad (29b)$$

$$\gamma \to \gamma' = \phi_{20} - \phi_{10} + \dot{\phi}_{20}\tau_0 + \omega_0 T_0 + \omega_0 \dot{T}_0 \tau_0 + (\omega_2 - \omega_1)\tau_0 + \frac{a}{\omega_0^2}(\omega_2 - \omega_1) I_{10} + \frac{a}{\omega_0}(I_{20} - I_{10}) + \frac{a}{\omega_0}\dot{I}_{20}\tau_0 \quad (29c)$$

$$A_j \to A_j' = T_j^2 + \left[\tau_0 - T_j - T_0 - \dot{T}_0\tau_0 - \frac{a}{\omega_0^2}\dot{I}_{20}\tau_0 + \frac{a}{\omega_0^2}(I_{10} - I_{20})\right]^2 \quad (29d)$$

$$B_j \to B_j' = (\beta')^{-1}\left\{\left[1 + \dot{\tau}_0 - \dot{T}_0 + \frac{a}{\omega_0^2}(\dot{I}_{10} - \dot{I}_{20})\right]\left[\tau_0 - T_j - T_0 - \dot{T}_0\tau_0 + \frac{a}{\omega_0^2}(I_{10} - I_{20}) - \frac{a}{\omega_0^2}\dot{I}_{20}\tau_0\right] - T_j\right\}^2 \quad (29e)$$

Terms containing the time derivative of the electron content $\dot{I}$ cannot be neglected in the expressions above. Typical time variations $\dot{I}$ are of the order of 10^{11} cm^{-2} s^{-1} (Ref. 6) leading to a value for an $\dot{I}/\omega_0^2$ of about 10^{-10}. Now, $\dot{T}_0$ is of the order of 10^{-6}, and it is desired that it be known to an accuracy of one part in 10^5, corresponding to an accuracy of 1 mm/s for the differenced range rate. Time variations of the intervening plasma are likely to be an order of magnitude larger than the desired accuracy. To proceed with the analysis we determine the minimum of $F_j' = A_j' - B_j'$ with respect to τ_0, which yields the maximum of the cross correlation according to Eq. (16). It is given by

$$\tau = \tau_0 = T_0\left(1 + \dot{T}_0 + \frac{a}{\omega_0^2}\dot{I}_{20}\right) + T_j\left[\dot{T}_0 - \dot{\tau}_0 - \frac{a}{\omega_0^2}(\dot{I}_{10} - \dot{I}_{20})\right] - \frac{a}{\omega_0^2}(I_{10} - I_{20}) \quad (30)$$

and is independent of T_j if

$$\dot{\tau}_0 = \dot{T}_0 - \frac{a}{\omega_0^2}(\dot{I}_{10} - \dot{I}_{20}) \quad (31)$$

With this choice of $\dot{\tau}_0$ the cross correlation is given by

$$C(\tau) = \sqrt{\frac{\pi}{2}}\frac{1}{8}\exp\left\{-\frac{\omega_b^2}{8}(\tau - \tau_0)^2\right\} \times \frac{1}{\omega_b \delta}\sum_j R_j^2 \cos\left[\gamma' - T_j\dot{\alpha}'\right] \quad (32)$$

in the neighborhood of the maximum. τ_0 is now given by Eq. (30), γ' and $\dot{\alpha}'$ are given by Eqs. (29a) and (29c). Again we have a very sharp maximum if Eqs. (30) and (31) hold. Also, in order that no cancellation occurs in the sum over j we must have

[6]Taking the dispersion into account as in Ref. 5, p. 408.

$$2\delta\left[\omega_1-\omega_2+\dot{\phi}_{10}-\dot{\phi}_{20}-\omega_2\dot{T}_0+\frac{a}{\omega_0^2}(\omega_1\dot{I}_{10}-\omega_2\dot{I}_{20})\right]<\pi \tag{33}$$

This condition on the beat frequencies is essentially the same as Eq. (23) because of the smallness of the plasma correction terms.

It is clear from the foregoing that it has been achieved to measure accurately the quantities:

$$\tau_0=T_0\left(1+\dot{T}_0+\frac{a}{\omega_0^2}\dot{I}_{20}\right)-\frac{a}{\omega_0^2}(I_{10}-I_{20}) \tag{34a}$$

and

$$\dot{\tau}_0=\dot{T}_0-\frac{a}{\omega_0^2}(\dot{I}_{10}-\dot{I}_{20}) \tag{34b}$$

and it is necessary to correct for the corrupting charged-particle effect. This can be done only with additional measurements. The well-known Differenced Range Versus Integrated Doppler (DRVID) method cannot be employed, since it measures only the time derivative of the total electron content and not its absolute value. There is another reason why DRVID is a poor choice for correcting the VLBI measurements contemplated here. DRVID measures the time variations of the plasma between the spacecraft and the ground station on both the uplink and the downlink. It does not differentiate between the two links. Therefore ½ $\dot{I}$ as determined by DRVID is not necessarily the same as the quantity $\dot{I}_1$ or $\dot{I}_2$ of Eq. (27) (Ref. 7). Therefore, an independent determination of the total electron content for each raypath has to be made using two different frequencies (dual-frequency method).

At this point there are essentially two avenues at our disposal, remembering that we have a dual-frequency system available. The first thing to do if we want to calibrate for charged-particle effects is to simply measure the quantities Eqs. (30) and (31) at a different carrier frequency ω_0'. Then we have, exactly as Eqs. (30) and (31),

$$\tau_0'=T_0\left(1+\dot{T}_0+\frac{a}{(\omega_0')^2}\dot{I}_{20}\right)-\frac{a}{(\omega_0')^2}(I_{10}-I_{20}) \tag{30a}$$

and again

$$\dot{\tau}_0=\dot{T}_0-\frac{a}{(\omega_0')^2}(\dot{I}_{10}-\dot{I}_{20}) \tag{31a}$$

Then subtracting Eq. (30a) multiplied by $(\omega_0')^2/\omega_0^2$ from Eq. (30), we have

$$\tau_0-\frac{(\omega_0')^2}{\omega_0^2}\tau_0'=T_0(1+\dot{T}_0)\left(1-\frac{(\omega_0')^2}{\omega_0^2}\right) \tag{31b}$$

and all charged-particle ambiguities are removed. However, the total electron content $I(t)$ is in itself a valuable quantity to know since it gives information on the solar wind. We like to propose, therefore, a method in the following which gives just that information without being unduly expensive and without impairment of the range and range rate accuracy.

Suppose there are two phase-locked wide-band transmitters on board the spacecraft operating at frequencies ω_0 and ω_0' with bandwidths ω_b and ω_b', respectively. A ground station receives simultaneously a noise voltage with its receivers, which may be expressed by

$$V_1=\int d\omega\, F(\omega)\cos\left[\omega t-\frac{a}{\omega}I(t)\right] \tag{35a}$$

and

$$V_2=\int d\omega\, F'(\omega)\cos\left[\omega t-\frac{a}{\omega}I(t)+\phi\right] \tag{35b}$$

The indices 1 and 2 now refer to the two transmitters. ϕ is a *constant* phase, since the transmitters are phase locked. The Fourier spectrum $F(\omega)$ is given by Eq. (12) and $F'(\omega)$ is[7]:

$$F'(\omega)=\frac{1}{\sqrt{\pi}\,\omega_b'}\sum_i R_j\cos[(\omega-\omega_0')T_j]\exp\left[-\frac{(\omega-\omega_0')^2}{(\omega_b')^2}\right] \tag{36}$$

The subsequent analysis is quite similar to the previous calculations so we shall be brief in the following. The intermediate frequencies are given by

[7]We assume coherent noise, of course, so that the signals from both transmitters stem from the same noise source.

$$V_1^{(if)}(t)\sim\frac{1}{2}\sum R_i\cos\left[(\omega_1-\omega_0)t+\phi_1(t)+\frac{a}{\omega_0}I(t)\right]\exp\left[-\frac{\omega_b^2}{4}\left(t-\frac{a}{\omega_0^2}I-T_i\right)^2\right] \tag{37a}$$

$$V_2^{(if)}(t)\sim\frac{1}{2}\sum R_i\cos\left[(\omega_2-\omega_0')t+\phi_2(t)+\frac{a}{\omega_0'}I(t)+\phi\right]\exp\left[-\frac{(\omega_b')^2}{4}\left(t-\frac{a}{(\omega_0')^2}I-T_i\right)^2\right] \tag{37b}$$

ω_1 and ω_2, etc., are, of course, not the same as in previous calculations since 1 and 2 refer to the two different channels of the same station rather than to the two stations. Again we use the linear approximation for $\phi(t)$ and $I(t)$ which is quite sufficient for the integration times involved (1 min). After some algebra analogous to previous calculations we obtain:

$$C_I(\tau) = \frac{\sqrt{\pi}}{8\omega_b \delta \sqrt{\epsilon}} \sum_j R_j^2 \cos\left(\dot{\xi}\sqrt{\frac{E_j}{\epsilon}} + \eta\right) \exp\left\{-\frac{\dot{\xi}^2}{\omega_b^2 \epsilon} - \frac{\omega_b^2}{4}(D_j - E_j)\right\} \tag{38}$$

where

$$\epsilon = 1 + \left(\frac{\omega_b'}{\omega_b}\right)^2 \left[1 + \left(\frac{1}{\omega_0^2} - \frac{1}{(\omega_0')^2}\right) a\dot{I}_0 + \dot{\tau}_0\right]^2 \tag{39a}$$

$$\dot{\xi} = \omega_2 - \omega_1 + \omega_0 - \omega_0' + \dot{\phi}_{20} - \dot{\phi}_{10} + (\omega_2 - \omega_0')\dot{\tau}_0 + (\omega_2 - \omega_1 - \omega_0')\frac{a}{\omega_0^2}\dot{I}_0 + \frac{a}{\omega_0'}\dot{I}_0 \tag{39b}$$

$$\eta = \phi_{20} - \phi_{10} + \phi + \left(\omega_2 - \omega_0' + \dot{\phi}_{20} + \frac{a}{\omega_0'}\dot{I}_0\right)\tau_0 + (\omega_2 - \omega_1 - \omega_0')\frac{a}{\omega_0^2}\dot{I}_0 + \frac{a}{\omega_0'}\dot{I}_0 \tag{39c}$$

$$D_j = T_j^2 + \left(\frac{\omega_b'}{\omega_b}\right)^2 \left[\tau_0\left(1 - \frac{a}{(\omega_0')^2}\dot{I}_0\right) + \left(\frac{a}{\omega_0^2} - \frac{a}{(\omega_0')^2}\right) I_0 - T_j\right]^2 \tag{39d}$$

$$E_j = \epsilon^{-1}\left\{-T_j + \left(\frac{\omega_b'}{\omega_b}\right)^2 \left[1 + \dot{\tau}_0 + a\dot{I}_0\left(\frac{1}{\omega_0^2} - \frac{1}{(\omega_0')^2}\right)\right]\left[\tau_0 + aI_0\left(\frac{1}{\omega_0^2} - \frac{1}{(\omega_0')^2}\right) - \frac{a}{(\omega_0')^2}\dot{I}_0\tau_0 - T_j\right]\right\}^2 \tag{39e}$$

The correlation (38) depends critically on the bandwidth differences of the two channels ω_b and ω_b'. If $\omega_b = \omega_b'$, C_I exhibits a pronounced maximum if the offset time τ is chosen to be:

$$\tau_0 = -aI_0\left(\frac{1}{\omega_0^2} - \frac{1}{(\omega_0')^2}\right) \tag{40a}$$

and

$$\dot{\tau}_0 = -a\dot{I}_0\left(\frac{1}{\omega_0^2} - \frac{1}{(\omega_0')^2}\right) \tag{40b}$$

and the electron content I may be measured accurately. If, however, the bandwidths differ, no such claim can be made; in that case the maximum of each individual term in the series (38) depends on T_j so that no common τ exists which maximizes all terms of the series (38) simultaneously. It follows also from Eq. (38) that the frequencies have to be chosen such that the product:

$$2\delta\left[\omega_2 - \omega_1 + \omega_0 - \omega_0' + \dot{\phi}_{20} - \dot{\phi}_{10} + a\dot{I}_0\left(\frac{\omega_2}{(\omega_0')^2} - \frac{\omega_1}{\omega_0^2}\right)\right] < \pi \tag{41}$$

a condition which can easily be met.

A possible implementation of this calibration technique is shown in Fig. 2.

Two problems finally remain before the system described here can be employed within the accuracy demanded, i.e., better than 1 m in range and 0.1 mm/s in range rate.

The first problem is the necessity to calibrate for tropospheric effects. This must, of course, be done at both stations independently since the atmospheric properties are expected to be quite different at the widely separated antenna sites. How the calibration is effectuated is explained in detail elsewhere (Ref. 8).[8] Range corrections are a sensitive function of the elevation angle and are typically of the order of 2 m (at zenith) to 100 m (at 0-deg elevation angle). The accuracy of this calibration is about 5% or 10 cm at zenith, which is quite adequate. However, it appears to be 7% at very low elevation angles, for instance,

[8]See also "New Tropospheric Range Corrections With Seasonal Adjustment," by C. C. Chao in this issue.

corresponding to about 4 m at 10 deg (quite inadequate), so that for elevation angles less than 10 deg the errors become intolerably large, and the data must be discarded if we wish to stay within the accuracy of better than 1 m.

The second problem is that of time synchronization. It is clear that if there is a time difference between the times measured independently at the two stations it will show up as a range error. Assuming the clocks have been synchronized once, how long will they stay this way? Now, it turns out that the very stable time standards which must be used in the VLBI system are hydrogen masers. They have an (unpredictable) drift of equivalent range of about 30 cm in 24 h. Assuming that the drift rates are solely due to the hydrogen masers (a rather bold assumption), it is then necessary to resynchronize again within three days to keep the range error below the 1-m level. We like to propose here a rather accurate method of synchronization which uses laser ranging.

It is known that the accuracy of a laser ranging system presently being used is 30 cm. It is also known that within the present state of the art the accuracy can be improved to the 3-cm level[9] without the need of any breakthrough. Suppose, then, that a VLBI is pointed at a synchronous earth satellite a few earth radii away and that at the same time two lasers, one at each site, are ranging the same satellite.[10] Then we would obtain from the lasers the information

$$cT_g^{(L)} = \rho_1 - \rho_2 \pm \sqrt{2} \cdot 30\,\text{cm (or better)} \qquad (42)$$

and from the VLBI:

$$cT_g = c\,(T_g^{(L)} + \Delta_S) \qquad (43)$$

where Δ_S is the error in clock synchronization which may be obtained from the two independent measurements (42) and (43) and corrected for within the accuracy of the laser ranging. Of course, Eq. (43) represents only an idealization in as much as the previously discussed error sources are not mentioned explicitly. They have to be accounted for as discussed above. Another trivial fact that needs mention in passing is that there is a difference in location between the satellite's antenna and corner reflectors as well as between the lasers and VLBI antennas that has to be accounted for.

[9]Private communication with R. Jaffe.

[10]The satellite must be equipped with a dual-frequency transmitter.

IV. Summary

On the preceding pages the feasibility and the potential enhancement of accuracy over the currently used ranging systems as described in the introduction have been shown. It has also been shown how to measure the total electron content separately within the raypath, a quantity which is of great interest to solar plasma physicists. The limitations in accuracy of the "coherent noise" system are due to *four* error sources:

(1) Bandwidth. A small bandwidth (as seen from Eq. 18) is quite detrimental. But, because of the exponential nature of the maximum of the correlation function, the bandwidth limitation is not critical. A 1-MHz bandwidth will yield a value of T_g good to 1 part in 10^7, approximately.

(2) Coherence between the X- and S-band transmitters. To take out the plasma effects, or in other words, to calibrate for the charged particles, the two transmitters on the spacecraft have to have a certain amount of coherence. First of all, they must be *phase*-locked; secondly, their bandwidths must be *identical*. The reason for these requirements is easily seen from Eqs. (39). A phase drift of the two receivers with respect to each other and a mismatch of the bandwidths would result in an unacceptable charged-particle calibration. However, we have to remember that the aforementioned calibration does not have to be performed to the same degree of accuracy as the differenced range measurements (the ubiquitous T_g of Eq. 6a). The correlation analysis may still be performed with the 1-MHz bandwidth originally assumed, the error in the charged-particle calibration amounting to no more than 1%.

(3) Tropospheric influences. They have been mentioned on the preceding pages and do not need any amplification, except that one should always be aware of their degrading influence on range accuracy.

(4) Synchronization. Synchronization is essential for this system to work. Without it, all advantages of the spacecraft VLBI will be utterly lost. It is therefore vital to implement a viable system allowing for the best accuracy available. The laser system proposed in this article seems to be more accurate in this context than any other known to the author at present.

References

1. *DSN Flight Project Interface Design Handbook*, 810-5, Rev. B, Aug. 1, 1971 (JPL internal document).
2. Ondrasik, V. J., and Rourke, K. H., "Applications of Quasi-VLBI Tracking Data Types to the Zero Declination and Process Noise Problems," presented at the AAS/AIAA Astrodynamics Specialists Conference 1971, Fort Lauderdale, Florida, August 17–19, 1971.
3. Callahan, P. S., *The VLBI Expected Correlation Over a Finite Bandpass*, Technical Memorandum 391-87, Apr. 8, 1970 (JPL internal document).
4. Swenson, G. W., and Mathur, N. P., "The Interferometer in Radio Astronomy," *Proc. IEEE*, p. 2114, Dec. 1968.
5. Ginzburg, V. L., *Propagation of Electromagnetic Waves in Plasma*. Gordon and Breach, Science Publishers, Inc., New York, 1961.
6. von Roos, O. H., "Second Order Charged Particle Effects on Electromagnetic Waves in the Interplanetary Medium," in *The Deep Space Network Progress Report*, Technical Report 32-1526, Vol. II. Jet Propulsion Laboratory, Pasadena, Calif., April 15, 1971.
7. von Roos, O. H., "Analysis of the DRVID and Dual Frequency Tracking Methods in the Presence of a Time-Varying Interplanetary Plasma," in *The Deep Space Network Progress Report*, Technical Report 32-1526, Vol. III, pp. 71–76. Jet Propulsion Laboratory, Pasadena, Calif., June 15, 1971.
8. Miller, L. F., et al., "A Cursory Examination of the Sensitivity of the Tropospheric Range and Doppler Effects to the Shape of the Refractivity Profile," in *The Deep Space Network Progress Report*, Technical Report 32-1526, Vol. I, pp. 22–30. Jet Propulsion Laboratory, Pasadena, Calif., Feb. 15, 1971.

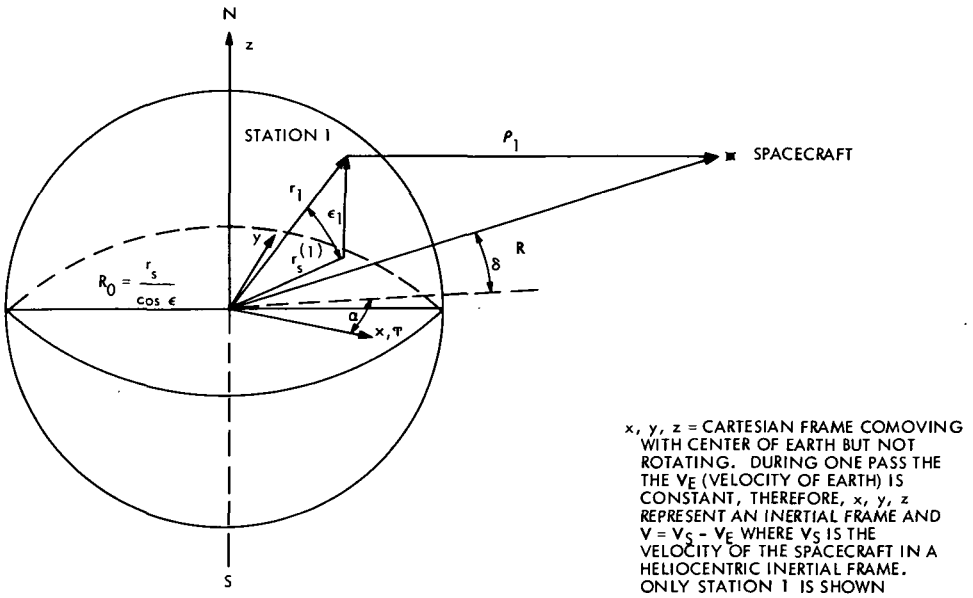

Fig. 1. Ranging geometry

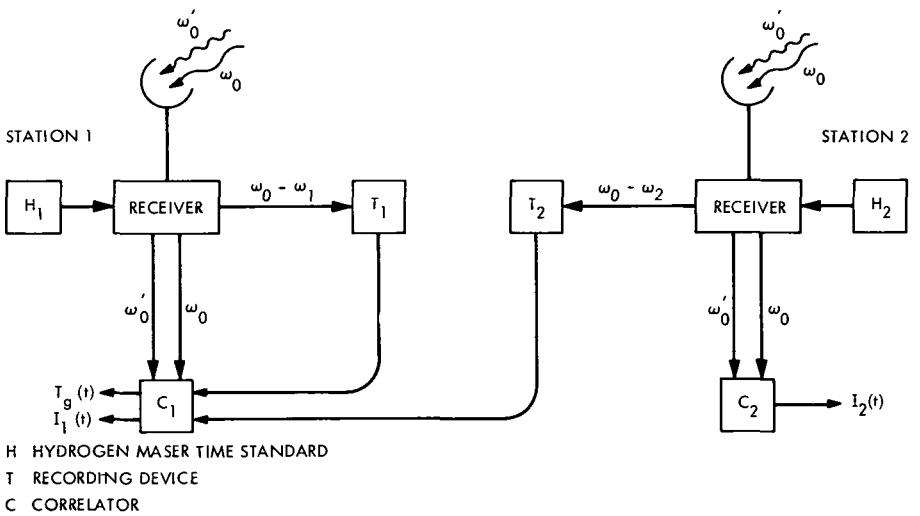

Fig. 2. Interferometer schematic (note the possible advantage for at least two correlators for independent charged-particle calibration)

Tropospheric Range Effect Due to Simulated Inhomogeneities by Ray Tracing

C. C. Chao
Tracking and Orbit Determination Section

A simple ray trace method is developed to study the effect in range correction of a radio wave passing through the troposphere with inhomogeneities. Inhomogeneities were simulated from previous observations. The uncertainties in range correction due to the unmodeled horizontal gradient in refractivity are mostly less than 1% for elevation higher than 5 deg. The average uncertainty due to local inhomogeneities, based on nine simulated cases, is below 1-m in one-way range correction for elevation angles greater than 5 deg.

I. Introduction

The purpose of the article is to investigate the influence of inhomogeneities in the troposphere based on the exact solutions from a two dimensional ray trace technique. Eighteen different cases of inhomogeneities were simulated, based on previous observations. A double-precision computer program called INHOMO was designed for numerical integration and analysis.

In the past, methods for reducing the troposphere-induced errors on interplanetary spacecraft orbit determination employed an exponential refractivity model which is independent of time. It was found that this model is not an adequate approximation to the true physical situation. First, the seasonal fluctuations in the refractivity profiles can cause a maximum of 10% deviation in zenith range effect.[1] Secondly, refractivity is not an exponential function of altitude in the first 12 km, where most of the refraction takes place.[2]

Currently an improved model, which uses Berman's (Ref. 1) time-dependent parameters for zenith range correction and maps it down to lower elevation angle by a two-stage quartic-exponential refractivity profile, is being introduced for tropospheric calibration. This model has reduced the errors in range correction due to seasonal fluctuations in the troposphere by 60%. However, it

[1]"The Repetition of Seasonal Variations in the Tropospheric Zenith Range Effect, by K. L. Thuleen and V. J. Ondrasik in this issue.

[2]New Tropospheric Range Corrections With Seasonal Adjustment," by C. C. Chao in this issue.

neglects the possible inhomogeneities (including asymmetry) in the troposphere that may contribute significant effect to range and range rate.

Bean and Dutton (Ref. 2) studied the effect of atmospheric horizontal inhomogeneity upon ray tracing. They computed only the ray-bending effect on elevation angles for two particular observed situations, and reached the tentative conclusion that the effect of horizontal inhomogeneity is normally small, since ducting, which causes inhomogeneity, will occur less than 15% of the time. For high-precision tracking techniques, i.e., very long baseline interferometry (VLBI) and laser ranging, which require tracking at very low elevation angles, such effect should be more carefully investigated. O. H. von Roos[1] has recently developed a first-order perturbation theory to examine the inhomogeneity influence on range.

He obtained a single integral, although it has to be integrated numerically, which gives the additional range effect due to inhomogeneities in good agreement (at 10-deg elevation angle) with the exact solution of this article. After further verification with the exact solution at various elevation angles his method may become a useful tool in calibrating the additional range effect from observed inhomogeneities.

The ray trace method introduced in this article can also be applied for the study of inhomogeneities in the ionosphere.

II. Ray Trace in an Inhomogeneous Atmosphere

The travel time of a radio wave between two fixed points in a medium can be written as

$$T = \int_1^2 \frac{dS}{V} \tag{1}$$

or

$$T = \frac{1}{c}\int_1^2 n\, dS \tag{2}$$

where

V is the speed of light in medium

c is the speed of light in vacuum

$n = c/V$ index of refraction ($n \geq 1$)

[1]"Tropospheric and Ionospheric Range Corrections for an Arbitrary Inhomogeneous Atmosphere (First-Order Theory)," by O. H. von Roos in this issue.

According to Fermat's Principle, the raypath takes the shortest time between two given points in a medium. Therefore, our problem is to find the path OB in Fig. 1 for which the travel time is a minimum. The infinitesimal change in distance, ds, is

$$dS = \sqrt{1 + r^2\left(\frac{d\phi}{dr}\right)^2}\, dr$$

Thus, we can rewrite the above equation as

$$\rho = cT = \int_{R_0}^{R_b} n\sqrt{1 + r^2\left(\frac{d\phi}{dr}\right)^2}\, dr \tag{3}$$

where

ρ = traveled distance between O and B

$\phi = \phi(r)$ along the raypath

and for a nonsymmetric atmosphere

$$n = n(\phi, r)$$

Since r is the independent variable, the integrand in Eq. (3) can be defined as the Langrangian of our problem.

$$L = L\left(\phi(r), \frac{d\phi}{dr}, r\right) = n\sqrt{1 + r^2\left(\frac{d\phi}{dr}\right)^2} \tag{4}$$

The Hamiltonian can then be obtained from the definition

$$H = H(\phi(r), p(r), r) = p\frac{d\phi}{dr} - L \tag{5}$$

where p is the momentum and can be given as

$$p = \frac{\partial L}{\partial \phi_1} = \frac{n r^2 \phi_1}{\sqrt{1 + r^2\phi_1^2}} \tag{6}$$

where $\phi_1 = d\phi/dr$, and it is expressed in terms of p as

$$\phi_1 = \frac{p}{r\sqrt{n^2r^2 - p^2}} \tag{7}$$

Upon substitution, we then easily obtain the Hamiltonian in the following simple form:

$$H = -\frac{\sqrt{n^2r^2 - p^2}}{r} \tag{8}$$

Therefore, the raypath of a radio wave passing through an inhomogeneous medium can be obtained by integrating the following equations:

$$\frac{d\phi}{dr} = \frac{\partial H}{\partial p} \tag{9}$$

$$\frac{dp}{dr} = -\frac{\partial H}{\partial \phi} \tag{10}$$

or

$$\frac{d\phi}{dr} = \frac{p}{r\sqrt{n^2r^2 - p^2}} \tag{11}$$

$$\frac{dp}{dr} = \frac{nr\dfrac{\partial n}{\partial \phi}}{\sqrt{n^2r^2 - p^2}} \tag{12}$$

For a spherically symmetric atmosphere, $\partial n/\partial\phi$ vanishes and p is a constant. Then Eq. (11) will lead to the familiar integral of ray trace.

$$\phi = \int_{R_0}^{r} \frac{c_0}{r\sqrt{n^2r^2 - c_0^2}}\, dr \tag{13}$$

where

$$c_0 = r_0 n_0 \cos \gamma_0$$

The above two-dimensional approach assumes that the perturbed raypath due to inhomogeneities is always remaining in the same vertical plane. The bending in the azimuth direction has been found insignificantly small from three-dimensional ray trace results. The horizontal gradients in refractivity due to tropospheric inhomogeneities are much smaller than the vertical gradients, which causes sizable bending effect at very low elevation angles.

III. Range Effect Due to Simulated Inhomogeneities

The inhomogeneities in troposphere are defined here as any departure from spherical symmetry and local irregularities in refractivity. Bean and Dutton made several nation-wide surveys of the variations in refractivity. Figure 2 shows the mean values of sea level refractivity N_0 in the August months over the U.S. A horizontal gradient of about 30 N units per 500 km can be found in California. When a bad storm is passing through, the horizontal gradient increases to 50 N units per 500 km, as shown in Figs. 3 and 4. A sample of the corresponding variation in refractivity in a space cross-section in N units is shown in Fig. 5. The local irregularities in refractivity were also shown by the observed results made along a straight path which began at Cape Kennedy in 1957 by Bean and Dutton (Fig. 6).

Based on the above observed results originating from Ref. 4, an analytic expression of the variation of refractivity N was developed for the two-dimensional ray trace computation. Figure 5 seems to indicate that the variations are sinusoidal in nature; thus, we can approximately simulate the inhomogeneities by the following analytic form:

$$N(r,\phi) = N_0\left(1 - \frac{r - r_0}{H}\right)^4 + \Delta N_{\text{inhomo}}(r,\phi)$$

where

$$\Delta N_{\text{inhomo}} = \Delta N_0\left(1 - \frac{r - r_0}{H_1}\right)^4\left[A\phi + B\sin\left(\frac{\pi}{2}\frac{\phi}{W}\right) + c\sin\left(\frac{\pi}{2}\frac{r - r_0}{L}\right)\right]$$

and

ΔN_{inhomo} = change of refractivity due to inhomogeneity

ΔN_0 = change of surface refractivity due to inhomogeneities

ϕ = raypath angle, rad

H_1 = the light of the layer in which inhomogeneities takes place

A = parameter of the constant gradient along ϕ direction

B,C = parameters of the amplitude of sine function along ϕ and r direction, respectively

W,L = one fourth of the wavelength of the two sine functions along ϕ and r direction

The values of those constants in the above equation are estimated based on the observed results shown in Figs. 2 to 6. Samples of 18 different cases (Table 1) were computed by the two-dimensional ray trace program. The first nine cases simulate the horizontal gradient, and

the second nine cases (from 10 to 18 in Table 1) approximate the local inhomogeneities as shown in Fig. 6. The additional influences on range correction of these 18 cases are tabulated in Table 2.

IV. Results and Discussion

The additional range effects due to the 18 different simulated inhomogeneities were ray traced by a double precision computer program called INHOMO. It employed a fifth-order Runge-Kutta integrator with automatic step size control. The results can be grouped into four types:

I. Horizontal gradient assumed in the entire troposphere ($H_1 = 42.6$ km).

II. Horizontal gradient occurs only in the first 13.6 km from surface ($H_1 = 13.6$ km).

III. Irregularities assumed in the entire troposphere ($H_1 = 42.6$ km).

IV. Irregularities are confined within the first 13.6 km from surface ($H_1 = 13.6$ km).

The results for type I are shown by the first three cases in Table 2. They have higher values than the type II results, as shown by cases 4 to 9 in Table 2. According to the radiosonde balloon data (Ref. 2), most of the fluctuations in refractivity were found in the first 14 km of altitude. Thus the actual influence on range correction due to horizontal gradient is expected to be in the same magnitude of type II results. A normalized range effect due to horizontal gradient is plotted in Fig. 7. The influence due to local irregularities similar to the one shown in Fig. 6 are difficult to simulate with a simple equation. However, the second nine cases in Table 1 will reveal, quantitatively, the effect on range due to local irregularities. As shown in Table 2, the effects on range caused by local irregularities are more significant than that induced by horizontal gradient. A 2 to 12% change in range effect can be found at various elevation angles in type III results (cases 11, 12, 13, 16, 17, 18), and the type IV results have a smaller variation from 1.2% to 6% (cases 10, 14, 15). Similarly, type IV results are expected to better approximate the actual normalized range effect due to local irregularities is plotted in Fig. 8.

From the above results, one conclusion may be reached that the additional range effects due to possible horizontal gradient are mostly insignificant for elevation angle greater than 5 deg ($\Delta\rho < 0.1$ m), the corresponding effects due to local inhomogeneities are sizable—from 5 to 20 deg of elevation ($0.1 \text{ m} < \Delta\rho < 1.0$ m). However, according to Bean and Dutton (Ref. 4), the local irregularities usually caused by bad storm and ducting will occur less than 15% of the time. Thus, in case of a bad storm or a noticeable ducting, the tracking data should be deleted or loosely weighed before advanced techniques of tropospheric calibration, such as line-of-sight correction by microwave radiometer, are available.

References

1. Berman, A., "A New Tropospheric Range Refraction Model," in *The Deep Space Network*, Space Programs Summary 37-65, Vol. II, pp. 140–153. Jet Propulsion Laboratory, Pasadena, Calif., August 30, 1970.

2. Bean, B., and Dutton, E., *Radio Meteorology*, Monograph 92, U.S. Department of Commerce, National Bureau of Standards, March 1966.

Table 1. Simulated tropospheric inhomogeneities

Case No.	N_0	ΔN_0	H_1	A	B	C	W, km	L, km
1	350	70	42.6	0	1	0	800	–
2	300	50	42.6	0	1	0	800	–
3	300	50	42.6	0	1	0	1600	–
4	300	50	13.6	6	0	0	–	–
5	300	50	13.6	12	0	0	–	–
6	300	50	13.6	0	1	0	300	–
7	300	50	13.6	0	1	0	1600	–
8	300	50	13.6	0	1	0	800	–
9	350	70	13.6	0	1	0	800	–
10	300	50	13.6	12	0	0.5	–	1.0
11	300	50	42.6	0	1	0.5	500	2.0
12	300	50	42.6	0	1	0.5	300	2.0
13	300	50	42.6	0	1	0.5	100	2.0
14	300	50	13.6	0	1	0.5	500	1.0
15	300	50	13.6	–	1	1.0	100	1.0
16	300	25	42.6	0	1	0.5	500	2.0
17	300	25	42.6	0	1	0.5	300	2.0
18	300	25	42.6	0	1	0.5	100	2.0

Table 2. Additional influence in tropospheric range correction due to simulated inhomogeneities

Case No.	Percent of total range correction					
	(70)[a] At 1 deg	(36) At 3 deg	(24) At 5 deg	(12.7) At 10 deg	(8.7) At 15 deg	(6.5) At 20 deg
1	6.15	4.67	3.35	1.96	1.36	1.00
2	4.28	3.31	2.4	1.41	0.94	0.72
3	2.23	1.68	1.23	0.70	0.47	0.36
4	0.47	0.24	0.15	0.08	0.05	0.04
5	0.93	0.48	0.31	0.15	0.10	0.08
6	2.38	1.33	0.84	0.43	0.28	0.21
7	0.47	0.25	0.16	0.08	0.05	0.04
8	0.96	0.50	0.32	0.16	0.10	0.08
9	1.36	0.70	0.44	0.22	0.15	0.11
10	2.42	1.71	1.43	1.23	1.15	1.15
11	8.87	7.43	6.02	4.33	3.58	3.22
12	11.30	10.20	8.30	5.79	4.56	4.00
13	7.17	11.10	12.58	11.11	8.95	7.54
14	2.88	2.00	1.63	1.34	1.23	1.20
15	6.92	5.61	4.51	3.41	2.94	2.77
16	4.66	3.79	3.04	2.18	1.79	1.62
17	5.86	5.16	4.17	2.89	2.30	2.0
18	3.63	5.55	6.31	5.59	4.47	3.76

[a]Values in parenthesis give the total range correction in meters.

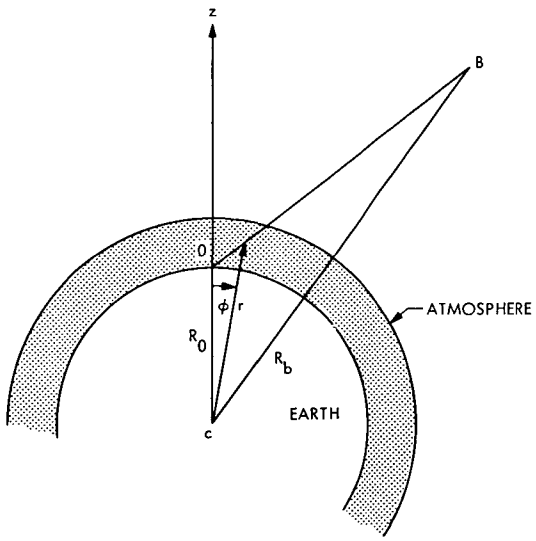

Fig. 1. Geometry of the radio wave refraction

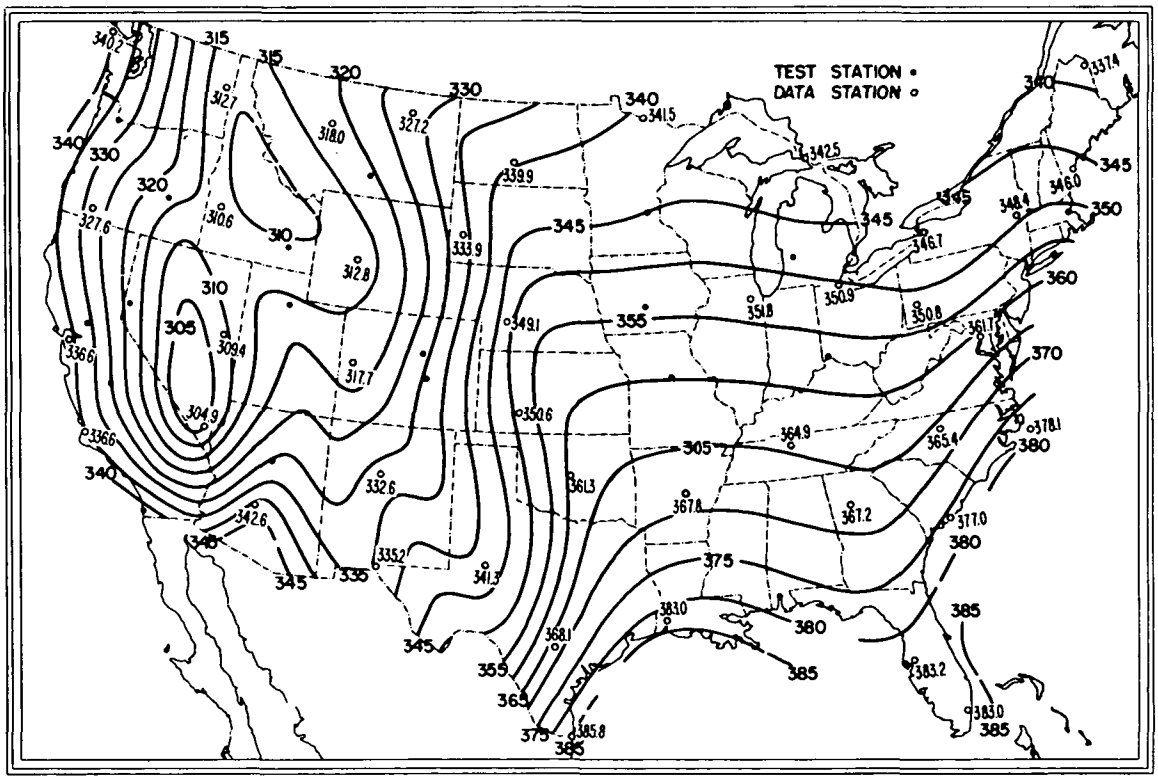

Fig. 2. Test chart of mean N_0 on August at 02:00 local time (taken from Ref. 2)

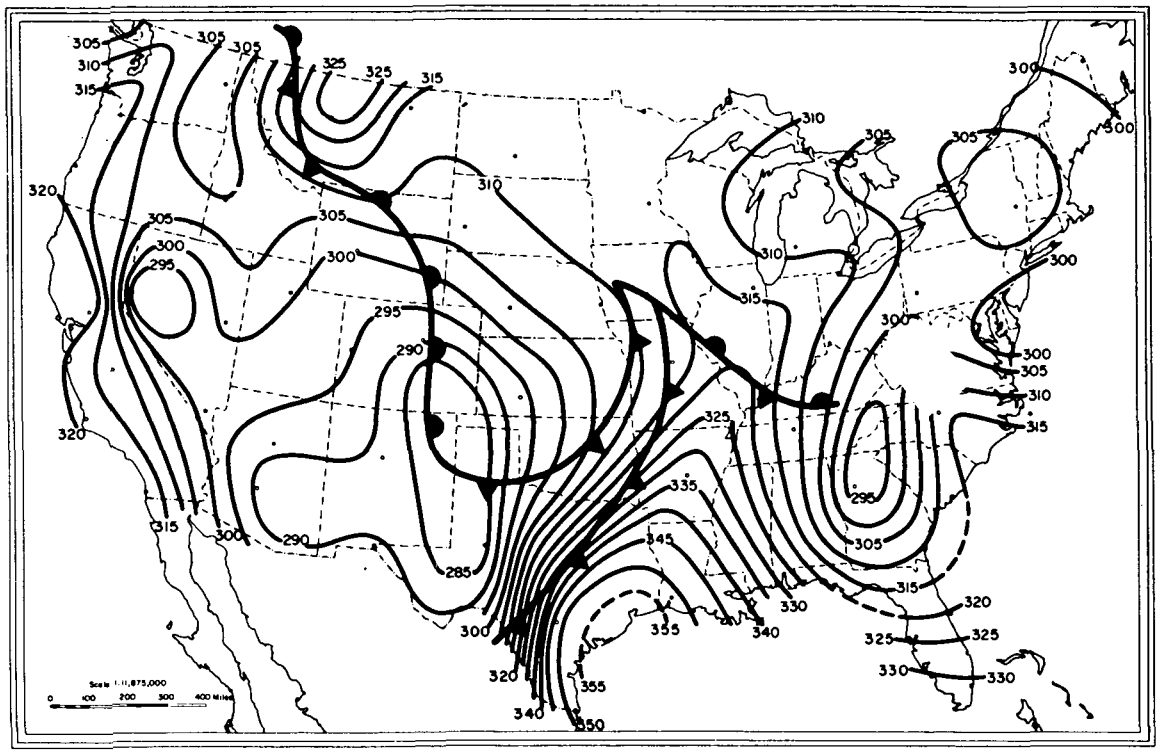

Fig. 3. N_0 chart for storm system 1330E, Feb. 19, 1952 (Ref. 2)

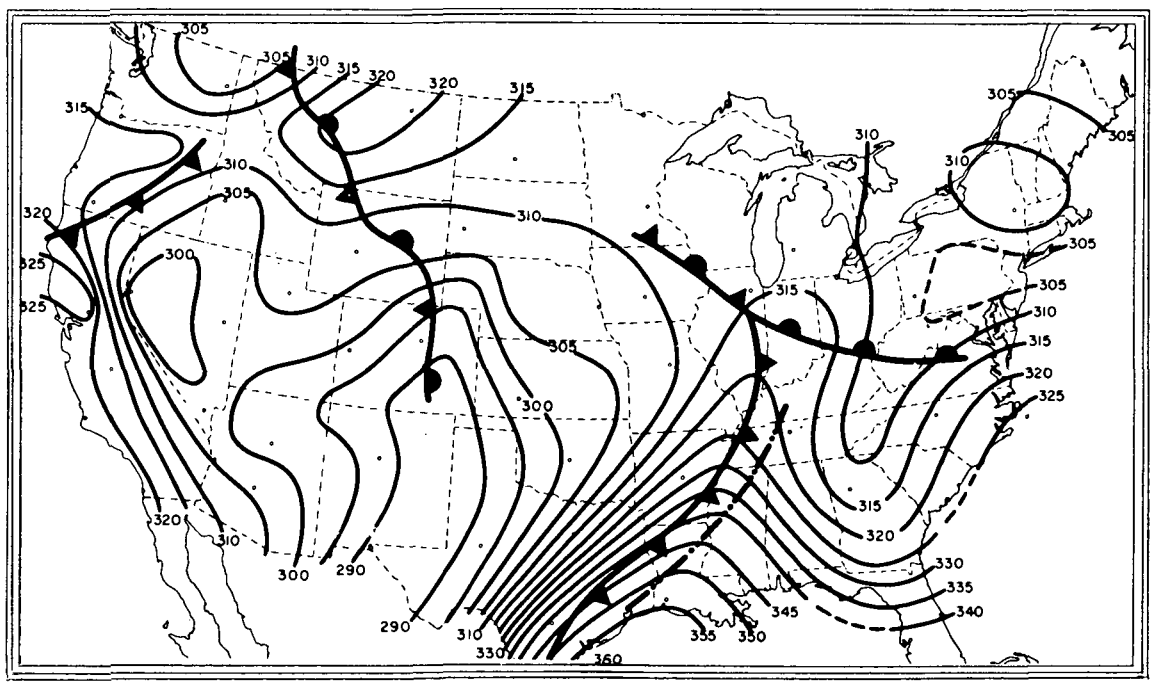

Fig. 4. N_0 chart for storm system 01330E, Feb. 20, 1952 (taken from Ref. 2)

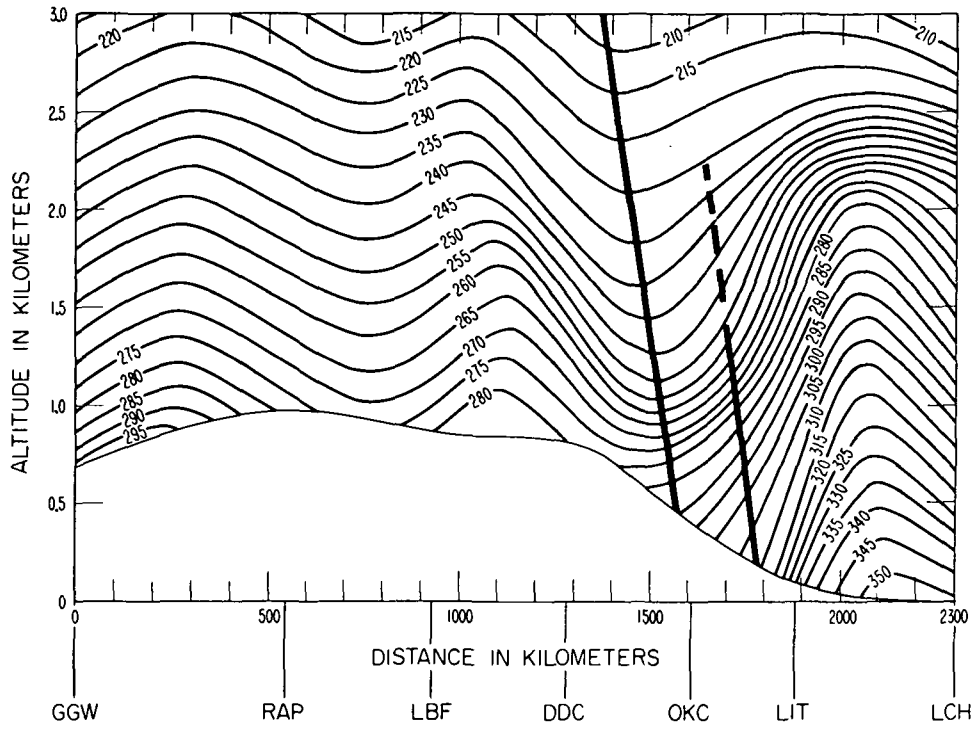

Fig. 5. Space cross section in *N* units, 15:00Z on Feb. 19, 1952 (taken from Ref. 2)

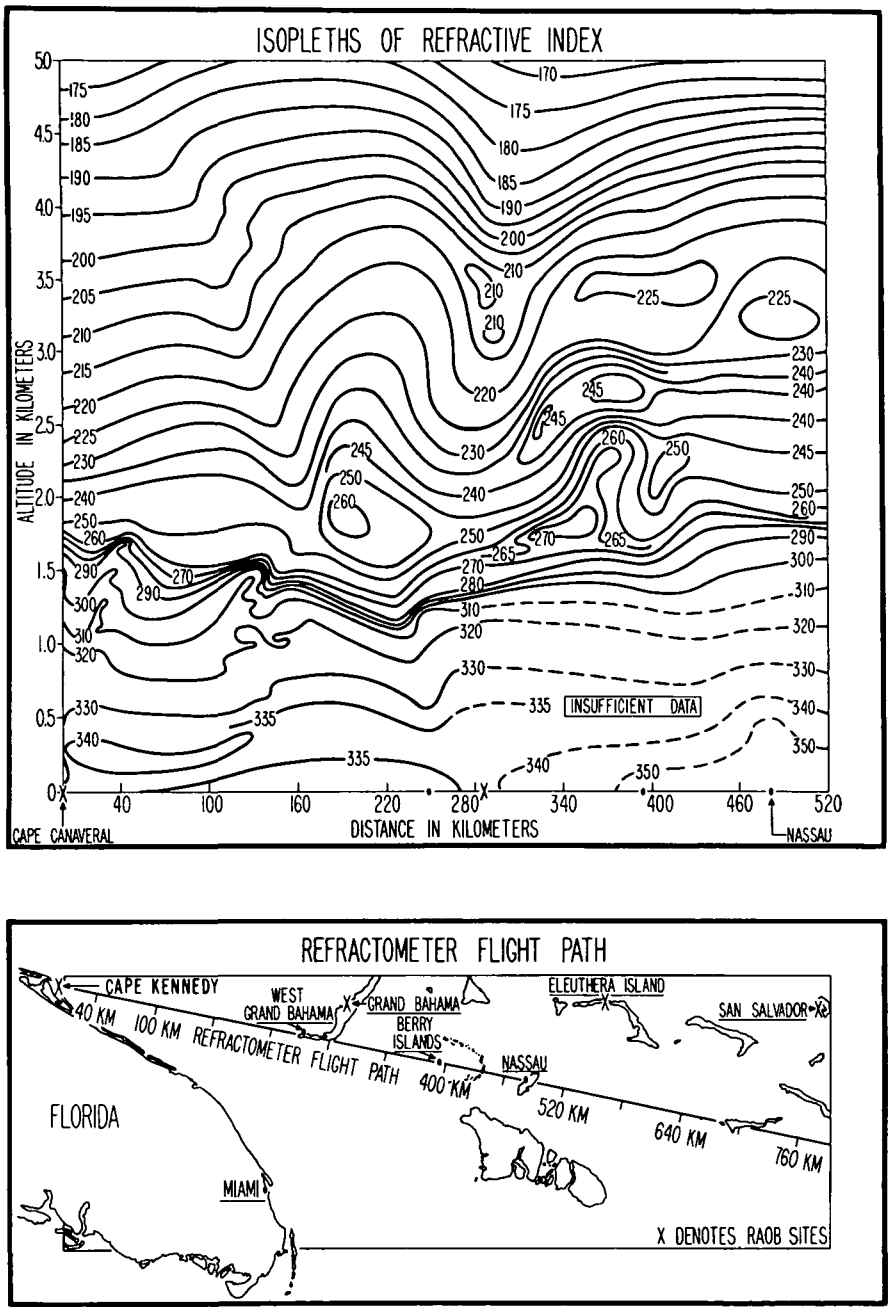

Fig. 6. Isopleths of refractive index and map of refractometer flight path for May 7, 1957, Cape Kennedy to Nassau (taken from Ref. 2)

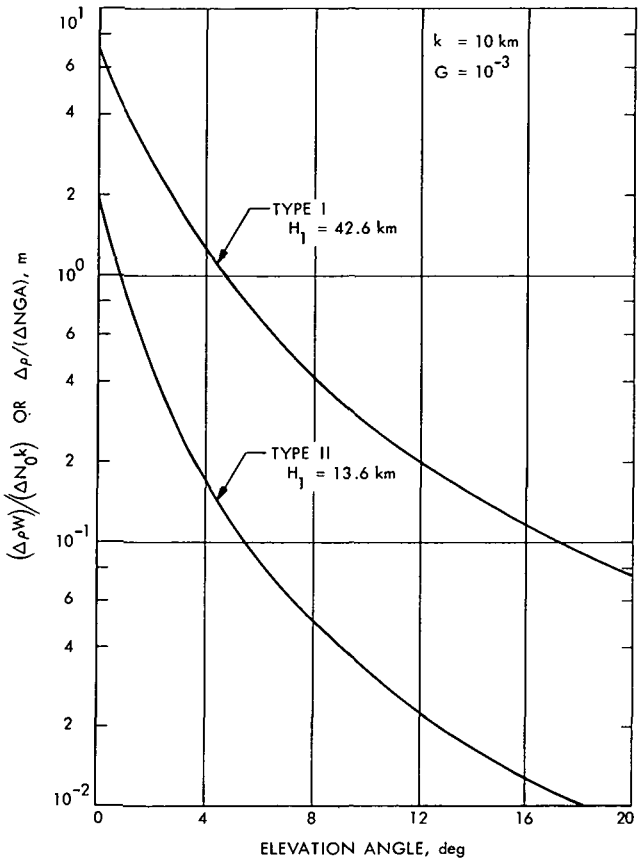

Fig. 7. Normalized range effect due to horizontal gradient effect

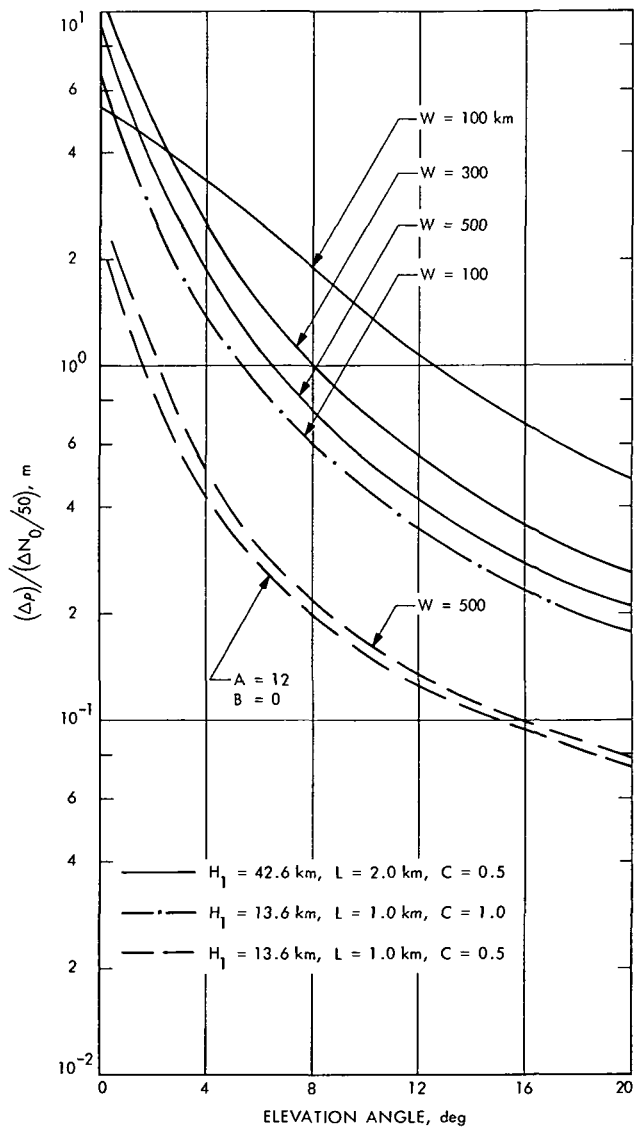

Fig. 8. Normalized range effect due to local inhomogeneities

New Tropospheric Range Corrections With Seasonal Adjustment

C. C. Chao
Tracking and Orbit Determination Section

A study of two years' radiosonde balloon measurement shows that most of the significant seasonal fluctuations in refractivity profiles are due to the variation of the water content in the troposphere. At each of the six weather stations, the long-term seasonal variation in refractivity profile repeats quite well through the two-year span. Based on the two years' data a new tropospheric range calibration method using monthly mean parameters at each station was developed.

The uncertainty of range correction with the new model over one pass is estimated to be 0.30–0.35 m for a 10-deg minimum elevation angle and 0.40–0.50 m for a 6-deg minimum elevation angle. This is below the required accuracy for tropospheric calibration of both Mariner Mars 1971 (MM71) and Viking 1975 missions.

I. Introduction

It is our current goal to examine the variations in the refractory profiles in the hope of reducing the uncertainty in range correction with a time-dependent model.

Radio tracking is directly affected by the refraction of the troposphere, and extensive efforts have been devoted to the correction of this error by many researchers. In the past, tropospheric refraction was calibrated with a model which was independent of time. This neglected the possible temporal fluctuations in the refractivity of the troposphere. A recent study of one year's radiosonde balloon data by Ondrasik and Thuleen (Ref. 1) indicated that the tropospheric zenith range effect has a variation of about $\pm 5\%$ of its yearly average. According to Ref. 2, the 5% uncertainty in zenith range effect may cause a greater percentage (6 to 8%) range effect uncertainty at low elevation angles because of the possible variations in the refractivity profile. An 8% uncertainty in range effect corresponds to more than 1 m in the overall uncertainty in range correction over the whole pass, which exceeds the requirement of the MM71 mission ($\sigma\Delta\rho/_{\text{pass}} = \frac{1}{2}$ m, lowest elevation = 10 deg) and the *Viking* 1975 Mission ($\sigma\Delta\rho/_{\text{pass}} = 1$ m, lowest elevation = 6 deg). When the two-station tracking or very long baseline interferometry (VLBI) techniques are employed, the low elevation angle data will become more important, since these long baselines generally result in data being obtained at low elevation angles (Ref. 3). The required uncertainty in range correction over one pass by VLBI is below 1 m, which

cannot tolerate the seasonal fluctuations in refractivity of troposphere.

The new model of tropospheric calibration was developed as a result of the following investigations:

(1) Examination of the seasonal variations in the refractivity profiles based on two years' radiosonde balloon measurement taken at six weather stations near five of the DSN stations.

(2) Comparison of the exponential model that has long been used with the measured profile of refractivity, and the derivation of an analytic expression which can more closely represent the actual dry refractivity profile than the exponential function does.

(3) Estimation of uncertainties of range effect due to the seasonal fluctuations in refractivity profiles found in (1). Examination of the improvement that can be obtained by using the monthly mean profiles.

(4) Development of a new tropospheric calibration model with seasonal adjustment. The zenith range effect is estimated from balloon data combined with prediction from surface measurement derived by Berman.

II. Refractivity Profiles

The refractivity of the troposphere at a given altitude is commonly determined from the following equation (Ref. 4)

$$N = \frac{77.6}{T} P + \frac{4810e}{T} \tag{1}$$

where

P = pressure, mb

T = temperature, °K

e = vapor pressure, mb

and

$$e = 6.1 \exp_{10}\left(\frac{7.4475\, T_c}{234.7 + T_c}\right)\left(\frac{RH}{100}\right)$$

where

RH = relative humidity, %

T_c = temperature, °C

$\exp_{10} y = 10^y$

The values of P, T, and RH are the measured data at a given altitude from the radiosonde balloon. An approximation to the errors in N resulting from the use of Eq. (1) due both to the errors in the equation itself and to errors in the meteorological measurements, is given by Bean and Dutton (Ref. 4) as shown in Table 1.

The first and second terms of Eq. (1) will be referred to as the dry and wet refractivity, N_D and N_W, respectively.

Because of the seasonal or daily variations of the parameters in Eq. (1), P, T, and RH, the values of N above a station are to have similar types of variations from time to time. The values of dry and wet refractivity, N_D and N_W, were calculated from the radiosonde balloon measurements taken at the six stations (Table 2). It is convenient to examine the dry and wet refractivity profiles separately from the two years' data.

A. Dry Refractivity Profiles

About 90% of the total refractivity, N, is due to the dry component in the first 6.1 km (20,000 ft). From there upward, the wet component diminishes and the dry part becomes the total refractivity. From Eq. (1), we can express the dry component refractivity as:

$$N_D = 77.6 \frac{P}{T} \tag{2}$$

The variations in N_D as resulted from the fluctuations in pressure P and temperature T in the troposphere were investigated using the radiosonde balloon measurements taken at six weather stations. The standard deviations of the dry refractivity, σ_{dry}, from the monthly mean at Edwards AFB were calculated and tabulated in Table 3. The results indicate that N_D has greater deviations at low altitude. Above 6.1 km (20,000 ft), most of the deviations are less than the magnitude of the uncertainties due to measurement of data and Eq. (1) (See Table 1). This implies that the fluctuations of N_D above 6.1 km (20,000 ft) are probably so small in magnitude that the current radiosonde balloon measurement fails to filter it out. In other words, the density of the troposphere above 6.1 km (20,000 ft) stays fairly constant. The variations of the monthly mean of N_D at various altitudes were also shown in Table 3. The fluctuation in N_D below 6.1 km (20,000 ft) is caused by the daily and seasonal variations in pressure and temperature resulting from the weather change in the area. As it will be shown later, the magnitude of these low-altitude fluctuations is less than the magnitude of the fluctuations of the wet component. Since the dry component

of refractivity dominates the total refraction and is relatively steady in most portions of the troposphere, an analytic expression for mapping the range effect down to lower elevation angles may be derived.

If we assume the atmosphere is in static equilibrium, spherically symmetrical and obeys the perfect gas law, then we can write the governing equations for the dry part as Berman did in Ref. 7.

$$-\rho g = \frac{dP}{dr} \tag{3}$$

$$P = \rho RT \tag{4}$$

where P, ρ, and T are functions of r only, and

ρ = density of air

P = pressure

T = absolute temperature

r = geocentric distance

R = gas constant

g = gravitational acceleration

The temperature profile, $T(r)$ in the atmosphere depends on the thermal property of the atmosphere and the heat balance of the Earth. According to the measured data from the U.S. Standard Atmosphere Supplements, 1966, the temperature profiles in the troposphere can be classified into two types; linearly decreasing up to about 10 km and then remain fairly constant up to 30 km (Fig. 1).

$$T \cong T_0 - \gamma(r - r_0) \qquad r_0 < r < r_m \tag{5}$$

$$T \cong T_m \qquad r_m < r < r_{\text{tropo}} \tag{6}$$

where

γ = temperature lapse rate

r_0 = surface altitude

r_m = altitude where temperature becomes constant with altitude

r_{tropo} = outer edge of troposphere (about 40 km)

Then we can combine Eqs. (3), (4), (5) and (6) and integrate to get

$$P = P_0\left(1 - \frac{\gamma h}{T_0}\right)^{\alpha} \tag{7}$$

$$P = P_m \exp\left[-\frac{g}{RT_m}(h - h_m)\right] \tag{8}$$

where $\alpha = g/\gamma R$, $h = r - r_0$, P_m, T_m are the values of P and T at r_m, P_0, T_0 are conditions at r_0. Substituting Eqs. (7) and (8) into the dry part of Eq. (1), we obtain the expression for dry refractivity profile:

$$N_D = \frac{77.6}{T}P = 77.6\frac{P_0\left(1 - \frac{\gamma h}{T_0}\right)^{\alpha}}{T_0\left(1 - \frac{\gamma h}{T_0}\right)}$$

$$= N_{D0}\left(1 - \frac{\gamma h}{T_0}\right)^{\alpha - 1} \tag{9}$$

$$N_D = \frac{77.6}{T_m}P_m \exp\left[-\frac{g}{RT_m}(h - h_m)\right]$$

$$= N_{Dm} \exp\left[-\frac{g}{RT_m}(h - h_m)\right] \tag{10}$$

where

N_{D0} = dry surface refractivity

N_{Dm} = dry refractivity at r_m

The profile in the first 10 km follows a polynomial of power $\alpha - 1$, that in the next 20 km decays exponentially under an approximately isothermal condition. The average value of $\alpha - 1$, based on the mean temperature profiles shown in Fig. 1, is about 4. This explains why a quartic profile as suggested by Hopfield (Ref. 5) has closer agreement with the data than a simple exponential profile does in the first 12.2 km (40,000 ft) (Fig. 2). The quartic model deviates by an appreciable amount when it is higher than 15.2 km (50,000 ft) where a second stage exponential model works nicely as shown in Fig. 3.

B. Wet Refractivity Profiles

As indicated in Ref. (1), the dominant error source in the zenith range tropospheric correction computed from radiosonde data comes from the variations in the wet

component of refractivity, N_W. It can be rewritten in the following way:

$$N_W = 3.733 \times 10^5 \frac{e}{T^2} \tag{11}$$

or

$$N_W = 2.277 \times 10^4 \frac{RH}{T^2} \exp_{10}\left(\frac{7.4475\, T_c}{234.7 + T_c}\right) \tag{12}$$

The value of the wet component of refractivity N_W is directly proportional to the water content in the troposphere. Equation (12) indicates that changes in temperature and relative humidity will cause variations in the values of N_W. As shown in Table 4, the value of N_W varies drastically when weather changes. The variation in relative humidity is a complicated function of the local weather nature, and thus it is very difficult to approximate the profile of N_W analytically as a function of altitude similar to the dry component N_D.

According to the balloon data, the wet refractivity profiles are confined within the first 6.1 to 7.6 km (20,000 to 25,000 ft) of altitude where most of the water vapor in the atmosphere is contained. The temperature and relative humidity for a particular area are known to have both daily and seasonal variations, thus the wet refractivity N_W computed from Eq. (12) should also have two types of variations.

1. Daily (short-term) fluctuations

The typical diurnal temperature change is around 10 to 15°C at the Goldstone DSCC, and the change in relative humidity is 20 to 25%. Thus from Table 4 the corresponding change in N_W will be around 10 to 20 units, which may lead to a significant change in range effect.

The actual daily fluctuations in the wet component, N_W, can be found from the computed data from radiosonde balloon measurements. Figures 4 and 5 show the profiles of N_W above a meteorological station for the first 6.1 km (20,000 ft), where N_W is significant. Due to the limitation of space, only the summer and winter type profiles are shown in these figures.

The three stations in the northern hemisphere, Edwards Air Force Base in California, Yucca Flats in Nevada, and Madrid in Spain, have very different types of profiles between summer and winter. About ten days' data in January plotted in Fig. 4 reveals the average low profiles and lesser daily fluctuations in winter. While the corresponding plot (Fig. 5) shows that the summer weather makes the wet component of refractivity very active and fluctuating. The profiles in the rest of the year fall between these two types of profiles, and they will be seen on the monthly mean profiles later.

The other three stations in the southern hemisphere, Woomera and Wagga in Australia, and Pretoria in South Africa, show similar characteristics in the summer and winter type of profiles except that the fluctuations in winter (June–August) are more active than that of the northern hemisphere stations.

2. Long-term (seasonal) fluctuations

The monthly mean of the wet refractivity profiles for stations at Edwards Air Force Base and Madrid were plotted in Figs. 6 and 7. The seasonal variations can be easily seen from those monthly mean profiles. The summer type profiles are consistently the highest of the year, while the winter type profiles are the lowest. The magnitude of the total variation in a year and the shape of the average profiles varies from station to station due to the particular local weather variation. For instance, the magnitude of variations at Edwards Air Force Base is greater than that at Madrid, and the former has a peculiar type of profile in the low altitude where a maximum usually occurs at a height of about 1000 ft above the surface. It should be noticed that the magnitudes of short-term fluctuations in winter, spring, and fall are generally several times smaller than those of the long-term fluctuations. In the summer, the short-term fluctuation becomes so active that it is almost equal to the long term in magnitude. The range of standard deviations from the monthly mean were shown in Table 5. It has higher deviations than the dry part.

It is also important to examine the repeatability of the seasonal variations at each station. Thuleen and Ondrasik[1] recently made a comparison of the two-year zenith range effects at the six weather stations, and the results showed good repeatability of the seasonal variations at each station. The results of this analysis also indicate that the seasonal variations in the shape of both dry and wet profiles repeat quite well based on the two years' data. Figures 4 and 5, and 8 and 9 give a sample of the wet refractivity profiles in the same months of the two years. Their agreement is generally good. The difference between the two years data are of the same magnitude as that of the

[1] "The Repetition of Seasonal Variations in the Tropospheric Zenith Range Effect," in this issue.

short-term fluctuations. This gives us confidence in that a new calibration model with seasonal adjustment can significantly reduce the uncertainties in range and range rate calibrations caused by seasonal fluctuations.

III. Uncertainty of Range Effect Due to Seasonal Fluctuations at Various Elevation Angles

Since the range and range rate correction for the troposphere are directly derived from the profiles of refractivity, N, any change in N will eventually affect the precision of a fixed-profile calibration model for the troposphere in radio tracking. An estimation is made here to reflect the uncertainties in range correction for troposphere caused by the fluctuations in the profiles of refractivity obtained from radiosonde balloon measurement. Table 6 shows the average uncertainties (1σ) in range correction at various elevation angles of a fixed calibration model (2-year mean) and a seasonally adjusted model (monthly mean). Values in Table 6 were computed by a ray trace program.

It is seen that the fixed model based on the two-year mean profile at each station has an uncertainty of about 0.11 m (5%) at zenith and 1.6 m (6.5%) at 5 deg of elevation angle. When the monthly mean profiles are used, the uncertainty in the range correction has been reduced by almost a factor of three. The greatest part of the uncertainty is due to the fluctuations in the wet component. The values at zenith as shown in Table 6 seem to agree with the results in Ref. 1.

IV. Range Correction Combined With Surface Measurement

It is expected that frequent radiosonde balloon measurements will reduce the uncertainty due to temporal fluctuations. However, it is not practically possible to take balloon measurement as frequently as one desires, say once every hour. Thus the method for predicting the profiles and zenith range effect through surface measurement which can be taken frequently or even continuously becomes very helpful.

Recently Berman (Ref. 6) derived a set of formulas which can predict the dry and wet component of the zenith range effect from ground surface measurement.

$$\Delta\rho_{z\,\mathrm{dry}} = 2.276\,P_0 \tag{11}$$

$$\Delta\rho_{z\,\mathrm{wet}} = 0.566\frac{(RH)}{\gamma}\left(1-\frac{c}{T_0}\right)^2 \exp\left(\frac{AT_0-B}{T_0-C}\right) \tag{12}$$

where

$\Delta\rho_z$ = zenith range correction, m

P_0 = surface pressure, bar

γ = temperature lapse rate, K/km

T_0 = linearly extrapolated surface temperature, K

$(RH)_0$ = surface relative humidity $(0 \leq (RH)_0 \leq 1)$

$A = 17.1486$

$B = 4684.1331$

$C = 38.45$

Equation (11) is obtained under the assumption of static equilibrium, perfect gas of the troposphere and constant gravitation acceleration, g. If these assumptions are true, Eq. (11) has the potential to be able to predict the dry zenith range effect with an uncertainty of ± 2 mm for a precision of ± 1 mb in surface pressure measurement (Ref. 7). According to Ref. 6, the uncertainty of the wet zenith range effect computed from Eq. (12) is 2.8 cm (1σ). Thus the total zenith range effect can be predicted from surface measurement with, potentially, the same accuracy as radiosonde measurement. Two of the four parameters P_0, and $(RH)_0$ can be measured continuously at each tracking station; for example, the micro-barograph measures surface pressure continuously.

The temperature lapse rate L and T_0 can be estimated from less frequent (perhaps every several days or use monthly mean) radiosonde measurement. Another advantage of Eq. (11) is that it gives the dry zenith range effect of the entire troposphere, while most of the radiosonde balloon data end at about 24.4 km (80,000 ft), and the contribution due to rest of the troposphere has to be estimated. Besides, the balloon, instead of ascending along zenith direction, may fly along a 30- to 45-deg elevation due to local wind. Equation (12) is derived under the assumption of constant RH, when RH varies drastically with altitude, the wet zenith range effect should be obtained directly from radiosonde measurement. Once the zenith range correction is accurately determined, the next

step is to map it down to lower elevation angles by employing a correct refractivity profile.

A cursory examination of the sensitivity of the tropospheric range effect to the shape of the refractivity profile has been made in Ref. 2. It indicates that for a slight variation in the profile of refractivity, the effect on the ratio of mapping zenith range effect to lower elevation is very small. According to measured data (Table 3), the variations in the shape of the dry refractivity profile is insignificantly small for most of the troposphere. Thus a mean profile closely approximating the real data can be obtained for generating a standard table to map the dry zenith range error down to 3 deg elevation angle within 3% uncertainty. After fitting the measured data with the previously derived function (Eqs. 9 and 10), a best-fit profile for the dry part refractivity is found.

$$N_{dry} = 269\left(1 - \frac{h}{42.7}\right)^4 \qquad h \leq 12.2\,\text{km} \qquad (13)$$

$$N_{dry} = 70\exp\left[-\frac{(h - 12.2)}{6.4}\right] \qquad h \geq 12.2\,\text{km} \qquad (14)$$

Although the wet profiles were found varying drastically from time to time, most of them seem to have similar monotonically decreasing shape (Figs. 4 and 5). They can be approximated by the following expression without loss of significant accuracy, if the deviations in shape are not too great.

$$N_{wet} = N_s\left(1 - \frac{h}{13}\right)^4 \qquad h \leq 13\,\text{km} \qquad (15)$$

$$N_{wet} = 0 \qquad h \geq 13\,\text{km} \qquad (16)$$

In case of bad weather, when the shape of the profile from special balloon measurement is significantly different from the quartic profile of Eq. (15), a special ray tracing should be made for the mapping.

The above calibration which based on Berman's formula for zenith range correction from monthly mean parameters, and the mapping table for range correction at lower elevation angles was adopted as the new model for tropospheric correction in DPODP for the *Mariner* Mars 1971 Mission. The values of the monthly means of the four parameters in Berman's formulas calculated from the two years' data and the standard mapping table can be found in Ref. 8.

The past time-independent model in DPODP assumes that the refractivity decreases exponentially with height above sea level. Based on the specified profile ($N = 340 \exp[-h/7]$) two empirical formulas were fitted to give the range correction at any elevation angle.

$$\Delta\rho = 1.8958\,\frac{N}{340}(\sin\gamma + 0.06483)^{-1.4} \qquad (17)$$

$$\Delta\rho = \frac{2.6}{\sin\gamma + 0.015}\,\frac{N}{340} \qquad (18)$$

The two formulas, Eq. (17) and Eq. (18), were originated from D. Cain. The second equation is a modified function for better results when the elevation is 15 deg or higher. The zenith range effect computed from the two formulas with the recommended values of total surface refractivity N at each station were shown and compared with measurements in Table 7. The values computed from Eq. (17) are almost 1 m lower than the average values from radiosonde balloon measurement. The corresponding uncertainties in range correction over a symmetrical path were estimated (Ref. 9) and are shown in Table 8. The new seasonally adjusted (monthly mean) calibration model can almost reduce the range correction uncertainty over a pass by one order of magnitude.

Recently, B. Winn (Ref. 10) has compared the old and new methods by applying them to calibrate the real tracking data, and the preliminary results already showed significant improvement of the new monthly mean model.

V. Conclusion

A study of two years' radiosonde balloon measurement shows that most of the significant seasonal fluctuations in refractivity profiles which occur in the first 7.6 km (25,000 ft) are due to the variation of the water content in that portion of the troposphere. At each of the six weather stations, the long term seasonal variation in refractivity profile repeats quite well through the two-year span.

An analytic expression which can more closely represent the actual dry refractivity profile than the exponential function has been derived. The wet refractivity profile is approximated by a simple quartic equation. The uncertainties in range correction using a monthly mean profile were found in only 40 of the uncertainties in range effect with a 2-yr mean profile.

A new tropospheric calibration model with seasonal adjustment was developed, based on the monthly parameters obtained from the two-year radiosonde balloon

measurement combined with surface prediction. The uncertainty of range correction with the new model over one symmetrical pass is estimated to be 0.30 to 0.35 m for a 10-deg minimum elevation angle and 0.40 to 0.50 m for a 6-deg minimum elevation angle. This is below the required accuracy of both MM'71 and *Viking* 1975 missions.

Acknowledgment

The author would like to thank Kathryn L. Thuleen for supplying the computed refractivity from radiosonde balloon measurement and Nancy Hamata for her assistance in programming for making the necessary plots.

References

1. Ondrasik, V. J., and Thuleen, K. L., "Variations in the Zenith Tropospheric Range Effect Computed From Radiosonde Balloon Data," in *The Deep Space Network*, Space Programs Summary 37-65, Vol. II, pp. 25–35. Jet Propulsion Laboratory, Pasadena, Calif., Sept. 30, 1965.

2. Miller, L. F., Ondrasik, V. J., and Chao, C. C., "A Cursory Examination of the Sensitivity of the Tropospheric Range and Doppler Effects to the Shape of the Refractivity Profile," in *The Deep Space Network Progress Report*, Technical Report 32-1526, Vol. I, pp. 22–30. Jet Propulsion Laboratory, Pasadena, Calif.

3. Williams, J. G., "Very Long Baseline Interferometry and Its Sensitivity to Geophysical and Astronomical Effects," in *The Deep Space Network*, Space Programs Summary 37-62, Vol. II, pp. 49–55. Jet Propulsion Laboratory, Pasadena, Calif., March 31, 1970.

4. Bean, B. R., and Dutton, E. J., "Radio Meteorology," National Bureau of Standards, Monograph 92, p. 11, 1966.

5. Hopfield, H. S., "Two-Quartic Tropospheric Refractivity Profile for Correcting Satellite Data," *J. Geophys., Res.*, Vol. 74, No. 18, pp. 4487–4499, 1969.

6. Berman, A. L., "A New Tropospheric Range Refraction Model," in *The Deep Space Network*, Space Programs Summary 37-65, Vol. II, pp. 140–153. Jet Propulsion Laboratory, Pasadena, Calif., Sept. 30, 1965.

7. Hopfield, H. S., "Tropospheric Range Error at the Zenith," Preprint for 14th Plenary Meeting, July 1971, The John Hopkins University, Baltimore, Md.

8. Chao, C. C., "Improved Estimation of the Parameters and Mapping Tables of Tropospheric Calibration for MM'71," IOM 391.3-352, May 1971 (JPL internal document).

9. Chao, C. C., "Past vs. Current Tropospheric Calibration in DPODP and the Proposed Modifications for Future Missions," IOM 391.3-475, Oct. 4, 1971 (JPL internal document).

10. Winn, F. B., "Media Calibration for Radio Metric (Doppler) Tracking Data," TM 391-215, July 22, 1971 (JPL internal document).

Table 1. Errors in refractivity *N*

Error Sources	Ratio of rms error in refractivity to refractivity[a]	
Equation (1)	0.5%	(1.6)[b]
Surface observations ($\pm$ 1 mb, $\pm$ 0.1°C, $\pm$ 1% *RH*)	0.2%	(0.65)
Radiosonde observations ($\pm$ 2 mb, $\pm$ 1°C, $\pm$ 5% *RH*)	1.3%	(4.2)

[a] $P = 1013$ mb, $T_c = 15$°C, $RH = 60$%
[b] Terms in parentheses are ΔN.

Table 2. Radiosonde balloon site parameters

Radiosonde station	Elevation, m	Distance from nearest DSS, km	Nearest DSS	DSS elevation, m
Edwards AFB	724	100	Goldstone DSCC	1032
Yucca Flats	1190	200	Goldstone DSCC	1032
Madrid	606	70	Madrid DSCC	789
Wagga	214	140	Tidbinbilla DSCC	656
Woomera	165	12	Woomera	151
Pretoria	1330	50	Johannesburg	1398

Table 3. Monthly mean and standard deviation of dry refractivity at various altitudes above Edwards Air Force Base

Month	Dry refractivity, mean (1σ)								
	Surface 0.72 km (2375 ft)	3.66 km (12,000 ft)	6.70 km (22,000 ft)	9.75 km (32,000 ft)	12.8 km (42,000 ft)	15.8 km (52,000 ft)	18.9 km (62,000 ft)	25.0 km (82,000 ft)	31.1 km (102,000 ft)
Jan	262.4	187.9	136.9	97.3	63.6	40.1	24.4	8.8	3.2
	(6.18)	(2.83)	(1.20)	(1.41)	(2.56)	(1.77)	(0.98)	(0.18)	(0.15)
Feb	260.4	188.4	136.8	96.9	62.3	39.5	24.2	8.8	3.2
	(3.86)	(1.85)	(0.81)	(1.96)	(1.78)	(1.03)	(0.38)	(0.08)	(0.05)
Mar	255.8	187.2	136.1	96.9	62.7	39.4	24.0	8.6	3.3
	(5.52)	(1.70)	(0.96)	(1.42)	(1.98)	(0.92)	(0.42)	(1.65)	(0.69)
Apr	254.6	186.5	135.8	96.3	63.4	39.6	24.3	8.9	3.1
	(4.57)	(1.63)	(1.26)	(1.65)	(1.86)	(0.83)	(0.42)	(0.07)	(0.79)
May	249.7	185.3	135.5	96.7	64.0	39.8	24.4	9.0	3.5
	(7.37)	(3.90)	(2.42)	(2.06)	(2.42)	(1.24)	(0.79)	(0.24)	(0.09)
June	246.1	183.9	135.2	96.2	65.3	42.1	25.0	9.3	3.6
	(2.87)	(1.90)	(1.27)	(2.15)	(1.71)	(1.39)	(0.82)	(0.30)	(0.16)
July	243.2	182.2	134.3	95.5	67.3	44.6	26.2	9.6	3.7
	(1.97)	(0.92)	(0.60)	(4.65)	(2.18)	(2.47)	(3.20)	(1.06)	(0.38)
Aug	241.1	182.3	134.5	93.4	64.8	40.6	22.0	7.7	2.8
	(3.78)	(0.84)	(0.56)	(0.78)	(1.21)	(0.95)	(0.64)	(1.37)	(0.66)
Sept	246.7	184.3	133.9	96.6	65.9	42.7	25.4	8.7	3.4
	(2.43)	(1.26)	(0.69)	(0.55)	(1.39)	(0.68)	(0.15)	(2.58)	(0.78)
Oct	252.5	184.6	135.1	97.2	65.3	41.1	24.7	8.7	3.2
	(5.50)	(1.68)	(1.16)	(0.57)	(1.17)	(0.75)	(0.31)	(1.85)	(0.90)
Nov	255.0	184.4	134.9	96.9	65.9	41.2	24.6	8.9	3.1
	(5.98)	(3.38)	(1.08)	(1.82)	(1.91)	(1.05)	(0.33)	(0.09)	(0.90)
Dec	261.0	187.9	136.4	96.5	63.7	39.6	24.1	8.8	3.3
	(4.56)	(1.84)	(0.98)	(1.39)	(1.97)	(0.70)	(0.32)	(0.06)	(0.04)

Table 4. Values of N_W at different relative humidity and temperature

RH	0°C	10°C	20°C	30°C
10%	3.5	5.7	10.4	20.8
30%	9.1	17.2	31.2	62.4
50%	15.2	28.7	52.0	104.0
70%	21.4	40.1	72.8	145.5

Table 5. Summary of uncertainties (1σ) from monthly mean of wet refractivity at various altitudes for the six stations

Season	Surface	1.83 km (6000 ft)	3.66 km (12,000 ft)	7.32 km (24,000 ft)
Summer months	10 to 17	7 to 10	5 to 8	0.5 to 1.5
Winter months	4.5 to 9	3.5 to 7.5	2.5 to 6	< 0.5

Table 6. Uncertainties in tropospheric range correction (one-way) based on the two-year radiosonde balloon data (in meters)

γ deg	$\sigma\Delta\rho_{dry}$		$\sigma\Delta\rho_{wet}$		$\sigma\Delta\rho_{total}$	
	2-Year	Monthly	2-Year	Monthly	2-Year	Monthly
1	1.502	0.711	6.00	2.055	6.20	2.175
3	0.609	0.326	2.581	0.810	2.680	0.875
5	0.321	0.157	1.543	0.521	1.585	0.545
15	0.101	0.048	0.433	0.148	0.453	0.154
45	0.038	0.017	0.152	0.051	0.160	0.055
90	0.026	0.012	0.105	0.036	0.109	0.038

Table 7. Comparison of zenith range correction at each DSS

Deep Space Station	Eq. 1, m	Eq. 2, m	Average from 2-year balloon measurement, m
Goldstone DSCC	1.338	1.808	2.123 ± 0.105
Madrid DSCC	1.673	2.260	2.214 ± 0.110
Woomera DSS	1.895	2.562	2.374 ± 0.118
Tidbinbilla DSCC	1.729	2.336	2.259 ± 0.111
Johannesburg DSS	1.338	1.808	2.066 ± 0.101

Table 8. Values of the uncertainty over one symmetrical pass in tropospheric range correction

Tracking station	From Eq. (17)		From Eq. (18)		New model (monthly mean)	
	Lowest elevation					
	10 deg	6 deg	10 deg	6 deg	10 deg	6 deg
Goldstone DSCC	4.76	6.25	2.08	2.65	0.32	0.45
Madrid DSCC	3.57	4.59	0.85	1.05	0.34	0.47
Woomera DSS	2.87	3.77	1.40	1.74	0.31	0.43
Tidbinbilla DSCC	3.18	4.24	0.89	1.12	0.32	0.45
Johannesburg DSS	4.21	5.55	1.68	2.11	0.31	0.43

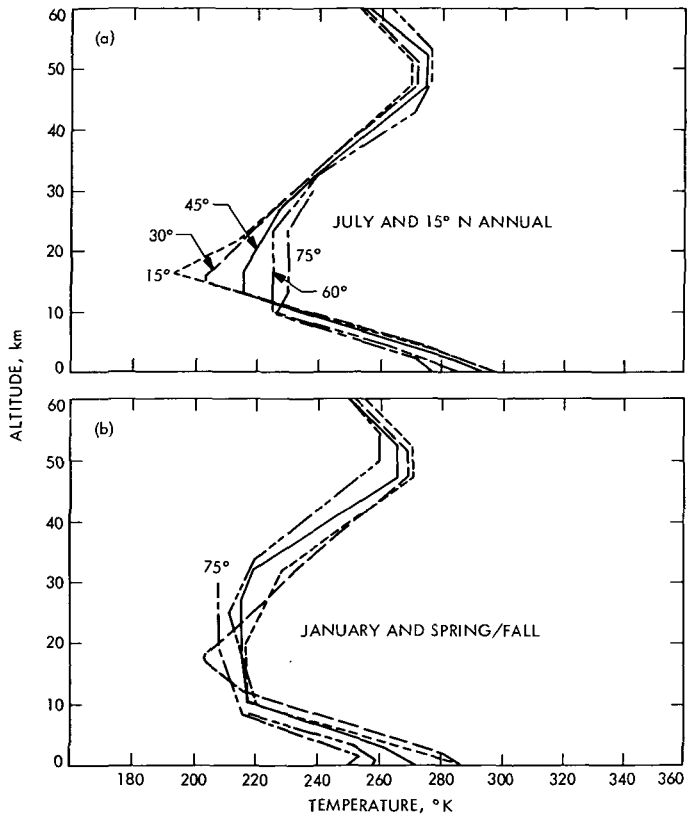

Fig. 1. Temperature-altitude profiles of the 30, 45, 60 and 75 deg N (a) July and 15 deg N mean annual Supplementary Atmospheres, (b) January and midlatitude spring/fall Supplementary Atmospheres (from the U.S. *Standard Atmosphere Supplements, 1966*)

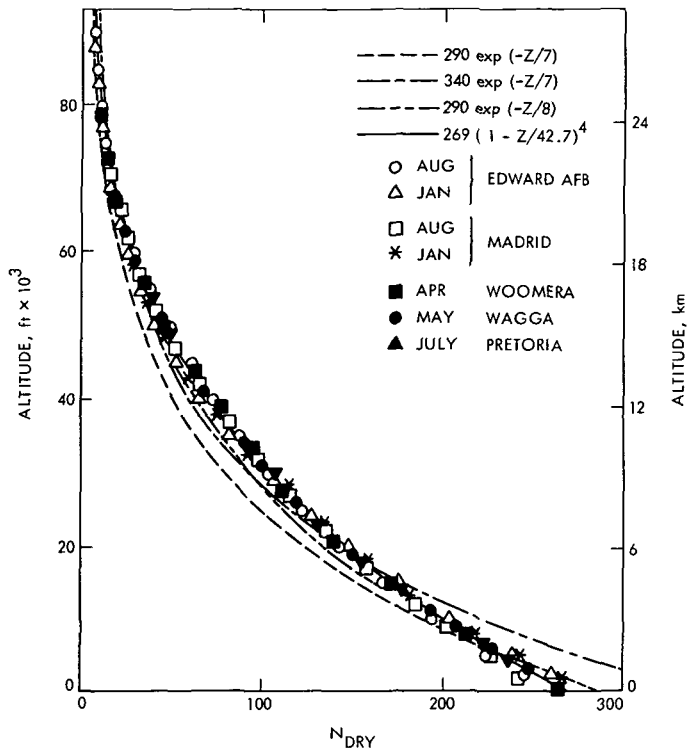

Fig. 2. Dry refractivity profiles

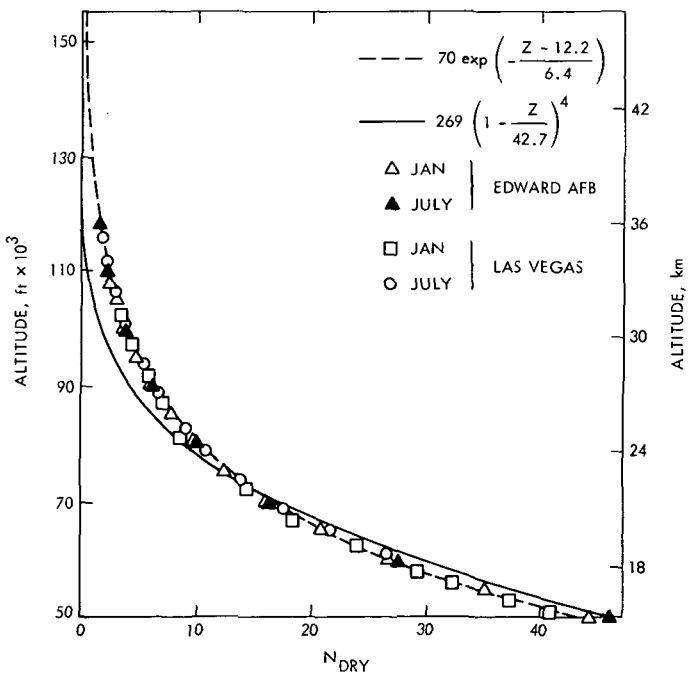

Fig. 3. Dry refractivity profiles for altitudes higher than 15.3 km (50,000 ft)

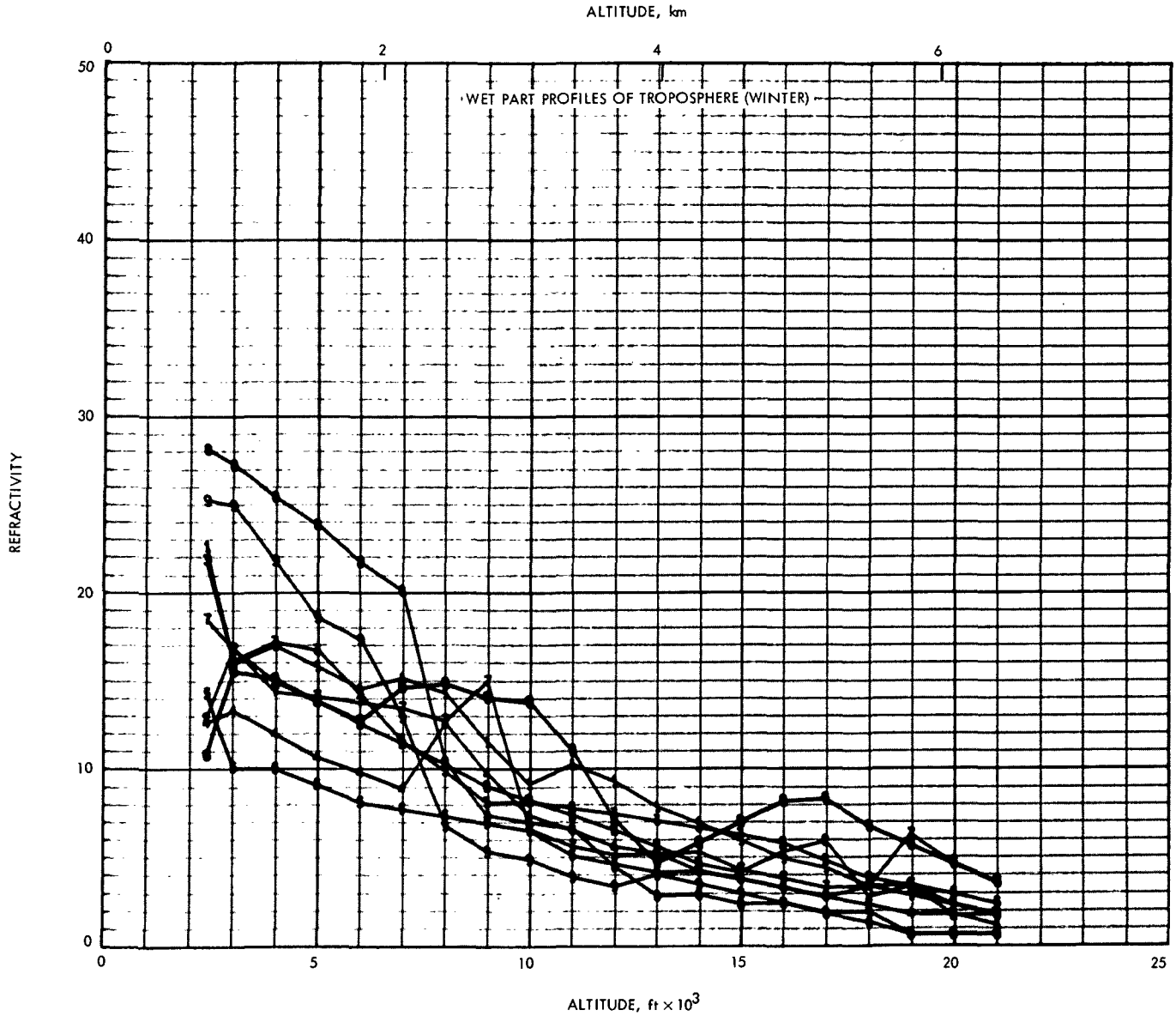

Fig. 4. Wet refractivity profiles for Edwards A.F.B. in January, 1967

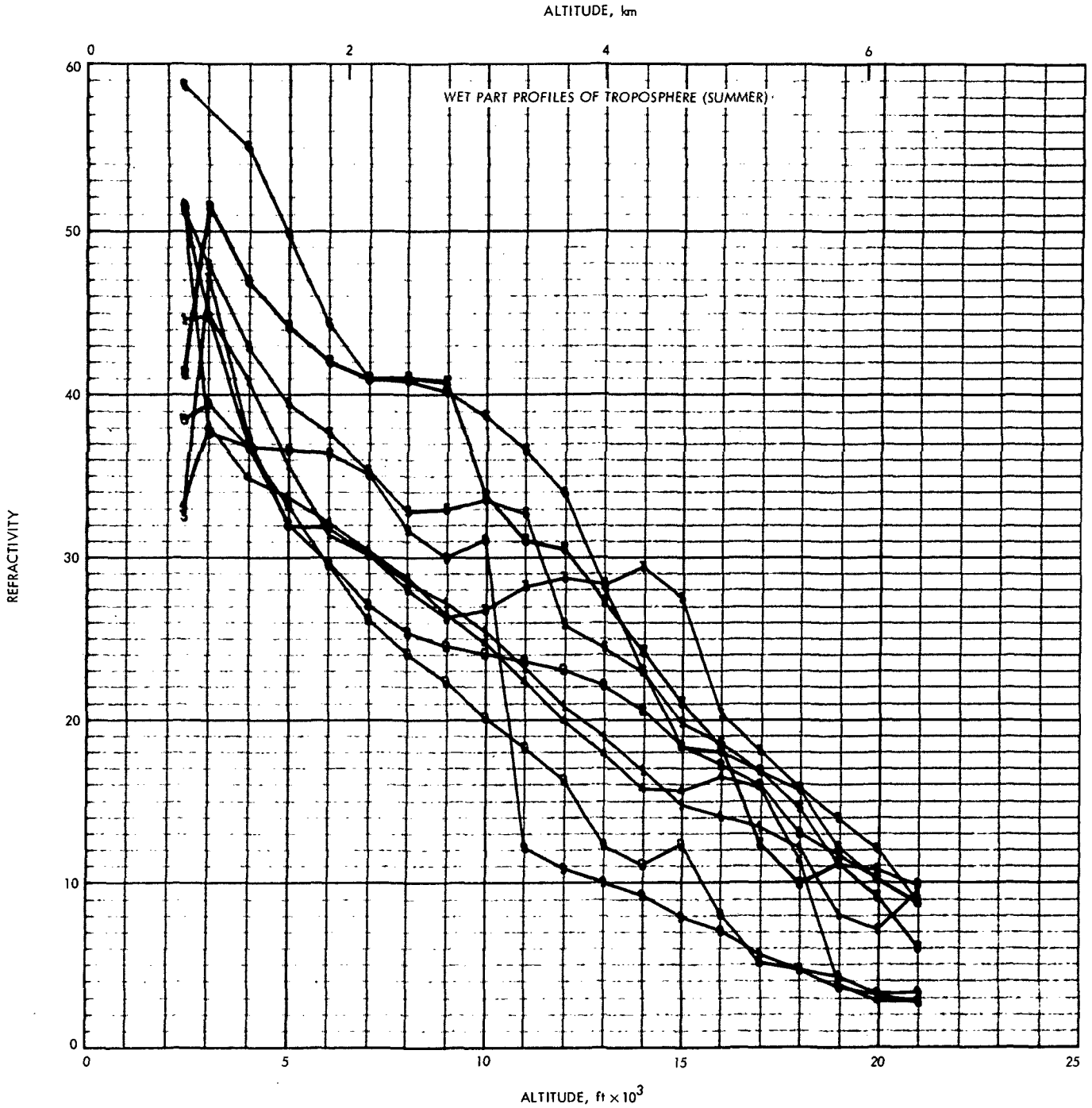

Fig. 5. Wet refractivity profiles for Edwards A.F.B. in July, 1967

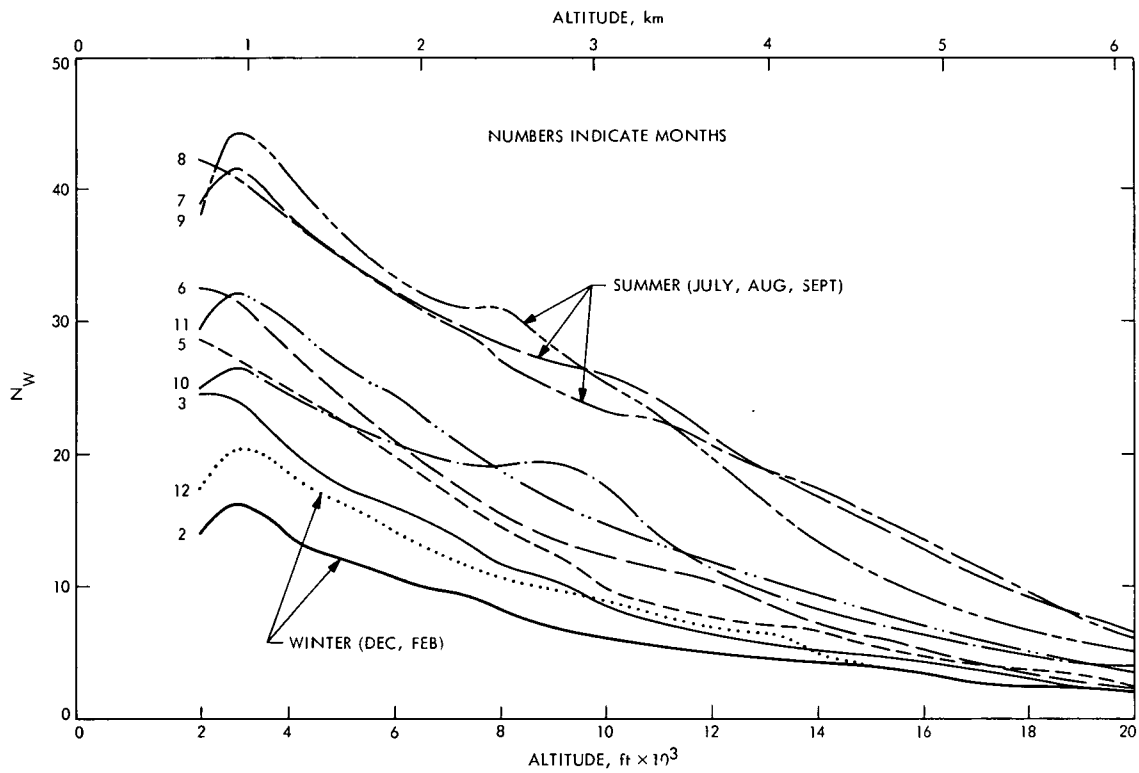

Fig. 6. Monthly mean profiles of wet refractivity, Edwards A.F.B.

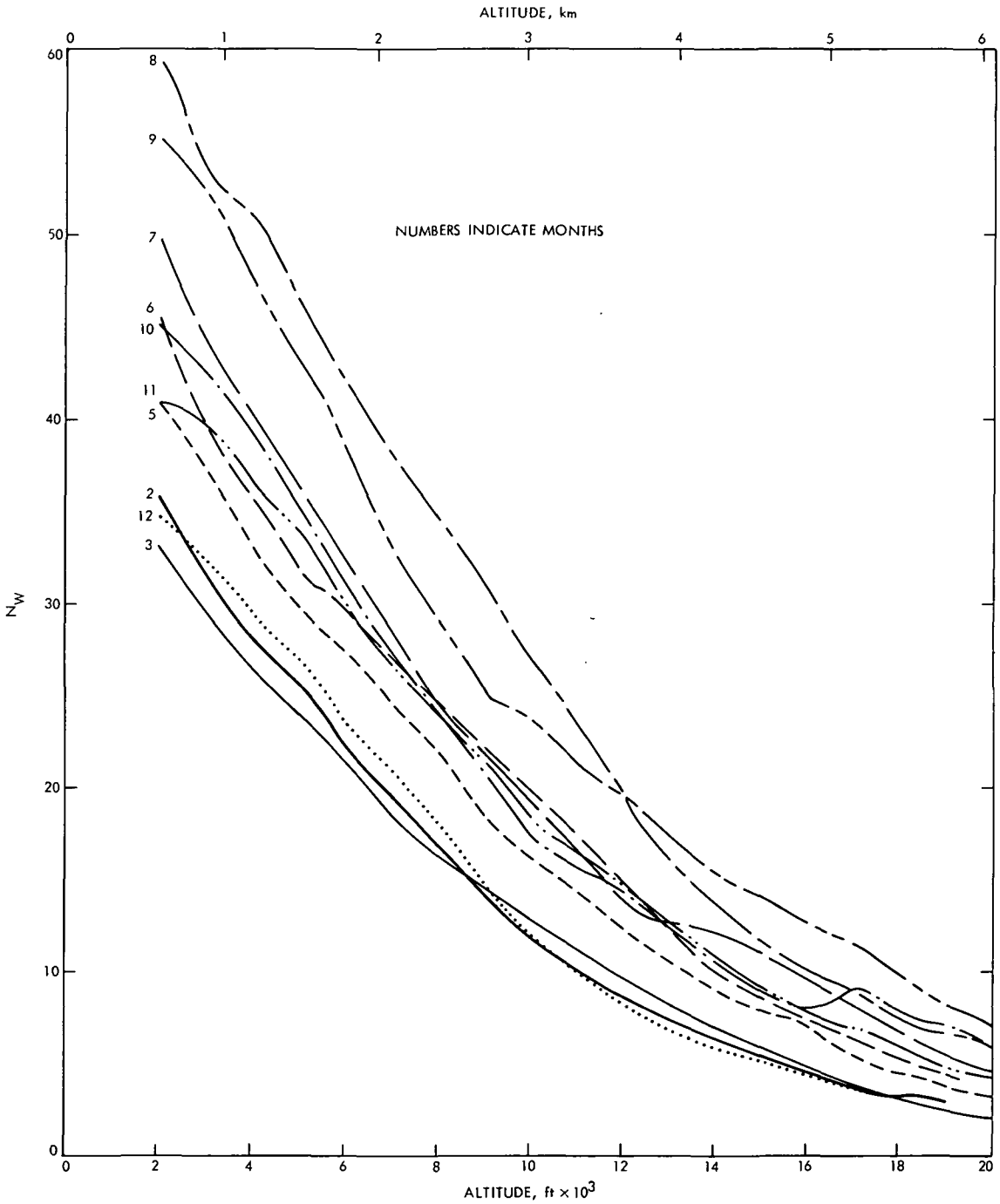

Fig. 7. Monthly mean profiles of wet refractivity, Madrid

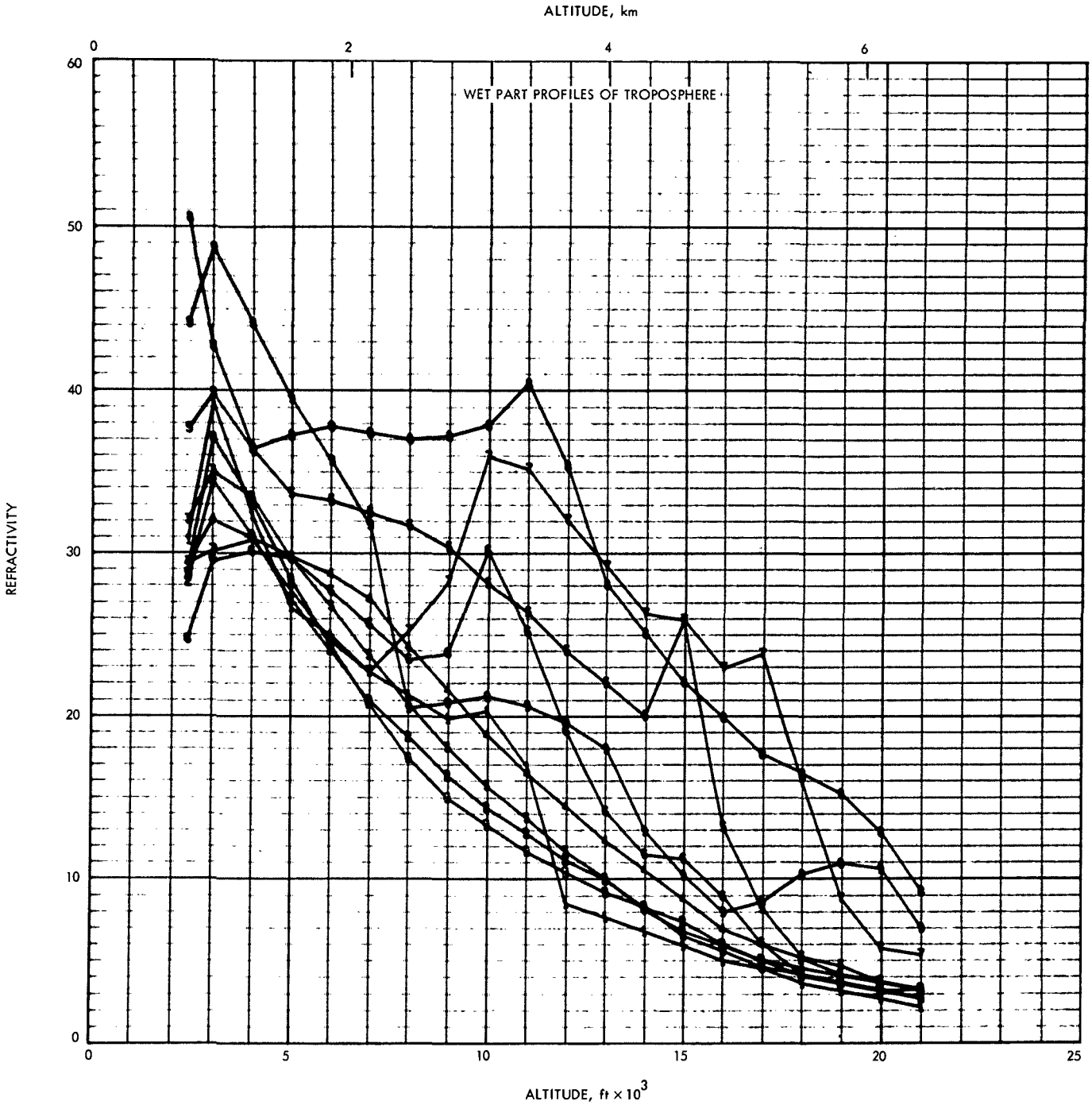

Fig. 8. Wet refractivity profiles for Edwards A.F.B. in January, 1968

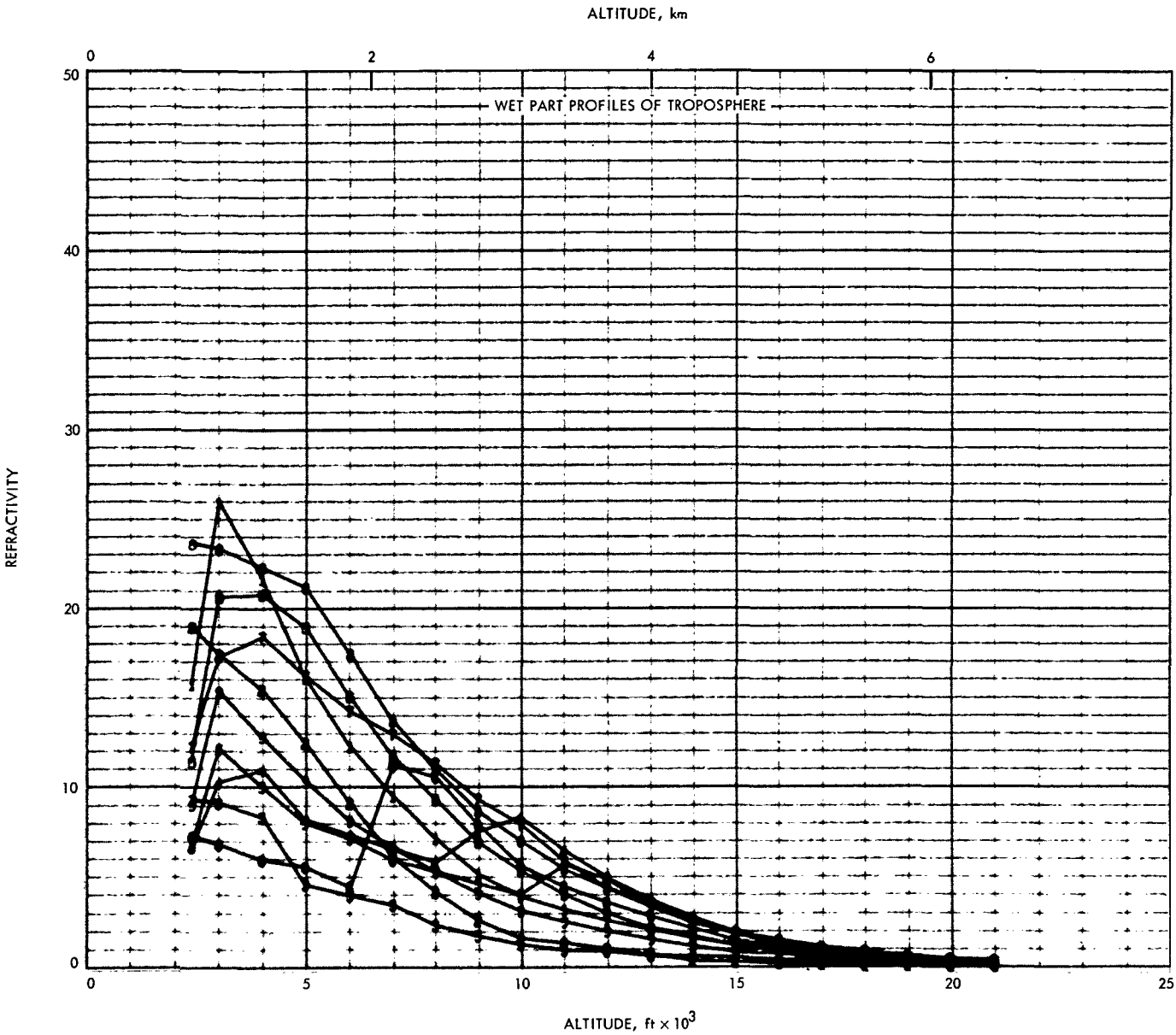

Fig. 9. *Wet refractivity profiles for Edwards A.F.B. in July, 1968*

The Repetition of Seasonal Variations in the Tropospheric Zenith Range Effect

K. L. Thuleen and V. J. Ondrasik
Tracking and Orbit Determination Section

Using radiosonde balloon data taken from sites close to the DSN tracking stations, the tropospheric zenith range effect $\Delta\rho_z$ has been computed throughout 1967 and 1968. The behavior of $\Delta\rho_z$ has definite seasonal trends which are similar in both years. With the modification of the tropospheric model, which is used to calibrate radio tracking data to include these seasonal trends, the navigational errors, produced by inaccuracies in representing the zenith range effect, may possibly be reduced by as much as 40%.

I. Introduction

One of the error sources which corrupts range and doppler data, and thereby degrades navigational capabilities, is the troposphere. To determine the amount of this tropospheric-induced degradation, and also to improve the tropospheric model used for calibrations, it is very valuable to examine the temporal behavior of the tropospheric zenith range effect $\Delta\rho_z$. A study of the 1967 behavior of $\Delta\rho_z$ was reported in Ref. 1 and led to the following tentative conclusions:

(1) $\Delta\rho_z$ is composed of a dry portion $\Delta\rho_z(d)$ and a wet portion $\Delta\rho_z(w)$.

(2) The dry portion is approximately 90% of $\Delta\rho_z$ and is very highly correlated with the surface pressure.

(3) Most of the variations in $\Delta\rho_z$ are due to the wet portion which often has little correlation with surface quantities.

(4) Assuming that the wet portion stays constant at its yearly average can lead to equivalent station location errors of 0.4 m (for a minimum elevation angle of 10 deg).

(5) The wet portion of the tropospheric zenith range effect appears to have definite seasonal trends.

It was also mentioned in Ref. 1 that if the apparent seasonal trends in $\Delta\rho_z(w)$ are repeatable from year to year, it should be possible to improve the troposphere model which is used to calibrate the tracking data, and thereby reduce the tropospheric-induced navigational errors. The primary purpose of this article is to show that the seasonal behavior of $\Delta\rho_z(w)$ was very similar in the years 1967 and 1968. If it can be established that this similarity continues for a few years, it may be valuable to include historical data in the tropospheric calibration model.[2]

Since $\Delta\rho_z(d)$ can be computed from surface pressure measurement, emphasis will be placed upon results involv-

[2]Such modifications have recently been made to the operational software supporting the *Mariner* Mars 1971 mission.

ing $\Delta\rho_z(w)$, although results will occasionally be given for $\Delta\rho_z(d)$.

The navigational errors produced by the variation of the zenith range effect should not be taken to represent the total effect of the troposphere. Unfortunately, there are other possible tropospheric error sources which may contribute significantly to the errors produced by the troposphere. Three such error sources arise from (1) translating $\Delta\rho_z$, computed from radiosonde balloon data, to the tracking station, (2) mapping zenith values to arbitrary elevation angles, and (3) effects produced by the inhomogeneous structure of the troposphere. These other tropospheric error sources are currently under investigation. In particular, the Chao article[1] in this volume reports on the range errors produced by mapping the zenith range effect down to arbitrary elevation angles with an incorrect refractivity profile.

II. Zenith Range Effect

As shown in Ref. 1, $\Delta\rho_z$, $\Delta\rho_z(d)$, and $\Delta\rho_z(w)$ may be computed from the following integral:

$$\Delta\rho_z = \Delta\rho_z(d) + \Delta\rho_z(w) = \int_0^\infty [N_d(h) + N_w(h)]\, dh$$

where

$N = (n - 1) \times 10^6$

n = index of refraction

h = altitude above surface

The dry and wet refractivities, N_d and N_w, may be calculated as a function of altitude by using data gathered by radiosonde balloons.

With the help of Mr. Richard Davis and Mr. Larry Snelson of the National Climatic Center in Asheville, North Carolina, radiosonde balloon data from the sites listed in Table 1 was obtained for the years 1967 and 1968.

By the methods described in Ref. 1, this data was converted into refractivity profiles and integrated to yield $\Delta\rho_z$, $\Delta\rho_z(d)$, and $\Delta\rho_z(w)$. Unfortunately, much of the data only went up to approximately 6.10 km (20,000 ft)[2] and it was necessary to terminate the integration at the terminal integration height of 4.57 and 6.10 km (15,000 and 20,000 ft) for the overseas and Yucca Flats stations, respectively. This is not a serious limitation because most of variability occurs within this region. Figure 1 shows the behavior of the wet portion of the tropospheric zenith range error during 1967 and 1968 above the radiosonde balloon sites listed in Table 1. From these figures it is clear that behavior of $\Delta\rho_z(w)$ during 1967 and 1968 was very similar. A clearer comparison between the two years may be obtained by averaging the total, dry, and wet tropospheric zenith range effects for each month. These monthly averages $\Delta\bar{\rho}_z$, $\Delta\bar{\rho}_z(d)$, and $\Delta\bar{\rho}_z(w)$ are shown in Figs. 2–6, along with the associated standard deviations and maximum and minimum values. In order that these averages be representative of the zenith range effect due to the entire troposphere, and not just the first 4.57 or 6.10 km (15,000 or 20,000 ft), dry and wet refractivity models have been employed to supplement the radiosonde balloon data. The dry model computes the contribution to $\Delta\rho_z(d)$ above the terminal integration height by the equation given on page 32 of Ref. 1 and gives a very accurate (1%) value. The wet model assumes a refractivity profile above the terminal integration height, which starts with the monthly average refractivity at this height and decreases linearly to zero at 9.14 km (30,000 ft). Refractivity profiles which have been averaged over a month have been computed by C. C. Chao (see Footnote 1). An example of such an average profile, and the wet model which has been used to supplement the integrated monthly average of $\Delta\rho_z(w)$, is shown in Fig. 7. The supplementary portions of the averaged $\Delta\rho_z(w)$ are shown in Figs. 2–6.

To facilitate the comparison of the 1967 and 1968 averaged zenith range effects, these averages have been overlayed in Fig. 8. From this set of figures, it is easily seen that the behavior of the tropospheric zenith range effects are very similar during 1967 and 1968.

III. Apparent Changes in Station Locations Produced by the Troposphere

A useful artifice for investigating navigational errors, such as the ones produced by the troposphere, is to describe them in terms of equivalent errors in tracking station locations. As described in Ref. 2, an effect which corrupts tracking data can be decomposed into parameters, one of which is the apparent change in the station's distance off the Earth spin axis, Δr_s, and another is the apparent change in the station's longitude, $\Delta\lambda$. These errors in equivalent station locations can be translated very easily into declination and right ascension by the method given in the above reference.

[1]Chao, C. C., "New Tropospheric Range Corrections With Seasonal Adjustment" (this volume).

[2]Values in customary units are included in parentheses after values in SI (International System) units if the customary units were used in the measurement or calculations.

Once the tropospheric-induced range error, $\Delta\rho$, has been specified as a function of elevation angle, the equivalent station location errors can be computed by the method described in Ref. 1. To obtain some feeling of the superiority of a tropospheric model which includes the seasonal variations in $\Delta\rho_z(w)$, equivalent station location errors will be computed for each month, from the following tropospheric range errors:

$$\Delta\rho = \frac{\delta\rho_z(w,i)}{\sin\gamma}, \qquad i = 1,2$$

where

γ = elevation angle

$\delta\bar{\rho}_z(w,1) = \Delta\bar{\rho}_z(w,1968) -$ yearly average of $\Delta\rho_z(w,1967)$

$\delta\bar{\rho}_z(w,2) = \Delta\bar{\rho}_z(w,1968) - \Delta\bar{\rho}_z(w,1967)$

The first model which uses $\delta\bar{\rho}_z(w,1)$ will give monthly errors that result from calibrating the 1968 data with a model which assumes $\Delta\rho_z(w)$ is constant and has a value equal to the 1967 yearly average of $\Delta\rho_z(w)$. The second model which uses $\delta\bar{\rho}_z(w,2)$ will give monthly errors that result from calibrating the 1968 data with a model which assumes $\delta\rho_z(w)$ is constant for a month, but changes to the 1967 value of $\Delta\bar{\rho}_z(w)$ from month to month. Figure 9 gives the monthly averages of apparent change in r_s, $\Delta\bar{r}_s$, for each of these models using $\delta\bar{\rho}_z(w)$ values taken from the radiosonde balloon sites closest to Goldstone and Madrid, as given in Figs. 8a and 8b. The values of $\Delta\bar{r}_s$ are computed for each station viewing a zero declination satellite during a symmetric tracking pass with minimum elevation angles of 10 deg. Since both $\Delta\rho$ and the tracking pass are assumed to be symmetric, $\Delta\lambda = 0$. Table 2 contains the yearly average of $|\Delta r_s|$ for the two models and two stations. From Fig. 9 and Table 2, it is easily seen that the inclusion of the seasonal variations of $\Delta\rho_z(w)$ in the model describing the tropospheric zenith range effect typically reduces the troposphere-induced equivalent station location errors by 25 or 40%.

IV. Summary and Conclusions

Using 1967 and 1968 radiosonde balloon data taken from sites close to the DSN tracking stations, values of the total, dry, and wet tropospheric zenith range effects were calculated. The behavior of $\Delta\rho_z(w)$ has definite seasonal trends which were very similar for each year. The effects on radio tracking data of modeling the 1968 $\Delta\rho_z(w)$ by assuming it to be constant, with a value equal to the 1967 yearly average, can grossly be represented by an equivalent station location error of $\Delta r_s = 0.3$ m for a minimum elevation angle of 10 deg. If the model of $\Delta\rho_z(w)$ includes historical data regarding the seasonal trends of $\Delta\rho_z(w)$, the equivalent station location errors may be reduced by 25–40%.

Clearly any conclusions which may be reached from an examination of the 1967 and 1968 data suffer from the fact that only two years of data have been investigated. Before a great deal of confidence may be given to these conclusions, several more years of data should be examined.

References

1. Ondrasik, V. J., and Thuleen, K. L., "Variations in the Zenith Tropospheric Range Effect Computed From Radiosonde Balloon Data," in *The Deep Space Network,* Space Programs Summary 37-65, Vol. II, pp. 25–35. Jet Propulsion Laboratory, Pasadena, Calif., Sept. 30, 1970.
2. Mulhall, B. D., "Evaluation of the Charged Particle Calibration to Doppler Data by the Hamilton–Melbourne Filter," in *The Deep Space Network,* Space Programs Summary 37-57, Vol. II, pp. 24–29. Jet Propulsion Laboratory, Pasadena, Calif., May 31, 1969.

Table 1. Radiosonde balloon site parameters

Radiosonde station	Latitude	Longitude	Elevation, m	Nearest DSS	DSS elevation, m	Distance from DSS, km
Yucca Flats	36°57′ N	116°5′ W	724	Goldstone[a]	1190	200
Madrid	40°28′ N	3°34′ W	606	Madrid[b]	789	70
Wagga	35°10′ S	147°28′ E	214	Canberra	656	140
Woomera	31°9′ S	136°48′ E	165	Woomera	151	12
Pretoria	25°44′ S	28°11′ E	1330	Johannesburg	1398	50

[a]DSS 14.
[b]DSS 61.

Table 2. Equivalent station location errors for a constant and variable model of $\Delta\rho_z(w)$

Model	Constant for	Assumed $\Delta\rho_z$	$\Delta\bar{r}_s$ (Goldstone)	$\Delta\bar{r}_s$ (Madrid)
1	1 yr	1967 yearly avg of $\Delta\rho_z$	0.19 m	0.26 m
2	1 mo	1967 monthly avg of $\Delta\rho_z$	0.14 m	0.15 m

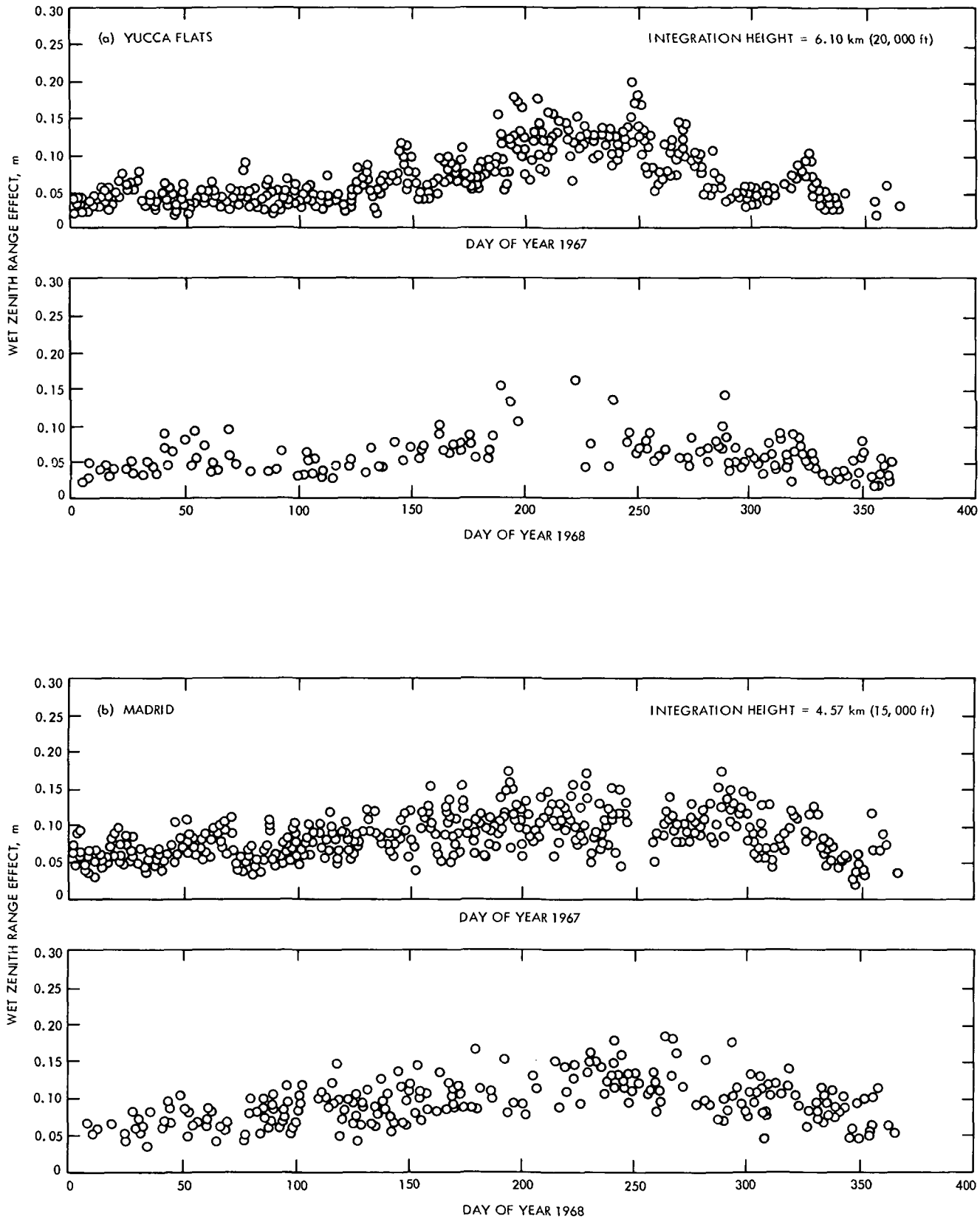

Fig. 1. Wet zenith range effects over various sites during 1967 and 1968

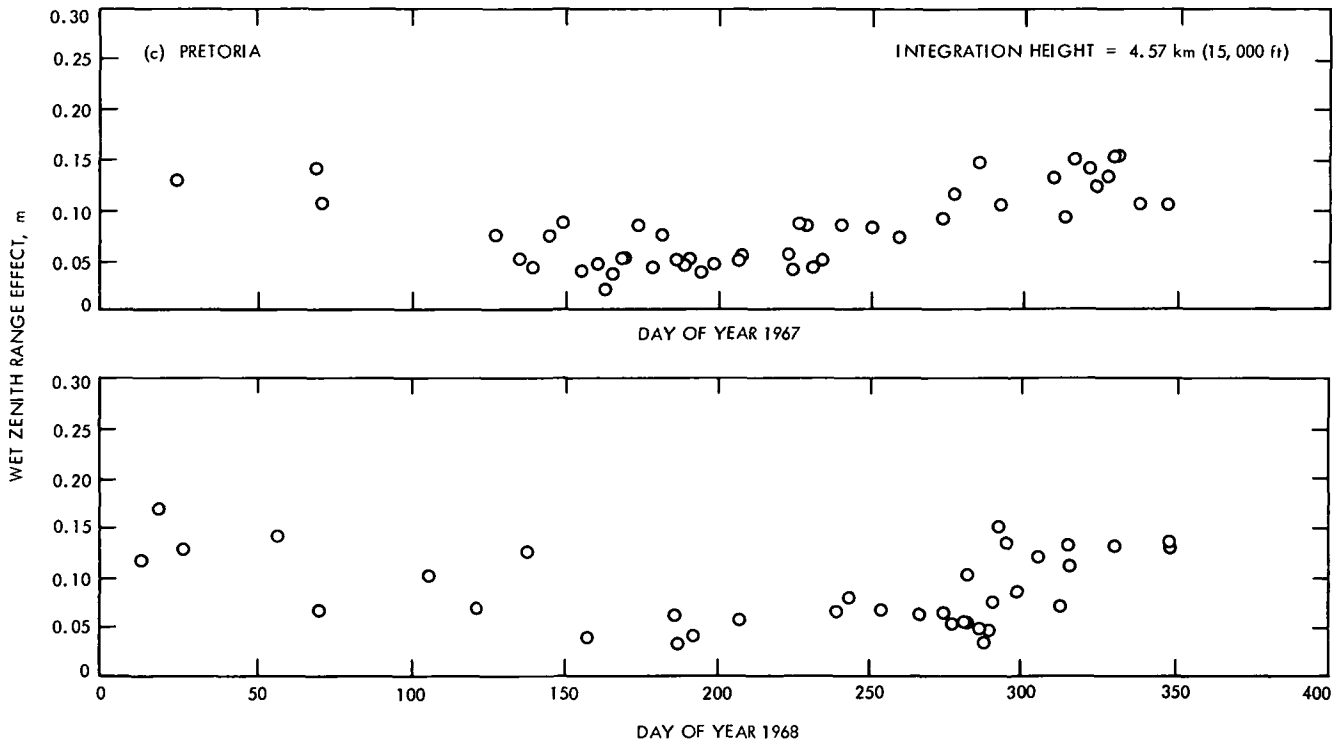
(c) PRETORIA
INTEGRATION HEIGHT = 4.57 km (15, 000 ft)
WET ZENITH RANGE EFFECT, m
0.30
0.25
0.20
0.15
0.10
0.05
0
DAY OF YEAR 1967
DAY OF YEAR 1968
0
50
100
150
200
250
300
350
400

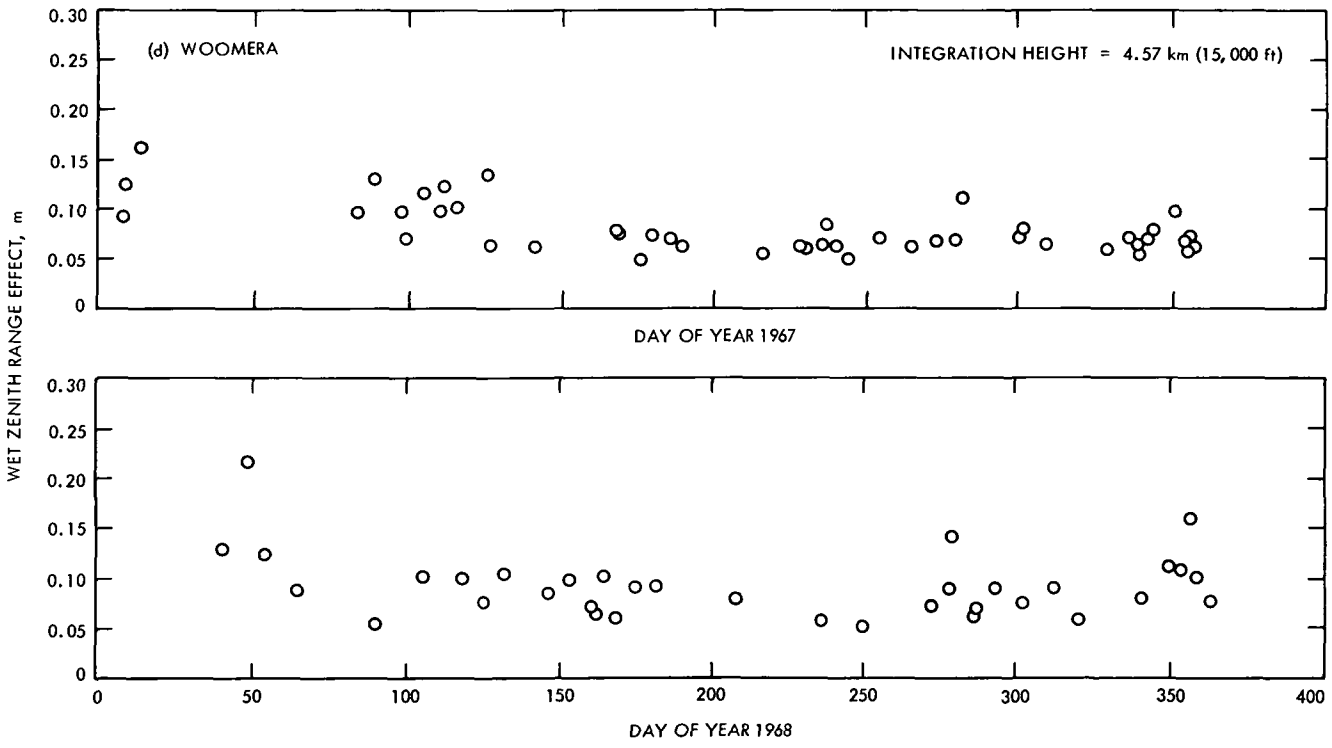
(d) WOOMERA
INTEGRATION HEIGHT = 4.57 km (15, 000 ft)
WET ZENITH RANGE EFFECT, m
0.30
0.25
0.20
0.15
0.10
0.05
0
DAY OF YEAR 1967
DAY OF YEAR 1968
0
50
100
150
200
250
300
350
400

Fig. 1 (contd)

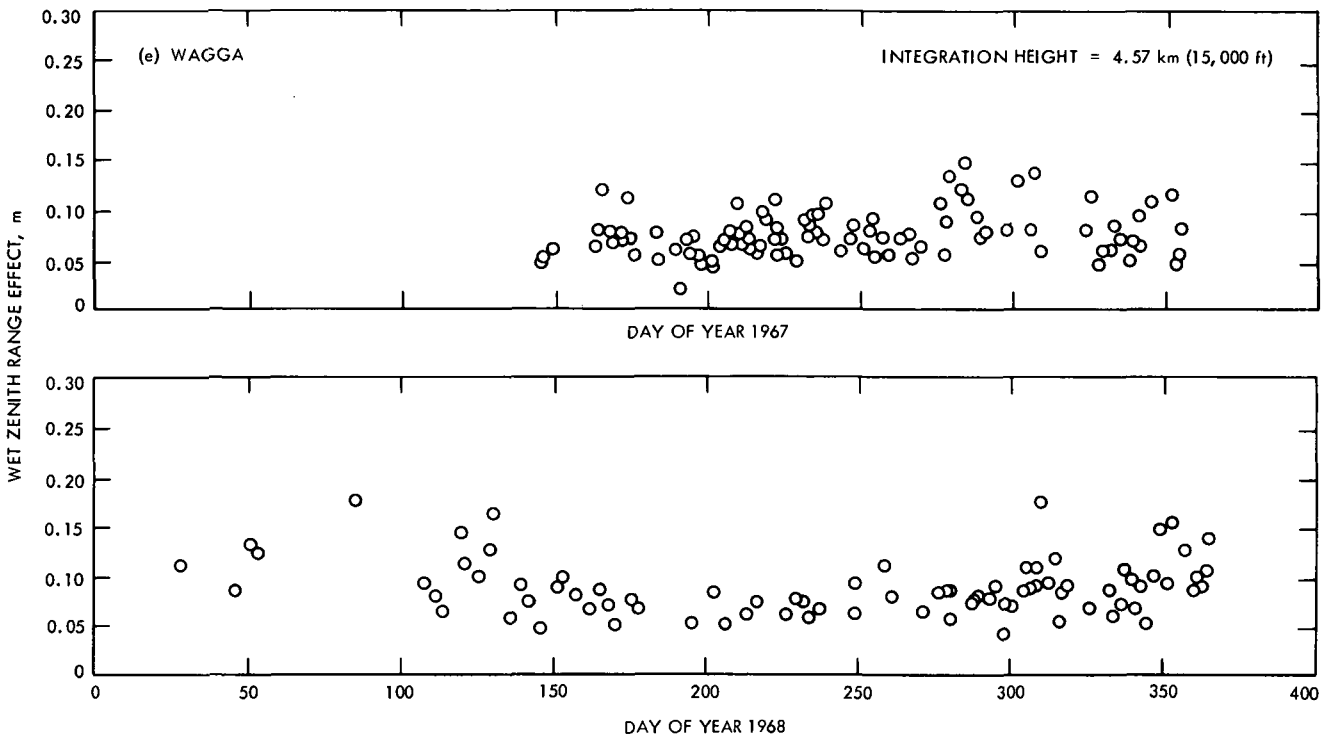
(e) WAGGA
INTEGRATION HEIGHT = 4.57 km (15,000 ft)
WET ZENITH RANGE EFFECT, m
0.30
0.25
0.20
0.15
0.10
0.05
0
DAY OF YEAR 1967
DAY OF YEAR 1968
0
50
100
150
200
250
300
350
400

Fig. 1 (contd)

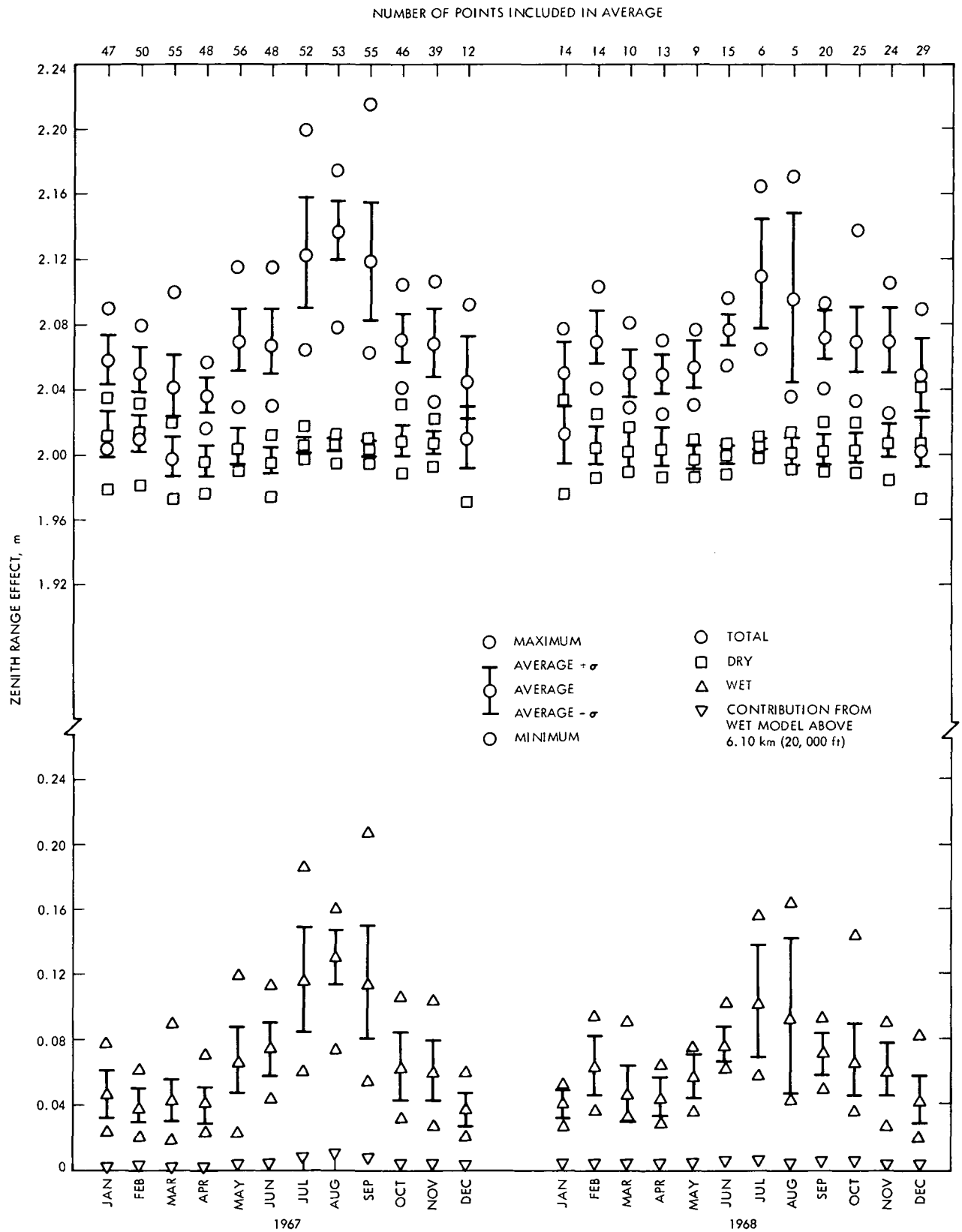

Fig. 2. Monthly averages and standard deviations of total, dry, and wet zenith range effects over Yucca Flats during 1967 and 1968

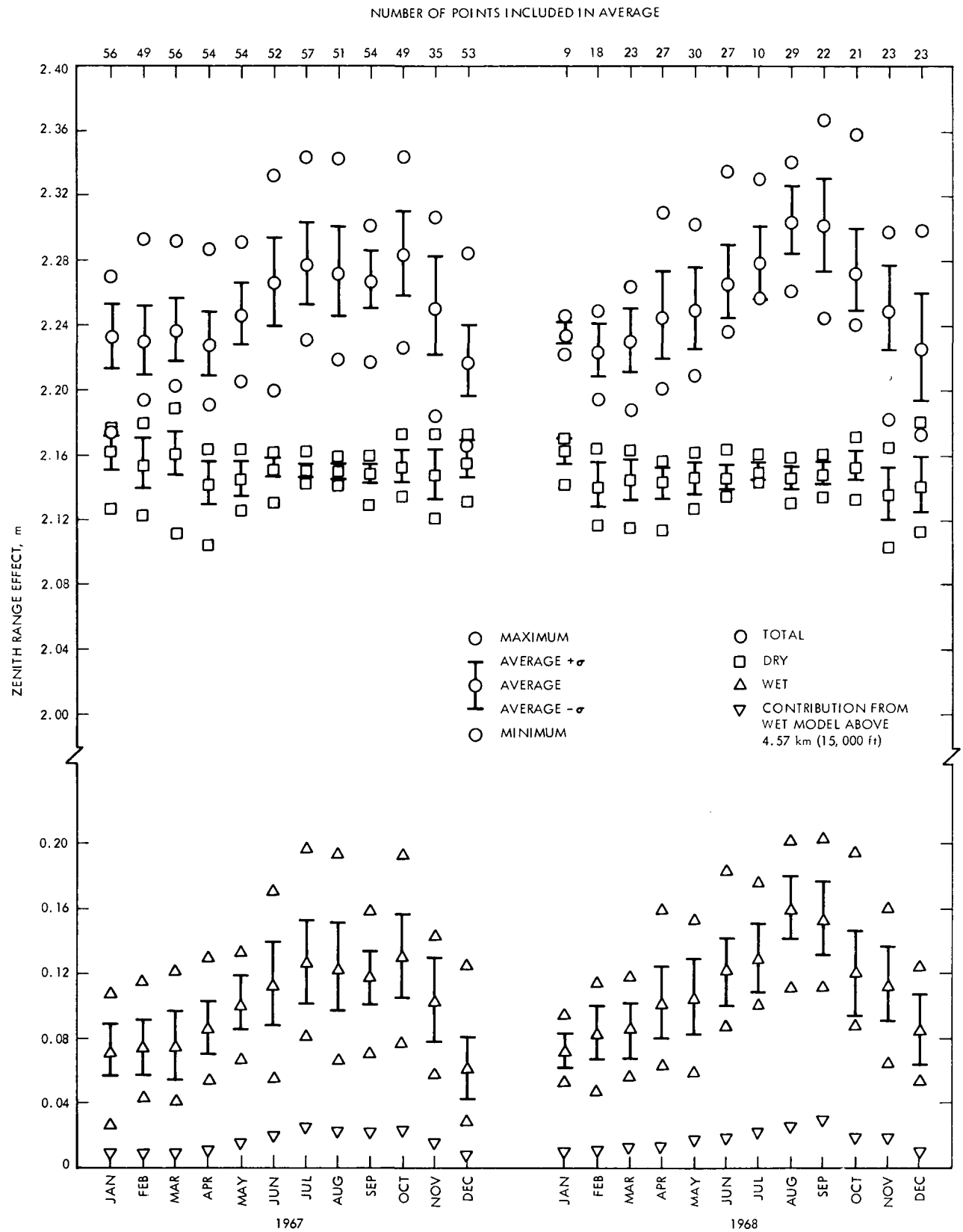

Fig. 3. Monthly averages and standard deviations of total, dry, and wet zenith range effects over Madrid during 1967 and 1968

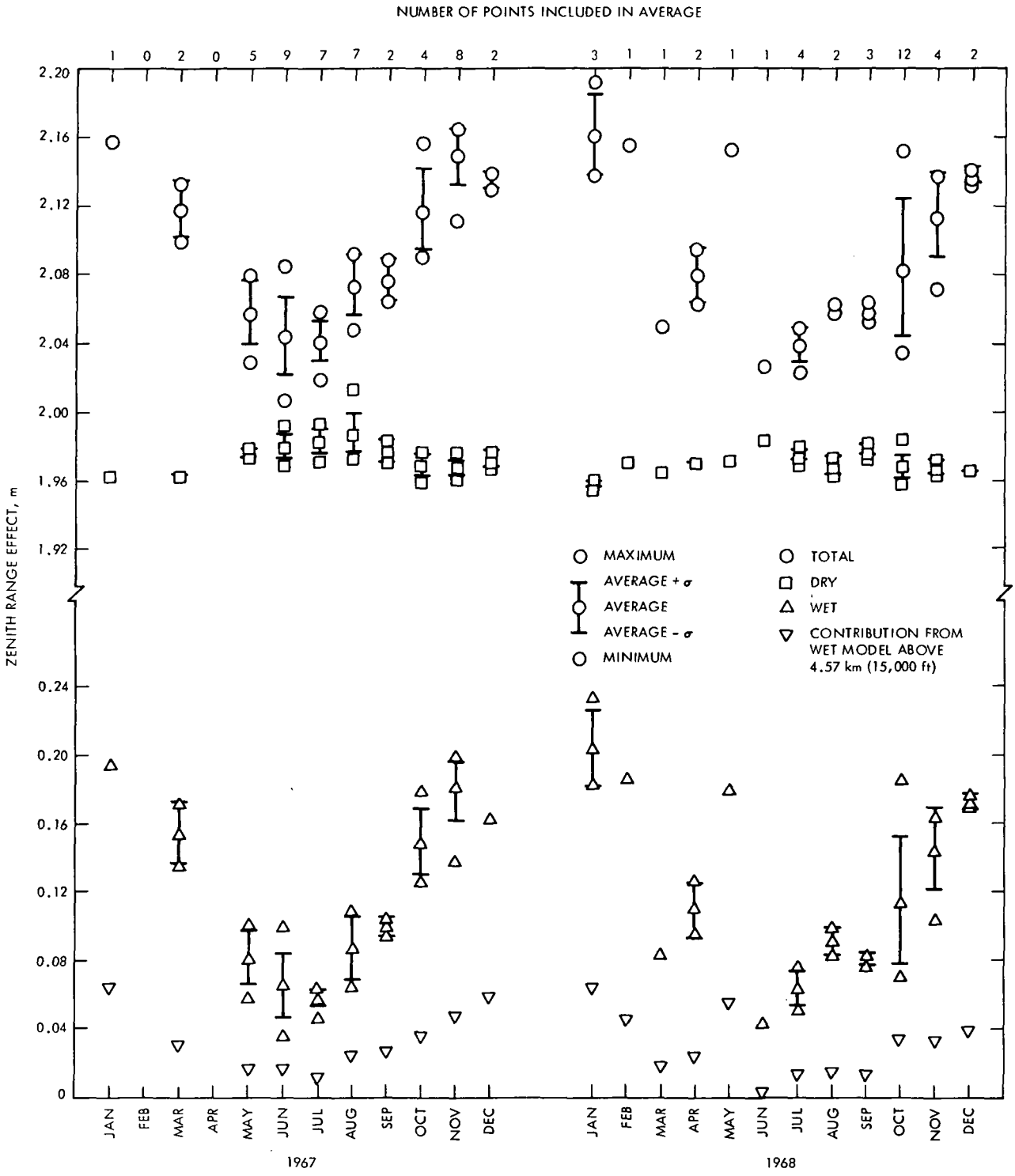

Fig. 4. Monthly averages and standard deviations of total, dry, and wet zenith range effects over Pretoria during 1967 and 1968

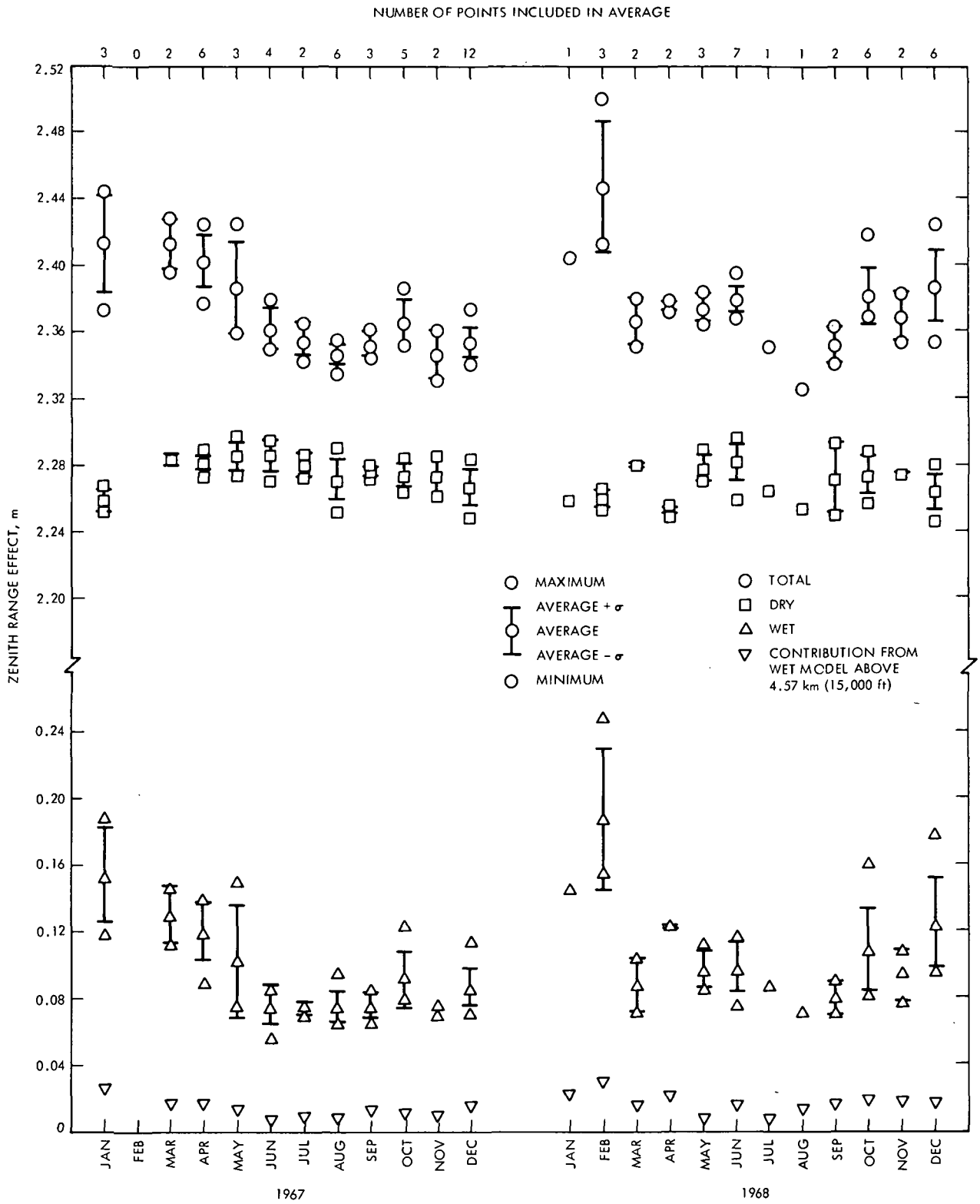

Fig. 5. Monthly averages and standard deviations of total, dry, and wet zenith range effects over Woomera during 1967 and 1968

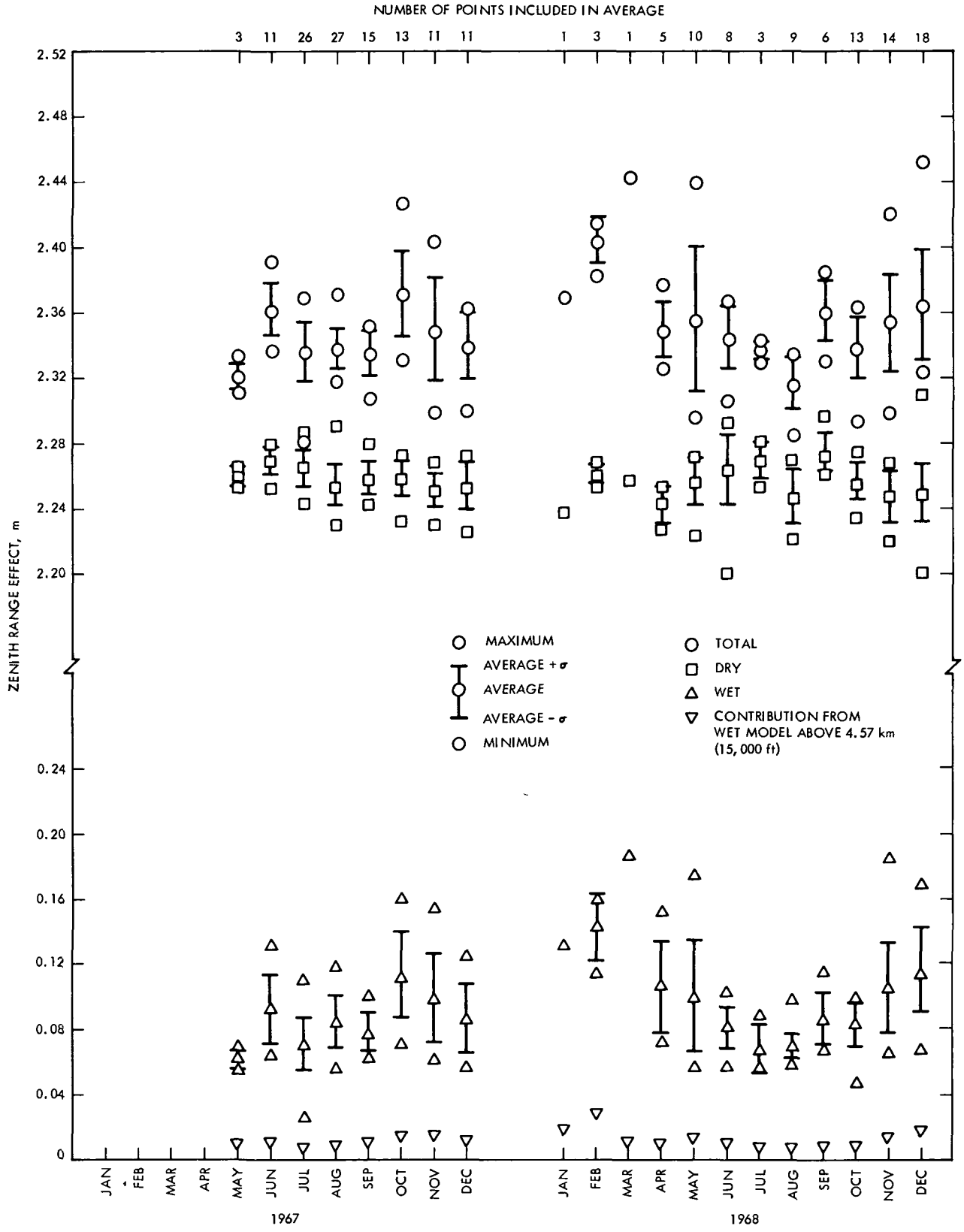

Fig. 6. Monthly averages and standard deviations of total, dry, and wet zenith range effects over Wagga during 1967 and 1968

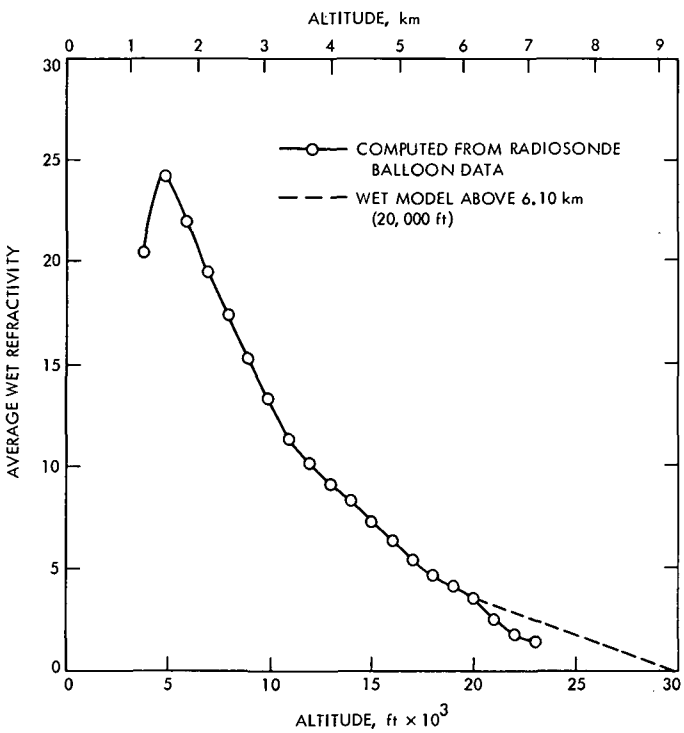

Fig. 7. Actual and modeled averaged wet refractivity above Yucca Flats during October 1968

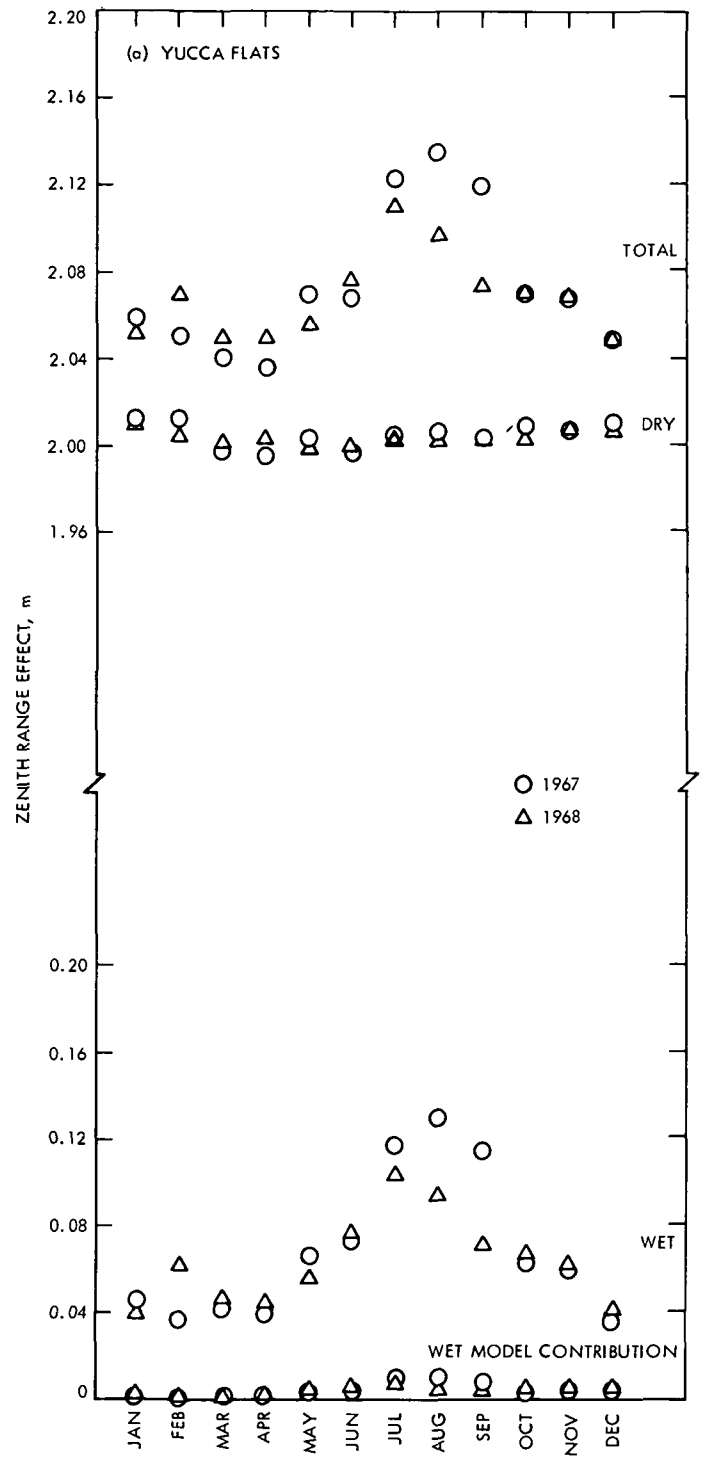

Fig. 8. Comparison of zenith range effect monthly averages over various sites

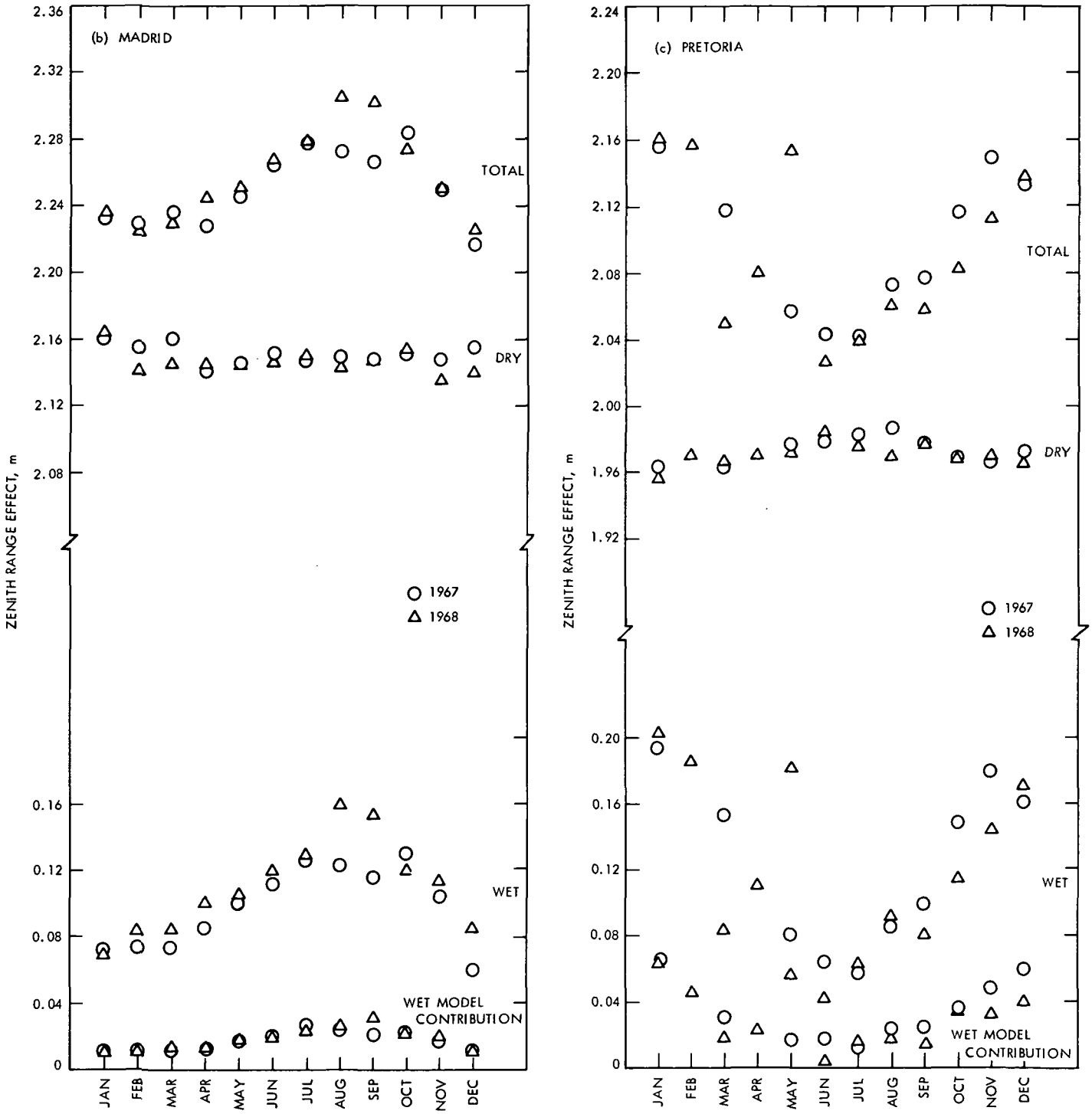
(b) MADRID
(c) PRETORIA
ZENITH RANGE EFFECT, m
TOTAL
DRY
WET
WET MODEL CONTRIBUTION
1967
1968
JAN
FEB
MAR
APR
MAY
JUN
JUL
AUG
SEP
OCT
NOV
DEC

Fig. 8 (contd)

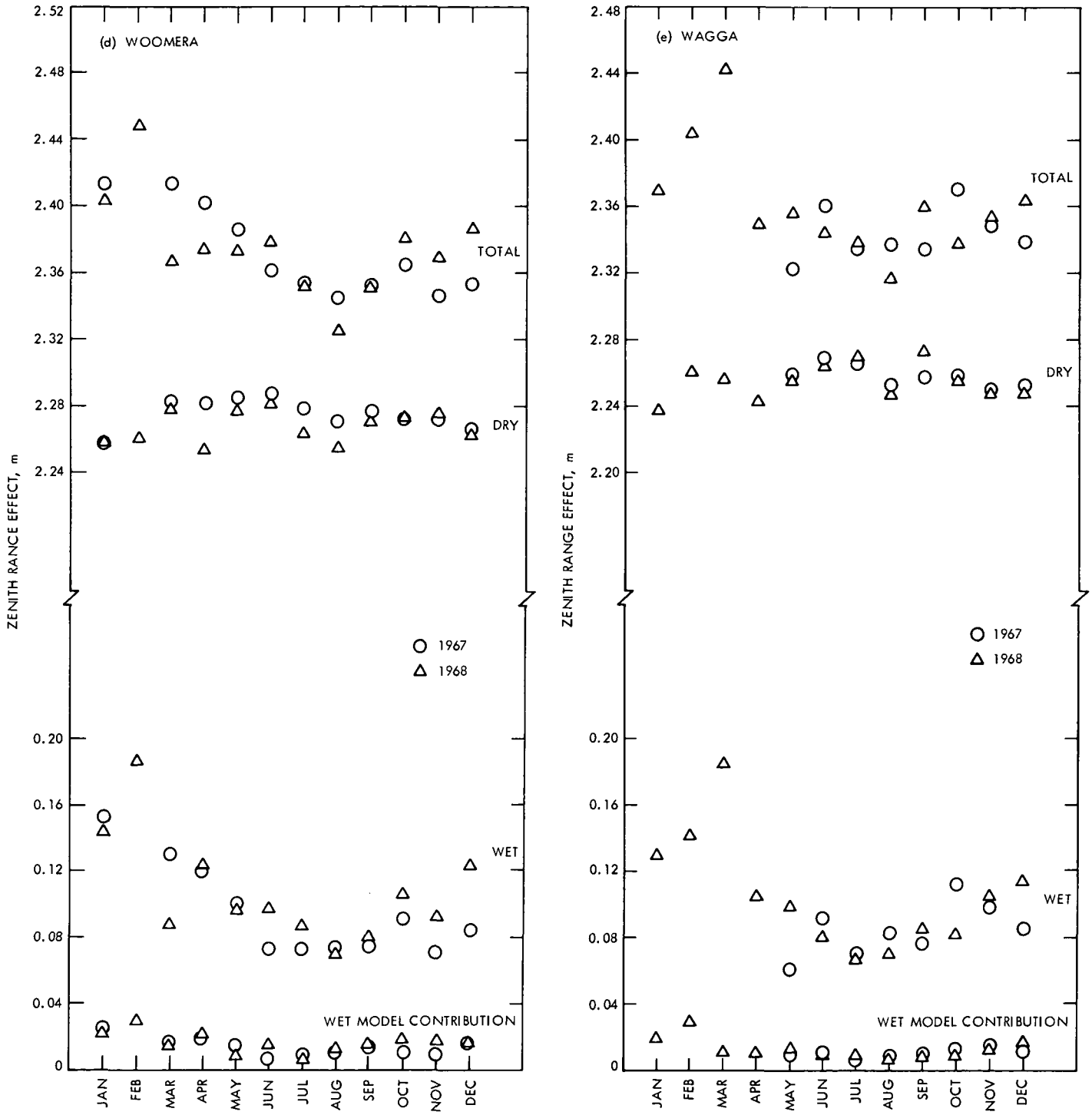
(d) WOOMERA
(e) WAGGA
ZENITH RANGE EFFECT, m
TOTAL
DRY
WET
WET MODEL CONTRIBUTION
1967
1968
JAN
FEB
MAR
APR
MAY
JUN
JUL
AUG
SEP
OCT
NOV
DEC

Fig. 8 (contd)

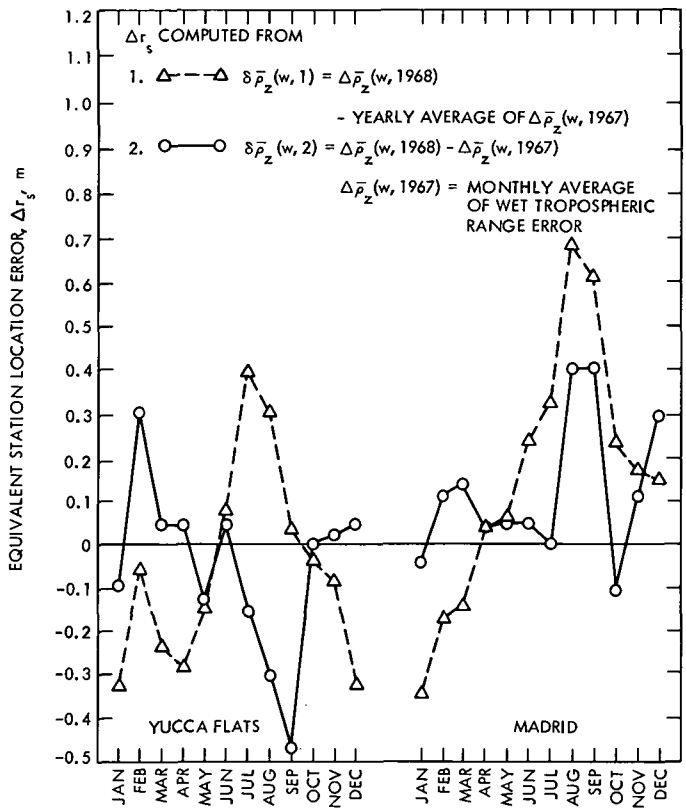

Fig. 9. Monthly averages of equivalent station location error produced by calibrating 1968 zero declination and 10-deg minimum elevation angle tracking data, using a wet troposphere model with 1967 parameters

Tropospheric and Ionospheric Range Corrections for an Arbitrary Inhomogeneous Atmosphere (First-Order Theory)

O. H. von Roos
Tracking and Orbit Determination Section

In this article a simple and concise expression for the range correction for an atmosphere which possesses arbitrary radial, lateral, and azimuthal gradients of the index of refraction is presented. The validity of this expression hinges only on the assumption that the index of refraction is close to unity, an assumption which is well satisfied for the Earth's atmosphere. Furthermore, it is shown that the range corrections for a simple model of the Earth's troposphere, including typical lateral variations, are in close agreement with existing computer solutions.

I. Introduction

Hand in hand with the ever increasing complexity of unmanned space missions, there is an ever increasing need for higher accuracies in orbit determinations. The orbit or trajectory is primarily determined by measuring the range, ρ, and by measuring the time rate of change of the range, $\dot{\rho}$. The present status of the accuracy is about 7 m for range and 1.3 m/12 h for the range rate (Ref. 1). That is, at a distance of 1 AU ($1.5 \cdot 10^8$ km) the range can be measured within 1 m (approximately 1 part in 10^{11}), and the velocity of the spacecraft (typically 10 km/s) is known to 1 part in 10^9. In order to achieve these enormous accuracies, a great number of error sources have to be analyzed and accounted for. Since the range is measured by a time measurement (the transit time of a radio signal between Earth and the spacecraft) and velocities are measured by cycle counting (doppler shift), there ensues a plethora of possible error sources. Those errors due to hardware and software of the DSN have been enunciated elsewhere (Ref. 2). Further, atmospheric and cosmic noise is, of course, degrading the signal. But this is not all. Severe degradation of the range determination comes about via the interaction of the radio signal with the intervening tenuous matter. These interactions can conveniently be classified as due to the troposphere, the ionosphere, and the solar wind. Although the refractive index of these strata

is close to unity, they nevertheless give rise to sizable range errors, sizable in the sense that the errors introduced are larger than the required accuracy (1 m). For instance, at an elevation angle of 10 deg in a configuration such that the spacecraft is at a distance of 1 AU and the Sun-Earth-probe angle is 40 deg and it happens to be local noon (the ionospheric electron concentration is higher in daytime), the range error due to the troposphere is 10 m, that due to the ionosphere is 10 m, and, finally, that due to the solar wind is 10 m, and *they are all additive*. Of course, the values just quoted are only representative and are by no means accurate, since all so-called "media range corrections" are sensitive functions of their respective variables (elevation angle for instance, etc.).

In this article, we address ourselves to two main culprits: the troposphere and the ionosphere or, generally speaking, the atmosphere. It will be shown that the range correction can actually be determined by a simple and concise expression (Eq. 42 of the text).[1] There is no need for extensive ray-tracing programs. All that has to be known is the refractive index profile within the unperturbed (straight) ray path. The accuracy of expression (42), which makes use of the fact that $n - 1 \ll 1$, where n is the refractive index, is proportional to $(n-1)^2$ and therefore lies well within the cm range. It is hoped that the simplification arrived at in the following pages alleviates to some extent the complex question of range calibration.

II. Troposphere

In the spherical coordinate system depicted in Fig. 1, we express the refractive index of the troposphere by

$$n(r,\theta) = 1 + \alpha F(r,\theta) \tag{1}$$

where $\alpha \ll 1$ and F is an arbitrary function of the two variables, r the distance from the Earth's center, and θ the angle between an (arbitrary) z axis and the radial distance to a point in space. A fairly accurate example is given by the following very simple model of the troposphere:

$$\left.\begin{aligned} \alpha &= 3 \cdot 10^{-4} \\ F(r,\theta) &= \exp\left[-\frac{r-R}{H}\right] \end{aligned}\right\} \tag{2}$$

an exponentially decreasing refractive index with scale height H. As we can see, the requirement $\alpha \ll 1$, which will play a vital role in our subsequent analysis, is indeed satisfied.

Let us suppose for a moment that $\alpha = 0$, or that the atmosphere is absent. In this case the ray path between a distant spacecraft and the point of observation, specified by the coordinates $r = R$ and $\theta = \bar{\theta}$, is a straight line. A convenient expression is

$$\theta(r) = \theta_0(r) = \bar{\theta} - \gamma + \cos^{-1}\left(\frac{R\cos\gamma}{r}\right) \tag{3}$$

that is to say that each point on the straight line, expressed analytically by Eq. (3), is uniquely determined by its geocentric distance r. From Eq. (3), it follows that

$$\frac{r^2\,\theta_0'}{\sqrt{1 + r^2(\theta_0')^2}} = R\cos\gamma \tag{4}$$

which we need for future references.[2]

Suppose now that the troposphere is present and represented by the refractive index (1). Taking r as the independent variable, the ray path may now be expressed by[3]

$$\theta(r) = \theta_0(r) + \theta_1(r) \tag{5}$$

where θ_0 is given by Eq. (3) and

$$\frac{\theta_1}{\theta_0} \ll 1 \tag{6}$$

due to the fact that $n - 1 \ll 1$. We do not need to solve the Euler equation associated with θ_1. All we have to do to determine θ_1 uniquely is to postulate that at the observation point:

$$\left.\begin{aligned} \theta_1(R) &= 0 \\ \theta_1'(R) &= 0 \end{aligned}\right\} \tag{7}$$

This is not a restriction since the differential equation governing θ_1 is of second order. Taking the elevation angle explicitly into account, we may write for the ray path disturbed by the troposphere:

$$\theta(r,\gamma) = \theta_0(r,\gamma) + \theta_1(r,\gamma) \tag{8}$$

[1]Knowing, of course, the intervening density profiles of both the troposphere and the ionosphere.

[2]The prime means differentiation with respect to r.

[3]Omitting azimuthal variations for the time being.

From Eq. (3), it is clear that the ray (8) will emerge from the troposphere at a certain angle, which for large r becomes

$$\theta(\infty,\gamma) = \frac{\pi}{2} + \bar{\theta} - \gamma + \theta_1(\infty,\gamma) \tag{9}$$

On the other hand, the unperturbed beam's limiting angle for large r is simply given by

$$\theta_0(\infty,\gamma) = \frac{\pi}{2} + \bar{\theta} - \gamma \tag{10}$$

The reason for this, of course, is that the unperturbed and the perturbed beams start off at the same elevation angle. To remedy the situation we must insist that the two beams are parallel to each other (for a distant spacecraft) after having left the troposphere. The angles (9) and (10) must therefore be the same. To achieve this we must correct the elevation angle γ in Eq. (8) in the following manner:

$$\begin{aligned}\theta(r,\gamma') &= \theta_0\,(r,\gamma + \theta_1(\infty,\gamma)) + \theta_1(r,\gamma)\\ &= \theta_0(r,\gamma) + \theta_1(\infty,\gamma)\frac{\partial\theta_0}{\partial\gamma} + \theta_1(r,\gamma)\end{aligned} \tag{11}$$

again in first order. From Eq. (3), it follows that

$$\frac{\partial\theta_0}{\partial\gamma} = -1 + \left(1 - \frac{R^2\cos^2\gamma}{r^2}\right)^{-1/2}\frac{R}{r}\sin\gamma \tag{12}$$

so that, indeed,

$$\theta(\infty,\gamma') = \theta_0(\infty,\gamma) \tag{13}$$

It is now an easy matter to compute the range correction due to the influence of the troposphere. It is clear that the topocentric distance to the spacecraft is simply given by

$$\rho_0 = \int_R^\infty \sqrt{1 + r^2\,[\theta_0(r,\gamma)']^2}\;dr \tag{14}$$

if the atmosphere is absent. The angle θ_0 in Eq. (14) is given by Eq. (3). Therefore the range Eq. (14) is merely an integral along a straight line. The upper limit ∞ is only taken for convenience, signifying that the spacecraft is many Earth radii away. On the other hand, the apparent topocentric range, taking explicitly the troposphere into account, is given by

$$\rho_1 = \int_R^\infty n(r,\theta(r,\gamma'))\;\sqrt{1 + r^2\,[\theta(r,\gamma')']^2}\;dr \tag{15}$$

where $\theta(r,\gamma')$ is found from Eq. (11) and therefore duly recognizes the correction to the elevation angle. In first order we have then for the range correction:

$$\begin{aligned}\Delta\rho = \rho_1 - \rho_0 = &\int_R^\infty \frac{r^2\,\theta_0'}{\sqrt{1 + r^2\,(\theta_0')^2}}\left(\theta_1' + \theta_1(\infty)\frac{\partial\theta_0'}{\partial\gamma}\right)dr\\ &+ \int_R^\infty (n-1)\sqrt{1 + r^2(\theta_0')^2}\;dr\end{aligned} \tag{16}$$

Taking into account Eqs. (4) and (12), we see that the first integral in Eq. (16) actually vanishes since

$$\begin{aligned}&\int_R^\infty \frac{r^2\,\theta_0'}{\sqrt{1 + r^2\,(\theta_0')^2}}\left(\theta_1' + \theta_1(\infty)\frac{\partial\theta_0'}{\partial\gamma}\right)dr\\ &\quad = R\cos\gamma\,\theta_1(\infty)\left(1 + \frac{\partial\theta_0(\infty)}{\partial\gamma}\right) = 0\end{aligned} \tag{17}$$

We have, therefore, the result, using explicitly Eq. (3) for θ_0:

$$\Delta\rho = \int_R^\infty (n-1)\left(1 - \frac{R^2\cos^2\gamma}{r^2}\right)^{-1/2}dr \tag{18}$$

We have then the remarkable result that as long as $n - 1 \ll 1$ and a first-order perturbation theory is adequate, the range correction is simply the integral over the unperturbed (straight) ray path weighted with that part of the refractive index which deviates from unity. There is no need to compute the actual ray path, the bending and twisting of it and so forth. Inserting Eq. (1) into Eq. (18) yields

$$\Delta\rho = \alpha\int_R^\infty F\,(r,\theta_0(r,\gamma))\left(1 - \frac{R^2\cos^2\gamma}{r^2}\right)^{-1/2}dr \tag{19}$$

where, of course, θ_0 is given by Eq. (3). Equation (19) holds for all elevation angles but must be computed numerically for most cases of interest, particularly at low elevation angles. However, at higher elevation angles ($\gamma > 10°$), considerable simplifications arise if simple but

adequate tropospheric models are used. We shall do so now. For $\gamma > 10°$ and an exponentially decreasing refractive index, the square root under the integral sign may be approximated by

$$\left(1 - \frac{R^2}{r^2}\cos^2\gamma\right)^{-1/2} \approx (\sin\gamma)^{-1} \tag{20}$$

and if we assume for $n - 1$:

$$n - 1 = \alpha\,[1 \pm 2\,(\theta_0 - \bar{\theta})]\exp\left[-\frac{r-R}{H}\right] \tag{21}$$

with $\alpha = 3 \cdot 10^{-4}$ and $H = 7$ km,[4] we obtain immediately from Eq. (19)

$$\Delta\rho = \frac{\alpha}{\sin\gamma}H \pm \frac{2\,\alpha}{\sin\gamma}\int_R^\infty dr \exp\left[-\frac{r-R}{H}\right](\theta_0(r,\gamma) - \bar{\theta}) \tag{22}$$

The first term on the right-hand side of Eq. (22) represents the contribution to the range correction due to the radially stratified troposphere. The second term is due to lateral inhomogeneities. With the aid of Eq. (3), it can be expressed as

$$\Delta\rho_L = \frac{2\,\alpha}{\sin\gamma}\int_R^\infty dr \exp\left[-\frac{r-R}{H}\right]\left\{\cos^{-1}\left(\frac{R\cos\gamma}{r}\right) - \gamma\right\} \tag{23}$$

The rapid decrease of the integrand, because of the exponential, makes it clear that for the curly bracket we can use the following approximation:

$$\cos^{-1}\left(\frac{R\cos\gamma}{r}\right) - \gamma = \left\{\frac{\partial}{\partial r}\cos^{-1}\left(\frac{R\cos\gamma}{r}\right)\right\}_{r=R}(R - r) = \frac{\cos\gamma}{\sin\gamma}\frac{r-R}{R} \tag{24}$$

Using Eq. (24) we obtain readily for the integral (23):

$$\Delta\rho_L = \frac{2\alpha\cos\gamma}{\sin^2\gamma}\frac{H}{R}H \tag{25}$$

Therefore, the total range correction is given by

$$\Delta\rho = \frac{\alpha}{\sin\gamma}H \pm \frac{2\alpha\cos\gamma}{\sin^2\gamma}\frac{H}{R}H \tag{26}$$

for elevation angles γ larger than 10 deg. For elevation angles less than 10 deg approximately, Eq. (19) must be determined numerically. However, determining $\Delta\rho$ from Eq. (26), together with the numerical values given above, yields at $\gamma = 10$ deg:

$$\Delta\rho = (12.1 \pm 0.2)\text{ meter} \tag{27}$$

in complete agreement with the work of other researchers (Ref. 4).[5]

We now extend this work to the case in which n is also a function of the azimuthal angle Φ, in other words $n = n(r, \theta, \Phi)$. It is clear that if $\bar{\theta} = 0$ in Fig. 1, every unperturbed ray lies in a meridian plane and its azimuthal angle is $\Phi_0 = $ constant. Suppose that n is also a function of Φ. In that case the ray path will be twisted ever so slightly, also in an azimuthal direction, and we have

$$\Phi(r) = \Phi_0 + \Phi_1(r,\gamma) \tag{28}$$

where again $\Phi_1/\Phi_0 \ll 0$ and

$$\left.\begin{aligned}\Phi_1(R,\gamma) &= 0\\ \Phi_1'(R,\gamma) &= 0\end{aligned}\right\} \tag{29}$$

just as in Eq. (7). In order for the ray path to be parallel to the unperturbed ray after leaving (or before entering) the troposphere (as the case may be), we must have

$$\Phi_0' = \Phi_0 + \Phi_1(\infty,\gamma) \tag{30}$$

But since the line element in this case is given by

$$dS = \sqrt{1 + r^2(\theta')^2 + r^2\sin\theta(\Phi')^2}\,dr \tag{31}$$

and noting that $(\Phi')^2 = (\Phi_1')^2$ is of second order, we see that the result (19) is still valid with the stipulation that

$$\Delta\rho = \alpha\int_R^\infty F(r, \theta_0(r,\gamma), \Phi_0) \times\left(1 - \frac{R^2\cos^2\gamma}{r^2}\right)^{-1\frac{1}{2}} dr \tag{32}$$

[4]The value $\pm 2(\theta_0 - \bar{\theta})$ for typical lateral inhomogeneities of the refractive index is a good approximation to existing data (Ref. 3).

[5]Also see Chao, C. C., "Tropospheric Range Effect Due to Simulated Inhomogeneities by Ray Tracing" (this volume).

This is true in the special coordinate system in which $\bar{\theta} = 0$. But since $\Delta\rho$ is an invariant length in any general coordinate system, expression (32) is still valid but the angles θ_0 and Φ_0 have to be replaced by their appropriate values. If, for instance, the angle between the projection of the line of sight and the meridian is α and if we put $\Phi_0 = 0$ for simplicity, the connection between the angles θ and Φ of the general coordinate system[6] and the special angles θ_0 and $\Phi_0 = 0$ is given by

$$\left.\begin{aligned} \sin\theta \sin\Phi &= -\sin\alpha \sin\theta_0 \\ \cos\theta &= -\cos\alpha \sin\bar{\theta} \sin\theta_0 + \cos\bar{\theta} \cos\theta \end{aligned}\right\} \tag{33}$$

In any case, it is clear from Eq. (32) that azimuthal gradients only give rise to second-order effects for the range correction.

III. Ionosphere

The work done so far has only dealt with the troposphere, but it is easy enough to incorporate the ionosphere in the same vein. For instance, consider the refractive index of a plasma:

$$n = \sqrt{1 - \frac{w_p^2}{w^2}} \tag{34}$$

where the plasma frequency w_p is given by

$$w_p = \left(\frac{4\pi e^2}{m} N\right)^{1/2} \tag{35}$$

with N the electron number density per cm^3, and w the frequency of the radio beam traversing the ionosphere. For the DSN frequencies $w \approx 10^{10}$ sec^{-1} and for the prevailing ionospheric electron densities of $N \approx 10^6$ cm^{-3}, we have

$$n = 1 - \frac{w_p^2}{2w^2} \tag{36}$$

since $w_p^2/w^2 \approx 10^{-5}$ is very small. For a determination of the ray path in the charged-particle medium, essentially the same Ferma principle holds as it does for the troposphere, namely,

$$\delta \int n(r,\theta,\Phi,w)\, ds = 0 \tag{37}$$

where n is now given by Eq. (36). To determine the range correction we must, however, be precise because of dispersion. The range is usually measured by comparing a received range code with an internally generated code carefully calibrated with a clock. A range code constitutes a modulated signal and propagates, therefore, with the group velocity which differs from the phase velocity by w_p^2/w^2 within the approximation used to obtain Eq. (36). Whereas the phase velocity is given by

$$v_p = c\left(1 + \frac{w_p^2}{2w^2}\right) \tag{38a}$$

the group velocity is given by

$$v_G = c\left(1 - \frac{w_p^2}{2w^2}\right) \tag{38b}$$

It is also clear that the modulation is "riding" on the carrier frequency or in Fourier language, the modulation consists of frequency components very close to the carrier frequency and therefore the ray path is governed by Eq. (37) with w being the carrier frequency ($\approx 10^{10}$ rad/s). Accordingly, the range correction due to the ionosphere is determined by the difference

$$\Delta\rho_i = c \int \frac{dS}{v_G} - \rho_0 \tag{39}$$

where dS is a solution of Eq. (37) and ρ_0 is given by Eq. (14). The same analysis which led to Eq. (18) can now be carried out without change to yield the following expression for the range correction:

$$\Delta\rho_i = \int_R^\infty \frac{w_p^2}{2w^2}\left(1 - \frac{R^2\cos^2\gamma}{r^2}\right)^{-1/2} dr \tag{40}$$

Furthermore, it can be shown from Maxwell's equations (Ref. 5) that the dielectric constant of a medium consisting of a neutral polarizable background (here the troposphere) and a plasma (here the ionosphere) is simply given by the sum:

$$\epsilon = \epsilon_0 - \frac{w_p^2}{w^2} \tag{41}$$

[6]A coordinate system which may have the Earth's spin axis as Z axis. We are thinking of a global chart of tropospheric conditions, something which does not exist yet.

where ϵ_0 is the dielectric constant of the neutral medium. Collecting Eqs. (32), (35), and (40) and expressing everything in terms of the unperturbed ray path, we have as a final result:

$$\Delta\rho = \int_R^\infty dr\left(1 - \frac{R^2\cos^2\gamma}{r^2}\right)^{-1/2}\left\{\alpha\, F(r, \theta_0(r,\gamma), \Phi_0) + \frac{2\pi e^2}{mw^2} N(r, \theta_0(r,\gamma), \Phi_0)\right\} \quad (42)$$

expressing the range correction as a single integral over the unperturbed ray path, combining both the troposphere and the ionosphere in one expression.

In conclusion we would like to mention and elaborate on the time variations of the atmosphere. First of all, it is clear that any time variations (day–night changes, seasonal changes, turbulent fluctuations, etc.) by and large have a very long time scale compared to the transit time of the signal which is of the order of 10^{-2} s at most. Therefore, time enters Eq. (42) strictly as an additional parameter t. The range rate or the time derivative of the range is then given by expression (42), in which both F and N are differentiated with respect to time. If, however, the range rate $\Delta\dot{\rho}_D$ is measured via doppler by referencing cycles of a received monochromatic signal with an internally generated monochromatic signal (a clock), the correct expression for $\Delta\dot{\rho}$, taking the phase velocity Eq. (38a) into account, is

$$\Delta\dot{\rho}_D = \int_R^\infty dr\left(1 - \frac{R^2\cos^2\gamma}{r^2}\right)^{-1/2}\left\{\alpha\frac{d}{dt}F(r, \theta_0(r,\gamma), \Phi_0; t) - \frac{2\pi e^2}{mw^2}\frac{d}{dt}N(r, \theta_0(r,\gamma), \Phi_0; t)\right\} \quad (43)$$

IV. Summary

On the preceding pages, simple expressions, both for the range correction $\Delta\rho$ and for the range rate correction $\Delta\dot{\rho}$ due to a tenuous atmosphere, have been derived. To be sure these expressions are approximate and are only valid if the refractive index of the atmosphere is close to unity. This is very well satisfied for the Earth's atmosphere. In as much as second-order effects may be neglected, the theory presented here is completely general. All that has to be known is the electron density profile and the neutral gas density profile within the undisturbed line of sight between the Earth-bound station and the spacecraft. Although, as already mentioned, the expression for the range correction is rather simple, for low elevation angles and realistic density profiles the integral must probably be computed numerically. Work along these lines and also the incorporation of the solar wind into our model is in progress.

References

1. *DSN/Flight Project Interface Design Handbook*, 810-5, Rev. B, Aug. 1, 1971 (JPL internal document).
2. Mulhall, B. D., et al., *Tracking System Analytic Calibration Activities for the Mariner Mars 1969 Mission*, Technical Report 32-1499. Jet Propulsion Laboratory, Pasadena, Calif., Nov. 15, 1970.
3. Bean, B. R., and Dutton, E. J., *Radio Meteorology*, NBS Monograph 92, p. 214, Mar. 1, 1966.
4. Miller, L. F., Ondrasik, V. J., and Chao, C. C., "A Cursory Examination of the Sensitivity of the Tropospheric Range and Doppler Effects to the Shape of the Refractivity Profile," in *The Deep Space Network Progress Report*, Technical Report 32-1526, Vol. I, pp. 22–30. Jet Propulsion Laboratory, Pasadena, Calif., Feb. 15, 1971.
5. Jackson, J. D., *Classical Electrodynamics*. John Wiley & Sons, Inc., New York, 1962.

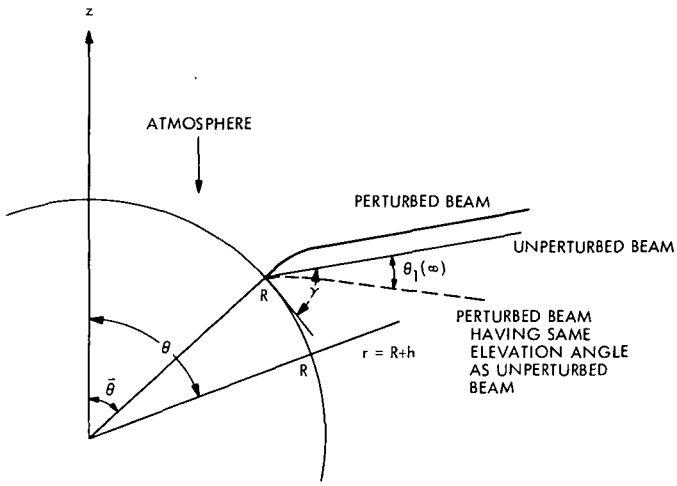

Fig. 1. Geometry of ray paths

An Optimum Buffer Management Strategy for Sequential Decoding

J. W. Layland
Communications Systems Research

Sequential decoding has been found to be an efficient means of communicating at low undetected error rates from deep space probes, but another failure mechanism known as erasure or computational overflow remains a significant problem. The erasure of a block occurs when the decoder has not finished decoding that block at the time that it must be output.

The erasure rate can be unacceptably high even when the decoder is spending over half of its time idly awaiting incoming data. By drawing upon analogies in computer time-sharing, this article develops a buffer management strategy which reduces the decoder idle time to a negligible level, and therefore improves the erasure probability of a sequential decoder. For a decoder with speed advantage of 10 and buffer size of 10 blocks, operating at an erasure rate of 10^{-2}, use of the new buffer management strategy reduces the erasure rate to less than 10^{-4}.

I. Introduction

Convolutional encoding and sequential decoding have been shown to be a useful technique for communicating at low error rates from deep space probes. This coding method has been flown successfully on *Pioneer 9* and will be used on *Pioneers F* and *G*, *Helios*, and possibly many other spacecraft in the future. While low undetected error rates are relatively easy to obtain with this technique, another failure mode, known as computational overflow or erasure, limits operation of the decoder to data rates that are less than half of channel capacity. Increasing the speed of the decoding computations provides some improvement, but only of a linear order. Despite operation with the very high-speed multiple omission sequential decoder (Ref. 1), the frequency of erasures was found to be in excess of two orders of magnitude over undetected errors. Pure decoding speed is not an adequate answer to the erasure problem. Heller (Ref. 2) suggested that more complete knowledge of the erasure mechanism and decoder buffer behavior might allow some improvement in erasure performance.

The investigation described in this article was initiated as a result of the observation that a sequential decoding machine spends much of its time idling, waiting for incoming data, but at the same time is unable to decode an intolerably large fraction of those data blocks. A method was sought and found which reduces decoder idle time to an insignificant level. This increased efficiency of the decoder results in a slight-to-moderate improve-

ment in erasure probability at high-to-moderate erasure rates, and a very marked improvement at low erasure rates.

II. Computation Problem

The sequential decoding of convolutionally encoded data proceeds by making local best estimates of the data sequence, based upon both the received symbol sequence and data estimates preceeding the current one in the block. If the received symbols are relatively noiseless, decoding proceeds rapidly with no searching. If the received symbols are noisy, some of the local estimates will be wrong. To make the ultimate bit-error probability low, the decoder must eventually recognize that an error has been made and search systematically backward through the local estimates to correct those in error. The amount of searching that must be done depends upon the amount of noise in the received data.

A considerable amount of experimental and theoretical work has been expended in determining the statistical behavior of the decoding search (Refs. 2 [pp. 36–45], 3, 4). It has been shown that the number of computations c performed by a sequential decoder in incrementing by one the number of bits for which a local estimate has been made has a Pareto distribution, i.e.,

$$P_r\{c > N\} \sim kN^{-\alpha} \tag{1}$$

The exponent α is a positive increasing function of the bit signal-to-noise ratio ST_b/N_0. The expected value of c becomes infinite for $\alpha \leq 1$. The signal-to-noise ratio at which $\alpha = 1$ is known as the computational cut-off point for sequential decoding.

The constant k in Eq. (1) has been estimated by Heller to be 1.9 (Ref. 2, p. 41). It has been further argued (Ref. 3) that the distribution of computations on an L-bit block of data is linear in L, so that

$$P_r\{c_L > N\} \sim kLN^{-\alpha} \tag{2}$$

is the probability that more than N computations are required to decode a given block of received data. For the remainder of this article, it will be assumed that Eq. (2) defines the per-block distribution of computation.

III. Lower Bound to Erasure Probability

Suppose a sequential decoder has been implemented which performs μ computations during the time one bit is received, has an infinitely large buffer to hold data waiting to be decoded, and a "magic genie" which informs the decoder before it begins decoding which blocks it should immediately erase in order to be able to decode the largest possible fraction of all blocks received. It is clear that in performing this task, the genie simply erases all blocks whose number of required computations exceeds a threshold T_0, and no blocks which require less than T_0. For if one block were erased which required fewer computations than one which was decoded, we could reverse the positions of these two blocks, decode the easier of the two, and have some number of decoder operations available to complete the decoding of one or more other blocks. This contradicts the known condition that the magic-augmented decoder is already decoding the largest possible fraction of the received data, and hence proves the correctness of our assessment of the genie's selection method.

Knowing the selection method and the distribution of computation of the data, we are able to compute the fraction of data erased by the genie. On the average, the number of computations available to decode each block is $\mu \cdot L$, where μ is the speed advantage. The number actually expended is

$$\int_0^{T_0} N dP(N)$$

where $P(N) = P_r\{c_L > N\}$. Since the decoder is doing as well as possible, it must almost always be busy, hence,

$$\int_0^{T_0} N dP(N) = \mu \cdot L \tag{3}$$

Note that $dP(N) = 0$ for $k \cdot L \cdot N^{-\alpha} > 1$, or $N < N_0$. Equation (3) can be easily and mechanically solved first for T_0, and then for $P(T_0)$, the fraction deleted.

$$P(T_0) = e^{-\mu/k} \qquad \alpha = 1$$

$$P(T_0) = kL\left[(kL)^{(1/\alpha)-1} - \left(\frac{\mu}{k}\right)\left(1 - \frac{1}{\alpha}\right)\right]^{\alpha/(\alpha-1)} \qquad \alpha \neq 1 \tag{4}$$

$P(T_0)$ can be made zero by increasing μ for all $\alpha > 1$; while $\alpha = 1$, $P(T_0)$ is exponentially decreasing in μ. $P(T_0)$ represents a lower bound to the erasure for sequential decoding which depends only upon the speed of the decoder and the received ST_b/N_0. This bound can only be

approached if the amount of computation necessary to decode a block is estimated with fair accuracy before decoding is started.

IV. A Realistic Bound to Achievable Performance

Suppose instead of informing the decoder before decoding which blocks required excessive computation, the genie encountered in *Section III* becomes whimsical and halts computation only on noisy blocks after the decoder has expended as much effort toward decoding them as in decoding the noisiest block that does get decoded. Observing that the available computations are fully utilized on the average, we have the equality

$$T_1 P(T_1) + \int_0^{T_1} N dP(N) = \mu L \tag{5}$$

Equation (5) can be solved for T_1 and $P(T_1)$, yielding

$$P(T_1) = e^{-[(\mu/k)-1]} \qquad \alpha = 1$$

$$P(T_1) = kL\left[\frac{\alpha}{1+\alpha}(kL)^{(1/\alpha)-1} - \frac{\alpha-1}{\alpha+1}\frac{\mu}{k}\right]^{\alpha/(\alpha-1)} \qquad \alpha \neq 1 \tag{6}$$

$P(T_1)$ is conjectured to be a lower bound to erasure probability under the condition that no estimate of decoding effort is made on the received data prior to decoding.

V. A Time-Sharing Model

The whimsical genie's performance can be achieved, or at least closely approximated, by some models from computer time-sharing literature. Define each block received as a *job* which must be processed by a computational facility—our sequential decoder. The amount of work required by each job has the Pareto distribution of Eq. (2). Jobs enter the decoder at a fixed rate and with a fixed priority of 0. The priority of a job changes by an amount $-\delta$ for each time unit that it spends being serviced, while the priority remains unchanged while a job is waiting in the buffer. At all times, the highest priority job receives service. If more than one job has the same priority, they share the processor equally. This has been called the "last-come-first-served with pickup" model for time-shared computations (Ref. 5). The priority in this case is the negative of the decoding effort received. Blocks which have received small amounts of decoding effort have a higher priority than those which have received larger amounts, and hence are given preference in receiving additional computation. On the average, all jobs requiring less than some amount T_x of computation will be completed, while those needing T_x or more will accumulate in the infinite buffer after having received T_x units of computation. This behavior is exactly that achieved with the help of the whimsical genie of *Section IV*, hence $T_x = T_1$. One possible disadvantage to decoding in this fashion is that jobs are completed in an order dependent upon the amount of computation required, instead of strictly in the order in which they arrived.

VI. A Practical Memory Management Scheme

The steps necessary to approximate the model of *Section V* with a practical and effective memory management scheme for sequential decoding are: (1) to use a finite buffer size, and (2) to quantize the amounts of computation provided, so that the decoder does not spend all of its time switching between blocks. Details of the scheme are as follows: blocks which have received some decoder effort are stored on a queue in priority order inversely related to the amount of decoder effort which they have received. After a new block is received, the decoder immediately begins decoding upon that new block. The block which the decoder had been working upon is placed in the queue in proper priority order. Whenever a block is completely decoded, its storage is released to be used by some future data block. Whenever a data block arrives for which no buffer space is available, the lowest priority block (not necessarily the oldest) is erased and its space made available for the new block. This algorithm is very similar to the feedback queuing strategy for processor allocation in time sharing (Ref. 5), and so will be called feedback queuing memory management (FBQM) in the following. Figure 1 is a flow chart of the FBQM algorithm.

FBQM has been simulated using the assumption that Eq. (2) is an accurate description of the per-block distribution of required decoder effort. A sequence of uniform (0, 1) pseudo-random variables was generated by a multiplicative-congruential generator and transformed to produce the distribution of Eq. (2). The resultant random variables, each representing a block of convolutionally encoded data, were supplied to a model of the FBQM structure, and simultaneously to a model of the linear buffer memory management traditionally used for sequential decoding. The results for one sequence of tests are shown in Fig. 2. Little improvement is seen at low values of μ and high erasure probabilities, but where performance of the linear buffer management is moder-

ately good, performance of FBQM is up to three orders of magnitude better. The one drawback is, as mentioned earlier, that data blocks are not completed in strictly time sequence but are completed in an order which depends both upon the order of arrival at the decoder and the amount of computation necessary to decode each. While this may be annoying to some, it should not be a significant drawback to deep-space science and video data which receive a large amount of post-flight non-real-time processing anyway, and to which could be added the task of reordering the data into strict time sequence; in the mission control center, perhaps.

VII. Summary

This article has developed both a lower bound to the erasure probability of a sequential decoder with an infinite buffer, and a memory management strategy (FBQM) for decoders with finite buffer which performs close to the bound. Both the erasure probability of FBQM and its lower bound exhibit exponential decrease with increasing decoder speed at the sequential decoding computational cut-off point, where the erasure probability of a conventional sequential decoder exhibits only inverse proportionality. For a decoder with speed advantage $\mu = 40$, the improvement is about 0.2 dB in required ST_b/N_0 at a fixed erasure rate of 10^{-3} or three orders of magnitude decrease in erasure probability at $\alpha = 1$. For a decoder with speed advantage of 10 and buffer size of 10 blocks, operating at an erasure rate of 10^{-2}, use of the new buffer management strategy reduces the erasure rate to less than 10^{-4}.

All of the results presented here depend strongly upon the validity of Eq. (2) as a definition of the per-block distribution of computation for a sequential decoder. Since some of the arguments which support Eq. (2) are asymptotic in nature, and the decoder performance with FBQM depends upon the distribution of computation at both large and small values of the computation variable, additional simulations with actual sequential decoding data will be needed to validate the results obtained.

References

1. Layland, J. W., "Information Systems: Multiple Mission Sequential Decoder—Comparing Performance Among Three Rate 1/2, $K = 32$ Codes," in *The Deep Space Network*, Space Programs Summary 37-64, Vol. II, pp. 50–52. Jet Propulsion Laboratory, Pasadena, Calif., Aug. 31, 1970.
2. Heller, J. A., "Decoding and Synchronization Research: Description and Operation of a Sequential Decoder Simulation Program," in *Supporting Research and Advanced Development*, Space Programs Summary 37-58, Vol. III, p. 42. Jet Propulsion Laboratory, Pasadena, Calif., Aug. 31, 1969.
3. Savage, J. E., "The Distribution of Sequential Decoding Computation Time," *IEEE Trans. Inform. Theory*, Vol. IT-11, pp. 143–147, April 1966.
4. Jacobs, I. M., and Berlekamp, E. R., "A Lower Bound to the Distribution of Computation for Sequential Decoding," *IEEE Trans. Inform. Theory*, Vol. IT-13, pp. 167–174, April 1967. (See also Jacobs, I. M., and Berlekamp, E., "A Lower Bound to the Distribution of Computation for Sequential Decoding," in *Supporting Research and Advanced Development*, Space Programs Summary 37-34, Vol. IV, pp. 270–276. Jet Propulsion Laboratory, Pasadena, Calif., Aug. 31, 1965.)
5. Kleinrock, L., "A Continuum of Time-Sharing Scheduling Algorithms," in *AFIPS Conference Proceedings*, Vol. 36, 1970, pp. 453–458, Spring Joint Computer Conference, Atlantic City, N. J., 1970.

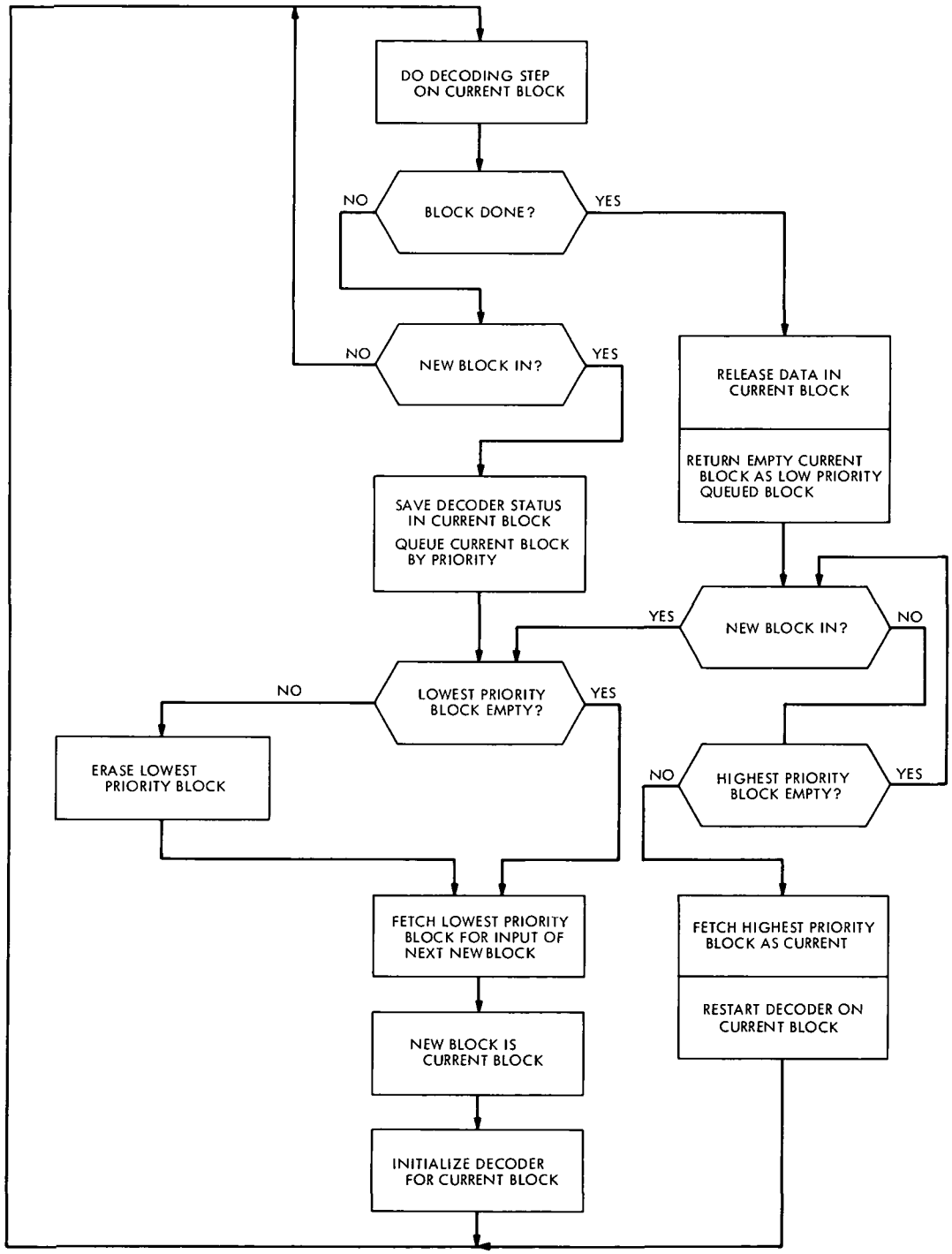

Fig. 1. Flow chart for FBQM

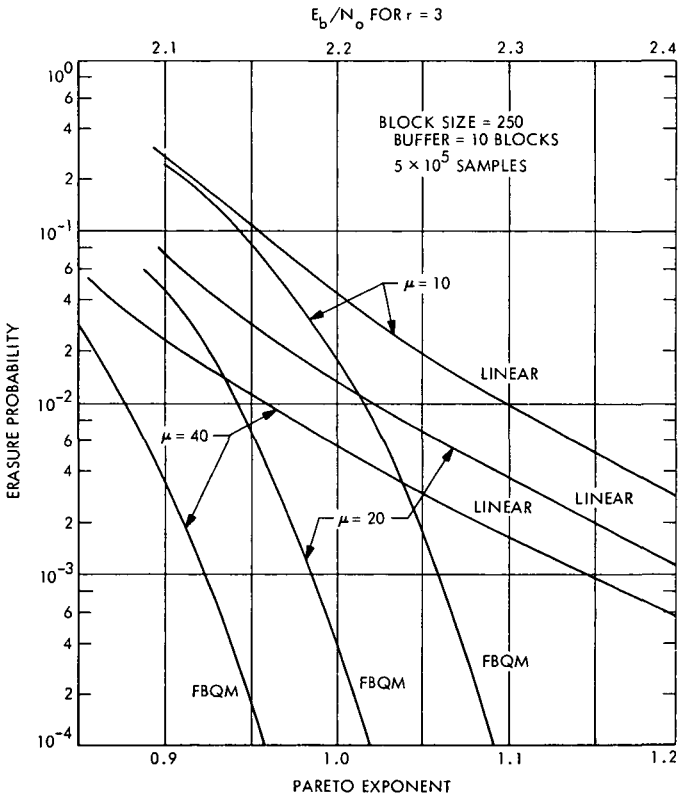

Fig. 2. Comparison of FBQM and linear buffer management

Data Storage and Data Compression

A. M. Odlyzko
Communications Systems Research Section

In this article a sharp upper bound is computed on the best possible data rate achievable as a function of data storage capability in certain very general situations. The result shows that a dramatic increase in rate can be caused by a small increase in storage capability.

I. Introduction

Consider an experiment in which samples x are taken from a sample space X, but no *a priori* probability distribution can be assumed on X. This is the situation, for example, when an experiment is performed for the first time on a distant planet. Further assume that the experimenter, who is separated from the experiment by a communications channel, does not need each value of x exactly, but rather is satisfied with knowing x "approximately." The object of this paper is to discover the relationship between data transmission rate and data storage capacity under these circumstances. We shall discover that a small increase in storage capacity can cause a dramatic increase in data rate.

We formalize the situation as follows. Let X be a set, and let S be a collection of subsets of X. When a sample $x \in X$ is obtained, we assume that the experimenter is satisfied to know only some $A \in S$ such that $x \in A$. Thus if n subsets from S, but no fewer, cover X, $\log_2 n$ bits are required to transmit the outcome of the experiment over a noiseless channel, except for roundoff in the logarithm. If, however, N outcomes $x_1, x_2, \cdots, x_N$ are stored before transmission, and n_N sets of the form $A_1 \times \cdots \times A_N$ cover $X \times \cdots \times X$, then similarly $\log_2 n_N$ bits will suffice to communicate the results of the N outcomes simultaneously; this corresponds to block source encoding of the data. Hence $(1/N) \log_2 n_N$ will be the number of bits per sample required when N samples can be stored. Thus if $n_N < n_1^N$ for some N, the data transmission rate can be improved, preserving the fidelity of each sample. We shall show that under some circumstances n_N actually grows only linearly in N, which implies that a spectacular gain in rate can sometimes be achieved with a small increase in storage. We shall in fact treat the case of simultaneously transmitting the outcomes of several different experiments, since it is no more difficult to handle this more general situation.

II. Results

Suppose that N is a positive integer and that $S_1, \cdots, S_N$ are collections of subsets of $X_1, \cdots, X_N$, respectively, such that n_i subsets belonging to S_i, and no fewer, cover X_i for $i = 1, \cdots, N$. The main result of this paper is that to cover $X_1 \times \cdots \times X_N$ requires no fewer than

$$\sum_{i=1}^{N} (n_i - 1) + 1$$

and no more than

$$\prod_{i=1}^{N} n_i$$

subsets of the form $A_1 \times \cdots \times A_N$, when $A_i \in S_i$ for all i. Moreover, we can choose the X_i and the S_i in such a way that

$$\sum_{i=1}^{N} (n_i - 1) + 1$$

of the specified subsets will cover $X_1 \times \cdots \times X_N$; the X_i, S_i, n_i, can be taken all equal here. Bounds for the spanning number (also called the coefficient of external stability) of a product of graphs are also obtained.

Let S be a collection of subsets of a set X such that $\cup S = X$. Define $c(X; S)$, the covering number of X with respect to S, to be the minimal number of elements of S whose union is X, if this number exists, and infinity if no finite subcollection of S covers X. If $S_1, \cdots, S_N$ are collections of subsets of $X_1, \cdots, X_N$, respectively, define a collection $S_1 \times \cdots \times S_N$ of subsets of the Cartesian product $X_1 \times \cdots \times X_N$ by

$$S_1 \times \cdots \times S_N = \{A_1 \times \cdots \times A_N : A_i \in S_i, i = 1, \cdots, N\}$$

This paper is concerned with the dependence of

$$c(X_1 \times \cdots \times X_N; S_1 \times \cdots \times S_N)$$

on the $c(X_i; S_i)$. We will restrict ourselves to the case in which all the $c(X_i; S_i)$ are finite, since otherwise $c(X_1 \times \cdots \times X_N; S_1 \times \cdots \times S_N) = \infty$.

If the sets A_{i,j_i} for $j_i = 1, \cdots, c(X_i; S_i)$ cover X_i for $i = 1, \cdots, N$, then the sets $A_{i,j_1} \times \cdots \times A_{N,j_N}$ cover $X_1 \times \cdots \times X_N$. We then easily obtain the upper bound

$$c(X_1 \times \cdots \times X_N; S_1 \times \cdots \times S_N) \leq \prod_{i=1}^{N} c(X_i; S_i)$$

Moreover, this bound cannot be improved, since equality holds whenever an X_i consists of n_i points and the subsets in S_i consist of single points. Now if $n_1, \cdots, n_N$ are positive integers, let

$$L(n_1, \cdots, n_N) = \min \{c(X_1 \times \cdots \times X_N; S_1 \times \cdots$$

$$\times S_N) : c(X_i; S_i) = n_i, 0 = 1, \cdots, N\}$$

We will prove (Theorem 1) the rather surprising result that

$$L(n_1, \cdots, n_N) = \sum_{i=1}^{N} (n_i - 1) + 1$$

The last part of this paper deals with direct products of graphs. Let us recall that if $G_1, \cdots, G_N$ are graphs, their product $G_1 \times \cdots \times G_N$ is defined as the graph having as its nodes ordered N-tuples $(a_1, \cdots, a_N)$, when a_i is a node of G_i for $i = 1, \cdots, N$, and whose two nodes $(a_1, \cdots, a_N)$ and $(b_1, \cdots, b_N)$ are connected by an edge if and only if they are distinct and for each $i = 1, \cdots, N$ either $a_i = b_i$ or a_i is connected to b_i by an edge of G_i. A *talon* is defined as a node together with all nodes that are connected to it by an edge. The spanning number $\beta(G)$ (also called the coefficient of external stability (Ref. 1) of a graph G is the smallest number of talons that cover (contain every node of) G. It is easy to see that if $G_1, \cdots, G_N$ are graphs,

$$\beta(G_1 \times \cdots \times G_N) \leq \prod_{i=1}^{N} \beta(G_i)$$

We will prove that

$$\beta(G_1 \times \cdots \times G_N) \geq \sum_{i=1}^{N} (\beta(G_i) - 1) + 1$$

and that given any positive integers $n_1, \cdots, n_N$ there are graphs $G_1, \cdots, G_N$ with $\beta(G_i) = n_i$ for $i = 1, \cdots, N$ such that

$$\beta(G_1 \times \cdots \times G_N) = \sum_{i=1}^{N} (n_i - 1) + 1$$

(Again if $n_i = n$, all i, then the G can be taken as equal.)

This paper may be regarded as the dual to the work of Erdős, McEliece, and Taylor (Ref. 2). If $\alpha(G)$ is the independence numbers (maximal numbers of nodes such that no two are connected by an edge, also called the coefficient of internal stability [Ref. 1]) of a graph G, then they proved that

$$\alpha(G_1 \times \cdots \times G_N) \leq M(\alpha(G_1) + 1, \cdots, \alpha(G_N) + 1) - 1$$

where $M(k_1, \cdots, k_N)$ is the Ramsey number of $k_1, \cdots, k_N$. It is easy to see that

$$\alpha(G_1 \times \cdots \times G_N) \geq \prod_{i=1}^{N} \alpha(G_i)$$

Moreover, they showed that given positive integers $n_1, \cdots, n_N$, it is possible to find graphs $G_1, \cdots, G_N$ such that $\alpha(G_i) = n_i$ for all i and

$$\alpha(G_1 \times \cdots \times G_N) = M(n_1 + 1, \cdots, n_N + 1) - 1$$

and the equality remark again holds.

These theorems correspond to our results on the spanning number of a product of graphs. In addition, however, they can be interpreted as results on packing. If S is a collection of subsets of a set X, define $p(X; S)$ to be the largest number of elements of S such that any two have an empty intersection (we will assume that this number is finite). We can associate with X and S a graph G, where the nodes of G will be the elements of S and two nodes will be joined by an edge if and only if this intersection (as subsets of X) is nonempty. Moreover, given any graph G we can find a set X and a collection S of subsets of X such that the graph associated with X and S will be isomorphic to G. The importance of this correspondence is that if G is the graph associated with X and S then

$$\alpha(G) = p(X; S)$$

and the theorem of Erdős, McEliece, and Taylor says that

$$p(X_1 \times \cdots \times X_N; S_1 \times \cdots \times S_N) \leqq M(p(X_1, S_1) + 1, \cdots, p(X_N, S_N) + 1) - 1$$

and that this bound is the best one possible.

LEMMA 1. *If $n_1, \cdots, n_N$ are positive integers, then*

$$L(n_1 + 1, n_2, \cdots, n_N) \geqq L(n_1, n_2, \cdots, n_N) + 1$$

Proof. Suppose that $S_1, \cdots, S_N$ are collections of subsets of $X_1, \cdots, X_N$, respectively, such that $c(X_1; S_1) = n_1 + 1$, $c(X_i; S_i) = n_i$ for $i = 2, \cdots, N$, and $c(X_1 \times \cdots \times X_N; S_1 \times \cdots \times S_N) = L(n_1 + 1, n_2, \cdots, n_N)$. Let $A_{1,j} \times \cdots \times A_{N,j}$ for $j = 1, \cdots, L(n_1 + 1, n_2, \cdots, n_N)$ be a minimal covering of $X_1 \times \cdots \times X_N$ by subsets from $S_1 \times \cdots \times S_N$. Consider

$$X_1' = X_1 - A_{1,1} = \{x \in X_1 : x \notin A_{1,1}\}$$

and

$$S_1' = \{A - A_{1,1} : A \in S_1\}$$

The sets $(A_{1,j} - A_{1,1}) \times A_{2,j} \times \cdots \times A_{N,j}$ for

$$j = 2, \cdots, L(n_1 + 1, n_2, \cdots, n_N)$$

belong to $S_1' \times S_2 \times \cdots \times S_N$ and cover $X_1' \times X_2 \times \cdots \times X_N$, so that

$$L(n_1 + 1, n_2, \cdots, n_N) - 1 \geqq c(X_1' \times X_2 \times \cdots \times X_N; S_1' \times S_2 \times \cdots \times S_N) \quad (1)$$

But $c(X_1'; S_1') = n_1$ or $n_1 + 1$, so that

$$c(X_1' \times X_2 \times \cdots \times X_N; S_1' \times S_2 \times \cdots \times S_N) \geqq L(n_1, n_2, \cdots, n_N) \quad (2)$$

or

$$c(X_1' \times X_2 \times \cdots \times X_N; S_1' \times S_2 \times \cdots \times S_N) \geqq L(n_1 + 1, n_2, \cdots, n_N) \quad (3)$$

Combining Eqs. (1) and (3) leads to an immediate contradiction, and hence Eq. (2) must hold. The lemma now follows from Eqs. (1) and (2).

THEOREM 1. *If $n_1, \cdots, n_N$ are positive integers, then*

$$L(n_1, \cdots, n_N) = \sum_{i=1}^{N} (n_i - 1) + 1 \quad (4)$$

Proof. Lemma 1, together with the fact that $L(k_1, \cdots, k_N)$ is a symmetric function and that $L(1, \cdots, 1) = 1$, implies that

$$L(n_1, \cdots, n_N) \geqq \sum_{i=1}^{N} (n_i - 1) + 1 \quad (5)$$

To prove Eq. (4) it will therefore suffice if we exhibit X_i and S_i such that $c(X_i; S_i) = n_i$ for $i = 1, \cdots, N$ and

$$c(X_1 \times \cdots \times X_N; S_1 \times \cdots \times S_N) \leqq \sum_{i=1}^{N} (n_i - 1) + 1$$

Let

$$n = \sum_{i=1}^{N} (n_i - 1) + 1$$

and define, for each $i = 1, \cdots, N$

$$X_i = \left\{1, 2, \cdots, \binom{n}{n - n_i + 1}\right\}$$

where $\binom{a}{b}$ are the binomial coefficients. The family S_i will consist of n subsets $A_{i,1}, \cdots, A_{i,n}$ formed as follows: number the

$$\binom{n}{n - n_i + 1}$$

possible $(n - n_i + 1)$ subsets (subsets with $n - n_i + 1$ elements) of S_i from 1 to

$$\binom{n}{n - n_i + 1}$$

and assign the integer i to each of the $n - n_i + 1$ sets in the ith collection. This way each element of X_i will belong to exactly $n - n_i + 1$ of the sets $A_{i,1}, \cdots, A_{i,n}$ and each $n - n_i + 1$ of these sets will have an element in common.

Let any $n_i - 1$ sets from S_i be given. By their definition the remaining $n - n_i + 1$ sets have a point $x \in X_i$ in common. Since x belongs to exactly $n - n_i + 1$ sets from S_i, it does not belong to any of the given $n_i - 1$ sets. Therefore these $n_i - 1$ sets do not cover X_i. On the other hand, if any n_i subsets from S_i are given, then every point $x \in X_i$ is contained in at least one of them since it is contained in $n - n_i + 1$ subsets from S_i and aside from the given ones there are only $n - n_i$ subsets remaining. Therefore $c(X_i; S_i) = n_i$.

Now consider the sets

$$\tilde{A}_j = A_{1,j} \times \cdots \times A_{N,j} \qquad \text{for } j = 1, \cdots, n$$

Suppose $x = (x_1, \cdots, x_N) \in X_1 \times \cdots \times X_N$. We know that if i is fixed, then $x_i \notin A_{i,j}$ holds for exactly $(n_i - 1)$ values of j. Since $x \in \tilde{A}_j$ occurs only when $x_i \notin A_{i,j}$ for at least one i, it cannot occur for more than

$$\sum_{i=1}^{N} (n_i - 1)$$

values of j. Since there are

$$n = \sum_{i=1}^{N} (n_i - 1) + 1$$

sets $\tilde{A}_j$, we conclude that $x \in \tilde{A}_j$ for at least one j. Thus the sets $\tilde{A}_j$ provide a cover for $X_1 \times \cdots \times X_N$, and hence

$$c(X_1 \times \cdots \times X_N; S_1 \times \cdots \times S_N) \leq n$$

This completes the proof of the theorem.

An interesting fact emerges from an examination of the above theorem. If $n_1 = n_2 = \cdots = n_N$ then a minimal covering with $L(n_1, \cdots, n_N)$ sets is obtained by taking all the X_i and likewise all the S_i equal. To prove this, just check that the above construction provides the desired covering, *mutatis mutandis*.

Theorem 2. *If $G_1, \cdots, G_N$ are graphs and $\beta(G)$ denotes the spanning number of a graph G, then*

$$\beta(G_1 \times \cdots \times G_N) \geq \sum_{i=1}^{N} (\beta(G_i) - 1) + 1 \qquad (6)$$

Moreover, given any positive integers $n_1, \cdots, n_N$ there are graphs $G_1, \cdots, G_N$ with $\beta(G_i) = n_i$ for $i = 1, \cdots, N$ and

$$\beta(G_1 \times \cdots \times G_N) = \sum_{i=1}^{N} (n_i - 1) + 1 \qquad (7)$$

Proof. Inequality (6) follows immediately from Eq. (5), since for each i we can take X_i to consist of the nodes of G_i and S_i to consist of talons of G_i, so that $\beta(G_i) = c(X_i; S_i)$ and $\beta(G_1 \times \cdots \times G_N) = c(X_1 \times \cdots \times X_N; S_1 \times \cdots \times S_N)$. In fact, Eq. (4) follows from Eqs. (5) and (7). Since the proof of Eq. (7) is considerably more complicated than that of Eq. (4), however, we treat products of graphs separately from products of arbitrary sets. Nevertheless, there will be very little duplication in the two proofs, since we will often refer to arguments used in proving Theorem 1. The proof of the last part of this theorem will be based on that of Theorem 1. To carry it out we will use the auxiliary result below (we might note that the bound $n > 2k + 10$ is introduced to simplify the proof and is not the best possible.) The proof of this lemma will be given at the end.

Lemma 2. *If n and k are positive integers such that $n > 2k + 10$, then there exists a graph G with $\beta(G) = k$ which has a subset of n talons such that every node of G belongs to at least $n - k + 1$ of these specified n talons.*

To complete the proof of Theorem 2 let $n_1, \cdots, n_N$ be given positive integers. Let us choose the positive integer r such that if

$$n = \sum_{i=1}^{N} (n_i - 1) + 1 + r$$

then $n > 2n_i + 10$ for $i = 1, \cdots, N$ and $n > 14$. Define $n_j = 2$ for $j = N + 1, \cdots, N + r$. By Lemma 2 there exists for each i, from 1 to $N + r$, a graph G_i with $\beta(G_i) = n_i$ and which has a subset of n talons, $A_{i,1}, \cdots, A_{i,n}$, such that every node of G_i belongs to at least $n - n_i + 1$ of these talons. It now follows, as in Theorem 1, that the n talons

$$\tilde{A}_j = A_{1,j} \times \cdots \times A_{N+r,j}, \qquad j = 1, \cdots, n$$

cover $G_1 \times \cdots \times G_{N+r}$, which implies that

$$\beta(G_1 \times \cdots \times G_{N+r}) \leq n = \sum_{i=1}^{N} (n_i - 1) + 1 + r \qquad (8)$$

But from Eq. (6) we find that

$$\beta(G_1 \times \cdots \times G_{N+r}) \geqq \beta(G_1 \times \cdots \times G_N) + \beta(G_{N+1} \times \cdots \times G_{N+r}) - 1 \tag{9}$$

Since

$$\beta(G_1 \times \cdots \times G_N) \geqq \sum_{i=1}^{N} (n_i - 1) + 1$$

and

$$\beta(G_{N+1} \times \cdots \times G_{N+r}) \geqq r + 1$$

The inequalities (8) and (9) imply that

$$\beta(G_1 \times \cdots \times G_N) = \sum_{i=1}^{N} (n_i - 1) + 1$$

which completes the proof of Theorem 2.

Proof of Lemma 2. Let n and k satisfy conditions of the lemma. We consider two cases.

Case 1: k odd. Let the nodes of G be $\{1, \cdots, \binom{n}{n-k+1}\}$. As in Theorem 1 we construct subsets $A_1, \cdots, A_n$ such that every $n - k + 1$ of these has a node in common and every node in G is in exactly $n - k + 1$ of these subsets. Let us look at the incidence matrix (a_{ij}) $(i = 1, \cdots, n$ and $j = 1, \cdots, \binom{n}{n-k+1})$ of this configuration, where $a_{ij} = 1$ if $j \in A_i$ and $a_{ij} = 0$ otherwise. Since every possible arrangement of $n - k + 1$ 1's and $k - 1$ 0's occurs exactly once in some column, we can permute the columns of this matrix until the first n of them form a circulant submatrix A of the form

$$A = \begin{array}{|c|c|} \hline \overbrace{1\ 0.....0}^{\frac{k-1}{2}}\ \overbrace{1.....1\ 0.....0}^{\frac{k-1}{2}} \\ 0\ 1.....0\ 1.....1\ 0....0 \\ \\ \\ 0.....0\ 1.....1\ 0.....0\ 1 \\ \hline \end{array} \tag{10}$$

Note that this construction can be carried out because each row (and column) has at least three 1's in it (if they each had two, some two columns would be identical), and because k is odd. For our purposes the most important feature of A is that it is symmetric.

Let us now consider again the full incidence matrix (a_{ij}), but in its permuted form so that A forms the first n columns. For each i from 1 to n connect the node i to the node j (for $i \neq j$) by an edge if and only if $a_{ij} = 1$. This defines our graph G. Since A is symmetric, the talon with center at $i (i \leqq n)$ consists precisely of these nodes j for which $n_{ij} = 1$. We will call them the "large talons." In addition we have many "small talons" which have centers at i, when $i > n$. A small talon with center at i contains the node i and $n - k + 1$ nodes j for $j \leqq n$. Since each node of G is in $n - k + 1$ of the large talons, we only need to show $\beta(G) = k$. Since any k large talons cover G (as shown in Theorem 1), we know that $\beta(G) \leqq k$.

Assume $\beta(G) < k$. Since $\beta(G) \geqq 1$, this implies $k \geqq 2$. Now $\beta(G) < k$ says that some $k - 1$ talons cover G. Suppose m of them are large talons. Then $m \leqq k - 2$, since we know from Theorem 1 that it requires k large talons to cover G. Moreover, $k \geqq 3$, since if $k = 2$ then there are no small talons. We can choose $n - k + 1$ large talons from the $n - m$ remaining ones in $\binom{n-m}{n-k+1}$ ways. Since each $n - k + 1$ large talons have a unique node in common, which is not in any other large talon, this gives $\binom{n-m}{n-k+1}$ nodes not covered by the m given large talons.

Suppose $m = k - 2$. This means that one small talon has to cover $\binom{n-k+2}{n-k+1} = n - k + 2$ nodes. Since exactly one node i with $i > n$ belongs to any small talon, the m given large talons had to leave $n - k + 1$ nodes j with $j \leqq n$ not covered. But any single large talon covers $n - k + 1$ of the nodes j with $j \leqq n$, and therefore our $m = k - 2 \geqq 1$ large talons leave uncovered no more than $k - 1$ nodes. Since $n > 2k + 10$, this leads to a contradiction.

Suppose $m < k - 2$. The $k - 1 - m$ small talons cover at most $(k - 1 - m)(n - k + 2)$ nodes, while the m large talons have $\binom{n-m}{n-k+1}$ nodes not covered. It will then suffice to prove that

$$\binom{n-m}{n-k+1} > (k - m - 1)(n - k + 2)$$

Now if $m = k - 3$,

$$\binom{n-m}{n-k+1} = \frac{(n-m)(n-m-1)}{2} > 2(n - m - 1)$$

since $n > 2k + 10 > m + 4$. Let $t = k - m - 3$. Then

$$\binom{n-m}{n-k+1} = \binom{n-m}{t+2} = \frac{(n-m)\cdots(n-k+2)}{(t+2)!}$$

$$\geq (n-k+2)\frac{(n-k+3)^{t+1}}{(t+2)!}$$

$$> (n-k+2)\frac{(k+13)^{t+1}}{(t+2)!}$$

$$> (n-k+2)(k-m-1)\frac{(k+13)^{t}}{(t+2)!}$$

$$> (n-k+2)(k-m-1)$$

for $1 \leq t \leq k-3$, since in that range

$$\frac{(k+13)^t}{(t+2)!} > 1$$

(easy induction proof). This completes the proof when k is odd.

Case 2: k even. Consider the same construction as in case 1, but with n and k replaced by $n+1$ and $k+1$, respectively. In the $(n+1) \times \binom{n+1}{n-k+1}$ incidence matrix (a_{ij}) which has its first $n+1$ columns in the form (10) delete the first row and the first column. The first n columns of the resulting $n \times \binom{n+1}{n-k+1}$ incidence matrix (b_{ij}) form a symmetric submatrix. The graph G will have as its nodes $\{1, \cdots, \binom{n+1}{n-k+1} - 1\}$. If $i \leq n$, we connect i to j $(i \neq j)$ by an edge if and only if $b_{ij} = 1$. It is easily seen that every node of G belongs to either $n-k+1$ or $n-k+2$ of the n talons with centers at $1, \cdots, n$. The proof of case 1 shows that $\beta(G) = k$, *mutatis mutandis*.

As a concluding remark we would like to pose another interesting problem. If G is a graph, $\gamma(G)$, the clique covering number, is defined to be the minimal number of cliques (complete subgraphs) which cover G. If $G_1, \ldots, G_N$ are graphs, then clearly

$$\gamma(G_1 \times \cdots \times G_N) \leq \prod_{i=1}^{N} \gamma(G_i)$$

and this bound cannot be improved. The question of obtaining the best possible lower bound for $\gamma(G_1 \times \cdots \times G_N)$ in terms of the $\gamma(G_i)$ is unsolved. The answer is different from that for spanning numbers, since if $\gamma(G_1) = 2$, then $\gamma(G_1 \times G_2) = 2\gamma(G_2)$. Combined with a modified version of Lemma 1 this provides a general lower bound for $\gamma(G_1 \times \cdots \times G_N)$, but it is not known whether it is the best possible. In particular, it is not known whether two sequences $\{G^{(n)}\}$ and $\{H^{(n)}\}$ of graphs can be found such that $\gamma(G^{(n)}) = \gamma(H^{(n)}) = n$ and $\gamma(G^{(n)} \times H^{(n)}) = o(n^2)$.

Acknowledgment

I would like to thank R. J. McEliece and E. C. Posner for proposing these problems and for their help. I would also like to thank H. Taylor for many stimulating conversations and especially for suggesting the basic construction used in proving Theorem 2.

References

1. Berge, C., *The Theory of Graphs and Its Applications*, Wiley & Johns, Inc., New York, 1962.
2. Erdős, P., McEliece, R. J., and Taylor, H., "Ramsey Bounds for Graph Products," *Pacific J. Math*, Vol. 37, pp. 45–46, 1971.

Microwave Maser Development

R. Clauss and H. Reilly
Communications Elements Research Section

A traveling-wave maser operating at 15.3 GHz has been used to test the noise temperature contribution of various waveguide components. An assembled system, consisting of the maser, a directional coupler, a waveguide switch, a polarizer, and a feed horn, measured 23 K total system operating noise temperature. Previously measured X-band data are shown for comparison. The maser was installed on the 64-m antenna at the Goldstone DSCC. Maximum changes of 2.2 deg signal phase and 0.25 dB signal amplitude were observed during antenna motion tests for maser phase and gain stability. The excellent stability performance is attributed to the use of a superconducting maser magnet.

I. Introduction

Noise temperature tests of waveguide feed system components are described in this article. A traveling-wave maser, operating at 15.3 GHz was used in the measurement system. The maser and waveguide feed system has been installed on the 64-m antenna at the Goldstone DSCC. Initial performance has been measured to show the gain and phase stability of the 15.3-GHz maser on a moving antenna.

II. Noise Temperature Measurements

The 15.3-GHz traveling-wave maser (Refs. 1 and 2) was used on the roof of Building 238 at JPL to measure the noise temperature contribution of various waveguide antenna feed components. A similar test at 8448 MHz was reported in March 1970 (Ref. 3). Measured values of system noise temperature were used to determine individual component noise contributions. These values are listed in Table 1. At 8448 MHz the waveguide switch, the polarizer, and the feed horns were made of aluminum; waveguide bends and straight sections were made of copper. At 15.3 GHz all waveguide components tested were made of copper or silver; two feed horns were made of copper and one aluminum horn was measured. Table 1 shows values for components which can be measured by insertion into an operating system.

Table 2 shows the operating noise temperature of three configurations measured on the roof of Building 238. Minimum configurations consist of a feed horn connected directly to a maser and a follow-up receiver with power recording instrumentation. The final configuration (for 15.3 GHz) includes a waveguide switch, a directional coupler, and a polarizer; the components are in the same configuration that is used in the Cassegrain cone on the 64-m antenna at Goldstone DSCC.

The sky temperatures shown in Table 2 were obtained by subtracting the receiver, feed horn, and waveguide component noise temperature contributions from the total system operating noise temperatures. The final configuration at 15.3 GHz was measured at 15-min intervals during a time period beginning July 1 and ending July 12, 1971. The waveguide switch was automated and data were

recorded on an almost continuous basis. Manual measurements interrupted the recording process on some occasions.

Roof-top air temperatures and humidity were recorded during the period of July 1 to 12. The absolute humidity varied from 7 gm/m^3 to 14 gm/m^3. The low and high temperatures recorded were 13.5 and 38°C, respectively. No attempt is made here to assign a particular noise contribution to the atmosphere at 15.3 GHz. Weather data were observed and recorded because the resulting changes in system noise temperature are a source of measurement error during component evaluation.

The receiver noise temperatures in Table 2 are the sum of calculated maser equivalent input noise temperatures (6.5 K at 8448 MHz; 8.6 K at 15.3 GHz) and the measured follow-up receiver contribution.

A comparative measurement using feed horns made of copper and of aluminum showed a 0.5 K higher noise contribution for the aluminum feed horn at 15.3 GHz. All feed horn values listed in Table 2 are estimates based on this measurement.

III. Measurement Technique and Accuracy

A large piece of microwave absorber was used as an ambient temperature termination for a feed horn. The system noise temperature data were obtained by covering the feed horn with the absorber and then removing the absorber, allowing the horn to "see" the cold sky; changes in total system noise power were recorded. A detailed description and analysis of noise temperature calibrations using ambient terminations have been published by C. T. Stelzried (Ref. 4).

Measurement errors introduced by mismatches (in the waveguide system) can be detected by using the microwave absorber as a sliding termination. A recording of total system power is made as the absorber is moved slowly away from the horn opening. At a distance of several signal frequency wavelengths the absorber still completely blocks the horn. Recorded power variations are due to mismatch and can be used to establish a limit on the mismatch error. The data recorded in Tables 1 and 2 contain no measurable error due to mismatch. The measurement system was able to resolve noise temperature variations of 0.05 K.

Waveguide component noise temperature contributions listed in Table 1 are accurate to ±0.2 K. Atmospheric changes during the time length required for the measurement, together with system resolution, determine the measurement accuracy. A ±0.05 K accuracy results from many rapid measurements of horn covering material.

The absolute accuracy of the total system noise temperature measurement is limited to ±1% by the precision attenuator used for power ratio measurements. The receiver and feed horn values shown in Table 2 are calculated values based on measurements which introduce an uncertainty of ±1 K. The sky, receiver, and feed horn values should be considered best estimates.

IV. Maser Gain and Phase Stability

A comparison of gain and phase stability recorded for the X-band maser and the 15.3-GHz maser is of particular interest. The X-band maser uses an external ambient-temperature 5000-G permanent magnet. The 15.3-GHz maser uses an internal 4.5 K 7500-G superconducting magnet. The difference in the stability of the two masers is a result of the different maser magnets used.

Use of the superconducting magnet has reduced, by more than half, gain and phase changes caused by relative motion between the maser and the magnet. Signal frequency phase changes caused by changing the alignment of the maser magnet with respect to the Earth's magnetic field (during antenna motion) have been reduced below the level of detection.

A Hewlett-Packard network analyzer has been used on the 64-m antenna to compare the phase of a signal passing through a reference path to the phase of a portion of the same signal amplified by the maser. Figure 1 shows the signal phase change which occurred in the X-band maser and in the 15.3 GHz maser measurement systems. The antenna was rotated 360 deg in azimuth with the elevation angle constant at 88 deg.

The X-band test began at an azimuth of 270 deg; the antenna rotation rate was 0.25 deg/s in the direction of decreasing azimuth. The 28-deg phase change (Fig. 1) is caused by a 0.9-G change within the permanent magnet air-gap. This magnetic field change occurs because the horizontal component of the Earth's magnetic field (0.25 G) alternately aids or opposes the permanent magnet during antenna rotation. The 1.8-to-1 ratio of field in the gap versus external field change is caused by the configuration of high and low permeability materials used in the permanent magnet. Antenna motion in both azi-

muth and elevation can cause phase changes of up to 45 deg in a maser with a permanent magnet.

The 15.3-GHz test began at an azimuth of 170 deg; rotation was in the direction of decreasing azimuth. Figure 1 shows a peak-to-peak phase change of 0.7 deg. Changes in antenna elevation (from zenith to the horizon) caused a maximum phase change of 2.2 deg through the 15.3-GHz maser.

Changes in maser gain with antenna motion are shown in Fig. 2. The two masers were switched to reference terminations; changes in system noise temperature due to antenna motion near the horizon did not affect the recorded data. The maximum gain change observed for the 15.3-GHz maser was 0.25 dB.

V. Conclusion

Construction and evaluation techniques previously used at X-band have been used to build and test a very low noise 15.3-GHz maser receiving system. A comparison of the new maser with a previously installed X-band maser (on the 64-m antenna) shows a large improvement in gain and phase stability. The improvement in maser stability is the direct result of the use of a superconducting magnet.

References

1. Clauss, R., and Quinn, R., "Tracking and Data Acquisition Elements Research: Low Noise Receivers: Microwave Maser Development," in *The Deep Space Network Progress Report*, TR 32-1526, Vol. V, pp. 102–108, Jet Propulsion Laboratory, Pasadena, Calif., Oct. 15, 1971.
2. Berwin, R., Wiebe, E., and Dachel, P., "Superconducting Magnet for a Ku-Band Maser," in *The Deep Space Network Progress Report*, TR 32-1526, Vol. V, pp. 109–114, Jet Propulsion Laboratory, Pasadena, Calif., Oct. 15, 1971.
3. Clauss, R. C., Reilly, H. F., and Reid, M. S., "Low Noise Receivers: Microwave Maser Development," in *The Deep Space Network Progress Report*, Space Programs Summary 32-62, Vol. II, pp. 74–78, Jet Propulsion Laboratory, Pasadena, Calif., March 1970.
4. Stelzried, C. T., "Operating Noise-Temperature Calibrations of Low-Noise Receiving Systems," *Microwave Journal*, Vol. 14, No. 6, June 1971, pp. 41–48.

Table 1. Component noise temperature contributions

Component	Noise temperature contribution, K	
	8448 MHz	15.3 GHz
Horn cover, 0.0025-cm thick Kapton	—	0.15
Horn cover, 0.008-cm thick Kapton	—	0.3
Horn cover, 0.013-cm thick Kapton	0.2	—
Horn cover, 0.008-cm thick Mylar	0.2	—
Waveguide rotary joint, TE_{11}	—	0.6[3]
Waveguide vacuum window	—	0.7
Linear to CP polarizer	0.9[2]	1.3[3]
Straight waveguide, 10-cm long	0.6[1]	1.4[1]
Waveguide switch, straight through	1.3[2]	1.3[3]
Waveguide switch, side arm and 90 deg bend	2.0[4]	3.2[5]
Directional coupler, 30 dB	—	2.0[3]

[1]Calculated value based on insertion loss of copper waveguide is shown for comparison.
[2]Material, aluminum.
[3]Material, copper.
[4]Switch material, aluminum; bend material, copper.
[5]Switch material, copper; bend material, silver.

Table 2. System operating noise temperature contributions

System or part of system	Noise temperature, K		
	8448 MHz	15.3 GHz	
	Minimum configuration	Minimum configuration	Final configuration[a]
Total system operating noise temperature, T_{op}			
Minimum	—	—	21.5
Maximum	—	—	26.0
Nominal	13.1	18.5	23.0
Sky (includes atmosphere and background)			
Minimum	—	—	6.4
Maximum	—	—	10.9
Nominal	4.3	8.1	7.9
Receiver (maser + follow-up contribution)	7.2	8.7	8.7
Feed horn	1.6	1.7	1.7
Waveguide components (switch, coupler, polarizer and horn cover)	—	—	4.7

[a]Waveguide system identical to cone configuration installed on 64-m antenna.

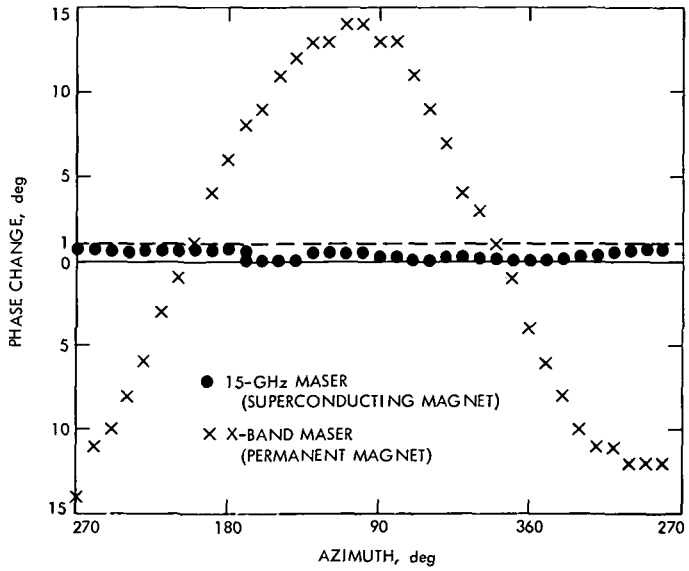

Fig. 1. Maser phase stability, antenna moving in azimuth

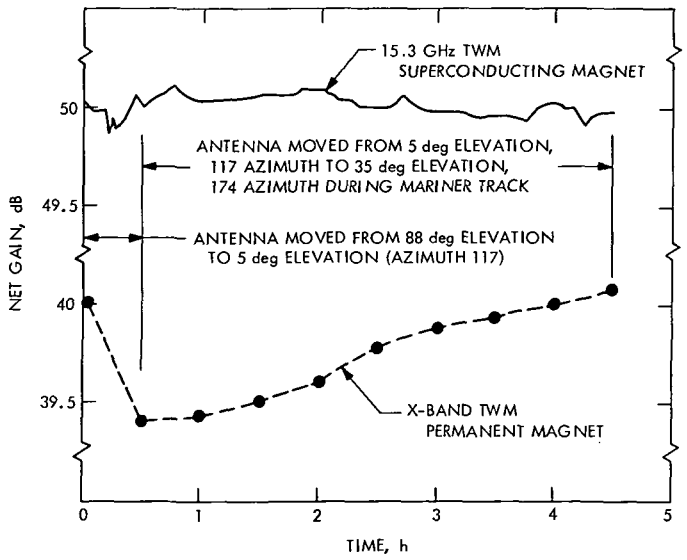

Fig. 2. Maser gain stability, antenna moving in elevation and azimuth

Waveguide Voltage Reflection Calibrations of the MXK Cone (Modification 1)

P. D. Batelaan
Communications Elements Research Section

A listing of reflection coefficients for the multiple-frequency X- and K-band (MXK) cone (Mod. 1), at both X- and K-band frequencies, is presented. Included is a short discussion of the measurement technique and results.

I. Introduction

This article presents a summary of reflection coefficient measurements made on the MXK cone waveguide system during the final assembly stages of the updated cone. These measurements were made on the ground at JPL and the Goldstone DSCC. Both the X-band (8.5 GHz) and K-band (15.3 GHz) systems were tested. Adequate calibration, checkout and long-term monitoring of the cone performance require accurate knowledge of the initial radio-frequency match at selected points in the waveguide system. The block diagrams of the MXK Mod. 1 cone system for both frequency systems are identical.[1]

II. Results

One criterion for RF matching is the transfer of maximum energy into the traveling wave maser (TWM). With this in mind, all the measurements listed here were made at port ⚠ (Fig. 4 of Reid's article) in both frequency systems. With one exception, all match measurements were made with a high-precision tuned reflectometer. The exception is that the ambient termination for the K-band system was tuned and measured in a broad-band mode over the frequency range of 15.0 to 15.5 GHz. This is because this termination will be used at a number of frequencies in this band, and therefore narrow-band tuning of the termination will not suffice. Similar reasoning applies to the ambient termination for the X-band system. However, this system was measured at the Goldstone DSCC, and swept frequency techniques were not available; therefore, it was only measured at a single frequency *in situ*. Manufacturers' data on this X-band termination *at its flange* is included.

Tables 1 and 2 show voltage reflection coefficients at K-band and X-band, respectively.

[1]Refer to Fig. 4 of "Improved RF Calibration Techniques: System Operating Noise Temperature Calibrations" by M. S. Reid in this issue.

Table 1. Voltage reflection coefficients MXK cone (K-band system)

Item measured	15.3 GHz
TWM	0.126
Main feed horn	0.016
Reference feed horn	0.038
Ambient load (swept-over frequency 15.0 to 15.5 GHz)	0.018 to 0.013

Table 2. Voltage reflection coefficients MXK cone (X-band system)

Item measured	7850 MHz	8427 MHz	8448 MHz
TWM	0.260	0.186	
Main horn			
RCP	0.062	0.059	
LCP	0.060	0.065	
LP	0.079	0.086	
Ambient load	0.007	0.012	
(Manufacturers' data at load flange)	0.006	0.012	0.010

Further Studies of Microwave Transmission Through Perforated Flat Plates

T. Y. Otoshi and K. Woo
Communications Elements Research Section

This article presents approximate formulas useful for predicting transmission loss characteristics of a circular hole array in a metallic flat plate having finite thickness. The formulas apply to perpendicular and parallel polarizations of an obliquely incident plane wave. The approximate formulas are experimentally verified by free space measurements made on a sample of the mesh material used on the 64-m antenna at DSS 14.

I. Introduction

Metallic plates having small round perforations are useful as reflective surface materials for spacecraft and ground antennas. Previous analytical work on mesh materials fabricated from flat aluminum plates having small round perforations has been reported in Ref. 1. The approximate formula given in Ref. 1 is useful for predicting transmission through a perforated plate of finite thickness when the incident plane wave is perpendicularly polarized (E-field is perpendicular to the plane of incidence).

To the authors' knowledge, there does not appear to be published information (theoretical or experimental) concerning the parallel polarization case behavior of perforated plates that are useful as reflector surface materials. To enable prediction of loss for the parallel polarization case, an approximate formula is presented in this article. Numerical values of transmission loss calculated from approximate formulas are compared to experimental values and also to numerical values obtained from more exact analytical methods.

II. Approximate Transmission Loss Formulas

For circular hole arrays having the geometry of Fig. 1 and an incident plane wave with the E-field polarized normal to the plane of the incidence (Fig. 2), the approximate expression for transmission loss is derived in Ref. 1 as

$$(T_{dB})_{\perp} = 10 \log_{10}\left[1 + \left(\frac{3ab\lambda_0}{2\pi d^3 \cos\theta_i}\right)^2\right] + \frac{32t}{d} \qquad (1)$$

where $a, b, d << \lambda_0$. The parameters a and b are the spacings between holes as shown in Fig. 1, d is the hole diameter, λ_0 is the free space wavelength, t is the plate thickness, and θ_i is the incidence angle.

Analysis of Eq. (1) will reveal that the perpendicular polarization transmission loss behavior of a circular hole

array as a function of incidence angle is very similar to that of a two-dimensional thin conducting sheet in free space. Assuming that the circular hole array behaves in the same way as a thin conducting sheet for the parallel polarization case, then

$$(T_{dB})_{//} = 10 \log_{10}\left[1 + \left(\frac{3ab\lambda_0 \cos\theta_i}{2\pi d^3}\right)^2\right] + \frac{32t}{d} \qquad (2)$$

where $a, b, d << \lambda_0$.

When incidence angles are small and when

$$\frac{3ab\lambda_0}{2\pi d^3} >> 1$$

then Eqs. (1) and (2) simplify even further to

$$(T_{dB})_{\perp} \approx 20 \log_{10}\left(\frac{3ab\lambda_0}{2\pi d^3}\right) + \frac{32t}{d} + 20 \log_{10}\left(\frac{1}{\cos\theta_i}\right) \qquad (3)$$

$$(T_{dB})_{//} \approx 20 \log_{10}\left(\frac{3ab\lambda_0}{2\pi d^3}\right) + \frac{32t}{d} - 20 \log_{10}\left(\frac{1}{\cos\theta_i}\right) \qquad (4)$$

It can be seen from Eqs. (3) and (4) that the transmission losses of the two polarization cases at an incidence angle of 30 deg will differ by about 2.5 dB. It should be emphasized that the formulas given by Eqs. (1)–(4) are only approximate and apply only for $a, b, d << \lambda_0$. When the hole diameter d becomes comparable to free space wavelength, then the corrections given in Ref. 2 should be applied.

III. Experimental Verification

For experimental verification of Eqs. (1) and (2), tests were conducted on a perforated plate sample having the same mechanical and electrical properties as the mesh used as the reflector surface on the outer 47% radius of the 64-m antenna at DSS 14. This mesh is characterized by a 60-deg hole pattern (Fig. 1):

$a =$ 6.35 mm (¼ in.)

$d =$ 4.76 mm (3⁄16 in.)

$t =$ 2.29 mm (0.090 in.)

Previous transmission loss tests on this mesh material were made by a TE_{10} waveguide method (Ref. 3). The TE_{10} waveguide method simulates the free space situation of an obliquely incident plane wave impinging upon an infinitely large sample of the mesh (see Fig. 2). However, simulation of free space measurements by the waveguide method is restricted to perpendicular polarization (E-field is normal to plane of incidence) and an incidence angle which is governed by the operating test frequency and the waveguide cutoff frequency.

Actual free space measurements are required to obtain experimental data for the parallel polarization case. The free space test setup that was employed may be seen in Fig. 3. The disadvantages of a free space setup are diffraction and multipath effects, and also the need for a large test sample. It is difficult to keep a large test sample mechanically flat over its entire surface. Multipath effects were reduced to about ±0.1 dB by careful placement of absorbers (see Fig. 3) and by averaging the readings obtained when the receiving horn was moved along a rail.

The free space transmission measurements were made on the 64-m antenna mesh test sample with the hole patterns oriented so that the incidence plane was located at $\phi = 0$ deg (see Fig. 2). Experimental and theoretical values are shown in Fig. 4. Experimental values at 8.448 GHz were obtained through the use of a Hewlett-Packard 8410A Network Analyzer and Recorder System. The accuracy of the experimental values are estimated to be ±0.5 dB. It can be seen that reasonably good agreement was obtained between experimental values and approximate theoretical values from Eqs. (1) and (2). Most of the disagreement between theory and experiment is attributed to rounded edges of the holes in the test sample formed during the hole punching process.

For additional verification, numerical values obtained by a more accurate theoretical method utilized by C. C. Chen (personal communication) are presented in Fig. 4. It can be seen that for the perpendicular polarization case, the numerical values calculated from approximate formulas and the computer solution values obtained from Chen are in excellent agreement (within 0.1 dB) for incidence angles up to 80 deg. For the parallel polarization case, the theoretical values deviate by about 1 to 2 dB at incidence angles larger than 40 deg. Chen's computer results also verified that the perpendicular and parallel polarization transmission losses for the 64-m antenna mesh material are independent of incidence plane angle ϕ (see Fig. 2) when the operating frequency is far below the cutoff frequency of the circular aperture.

Chen formulated the boundary value problem for the perforated plate in terms of Floquet and orthonormal mode functions and then numerically solved the problem by use of the method of moments and a digital computer (Ref. 4). Because Chen solves the perforated plate problem by rigorous analytical methods, his analyses apply to a large class of perforated plate problems and are not restricted to operating frequencies far below the cutoff frequency of the circular apertures. However, solution of Chen's equations requires the use of a computer program that has not been made available for general use. The approximate formulas presented in this article are amenable to desk calculator computations, and for highly reflective meshes the formulas are believed to be sufficiently accurate for obtaining numerical estimates of transmission loss.

IV. Conclusions

Good agreement was obtained between experimental and calculated values for transmission losses of the perforated plate used as the reflective surface material on the 64-m antenna. It appears that for highly reflective metallic perforated plates with transmission losses greater than 20 dB, the transmission losses for perpendicular and parallel polarizations can be predicted by approximate formulas to accuracies of about 0.2 dB and 2 dB, respectively, when the angles of incidence are less than 80 deg.

References

1. Otoshi, T. Y., "A Study of Microwave Transmission through Perforated Flat Plates," in *The Deep Space Network Progress Report*, Technical Report 32-1526, Vol. II, pp. 80–85. Jet Propulsion Laboratory, Pasadena, Calif., Apr. 15, 1971.
2. Culshaw, W., "Reflectors for a Microwave Fabry-Perot Interferometer," *IEEE Trans. Microwave Theory and Techniques*, Vol. MTT-7, p. 226, Apr. 1959.
3. Otoshi, T. Y., and Lyon, R. B., "Improved RF Calibration Techniques: A Study of the RF Properties of the 210-ft-diam Antenna Mesh Material," in *The Deep Space Network*, Space Programs Summary 37-66, Vol. II, pp. 52–57. Jet Propulsion Laboratory, Pasadena, Calif., Nov. 30, 1970.
4. Chen, C. C., "Diffraction of Electromagnetic Waves by Conducting Screen Perforated Periodically with Circular Holes," *IEEE Trans. MTT*, Vol. 19, No. 5, pp. 475–481, May 1971.

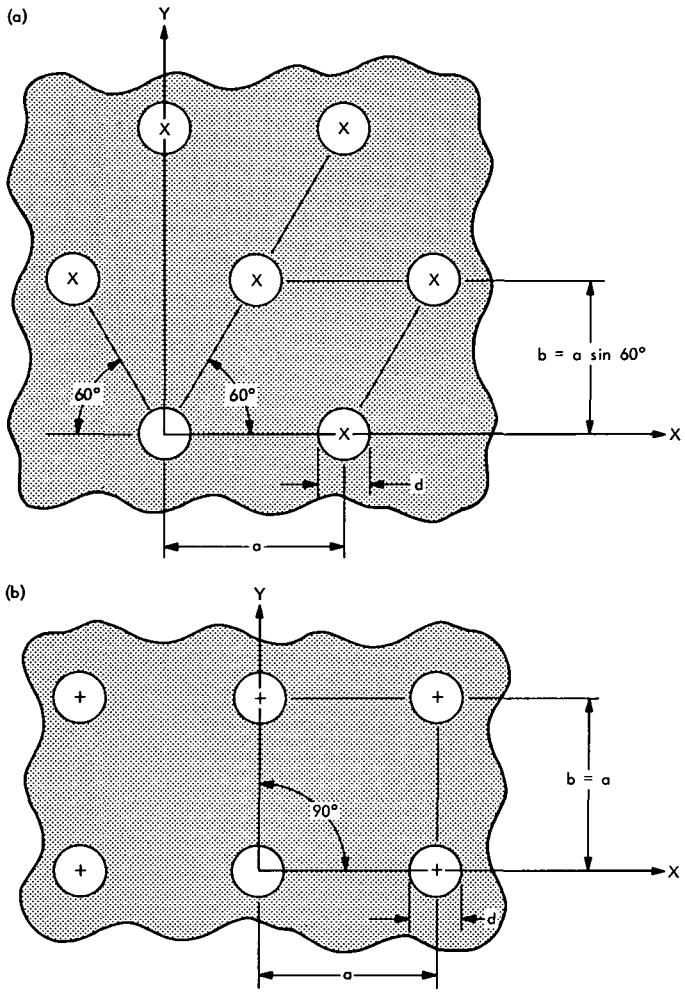

Fig. 1. Geometry for two-dimensional array of holes in a metallic flat plate having (a) 60-deg (staggered) and (b) 90-deg (square) hole pattern configurations

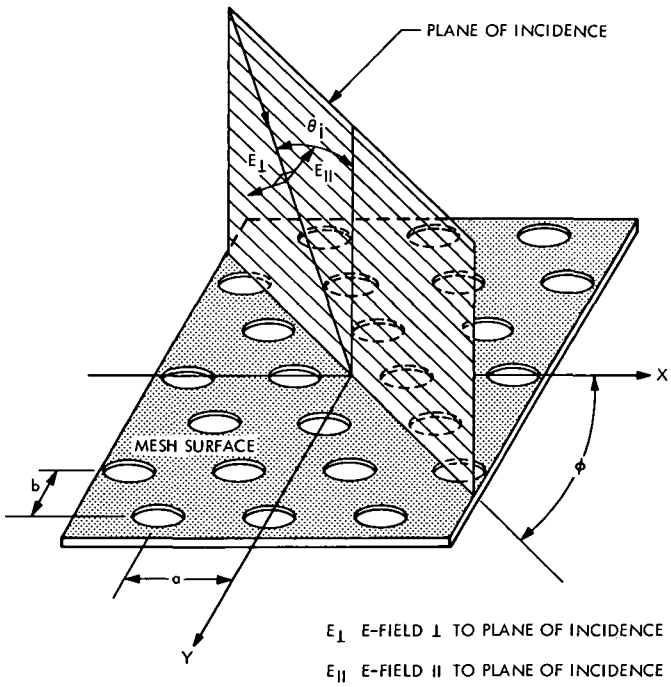

Fig. 2. Geometry of perpendicular and parallel polarizations of a plane wave incident on a perforated plate mesh sample

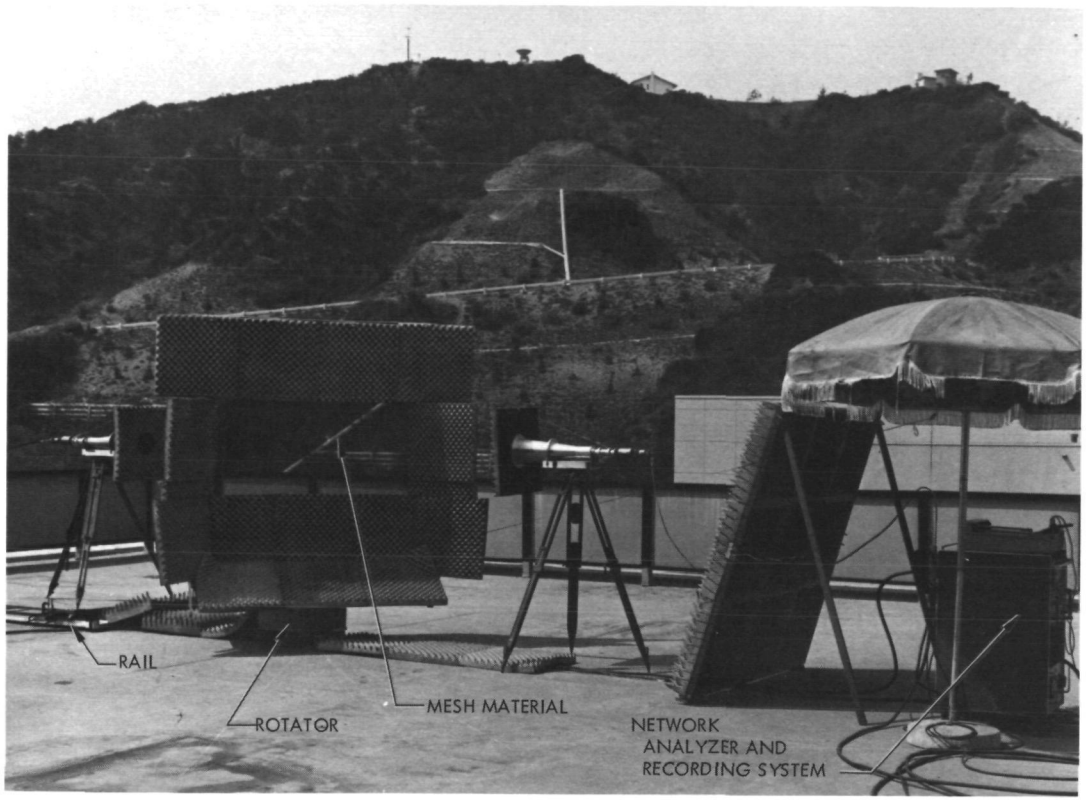

Fig. 3. Free space test setup for transmission loss measurements at 45-deg incidence angle

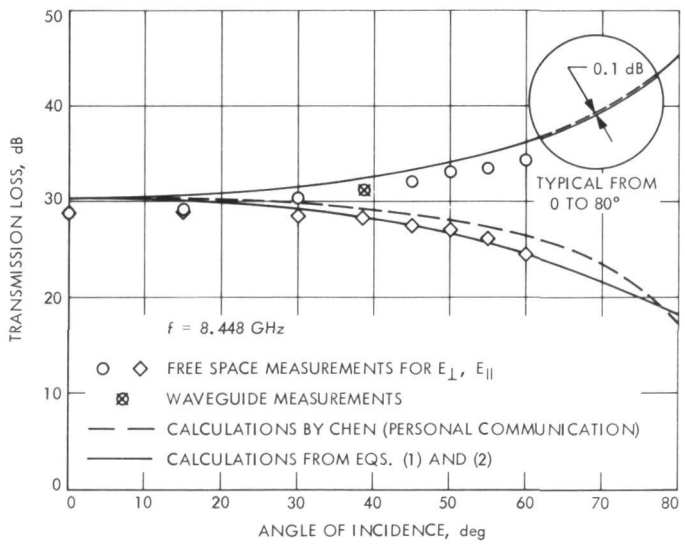

Fig. 4. Transmission losses of flat aluminum plate having same physical properties as mesh on 64-m antenna

Improved RF Calibration Techniques: System Operating Noise Temperature Calibrations

M. S. Reid
Communications Elements Research Section

The system operating noise temperatures of the S-band research operational cone at the Venus Deep Space Station and the polarization diversity S-band cone at the Mars Deep Space Station are reported for the period June 1, 1971 through September 30, 1971. In addition, the performance of the multi-frequency X- and K-band cone on the ground at the Venus Deep Space Station is reported for X-band operation, as well as for X-band operation on the 64-m antenna at DSS 14, for the same period.

This article presents system operating noise temperature calibrations of the K-band system in the following configurations: before installation in the MXK cone (approximately 23 K), installed in the cone, with the cone on the ground (approximately 25 K), and with the cone installed on the 64-m antenna at the Mars Deep Space Station (approximately 29 K).

The system operating noise temperature performance of the low noise research cones at the Goldstone Deep Space Communications Complex is reported for the period June 1, 1971 (day 151) through September 30, 1971 (day 273). Most of the operating noise temperature calibrations were performed with the ambient termination technique (Ref. 1). The cones on which this technique[1] was used during this reporting period are:

(1) S-band research operational (SRO) cone at DSS 13.

(2) Polarization diversity S-band (PDS) cone at DSS 14.

(3) Multi-frequency X- and K-band (MXK) cone at DSS 14 and DSS 13.

[1]Most of the measurements were taken by DSS 13 (Venus) and DSS 14 (Mars) personnel.

The averaged operating noise temperature calibrations for the SRO cone at DSS 13 and the PDS cone at DSS 14, and other calibration data, are presented in Table 1. Table 2 presents similar data for the MXK cone on the ground at DSS 13 and on the 64-m antenna at DSS 14. The calibration data were reduced with JPL computer program number 5841000, CTS20B. Measurement errors of each data point average are recorded under the appropriate number in the tables. The indicated errors are the standard deviation of the individual measurements and of

the means, respectively. They do not include instrumentation systematic errors. The averages were computed using only data with:

(1) Antenna at zenith.

(2) Clear weather.

(3) No RF spur in the passband.

(4) Standard deviation of computed operating noise temperature due to measurement dispersion less than 0.15 K.

Table 1 shows that one data set was made at DSS 13 at the ALSEP frequency (2278.5 MHz) with the maser connected to a gain standard horn looking through a section of the 26-m antenna surface opened for this purpose. The antenna was at zenith and the system operating noise temperature in this configuration was 26.3 K.

Figures 1 and 2 are plots of the system operating noise temperatures of the SRO cone as a function of time in day numbers, at 2388 and 2278.5 MHz, respectively. Figure 3 is a similar plot with the maser connected to the gain standard horn at 2278.5 MHz. In all the figures in this report, data that satisfy the four conditions stated above are plotted as solid circles while data that fail one or more conditions are plotted as open circles.

The MXK cone was removed from the 64-m antenna at DSS 14 and taken to DSS 13 on June 28, 1971. The X-band system was reworked and the K-band system installed. This work was performed at DSS 13.[1] The cone was reinstalled on the 64-m antenna on August 5, 1971. Figure 4 shows a simplified block diagram of the MXK cone (modification 1) after installation of the K-band system. The block diagram is the same for both the X- and K-band systems. Table 2 shows X-band calibration data for the MXK cone both on the ground at DSS 13 and mounted on the 64-m antenna as modification 1. The first column presents data taken at DSS 13 with the cone on the ground just prior to the rework and K-band installation. In this condition only one horn was available and a set of 70 measurements was made over a 37-hour period at 8427.2 MHz. Figure 5 shows a graph of the system operating noise temperature as a function of time plotted as day number. Midday, local time, occurs at about day 188.8.

All the other columns in Table 2 present X-band data after the cone rework (mod. 1). Two calibration techniques were used for these measurements. One was the ambient load technique referred to above, and the other was a similar technique which used an absorbing aperture load. The measurement method used for each set of data is indicated in Table 2.

Figure 6 is a graphical presentation of the data set in the second column of Table 2. This is the system operating noise temperature of the MXK cone (mod. 1) on the ground at DSS 13 with the maser connected to the reference horn at 8427.2 MHz plotted as a function of time in day numbers. Figures 7 through 10 show similar plots for: main horn, aperture load, 8427.2 MHz, cone on the ground; main horn, ambient load, 8427.2 MHz, cone on the ground; main horn, ambient load, 8415 MHz, cone on the ground; and main horn, ambient load, 8415 MHz, cone on the 64-m antenna, antenna at zenith, respectively.

Figure 11 shows the profile with elevation angle of the X-band system, MXK cone on the 64-m antenna at 8415 MHz. System temperature in Kelvins is plotted as a function of antenna angle with the subreflector correctly focused on the X-band main horn. This is the solid curve. The circled points are data obtained with the subreflector focused on the PDS cone. Each profile is the average of four data sets taken in August and September 1971. It must be noted that the difference in system temperature at zenith with the subreflector correctly and incorrectly positioned is about 6.25 K. This may be explained by the diagram of Fig. 12, where the solid ray paths show the geometry configuration with the subreflector focussed on the X-band main horn. The dotted lines trace the ray paths when the subreflector is focussed on the PDS cone. In this configuration some ground radiation is received by the X-band system.

System operating noise temperature calibrations of the K-band system were made before and after installation in the MXK cone. Before installation in the cone the system was measured at JPL, on the roof of building 238. K-band data with the cone on the ground were taken at DSS 13, and the antenna measurements were made with the cone mounted on the 64-m antenna at DSS 14. All calibrations were made at zenith at 15.3 GHz.

Table 3 presents averaged operating noise temperature calibrations in the various configurations. The calibration data were reduced with JPL computer program 5841000, CTS20B. Whenever possible measurement errors of each data point average are recorded under the appropriate number in the table. The indicated errors are the standard deviation of the individual measurements and of the

[1]See "Waveguide Voltage Reflection Calibrations of the MXK Cone (Modification 1)" by P. D. Batelaan and "Microwave Maser Development," by R. Clauss and H. Reilly in this issue.

means, respectively. They do not include instrumentation systematic errors. The averages were computed using only data that satisfied the four conditions referred to above.

The first two columns of data in the table were taken on the roof of building 238 at JPL before the K-band system was installed in the cone. For these measurements the maser, waveguide and switch were in the same configuration that they have in the cone. Two measurement techniques were used, as shown in the table. One technique used a waveguide ambient load[2] and the other an absorbing aperture load. The average system temperature as measured by these techniques differed by 2.2 K, as shown in the table. This difference is probably due to the different pump frequency matches presented to the maser by the two techniques, and might be solved by incorporat ing a suitable filter in the maser input line.

Each of the above two measurement sets included a 24-hour run where data were taken every 30 min. Figure 13 is a plot of the aperture load data. System operating noise temperature is plotted as a function of time in day number (GMT) so that local mid-day occurs at about 0.8 day. The figure shows that the system temperature is lowest during the night and lies between 21 and 22 K for several hours. Highest temperatures, about 25.5 K, are recorded around mid-day with a gradual cooling in the afternoon. The weather was clear and dry during this measurement set. The data set using the ambient load technique showed similar characteristics.

The measurements made on the ground at DSS 13 show that the system temperature increased by 1.3 K (ambient load technique) and by 1.9 K (aperture load) when the system was built into the cone.

The system temperature was 29.1 K with the maser connected to the reference horn using the ambient load technique.

Measurements made with the cone mounted on the 64-m antenna show that the system temperature increased a further 2.4 K by the ambient load technique.

[2]Batelaan, P., "Waveguide Voltage Reflection Calibrations of the MXK Cone (Modification 1)" in this issue.

Reference

1. Stelzried, C. T., "Operating Noise-Temperature Calibrations of Low-Noise Receiving Systems", *Microwave J.*, Vol. 14, No. 6, pp. 41–48, June 1971.

Table 1. Averaged operating noise temperature calibrations for the SRO and PDS cones at GDSCC

Station	DSS 13				DSS 14	
Cone	SRO				PDS	
Configuration	Cone on antenna			Gain standard horn	Low-noise path	Diplexed
Frequency, MHz	2388	2295	2278.5	2278.5	2298	2292
Maser serial number	96S2	96S2	96S2	96S2	96S3	96S3
Maser temperature, K	5.2	5.2	5.2	5.2	4	4
Maser gain, dB	36.7 ±1.31/0.15 74 Measurements	51.4 ±0.28/0.20 2 Measurements	45.9 ±2.70/0.39 49 Measurements	45.6 ±4.13/1.03 16 Measurements	53.0 ±0.21/0.15 2 Measurements	52.5 ±0.21/0.15 2 Measurements
Follow-up noise temperature contribution, K	0.54 ±0.06/0.01 60 Measurements	0.08 1 Measurement	0.28 ±0.13/0.02 40 Measurements	0.27 ±0.09/0.03 12 Measurements	0.02 ±0.001/0.0008 2 Measurements	0.03 ±0.0009/0.0006 2 Measurements
System operating noise temperature, K	16.9 ±0.40/0.05 60 Measurements	16.3 ±0.20 1 Measurement	18.4 ±0.89/0.14 40 Measurements	26.3 ±0.46/0.13 12 Measurements	20.2 ±0.26/0.19 2 Measurements	24.3 ±0.11/0.08 2 Measurements

Table 2. Average operating noise temperature calibrations for the MXK cone on the ground at DSS 13 and on the 64-m antenna at DSS 14

Station	DSS 13								DSS 14	
Configuration	Cone on ground								Cone on antenna	
									Main horn	
	Mod 0	Reference horn	Main horn	Main horn	Main horn	Main horn	Reference horn	Reference horn	Subreflector on main horn	Subreflector on PDS cone
Frequency	8427.2	8427.2	8427.2	8427.2	8415	8415	8415	8415	8415	8415
Measurement method	Ambient load	Ambient load	Aperture load	Ambient load	Ambient load	Aperture load	Ambient load	Aperture load	Ambient load	Ambient load
Maser temperature, K	7	7	7	7	7	7	7	7	7	7
Maser gain, dB	35.2 ±1.5/0.50 70 Measurements	33.0 ±0.40 1 Measurement	No measurement	33.0 ±0.17 1 Measurement	No measurement	–	–	–	–	–
Follow-up receiver contribution, K	0.28 ±0.04/0.004 70 Measurements	0.33 ±0.18/0.07 7 measurements	0.44 ±0.13/0.05 6 Measurements	0.38 ±0.20/0.04 29 Measurements	0.33 ±0.12/0.03 18 Measurements	0.36 ±0.12/0.06 4 Measurements	0.42 ±0.10/0.03 9 Measurements	0.32 ±0.12/0.07 4 Measurements	0.79 ±0.12/0.04 10 Measurements	0.82 ±0.04/0.02 6 Measurements
System operating noise temperature, K	17.0 ±0.61/0.07 70 Measurements	21.0 ±0.13/0.05 7 Measurements	19.0 ±0.47/0.19 6 Measurements	18.2 ±0.56/0.10 29 Measurements	18.1 ±0.26/0.06 18 Measurements	18.8 ±0.32/0.16 4 Measurements	20.2 ±0.18/0.06 9 Measurements	20.0 ±0.33/0.19 4 Measurements	24.0 ±0.24/0.08 10 Measurements	30.5 ±0.41/0.17 6 Measurements

Table 3. System operating noise temperature calibrations of the K-band system in various configurations

Configuration	Before cone installation		Cone on ground			Cone mounted on 64-m antenna
Location	JPL	JPL	DSS-13			DSS-14
Measurement technique	Ambient load	Aperture load	Ambient load	Aperture load	Ambient load	Ambient load
Horn	*Main*	*Main*	*Main*	*Main*	*Reference*	*Main*
Follow-up receiver contribution, K	0.15 ±0.09/0.01 56 Measurements	0.14 ±0.08/0.01 56 Measurements	0.16 ±0.09/0.02 17 Measurements	0.13 ±0.07/0.02 11 Measurements	0.62 1 Measurement	0.17 1 Measurement
System operating noise temperature	24.8 ±0.79/0.11 56 Measurements	22.6 ±1.07/0.14 56 Measurements	26.1 ±0.55/0.13 17 Measurements	24.5 ±0.37/0.10 11 Measurements	29.1 1 Measurement	28.5 ±0.29 2 Measurements

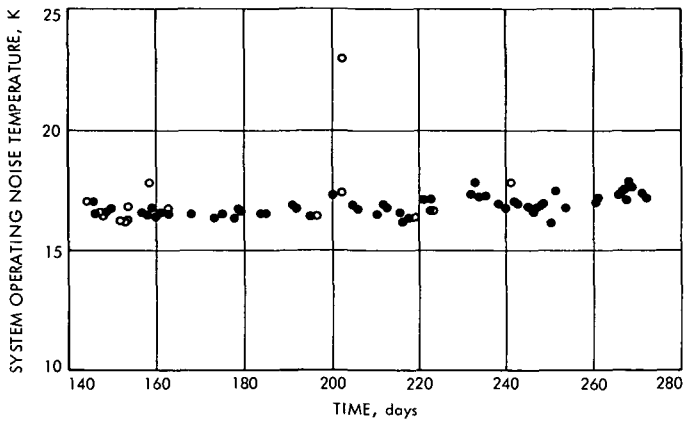

Fig. 1. System operating noise temperatures of the SRO cone at 2388 MHz

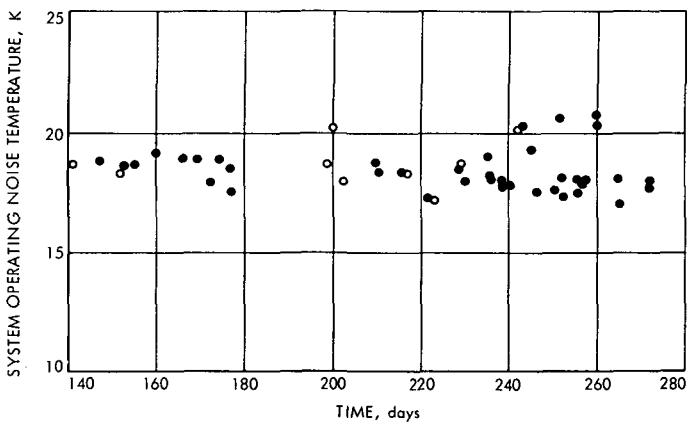

Fig. 2. System operating noise temperatures of the SRO cone at 2378.5 MHz

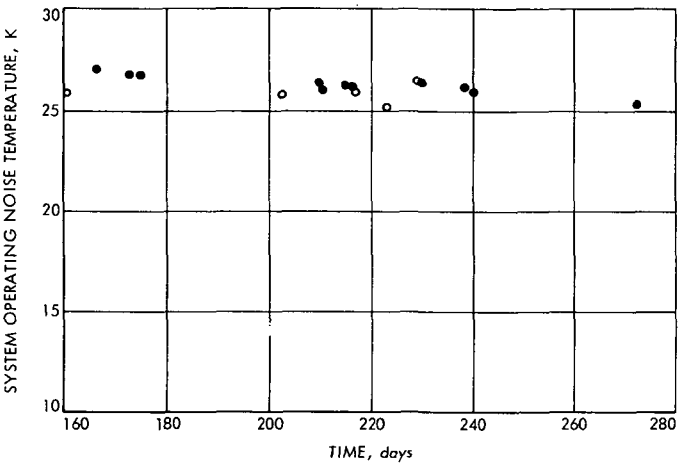

Fig. 3. System operating noise temperatures with the maser connected to the gain standard horn at 2378.5 MHz

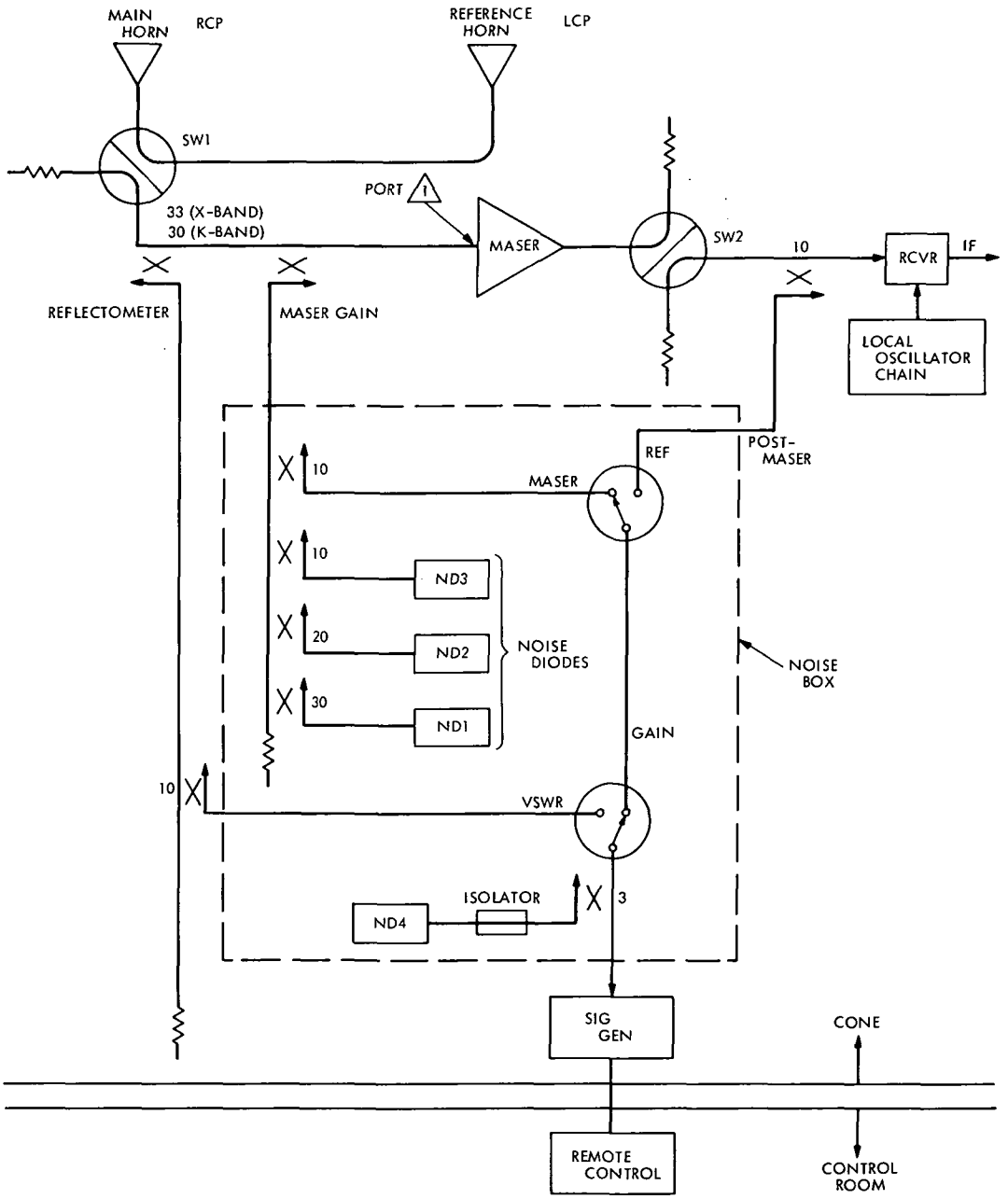

Fig. 4. Simplified block diagram of the X-band and K-band systems in the MXK cone

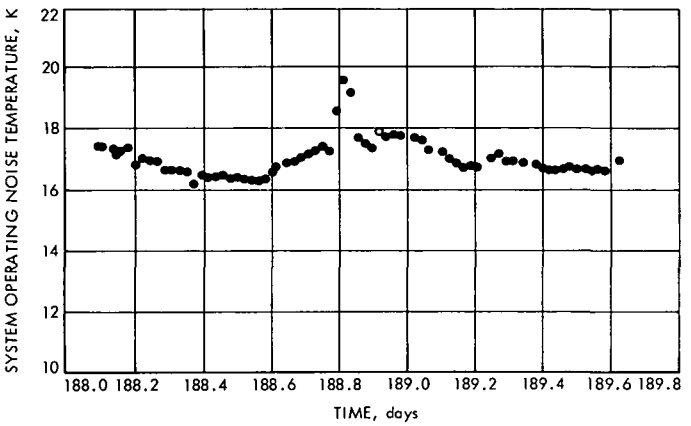

Fig. 5. System operating noise temperatures of the MXK cone (Mod. 0) on the ground at DSS 13 at 8427.2 MHz; ambient load technique

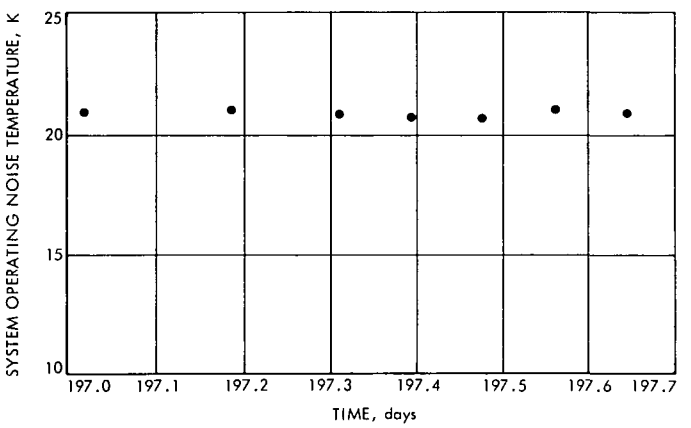

Fig. 6. System operating noise temperatures of the MXK cone (Mod. 1) on the ground at DSS 13 at 8427.2 MHz; reference horn; ambient load technique

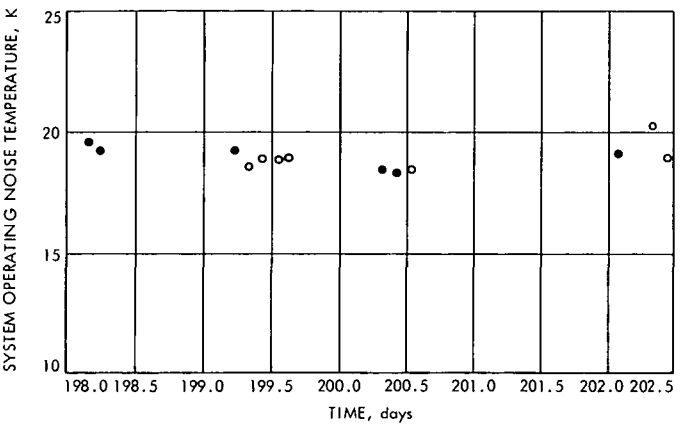

Fig. 7. System operating noise temperatures of the MXK cone (Mod. 1) on the ground at DSS 13 at 8427.2 MHz; main horn; aperture load technique

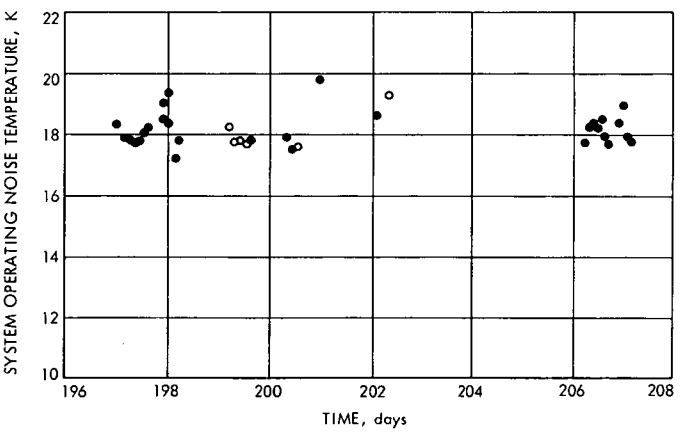

Fig. 8. System operating noise temperatures of the MXK cone (Mod. 1) on the ground at DSS 13 at 8427.2 MHz; main horn; ambient load technique

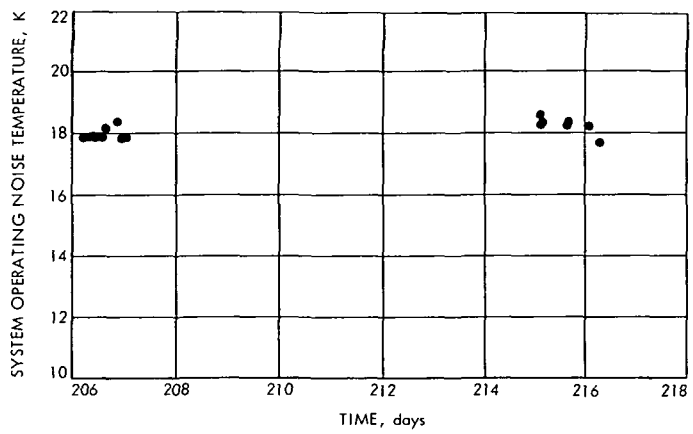

Fig. 9. System operating noise temperatures of the MXK cone (Mod. 1) on the ground at DSS 13 at 8415 MHz; main horn; ambient load technique

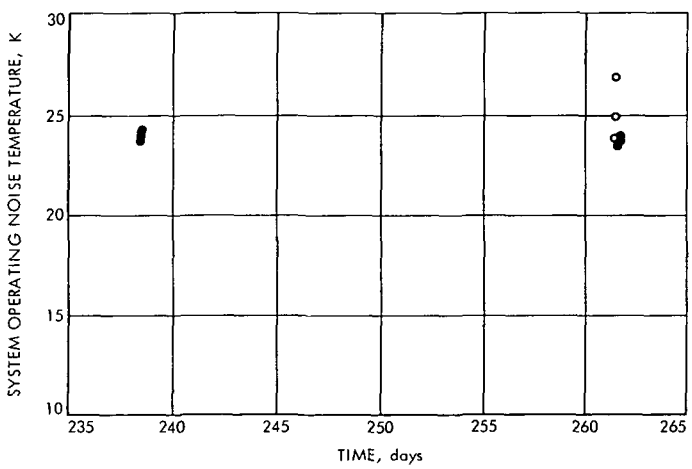

Fig. 10. System operating noise temperatures of the MXK cone (Mod. 1) on the 64 m antenna at DSS 14 at 8415 MHz; main horn; ambient load technique

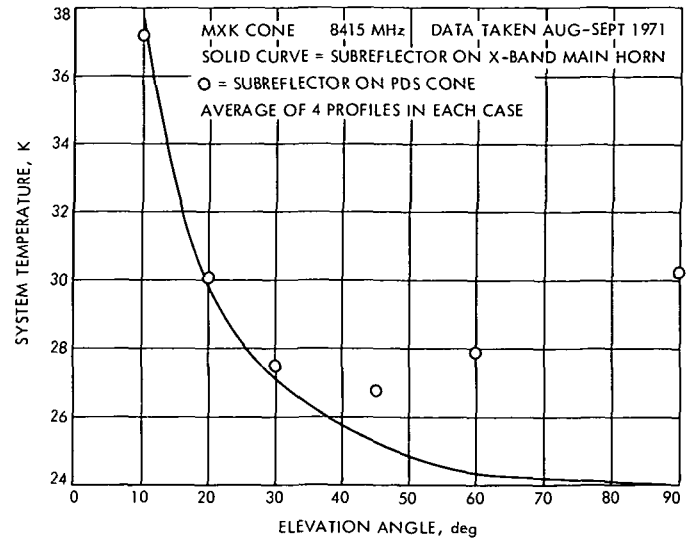

Fig. 11. System temperature profile with antenna elevation angle of the MXK cone (Mod. 1) at 8415 MHz

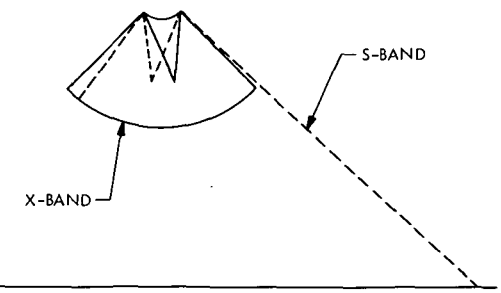

Fig. 12. X-band ray path geometry for the MXK cone with the subreflector focused for X-band and for S-band

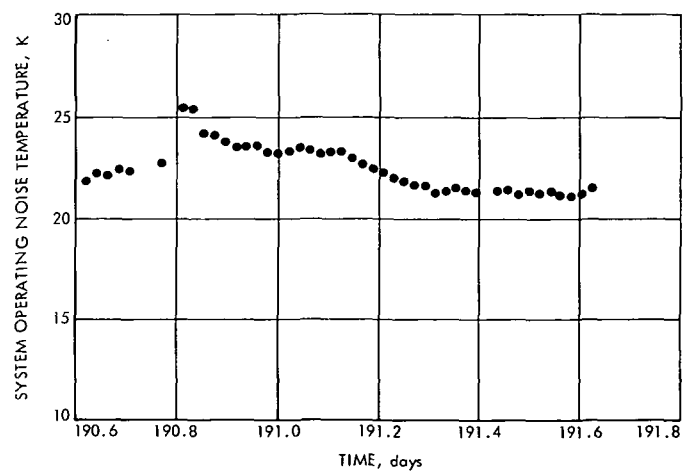

Fig. 13. System operating noise temperature calibrations of the K-band system as a function of time for a 24-hour run; aperture load technique; roof of building 238

S- and X-Band RF Feed System

M. Katow
DSIF Engineering Section

The S-X feed system proposed by the Communications Elements Research Section provides for simultaneous RF propagation from the 64-m antenna for both S- and X-band signals along the same boresight direction. This Section is charged with providing the hardware for the tri-cone system, which consists of an ellipsoid reflector over the S-band horn and a dichroic reflector plate over the X-band cone. The ellipsoid reflector focuses the S-band signal in front of the dichroic plate. The dichroic plate is capable of transmitting X-band signal through it and reflecting S-band. The dichroic plate, mounted in a position about 60 deg to the centerline of the X-band signal, then reflects the S-band signal coincident to the X-band signal. Preliminary hardware mounting schemes are outlined with probable operation requirements.

I. Introduction

To propagate S-band and X-band radio-frequency signals along the same boresight direction for the 64-m antenna, in a simultaneous propagation mode, two cone positions of the tri-cone system will be used. One position utilizes the S-band RF horn and the other, the X-band RF horn. As shown in Fig. 1, the X-band signals are transmitted with no change in their direction through the dichroic plate, which is placed over the X-band. An ellipsoid reflector placed over the S-band horn reflects and focuses the S-band signals in front of the dichroic plate equal distance to the X-band phase center below the plate. By positioning the angular position of the dichroic plate correctly, the S-band signals are reflected in line with the X-band signals.

The hardware mounting scheme must provide for use of the individual horns in a normal manner by retraction mechanisms. The added mechanisms should be easily mountable and replaceable and, of course, withstand the environmental loads without affecting the performance.

II. Feasibility Study Results

The present plan for manufacturing the ellipsoid will be similar to that used for the existing subreflector. The reflector will consist of a stretch pressed sheet of per-

forated aluminum backed by formed Z-section framework. This will be connected to a stiff circular ring so that concentrated loads from the few attachment points will be possible.

A mechanism using tube-type links and speed-regulated air hoists provides for retraction alongside the feed cone to a minimum blockage position. To aid operations, remote controls will be needed with positive locks in each position, which are now provided by the linkage system. Before the design is finalized, further checks for stiffness and strength to withstand the environmental loads will be needed.

The dichroic plate is now planned also to retract. This problem is more difficult, since the plate must be protected from moisture and dirt. In the operating position, a thin RF reflective plastic cover will be in position. Also, it is planned to keep a nitrogen gas environment around the dichroic plate with a very low pressure.

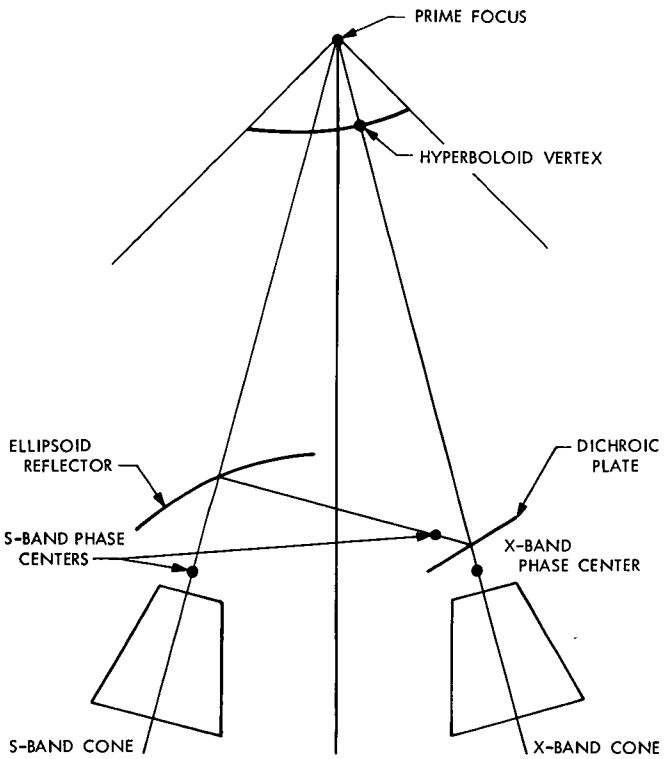

Fig. 1. S-X system on 64-m tri-cone antenna

Movement of the Antenna Instrument Tower at DSS 14

H. D. McGinness
DSIF Engineering Section

The motions of the top of the instrument tower and its surrounding windshield have been measured. A relationship between a static horizontal displacement and angular displacement of the tower have been established through the use of optical apparata. Displacements during excitation of the windshield have been determined by the use of accelerometers. The nature of the coupling between windshield and tower is discussed and the conclusion reached that the coupling is primarily an acoustical one.

I. Introduction

The instrument tower is located at the center of the antenna pedestal. The top of the tower is 32 m above ground, and its foundation extends 10.7 m below ground level, being connected to the antenna pedestal only through the soil. The lower part of the tower is enclosed by the pedestal and alidade rooms, whereas the upper 15 m is surrounded and protected by a windshield spaced approximately 15 cm from the tower. The purpose of the tower is to support the precision reference instrument to which the antenna dish is optically connected. Figure 1 shows the configuration of the tower, windshield, and precision reference instrument. It should be noted that the astrodome is connected to the windshield only. The top of the instrument tower is coplanar with the floor of the astrodome; a space of approximately 2 cm separates the two structures. Attached to the edge of the tower top is an annular neoprene ring which bears lightly on the floor of the astrodome and serves to seal the gap so as to allow a temperature-controlled environment within the astrodome.

It is clear that in order for the precision reference instrument to serve its intended purpose, the angular positional stability of the tower should be better than the pointing accuracy of the instrument which is to within 5 arc seconds.

Instrument tower motion has been observed in three ways. When standing in the astrodome, a relative motion between the floor of the astrodome and the tower top is visually quite obvious, especially when the antenna is being accelerated or when the wind is blowing. During the times of relative motion, one can feel motion if he is standing on the instrument tower, thus leading him to wonder how much of the rather large relative motion is contributed by the tower. Instruments including accelerometers and level sensors have been used to detect motion.

There are two general types of tower motion: a long period motion caused by thermal gradients in the structure (reported in Ref. 1), and vibratory motion, which is discussed here.

II. Miscellaneous Experiments

Since the relative motion between the astrodome floor and the tower top has a total excursion of 2 or 3 mm during a moderate wind, and because all observers have been able to feel the tower motion, it was suspected that

there was an inadvertent connection between tower and windshield. A rope was dropped through the space between the tower and windshield so that its lower end was at the bottom of the windshield. By sweeping this rope around the entire periphery, it was proved that no such connection existed. The neoprene ring covering the gap in the astrodome floor was removed and no reduction in tower movement was observed.

A sheet of plywood was set horizontally in a JPL laboratory so that it could be vibrated laterally at a frequency of 2.5 Hz and at an adjustable amplitude. Several persons stood and sat on this plywood while it was being shaken. All could feel the motion at amplitudes as small as ± 0.12 mm, and it was generally agreed that it felt like a much larger displacement.

The first mode natural frequency of the tower was measured by displacing its top horizontally, releasing it, and measuring the subsequent accelerations with an accelerometer. This was achieved by bolting a special bracket to the top of the tower, connecting a cable between the bracket and part of the antenna wheel structure, tightening the cable, and then suddenly cutting the cable. The resulting accelerometer record was sufficiently pure to allow a frequency count to be made. It was approximately 3.6 Hz, which was reasonably close to the calculated value.

Another experiment established the relationship between the horizontal and angular displacements of the tower top. While the autocollimator of the precision reference instrument was directed onto a gravity mirror placed on the tower top, the tower was pulled horizontally with a cable and the force measured with a dynamometer. The horizontal motion of the tower was measured with dial gages and compared with angular reading of the autocollimator. Also the windshield was pulled horizontally and the forces and displacements measured. The results of these tests are shown in Figs. 2 and 3.

III. Measurement of Tower Motion With Accelerometers

Two $\frac{1}{10}$-g accelerometers were mounted on the top of the tower. One was aligned with a north–south line and the other was perpendicular to it. Two 1-g accelerometers were clamped to the astrodome structure (to the structural channel at waist level) so as to measure its horizontal acceleration. These were placed parallel to the accelerometers on the tower. It had previously been determined that the astrodome could be shaken at its resonance frequency simply by swaying one's body. All four accelerometers were connected to a Sanborn recorder and the calibrations made by tilting the accelerometers by a known amount.

Recordings of astrodome resonance were made on two occasions. Its frequency was 2.1 Hz and its maximum amplitude was ± 6.55 mm. The oscillograph of the tower accelerometers appeared to be composed of two frequencies, namely, one of 2.1 Hz and one of 10.5 Hz. It was assumed that the amplitude of the 2.1-Hz component was 50% greater than the component of the 10.5-Hz component. The sum of these two vibration components was plotted and found to match the oscillograph very closely. The displacement amplitudes were computed by dividing the measured accelerations by the squares of the circular frequencies. The results are as follows: When the astrodome was resonating at 2.1 Hz and ± 6.55 mm, the tower had a 2.1-Hz amplitude of ± 0.167 mm and a 10.5-Hz amplitude of ± 0.0043 mm. Assuming the dynamic relationship between lateral and angular displacements is the same as the static one shown in Fig. 2, the angular displacement of the tower in arc seconds is obtained by multiplying the lateral displacement in millimeters by 16.3. Thus, the angular motion of the tower was ± 2.7 arc seconds. The oscillograph records indicate that the tower accelerations are proportional to the astrodome accelerations. Hence, the tower displacements would be proportional to the astrodome displacements.

It should be emphasized that an astrodome amplitude of ± 6.55 mm is many times greater than has ever been observed during operation in strong winds. We may conservatively say that the astrodome amplitude does not exceed one-fifth of that obtained during the resonance test. Thus, it is expected that the angular displacement of the tower top will not exceed ± 0.50 arc second from vibratory motion under normal conditions.

According to the oscillographs, the larger amplitude frequency of the tower matches the frequency of the astrodome. Hence, it appears that the tower vibration is a forced one. Since the frequency of the astrodome is 2.1 Hz and the tower is forced at this frequency, which is substantially different from the tower natural frequency of 3.7 Hz, the magnification factor is small; that is, it is approximately 1.30 or 30% more than a static deflection.

IV. Nature of the Coupling Between Tower and Antenna

The preceding experiments indicate that the vibratory motion of the tower produces an error that is small in

comparison to that of the precision reference instrument. However, there is an important disadvantage to this vibration. In order to control the tower motion caused by thermal gradients and described in Ref. 1, it is necessary to use a level sensor. Several commercial level sensors which have been tested in this vibratory environment do not work. For example, in Ref. 2, errors are tabulated for a representative level when tested at an amplitude of 0.012 mm over a frequency range from 2 to 10 Hz. Therefore, it is proper to inquire about the nature of the coupling between the antenna and the instrument tower.

It has been noticed that an instrument tower movement is always accompanied by an astrodome movement. Thus, the probability is high that the principal coupling medium is the air between the tower and windshield. However, it cannot be ruled out with certainty that some coupling is constituted by the soil between the pedestal and tower.

The following analysis indicates that the primary coupling is an acoustical one. As the windshield vibrates, it causes a change in the pressure of the connecting air. If the concentric cylindrical tower and windshield are considered to be infinite parallel plates, the one-dimensional acoustic theory may be applied. The change in absolute pressure ΔP may be expressed as follows (Ref. 3):

$$\Delta P = \frac{2\pi \rho_0 a^2 y}{\lambda} \tag{1}$$

where

ρ_0 = mass density of the undisturbed air

a = sonic velocity

y = amplitude of the disturbing source

λ = wavelength

Using the relationship $\lambda = a/f$, where f is the frequency of the source in cycles per unit time, ΔP may be expressed as

$$\Delta P = 2\pi f a \rho_0 y \tag{2}$$

The amplitude of the top of the windshield is greater than that of the lower parts. If it is assumed that the amplitude y is related to the coordinate x as

$$y = A\left(1 - \cos\frac{\pi x}{2\ell}\right) \tag{3}$$

where

A = amplitude at the top of the windshield

x = distance along windshield axis with origin at bottom of windshield

ℓ = length of the windshield

then the change in absolute pressure may be written as

$$\Delta P = 2\pi f a \rho_0 A\left(1 - \cos\frac{\pi x}{2\ell}\right) \tag{4}$$

The total instantaneous force F acting on one side of the tower may be obtained by integrating ΔP over the surface of the tower:

$$F = 2\pi f a \rho_0 D A \int_0^{\ell}\left(1 - \cos\frac{\pi x}{2\ell}\right)dx$$

$$= 2\pi f a \rho_0 D A \ell\left(1 - \frac{2}{\pi}\right) \tag{5}$$

where D is the diameter of the instrument tower.

Equation (5) represents the instantaneous force on one side of the tower caused by a pressure increase. Simultaneously, there would be a pressure decrease on the opposite side of the tower; hence, the total simultaneous force acting on the tower would be twice that of Eq. (5), namely,

$$F_{\text{TOTAL}} = 4\pi f a \rho_0 D A \ell\left(1 - \frac{2}{\pi}\right) = 4.55 f a \rho_0 D A \ell \tag{6}$$

This total force is distributed over approximately half the length (that portion surrounded by the windshield) of the cantilever tower. In order to compare with experimentally measured values, it is necessary to convert F_{TOTAL} of Eq. (6) to an equivalent concentrated force applied at the tower top, since the static deflection measurements were made when the force was so located. A comparison of the end deflections of two cantilever beams, one loaded with an end concentrated load W, and the other loaded with a distributed load per Eq. (3) of total magnitude W, gives the required modification factor, which is 0.75. The equivalent end force F_E is

$$F_E = (0.75)\,4.55 f a \rho_0 D A \ell = 3.42 f a \rho_0 D A \ell \tag{7}$$

Substituting the following values into Eq. (7),

$f = 2.1$ hertz

$a = 335$ meters/second

$\rho_0 = 1.22$ kg/meter^3

$D = 2.75$ meter

$\ell = 15.2$ meter

there is obtained:

$$F_E = 122\,000\,A \tag{8}$$

where A is the amplitude of the top of the windshield in meters and F_E is in newtons.

For $A = 0.00655$ meter, Eq. (8) becomes

$$F_E = 122\,000\,(0.00655) = 800 \text{ newtons} \tag{9}$$

This value of 800 newtons is an effective static force derived from a consideration of the one-dimensional acoustic equation. From Fig. 2, the relationship between static force and horizontal tower displacement z is

$$z = \frac{F}{5663610} \tag{10}$$

where z is in meters and F in newtons.

Substituting the calculated value of $F = 800$ into Eq. (10), there is obtained:

$$z = \frac{800}{5663610} = 0.000141 \text{ meter} \tag{11}$$

From the accelerometer tests, the tower amplitude was 0.000167 m when the astrodome amplitude was 0.00655 m. But under this vibration, the magnification factor was 1.3. If the value 0.000167 is divided by 1.3, there is obtained 0.000128, which checks well with the calculated value of 0.000141.

V. Conclusions

The results of the accelerometer tests show that the amplitude of tower vibration produces a tower angular error that is small in comparison to the error of the precision instrument mount. The above analysis of an acoustical coupling between the tower and windshield, although based on boldly simplifying assumptions, gives an answer that matches the measured value to within 10%. If this is indeed the nature of the coupling, how can it be reduced? The outside of the tower is already covered with a heat insulation urethane foam. In the low frequency range at hand, it is thought that the addition of sound absorbing materials would be useless. The addition of holes in the tower would reduce the coupling but only by the percentage of area reduction. Since the only real problem caused by the vibration is the difficulty of making a level sensor work, it is best to concentrate our efforts toward developing a level sensor which will function in this kind of vibratory environment.

References

1. McGinness, H. D., "210-ft Antenna Tower Positional Stability," in *The Deep Space Network*, Space Programs Summary 37-50, Vol. II, pp. 151–158. Jet Propulsion Laboratory, Pasadena, Calif., Mar. 31, 1968.
2. Peterschmidt, W. M., "Instrument Tower Position Control for 210-ft Antenna," in *The Deep Space Network*, Space Programs Summary 37-51, Vol. II, pp. 104–109. Jet Propulsion Laboratory, Pasadena, Calif., May 31, 1968.
3. Sears, F. W., *Mechanics, Heats and Sound*, Second Edition, p. 499. Addison-Wesley Publishing Co., Inc., Reading, Mass., 1950.

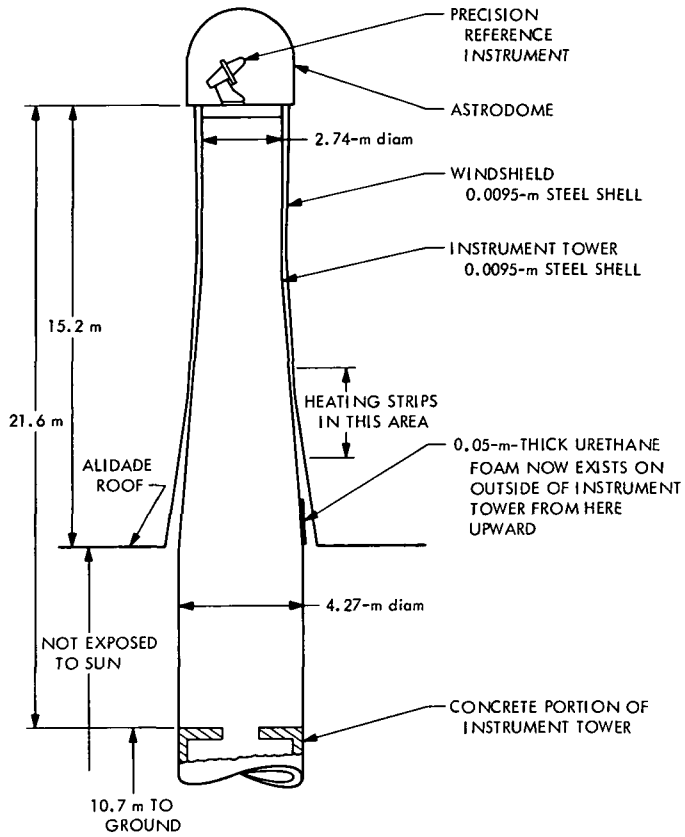

Fig. 1. Instrument tower configuration

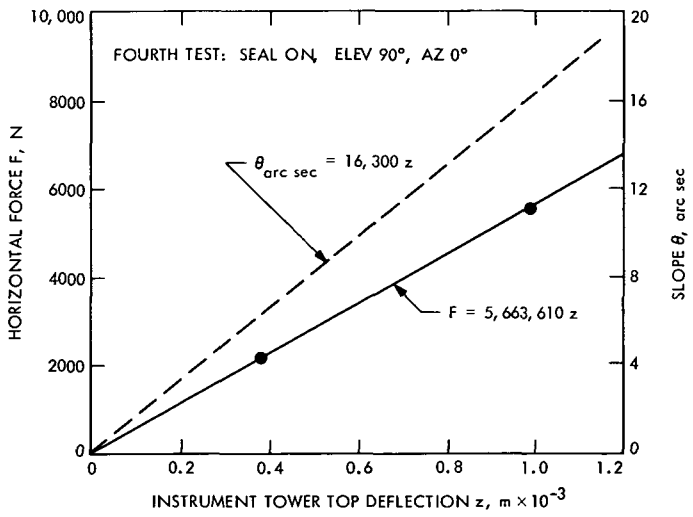

Fig. 2. Horizontal force versus tower deflection and angular deflection versus horizontal deflection

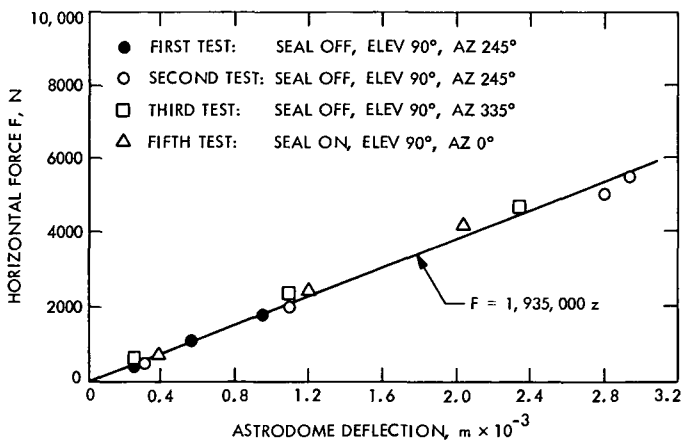

Fig. 3. Horizontal force versus astrodome deflection

DSN Research and Technology Support

E. B. Jackson
R. F. Systems Development Section

The major current activities of the Development Support Group at both the Venus Deep Space Station and the Microwave Test Facility are presented, and accomplishments and progress are described. Activities include: pulsar observations, planetary radar with very high resolution range measurement of the planet Mars, tri-cone support structure assembly, 100-kW clock synchronization implementation, precision antenna gain measurement on the 26-m antenna, Block IV receiver/exciter installation and testing, weak source observations of 13 sources, and observations of the planet Jupiter.

The Development Support Group of the RF Systems Development Section is currently engaged in the following activities at the Venus Deep Space Station and the Microwave Test Facility (MTF) at GDSCC:

I. DSS 13 Activities

A. In Support of Section 331

1. Pulsars. The twenty pulsars tabulated in Ref. 1 continue to be regularly observed (24 h per week are used for this activity) and data on pulse-to-pulse spacing, power density spectra, and pulse arrival time continue to be collected.

2. Planetary radar. This program continues to track the planet Mars. Range measurements with an rms resolution of a few microseconds are being made as a total of twenty-three passes were observed during the period August 16 to October 15, 1971. The Venus ranging program also continued, but only nine Venus passes were observed during this same period.

B. In Support of Section 332

1. Tri-cone support structure (TCSS). The first TCSS arrived at DSS 13, was assembled, and cable trays, heating, air conditioning, waveguide, waveguide switches, and receiver mounts have been installed therein. A multi-level platform serviced by an elevator has been erected to make work easier and faster to complete.

2. Nine-meter antenna alignment. The deviation of the 9-m antenna main reflector from the best-fit paraboloid was measured and antenna position readouts were aligned by performing tracking of the planet Mars with an "on-axis" mounted theodolite and reference to a precision elevation bubble level with a resolution of 10 arc-sec.

C. In Support of Section 333

1. Precision antenna gain measurement (26 m). This program continues with data being gathered by observing the radio star Cygnus A and the *Apollo* lunar surface experiments package (ALSEP) left on the Moon by

Apollo 12. Data continue to be collected by Development Support Group personnel with assistance from Paul Batelaan of Section 333.

2. Weak source observation. Data collection utilizing the noise adding radiometer and an improved antenna pointing computer program (developed by Dr. Michael Klein) continue. Radio sources observed during this period were 3C17, 3C161, 3C218, 3C270, 3C340, 3C348, 3C353, 3C444, CTA21, CTA102, NGC247, NGC772, NGC1275, and the planet Jupiter. Additionally, substantial amounts of time have been devoted to calibration and "sky survey" measurements with the antenna positioned pointing either at Polaris or at an azimuth of 180 deg and elevation of 87 deg. This program is heavily supported by both Section 333 and 825 personnel who participate actively in most of the observations performed.

D. In Support of Section 335

1. 100-kW Clock synchronization transmitting system. Except for minor cleanup and modification action, the installation onto the antenna has been completed and test transmissions have been made to all deep space stations which are equipped to receive. Time correlation has already been achieved by DSSs 14, 41, 42, 51, and 62. However, there are still some unsolved problems with the computer control program, some hardware problems with the exciter/programmed oscillator, and some antenna-pointing anomalies which are not yet completely understood. Some trouble has been experienced with the waveguide switch, but the transmitter has proved to be quite stable and trouble-free at the 100-kW power level.

Very early in the testing period an RF survey was conducted which included not only ground measurements but measurements on the edge of the antenna dish and the back-up structure as well. Hazardous areas (areas with a measured power in excess of 1 mW/cm^2) were observed and a strict program of limited entry is being observed as well as banning radiation out the horn while the antenna is below 10 deg in elevation.

2. Block IV receiver/exciter. After installation and extensive testing, phase-lock tracking of spacecraft *Pioneers* 6 and 8 was accomplished. Development of the computer program to allow control of the system by the station SDS 910 computer continues along with regular spacecraft tracking.

II. Microwave Test Facility

A. In Support of Section 332

1. Tri-cone support structure (TCSS). Extensive machine shop and electromechanical support has been afforded the TCSS during this period.

B. In Support of Section 333

1. DSS 14 noise bursts. In support of the continuing investigation into the noise burst problem at DSS 14, a section of WR-430 waveguide, 208.3 cm (82 in.) long with water cooling attached, was fabricated for installation in place of a suspect piece.

C. In Support of Section 335

1. 100-kW Clock synchronization transmitter. Heavy support was given this project during this period with the machine shop fabricating HV connector parts, various brackets, mounts, etc. An RF survey at 7149.9 MHz was also conducted and dangerous areas were delineated. A 10X multiplier was fabricated and the 10-W buffer amplifier, along with an almost complete spare unit, was completed and tested.

Reference

1. Jackson, E. B., "DSN Research and Technology Support," in *The Deep Space Network Progress Report*," Technical Report 32-1526, Vol. III, p. 158. Jet Propulsion Laboratory, Pasadena, Calif., June 15, 1971.

Ground Communications Facility 50-kbps Wideband Data Error Rate Test

J. P. McClure
SFOF/GCF Development Section

During June 1971 a seven-day wideband data error test was conducted between the SFOF Communications Terminal and the NASCOM Madrid Switch Center.

The test, which was run at 50 kbps, was conducted to determine both long-term and fine-grained error data for a wideband circuit comparable to those expected to be used to support Mariner Venus-Mercury 1973. The test was quite successful.

Long-term end-to-end error rates of 6×10^{-5} or better were measured in both directions. The hourly and 5-min error distributions indicate that the errors are grouped into bursts (as expected). The majority of the time the error rate is substantially less than the average.

I. Introduction

During the period June 8–14, 1971, a lengthy wideband data test was conducted between the SFOF Communications Terminal at JPL and the NASCOM Madrid Switch Center adjacent to DSS 61.

The test, which was run at 50 kbps, had two purposes; (1) to determine the error rates of a circuit generally comparable to those expected to be used in support of *Mariner* Venus-Mercury 1973 (MVM'73), and (2), to determine the statistical distribution of the errors. The test was quite successful and the resulting data satisfies both needs.

This article reports the measured error rates and the long-term (5-min to 1 day) error distributions. The fine-grained error statistics data are presently being reduced and will be reported in the future.

II. Test Configuration and Procedure

The configuration used for the test is shown in Fig. 1. Circuit GW 58619, provided by NASCOM, used 303C data sets operating synchronously at 50 kbps. The routing of this American Telephone and Telegraph circuit is not known nor are the facilities from which it was derived. The 303C data set requires substantially all of a 48 kHz passband; hence, a group bandwidth was used.

At Goddard Space Flight Center the continental circuit was connected to an overseas group circuit GW 58530, again using 303C data sets. The GSFC interconnection

was at the direct current sides of the data sets, thus providing digital regeneration of the signal at this point. The routing of the overseas circuit via Comsat to the Madrid switch is shown on Fig. 1.

Test data consisted of the 2047-bit pseudo-random pattern generated by Frederick Electronic Company Model 600 test sets. At each receive location the pseudo-random pattern was also synchronized and compared against the standard pattern by Frederick 600 (F600) sets.

The bit-error pulse outputs generated by the Frederick 600's were handled in various ways depending on the location. At GSFC modified F600's outputted a pulse each time a bit error occurred and, on a separate line, simultaneously outputted a pulse each time a block error was detected. For this test the F600 block size was set to 600 bits, thus a block error output pulse occurred each time a set of 600 bits contained one or more errors. Printer-punch-recorders (PPRs) were used to accumulate either bit or block error counts for 5-min periods and then destructively print out the total. The PPR also punched a paper tape containing the same data as was printed. A TTY printout from the paper tape was the prime data for analysis.

At the Madrid switch center a modified F600 was used to drive two PPRs, one each for bit and block error counts.

At the SFOF Communications Terminal a conventional F600 was used. Block error data were obtained through use of a programmable block error counter (PBEC) set to produce error pulses for each 600-bit block. On two occasions the data received at the SFOF was routed to a computer for logging on magnetic tape. This recorded data will be reduced to determine the fine-grained error distribution.

The test configuration used, i.e., 303C data sets with regeneration at GSFC, closely approximates the expected configuration to be used for *Mariner* Venus-Mars 1973. One difference is anticipated, namely that a Western Electric Company 303B data set will be used operationally instead of the 303C used in this test. The 303C uses nearly a full 48-kHz group channel to handle 50 kbps whereas a 303B uses somewhat more than a half-group to support 28.5 ± kbps. The two data sets (and their associated modems) have only minor differences. Both use the same modulation scheme (binary vestigial side band amplitude modulation) and detection process.

NASCOM/GSFC served as the test conductor. Though the period June 8 through June 14, 1971 (Days 159 through 165) was used, the test was not conducted continuously. The overseas circuit (GW 58530) was diverted several times for operational purposes (voice/data channels). Channel outages occurred and on occasions the test was not restarted until the next day. A total of approximately 99 h of inbound data to JPL was recorded and about 98 h of outbound data was obtained at Madrid. GSFC recorded a total of 179 h in both directions.

III. Test Results and Preliminary Analysis

When data circuits fail they sometimes do so abruptly. Other times they slowly degenerate with the error rate increasing accordingly. In error rate tests it is always difficult to decide when the error rate is bad enough to declare the line "out", and thus not include subsequent errors in the totals. In this analysis the circuit was generally considered to have failed when the 5-min error rate exceeded 10^{-3}. The circuit was considered restored when the rate fell back below 10^{-3}.

The measured data and resulting error rates for the total period are shown in Table 1.

Tables 2 through 5 show the same information on a per-day basis. Several observations can be made regarding the table data:

(1) Day-to-day error rate variations of 20 to 1 were experienced (Table 1, Col. 3).

(2) In total, Madrid-to-JPL showed a lower error rate than Madrid-to-GSFC, an impossibility. Examination of hourly and 5-min data indicates numerous times when JPL recorded fewer errors than GSFC-inbound. An instrumentation error is suspected as the cause of these anomalies. Operator error, though possible, does not appear plausible.

(3) Madrid's simultaneous recording of bit and block errors makes it possible to derive the average number of error bits in an error block. This value, K, ranges from 26 to 116 on a daily basis, with a long term average of 62.4. With numerous assumptions one could conclude that the average burst length should be about 128 bits long. Actual burst length data must await the reduction of the magnetically recorded data.

(4) On a daily basis there appears to be some correlation between the performance of the inbound and outbound portions of the end-to-end circuit. On

four days the BER slope was the same, and on two days it differed.

Figure 2 is a representative logarithmic plot of the hourly end-to-end bit errors in each direction. No diurnal trend is evident, and no significant correlation between the inbound and outbound direction is evident. As in high speed data, the error counts range over wide limits, typically three orders of magnitude or more.

Figures 3 and 4 are bar chart plots of the hourly distribution of bit-error rates. For instance, Fig. 3 shows that on the Madrid-to-JPL circuit there were five 1-hour intervals when the hourly error rate ranged between 2×10^{-6} and 4×10^{-6}. The median M value is marked on each figure, this being the value below and above which there are an equal number of intervals. The average bit-error rate A is also shown.

The span between the median and the average plainly shows how much effect a few "bad" hours can have on the average. In the Fig. 3 case there were few hours with really poor error rates and as a result the median and average values are close. In contrast, Fig. 4 shows a wider spread due to several hours with heavy errors. Restated, the figures indicate that the majority of the time the error rate is well below the average. Despite this satisfying fact, the overall system design must be capable of handling the higher rate intervals.

Figures 5 and 6 are also plots of the bit-error rate distribution; however, these figures are based on 5-min intervals, the maximum resolution available. Most noteworthy is the large number of intervals having no errors. In all cases the median value is significantly lower than the equivalent hourly median rate. Both of these observations simply verify what the raw data show, i.e., performance on a 5-min interval can range from very bad to the very best. Despite the wide interval over which the errors range, each figure has a definite non-zero peak in the 10^{-5} to 10^{-6} area.

IV. Conclusions

If the 1973 wideband configuration is implemented in the planned manner we may expect operational bit error rates of 6×10^{-5} or better, measured on a long-term basis. The errors will be bunched, with the error rates showing wider variations as the sample interval becomes shorter. The majority of the time the error rate will be substantially less than the average.

Table 1.

	Bit test hours	Bit error rate	Block test hours	Block error rate (600 bits)
Madrid to GSFC (Overseas leg)	117.24	3.66×10^{-5}	2.58	11.9×10^{-4}
Madrid to JPL (End-to-end)	85.0	1.83×10^{-5}	14.42	6.04×10^{-4}
JPL to GSFC (Continental leg)	55.2	2.72×10^{-5}	4.0	14.6×10^{-4}
JPL to Madrid (End-to-end)	97.67	5.95×10^{-5}	99.58	5.69×10^{-4}

Table 2. Results (inbound) Madrid to GSFC

Madrid to GSFC						
Day	Bits			Blocks (600 bit)		
	Hours	Errors	Bit error rate $\times 10^{-5}$	Hours	Block errors	Block error rate $\times 10^{-4}$
159	—	—	—	2.58	922	11.9
160	8.83	50411	3.17	—	—	—
161	20.16	52964	1.45	—	—	—
162	20.0	225717	6.26	—	—	—
163	24.0	35446	0.82	—	—	—
164	24.0	20737	0.48	—	—	—
165	20.25	387770	10.77			
TOTAL	117.24	773045	3.66	2.58	922	11.9

Table 3. Results (inbound)—Madrid to JPL

Madrid to JPL						
Day	Bits			Blocks (600 bit)		
	Hours	Errors	Bit error rate $\times 10^{-5}$	Hours	Block errors	Block error rate $\times 10^{-4}$
159	—	—	—	1.92	553	9.59
160	2.25	7504	1.85	—	—	—
161	4.25	21430	2.80	12.5	2058	5.48
162	17.75	101724	3.18	—	—	—
163	24.0	49810	1.15	—	—	—
164	24.0	45842	1.06	—	—	—
165	12.75	53924	2.34	—	—	—
TOTAL	85.00	280234	1.83	14.42	2611	6.04

Table 4. Results (outbound)—JPL to GSFC

JPL to GSFC						
Day	Bits			Blocks (600 bit)		
	Hours	Errors	Bit error rate $\times 10^{-5}$	Hours	Block errors	Block error rate $\times 10^{-4}$
159	—	—	—	4.0	1756	14.6
160	9.5	28501	1.66	—	—	—
161	14.7	169061	6.38	—	—	—
162	20.0	55268	1.53	—	—	—
163	11.0	18334	0.92	—	—	—
164	—	—	—	—	—	—
165	—	—	—	—	—	—
TOTAL	55.2	271164	2.72	4.0	1756	14.6

Table 5. Results (outbound)—JPL to Madrid

JPL to Madrid							
Day	Bits			Blocks (600 bit)			K
	Hours	Errors	Bit error rate $\times 10^{-5}$	Hours	Block errors	Block error rate $\times 10^{-4}$	
159	—	—	—	—	—	—	
160	9.75	64917	3.69	9.33	1381	4.93	45
161	14.00	225352	8.94	14.58	2024	4.62	116
162	13.92	308934	12.32	15.00	3284	7.29	101
163	24.00	217359	5.03	24.00	2150	2.98	101
164	24.00	157100	3.63	24.00	5157	7.15	30
165	12.00	73811	3.41	12.67	3019	7.93	26
TOTAL	97.67	1047473	5.95	99.58	17015	5.69	62.4

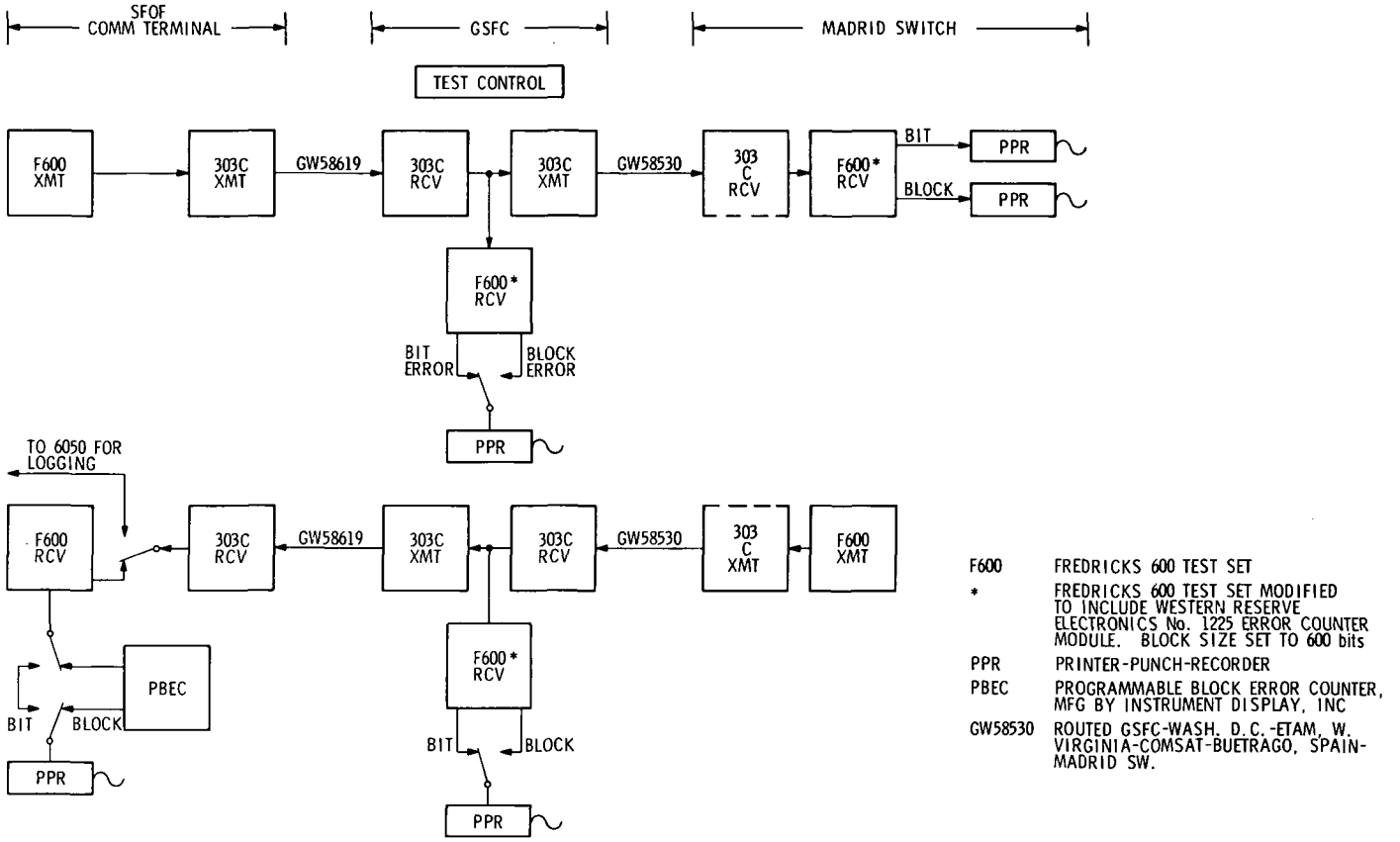

Fig. 1. 50-kbps Wideband test configuration, June 1971

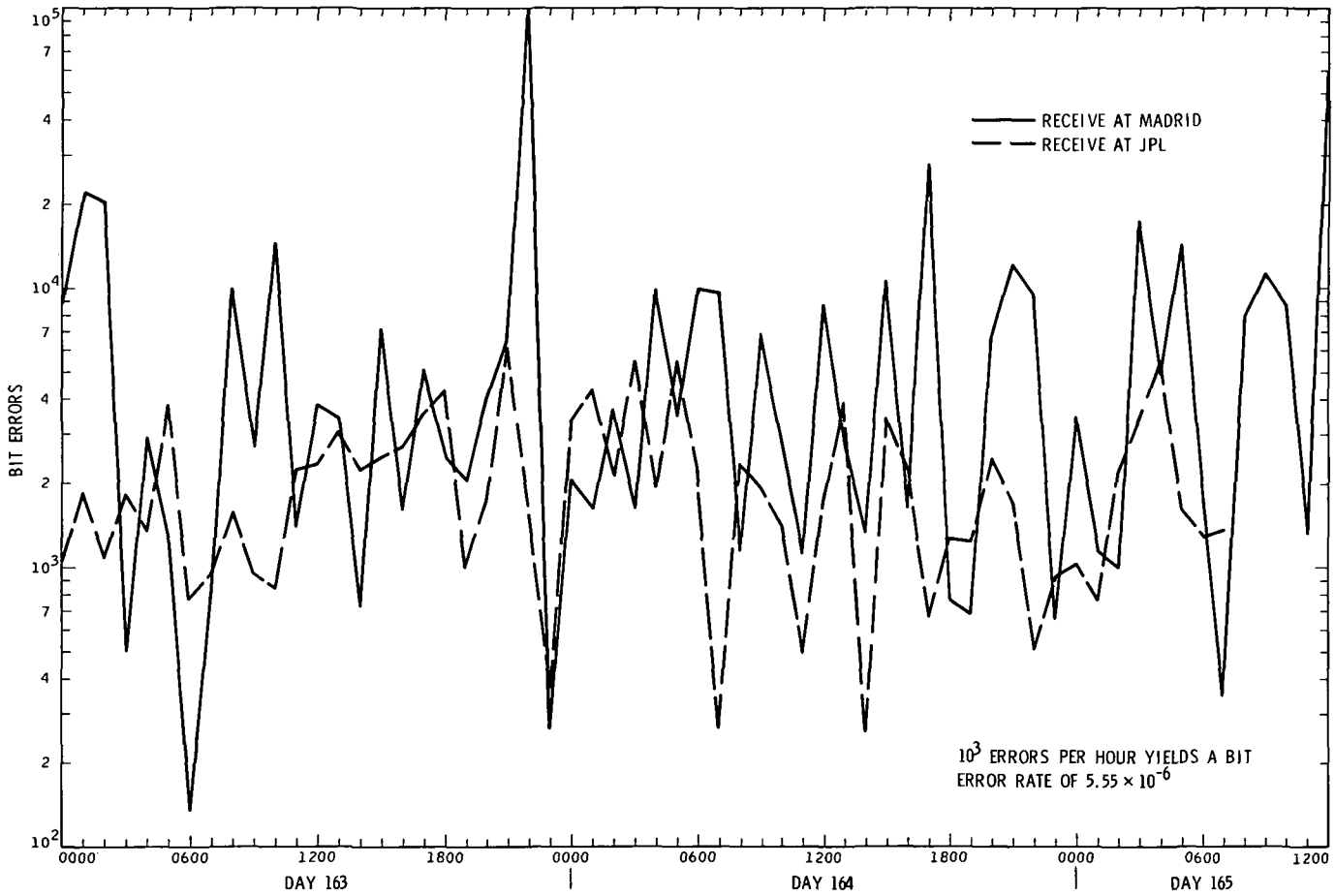

Fig. 2. Bit errors per hour

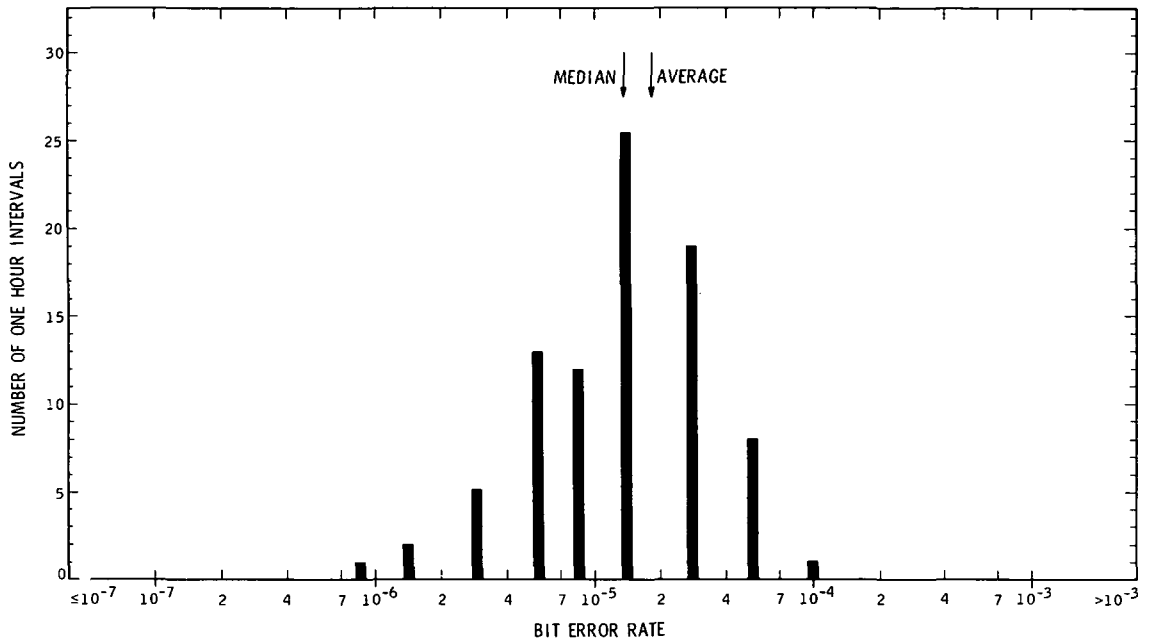

Fig. 3. Bit-error rate distribution (hour basis) Madrid to JPL

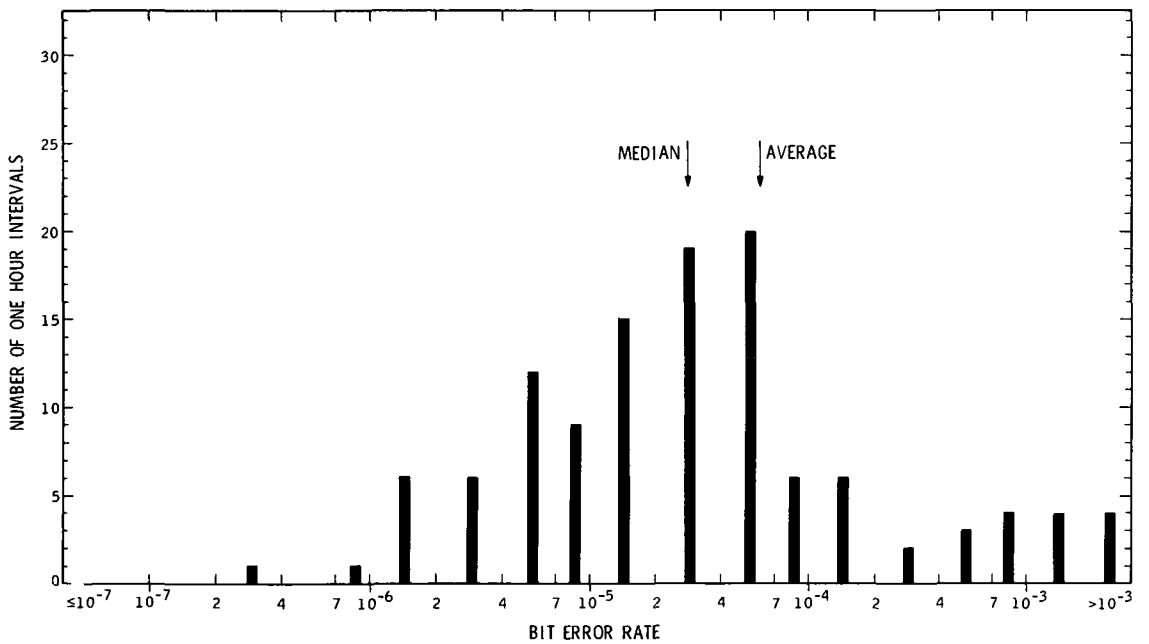

Fig. 4. Bit-error rate distribution (hour basis) JPL to Madrid

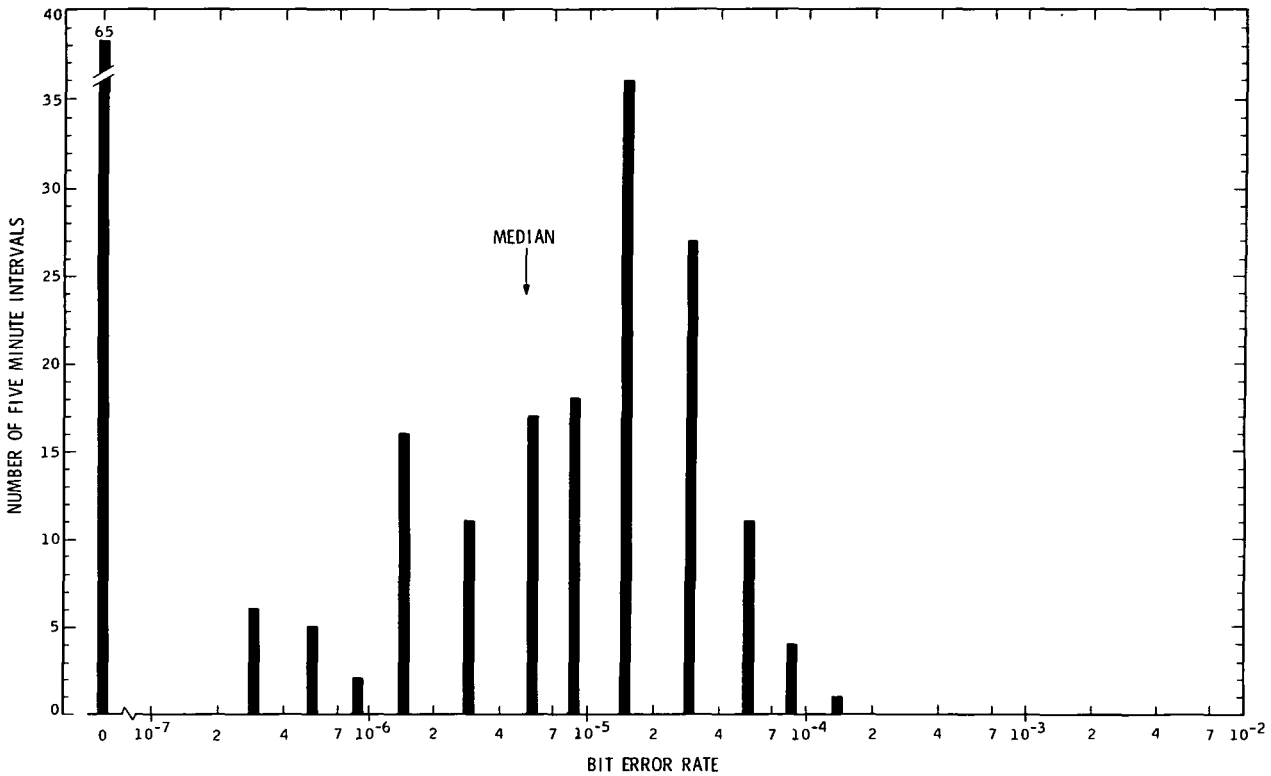

Fig. 5. Bit-error distribution (5-min. basis) Madrid to JPL

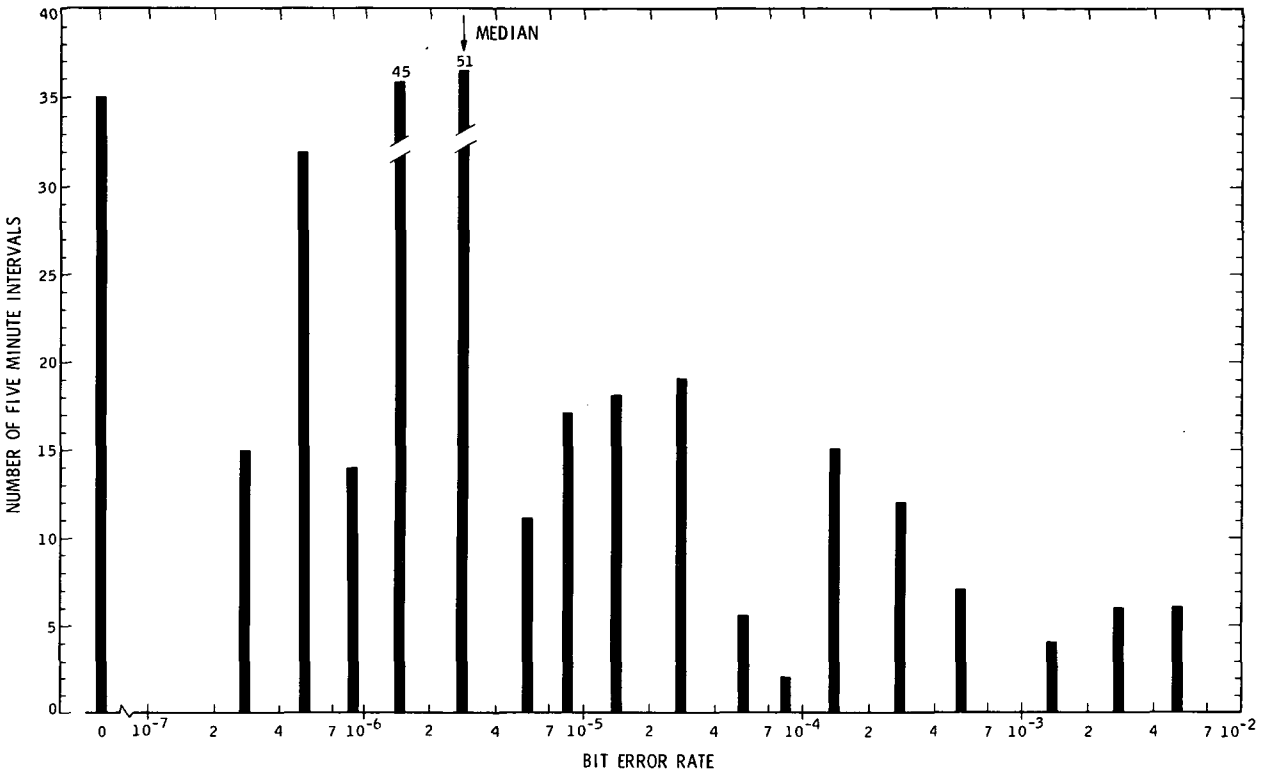

Fig. 6. Bit-error distribution (5-min. basis) JPL to Madrid

Overseas 64-m RMS Program for SDS 920

D. McCarty and M. S. Katow
DSIF Engineering Section

With the completion of the 64-m antennas overseas and their performance testing, an important test measurement required is the reflector distortion RMS from gravity loading. In order to provide the paraboloid best fitting capability for the available SDS 920 computers at overseas sites, the RMS program was modified to suit the typewriter and two tape units I-O capabilities of the computers. The program computes the RMS after paraboloid best fit from field angle readings using typed inputs. The constant data, such as coordinates of targets, are supplied in a data tape with the Binary Program supplied in a second tape.

I. Introduction

One of the JPL specifications required to be met by the contractor erecting the 64-m antennas overseas is the distortion RMS of the reflector structure under gravity loading. To supply a readily available checking tool for use by the JPL's alignment checking personnel, the Utku/Schmele RMS paraboloid best fitting program (Refs. 1, 2 and 3) was modified to be used with the SDS 920 computer available at the overseas sites.

To satisfy the 8000-word core size of the computer with only a typewriter and two tape input devices, the program was stripped to include only the solution for the required field measurements plus coding modifications to simplify and reduce the quantity of the input data. The constants for the 64-m antenna peculiar data were supplied in a prepared tape written with data only.

The typing data inputs required are the Z offset of the theodolite from the basic position plus the actual angle readings of the targets with the assigned target numbers.

II. Program Modifications

The coding of the Utku-Schmele RMS program was changed to compute from field data only, using as input the actual angle readings of the measuring theodolite plus the target defining number.

By predefining the target numbers and providing a map for the field personnel to use, it was possible to supply the coordinates as constants written on a data tape. By interrogating this tape when data is required, the core space requirement was minimized. Supplied also on the data tape are the correct angle readings for zero errors so that the actual field angle readings may be differenced to them and the residual would be the deflection or error.

III. Formulation and Review

The 64-m antenna specification requires a particular geometric interpretation of the theodolite data to be input to the RMS program. That is, the differential between the field angle reading and the geometrically correct angle

is converted to a linear displacement normal to the correct line of sight which in turn is divided by the cosine of the instrument angle (Fig. 1 and *Subsection VI-A*). This results in a distortion component parallel to the symmetric axis of the paraboloid which is then input as a Z displacement in the RMS program.

It should be noted that the theodolite sees only the component of the distortion normal to its line of sight. In the above described calculations, the distortions are assumed to be in the direction of the symmetric axis of the paraboloid. The resulting computed rms is, at least for the 64-m antenna, smaller in value than the correct value, and the truer value seems to be output if the distortions are assumed to be normal to the paraboloid surface (Ref. 4).

The program uses a theodolite height of 38.1 cm (15 in.). Changes in this quantity are input as the "instrument height bias." The bias is equal to the actual height minus the assumed height of 38.1 cm (15 in.). Formulation used to convert the configured height to the actual height may be found in *Subsection VI-B*.

IV. Usage with SDS 920 Computer

The program is written in FORTRAN II, designed for use with the SDS 920 computer. Two input devices are employed—magnetic tape and the keyboard. All output is via the console typewriter.

To eliminate re-compilation each time the program is used, it is stored in binary form on magnetic tape. It is loaded off of logical unit 1. A listing of the FORTRAN II source program will be included with the binary tape so that any necessary changes may be made.

The invariant 64-m configuration data is stored on another magnetic tape in BCD. Due to core limitations (8K) on the SDS 920, this data is not stored in core. Thus it must remain on the tape unit during the entire execution of the program.

The program includes halts at various spots in order to give the user time to perform various functions. At the beginning of the program, it halts for the user to mount the constant data tape on logical unit 2. After each set of field data is entered, it halts again for the user to position the typewriter at the first line of the next page. This enables headings to be printed at the top of each page of output.

V. Input

The input data is divided into two sets. The first set contains constants for the 64-m antenna. It is stored on magnetic tape and is supplied with the program. It is read in off magnetic tape unit 2.

The second data set is made up of field measurements from an angle-measuring theodolite on the antenna. It is entered at the keyboard.

A. Data Description

1. Magnetic tape data

1st–648th records—Antenna constants

FORMAT (4F10.5)

Parameters (X, Y, U, A)

Description

X = X coordinate of target point on undeformed dish (in meters).

Y = Y coordinate of target point on undeformed dish (in meters).

U = instrument angle (in radians) to target point on undeformed dish (angle d_i in Fig. 1).

A = area of panel associated with this target point (in square meters).

Target points have been assigned point nos. 1–648. A sketch illustrating these numbered points accompanies the program. The constant data above is arranged by point number in increasing order, starting with point 1.

2. Keyboard data

1st Record. Instrument height bias

FORMAT (F6.3)

Parameters–(BIAS)

Description

BIAS = Instrument height bias (in meters). The program assumes an instrument height of 38.1 cm.

BIAS = (actual height)–(38.1 cm).

2nd Record—Output heading

FORMAT (12A6)

Parameters—(TITLE)

Description

TITLE = alphanumeric data which will be heading on each page of printed output.

3rd—to n Records—Field Measurements

FORMAT (I3, 2X, 3I3, 2X, 3I3)

Parameters—(K, IDEG, IMIN, ISEC, JDEG, JMIN, JSEC)

Description

K = point number of target point.

IDEG, IMIN, ISEC = Theodolite angle—reading of distorted target point (angle ϕ_i in Fig. 1) (in degrees, minutes, and seconds, respectively).

JDEG, JMIN, JSEC = Reverse theodolite angle reading (in degrees, minutes, and seconds, respectively) (approximately equal to 180 deg—theodolite angle above).

Field measurements may be entered for all or part of the target points, and need not be entered in any particular order. If more than one field measurement is entered for the same point, the latest value will be saved and all previous values will be deleted. This provides a means for the correction of typing errors.

A blank record signals the end of the data set. The program then computes the RMS after best fitting.

Provision has been made to execute multiple data sets. The program may be terminated by typing in a blank record for the first field measurement record. A block diagram illustrating the usage of the RMS program on the SDS 920 computer is shown in Fig. 3.

VI. Output

The first section of output lists the individual distortions, normal to the surface of the paraboloid, for each target point for which field measurements were entered after the best fitting of the paraboloid. The error in path-length sense is also listed in this section.

The second section lists various quantities associated with the best fit paraboloid. Included are the RMS of half path length change, focal length of the best fit paraboloid, coordinates of the vertex of the best fit paraboloid, and rotation about the X and Y axes.

A. Computation of Z-Component of Deflection Vector from Theodolite Measurement of Distortion Angle (Fig. 1).

The radial distance, in the X–Y plane, to the ith target point, R_i, is given by

$$R_i = X_i^2 + Y_i^2$$

where X_i and Y_i are the X and Y coordinates of the ith target point (right-hand coordinates system).

Therefore

$$a_i = R_i/\cos\alpha_i$$

where α_i = angle made by $\vec{QO}_i$ with the XY plane. The deflection vector normal to the line of sight, b_i, is then given by

$$b_i = (a_i)(\tan\theta_i)$$

where θ_i = theodolite measurement of distortion angle.

For small deflections, QB_i & QD_i may be considered to be parallel to QO_i, it follows that $\gamma_i = \alpha_i$

Therefore, the Y-component of the distortion vector, d_i, is then given by

$$d_i = b_i/\cos\alpha_i$$

B. Correction Calculations for Theodolite Height Changes (Fig. 2)

Figure 2 illustrates field measurements taken using a theodolite with a height bias of AB difference from the correct height of 38.1 cm (15 in.) This causes the theodolite angle for the distortion reading to be read as λ_i in-

stead of ϕ_i. The component normal to the line of sight is therefore computed to be CE rather than DF.

To evaluate this error, for small distortions:

$$DF \parallel CE \text{ and } DG = CE \text{ and } DF = GF + CE$$

It follows that since $EF = AB$, $GF = AB/\cos\alpha_i$

Therefore

$$DF = CE + AB/\cos\alpha_i$$

References

1. Utku, S. and Barondess, S. M., "Computation of Weighted Root-Mean-Square of Path Length Changes Caused by Deformations and Imperfections of Rotational Paraboloidal Antennas," Technical Memorandum No. 33-118, Jet Propulsion Laboratory, Pasadena, Calif., March 1963.
2. Katow, M. S., and Schmele, L. W., "Antenna Structures: Evaluation Techniques of Reflector Distortions," in *Supporting Research and Advanced Development*, Space Programs Summary 37-40, Vol. IV, pp. 176–184, Jet Propulsion Laboratory, Pasadena, Calif., August 1966.
3. Katow, M. S., "Antenna Structures: Evaluation of Reflector Surface Distortions," in *The Deep Space Network Progress Report*, Technical Report 32-1526, Vol. I, pp. 76–80, Jet Propulsion Laboratory, Pasadena, Calif., February 1971.
4. Marcus, B. and Katow, M. S., "Antenna Structures: Evaluation of Field Measurements of Reflector Distortions," in *The Deep Space Network Progress Report*, Technical Report 32-1526, Vol. II, pp. 113–121, Jet Propulsion Laboratory, Pasadena, Calif., April 1971.

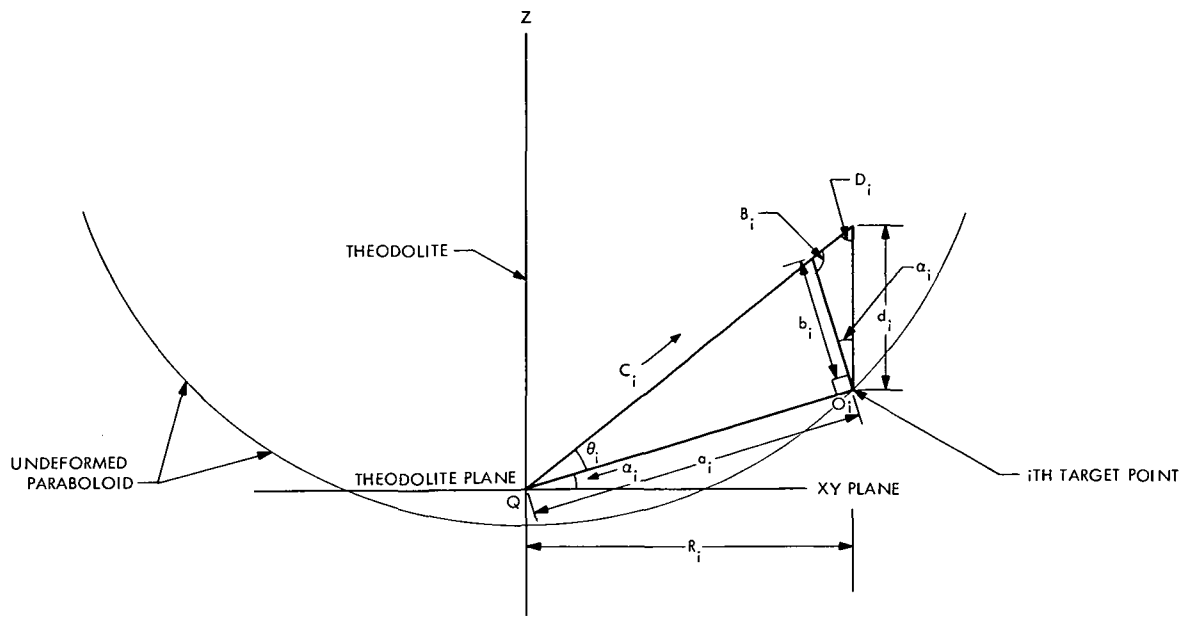

Fig. 1. Computation of Z-component of deflection vector from theodolite measurement of distortion angle

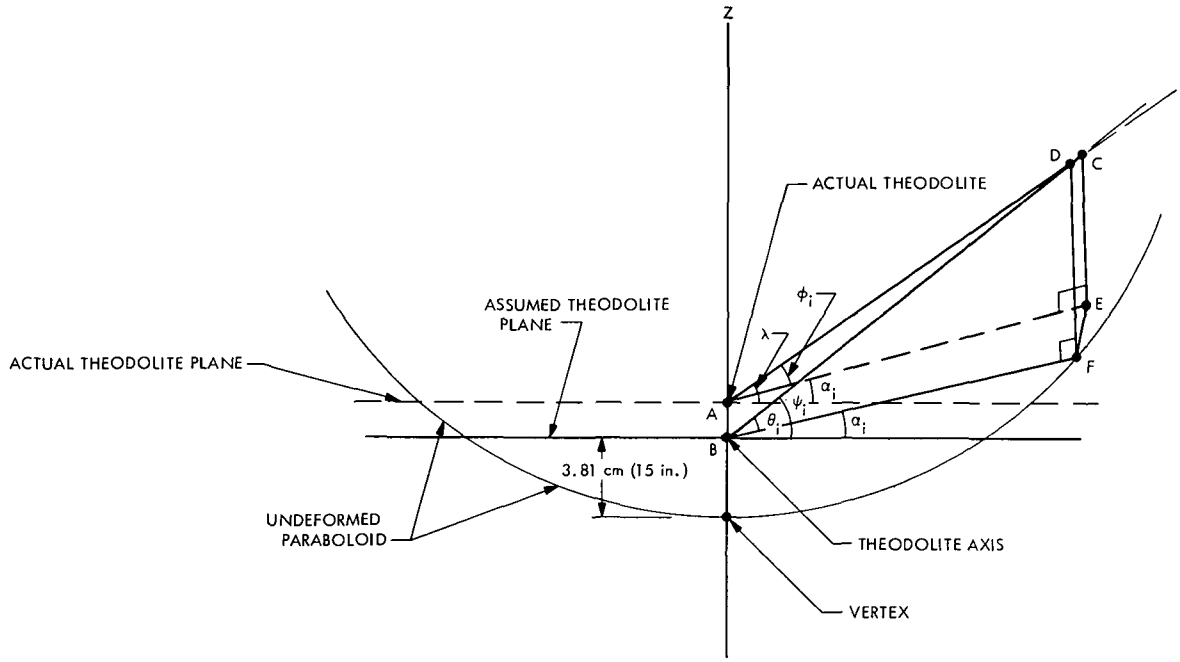

Fig. 2. Correction calculations for theodolite height changes

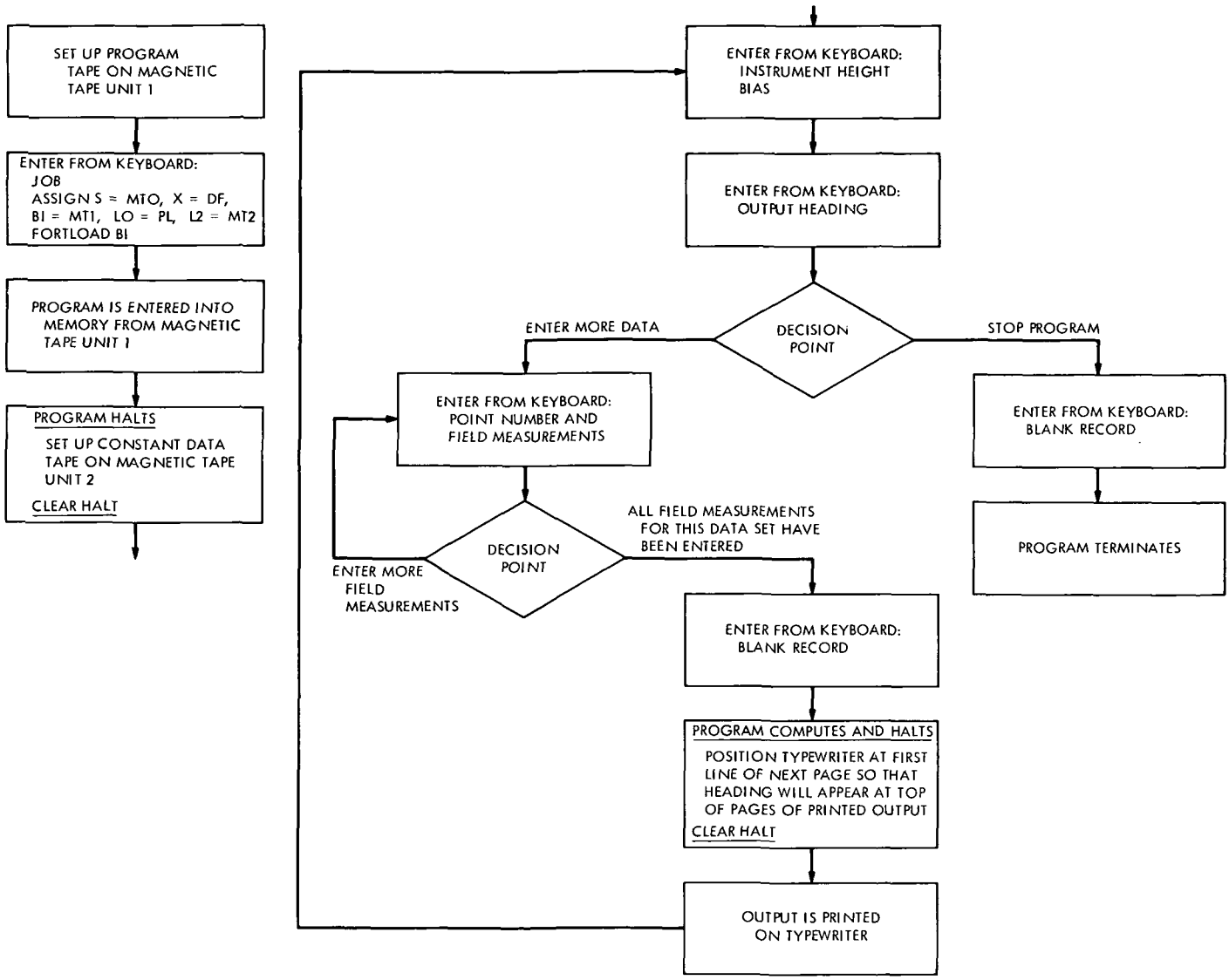

Fig. 3. Block diagram illustrating usage of RMS program on SDS 920 computer

Operational Time Sync Microwave Subsystem

R. W. Hartop
R. F. Systems Development Section

The prototype Operational Time Sync (OTS) Microwave Subsystem has been redesigned to accommodate the change in operational frequency and to increase its power handling capability. The completed system has been successfully tested to 115 kW CW at 7150 MHz and is expected to operate at 150 kW CW, the design goal.

The increase in transmitted power from 20 kW CW in the prototype Operational Time Sync (OTS) Microwave Subsystem to the present level of 100 kW CW, together with the 1300-MHz change in frequency from 8450 to 7150 MHz, required extensive redesign of the antenna feed system. The prototype system used a dual-mode horn of the Potter type (Ref. 1) and obtained circular polarization with a waveguide turnstile junction. Since the Potter horn is not broadband, it would have required a replacement for the new frequency. It was decided to use the corrugated horn instead, since it has been perfected at X-band frequencies for prior JPL projects (Ref. 2).

The turnstile junction is not a satisfactory waveguide device for extremely high power applications. It was, therefore, replaced with a quarter-wave plate polarizer similar to those proven successful in 500-kW CW S-band systems. An optimum design at 2295 MHz was scaled to 7150 MHz and mechanically adapted to be suitable for X-band flange hardware. The resulting circular waveguide size had a diameter of 4.11 cm (1.618 in.). After examination of the propagation characteristics of this size waveguide at 7150 MHz, it was decided to adopt this as standard (WC-162 would be the correct EIA nomenclature) for all the circular waveguide components, rather than transforming to other diameters by means of cosine tapers.

Since previous X-band work at JPL had been at frequencies around 8448 MHz, existing microwave components and test equipment were all in 3.477-cm (1.369-in.)-diameter waveguide (WC-137). Accordingly, some work had to be done to accommodate the new size. A cosine taper between the two diameters was designed and two units were fabricated. Their voltage standing wave ratio (VSWR) was determined to be less than 1.010, thus permitting the use of existing sliding loads and other equipment to be used without significantly degrading measurement accuracy.

The corrugated X-band horn also had a throat diameter of 3.477 cm (1.369 in.) and a VSWR of about 1.11 at 7150 MHz, this frequency being below its optimal bandwidth. It was expected that a matching section would have to be added next to the input of the horn in order to lower this mismatch. Before any attempt was made to design this matching section, the horn throat was opened to 4.11 cm (1.618 in.), thus removing the internal taper between the input and the large matching iris. It was assumed that the effect of this machining operation would

be slight with respect to impedance and beneficial with respect to power handling capacity. When the horn was measured, the VSWR had decreased to 1.07, apparently due to the more gradual change in diameter seen by the propagating field. This improvement in performance eliminated the need for a matching section.

Another design problem was posed by the need for a transition between circular and rectangular waveguide capable of handling 100 kW CW (previously, the turnstile junction performed this function as well as generating circular polarization). Consideration was given to designing a five-step transition similar to those previously used at S- and X-band, but it was decided to use this type of transition as a backup while a higher power design was attacked. A mathematical design was obtained[1] for a uniform taper transition between the WC-162 (round) waveguide and the WR-137 (rectangular) waveguide. A computer program was written,[1] from which punch cards were obtained to operate a programmable machine tool. A master tool was cut, several duplicates were made on a copying lathe, and the final transition was formed out of solid OFHC copper by electron discharge machining. The VSWR of the 12.7-cm (5-in.) transition is less than 1.04 over the frequency band of 7150 to 8500 MHz. Because it has no discontinuities of any kind other than the gradual change of shape, it should be capable of carrying the same power as the rectangular waveguide input.

All of the above components must be water-cooled for full power operation. Instead of fabricating the water-cooling passages as an integral part of the microwave component, as is usually the practice, it was decided to design water-cooling blocks which bolt onto the waveguide parts. The advantages of this approach are twofold: (1) the final component is less expensive since the microwave part is precision made out of OFHC copper, while the cooling block is a low-tolerance brass or aluminum part and is identical for several different waveguide components; and (2) replacement or redesign of a microwave part does not involve the water cooling part and vice versa.

The completed feed cone assembly, with the outer shell partially removed, is shown in Fig. 1. At the time of this writing, the microwave system has transmitted 115 kW CW without incident. The transmitter back power indicates a system VSWR of 1.045. It is expected that test runs to 150 kW CW will be completed in the near future.

[1]With the assistance of Dr. J. R. Radbill.

References

1. Potter, P. D., *A New Horn Antenna with Suppressed Sidelobes and Equal Beamwidths*, Technical Report 32-354. Jet Propulsion Laboratory, Pasadena, Calif., Feb. 25, 1963.
2. Brunstein, S. A., "A New Wideband Feed Horn with Equal E- and H-Plane Beamwidths and Suppressed Sidelobes," in *The Deep Space Network*, Space Programs Summary 37-58, Vol. II, pp. 61–64. Jet Propulsion Laboratory, Pasadena, Calif., July 31, 1969.

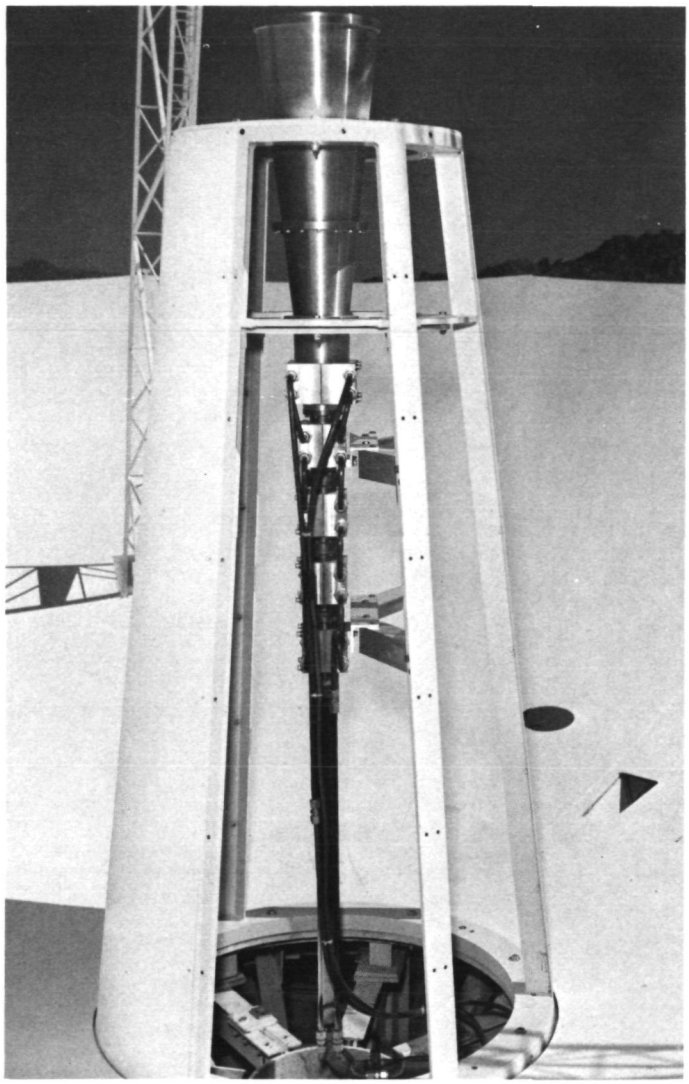

Fig. 1. Completed feed cone assembly with outer shell partially removed

Network Allocation Schedules

D. G. Tustin
DSN Engineering and Operations Office

This article reviews the reasons and needs for the Network Allocation Schedule and briefly describes the make up of these schedules and how they are used. The major emphasis is placed on the implementation of these schedules, including a new special-purpose software. This software makes use of an existing file management program and IBM 360 utility programs.

I. Introduction

The Network Allocation Schedules are a part of the DSN Operations and Analysis function, and are the means by which all operational activities of the Deep Space Network are committed and scheduled.

The basic need for the forecasting and scheduling of the network support requirements, and methods of accomplishing this were discussed in Ref. 1, and will be reviewed only briefly here. This article will deal with the implementation of these methods and their initial results.

II. Function

The Network Allocation Schedules provide the means of sizing the network and committing its resources to the various users. These commitments are made far enough in advance, and iterated enough times, to allow for adjustment in the resources and/or changes in the user's basic project design, then compensating for any period when the requirements exceed the base resources.

III. Elements

The Network Allocation Schedules originally consisted of four levels of schedules involving ever-increasing detail regarding time and equipment required, and covering ever-decreasing periods of time.

The four levels of schedules as originally planned were the 130-Week Network Loading Schedule, the 72-Week Network Allocation Schedule, the 8-Week Operations Planning Schedule, and the 7-Day Operations Schedule. In actual operation during the past eighteen months, it was found that there was a great deal of duplication in the 72- and 130-Week Schedules, and that the 72-Week Schedule was far too voluminous to be useful. It was

therefore decided to delete the 72-Week Schedule, using the 130-Week Schedule to cover the period and, further, to expand the 130-Week Schedule to a 150-Week Schedule, thus covering a full budget period.

IV. Implementation

Two approaches were taken for the implementation of these schedules. Initially, it was necessary to get them into operation as soon as possible, first manually then with computer assistance. On a longer term, the detailed design and implementation of a fully interactive software package was required.

The latter effort was initiated by letting a contract for a design study and the preparation of a design specification covering a new interactive scheduling software package (JPL 70-246, Software Requirements Document for JPL Mark IIIA DSN Scheduling Program). This design specification is currently being implemented and the preliminary software should be available by January 1, 1972.

The initial effort to put the new schedule in operation was undertaken by the DSN Scheduling Office as an internal effort. All of the various forms in use were reviewed, revised as required, and reduced from seven forms to two forms, which could be used at all levels of scheduling. A controlled dictionary of schedule configurations was established so that users could schedule their various requirements by referencing the appropriate configuration code(s) rather than having to call out each piece of equipment required separately.

To provide computer support for this effort, it was decided to make use of a general-purpose file management program MARK IV, which was available on the 360/75 computer. The use of this software package greatly reduced the raw programming and coding time required, allowing more effort to be spent in developing the special output requirements. Using this system the basic scheduling software was operational in less than three months, and the complete program was fully operational in less than six months. The software was designed to support all four of the original levels of scheduling providing both tabular and graphic listing, as well as punched cards to interface with the Sequence of Events program and a magnetic tape containing the schedule in special format that can be directly transmitted to any remote site via teletype or high-speed data line using a 360/75 real-time program.

One added benefit in using the MARK IV software package became evident as the *Mariner* Mars 1971 mission progressed and 360/75 time became increasingly difficult to schedule. This MARK IV package, and its user software, can be run on just about any 360 or 370 machine, thus allowing scheduling operations to be shifted to another less loaded machine.

V. Conclusion

The implementation of these schedules has proceeded satisfactorily and their worth has been well proven. During the next year it is anticipated that the new (second generation) interactive software will become operational, greatly reducing the manual effort now required as well as improving response time and accuracy.

Reference

1. Tustin, D. G., "Network Allocation Schedules," in *The Deep Space Network*, Space Programs Summary 37-64, Vol. II, pp. 105–106. Jet Propulsion Laboratory, Pasadena, Calif., Aug. 31, 1970.

Angle Tracking Analysis and Test Development

R. D. Rey
DSIF Operations Section

The angle tracking systems are currently being analyzed and tests are being developed to measure their performance. This article presents the progress made on the analysis and testing of the standard 26-m-diam antenna station automatic angle tracking system. The model is discussed and certain important system constants are developed. Simulation runs of the model were performed and comparisons are made with preliminary tests performed at the Echo Deep Space Station. The article also outlines the design of the test and software processing.

I. Introduction

Efforts have been undertaken to analyze the angle tracking systems and to develop tests which will measure their performance. The overall purpose was to determine the characteristics of the 26-m automatic angle tracking system and develop a system test to assure its proper performance during operations. The test will be used for station countdown and periodic system maintenance tests.

In order to fulfill the purpose of this task a number of efforts were undertaken. First, existing test procedures were evaluated to determine whether they could be used as tests. Next, a model of the automatic angle tracking system was developed which could be analyzed and simulated. This model was used for simulating the system using the CSSL[1] III simulation program available on the Univac 1108 and for analysis of the angle error variance. Test design was performed concurrently with the above efforts and was composed of selecting those parameters which best describe the performance of the angle tracking system and to develop automated processing methods. The software development effort was also performed concurrently. This effort implemented the processing method and developed the system interface routines. As a final effort, the station countdown and periodic system maintenance test procedures will be written.

The efforts are being applied to the angle tracking systems of the standard 26-m stations, the mutual DSIF/

[1]Continuous system simulation language.

MSFN 26-m stations and the 64-m stations. Analysis and test development on the mutual station is under way and will be completed this quarter. Analysis of the 64-m antennas is beginning in this quarter. The emphasis has been on the automatic angle tracking system of the standard 26-m station. Although the task pertains to automatic angle tracking, a large amount of the analysis and tests will apply to the antenna pointing subsystem (APS) with some modifications. Also the methods and techniques developed are directly applicable to the 26-m mutual antennas and the 64-m antennas.

II. Evaluation of TD-11 and TD-12 Analysis and Software

TD-11 and TD-12 are system test descriptions for 26-m hour angle declination (HA-dec) DSN antennas. TD-11 is formally titled Angle Jitter and Boresight Shift versus Signal Level—DSIF S-Band Tracking and Communications System (DZX-1150-11-TD); while the formal title of TD-12 is Angle Tracking Bandwidth (DZX-1150-12-TD).

It was first believed that TD-11 and TD-12 could be used for testing the 26-m antenna tracking. After evaluation of these tests it was found necessary to supply analysis and new software. The purpose of this section is to discuss the results of the evaluation, i.e., the decision to develop new test software and analysis.

The TD-11 analysis and software was found to be valid. Yet, the analysis does not define the antenna error slope gain constant quantitatively. Thus, the curves of angle jitter versus signal level cannot be verified, also the use of the servo control panel bandwidth as noise bandwidth is not necessarily correct. It was decided that an angle error variance analysis would be performed in order to verify the curves and quantitatively define the parameters used.

The TD-11 software for measuring angle jitter was studied. The software is useful and offers some advantages over the new angle jitter software. The TD-11 software resides in the DIS computer. From the DIS computer it can monitor the output angle and AGC voltage. It computes the angle mean and error variance, AGC voltage mean and variance. Therefore, TD-11 will be retained as a separate test with some refinement of the analysis.

Both the TD-12 software and the analysis used to support it were found unacceptable. The analysis was based on work performed years ago. In this work the servo transfer function was derived from measured transfer functions. The coefficients determined in this manner cannot be verified analytically. Also, the coefficients of the transfer function cannot be related to parameters of the system.

The software used in TD-12 was written to calculate delay times, percent overshoots, maximum-minimum points, rise time, and settling time of a step response. These calculations were found to be correct. The program then takes a direct discrete Fourier transform of the step response to calculate the closed-loop transfer function; but the result is not the closed-loop transfer function, since the *one over s* term due to the step function has not been removed. A weakness of the program was that it takes a direct Fourier transform instead of the computationally more efficient fast Fourier transform. The program was also difficult to operate, since it resided in the DIS computer, which has no control over the angle tracking servo system.

A decision was made to perform analysis which would relate the system parameters to the performance of the system and to write a new software test program which would accurately measure the performance of the system.

III. Angle Tracking Model and Analysis

A. System Model of the Automatic Angle Tracking System

Automatic angle tracking is performed, using a two-coordinate amplitude comparison system. A four-feed horn feeds a unit of "magic T's" which are used to generate a reference channel (sum channel), hour angle (HA) and declination angle (dec) error channels. Since the two-error channels are essentially the same only the HA channel will be considered.

Shown in Fig. 1A is the basic pattern. This pattern is shifted by each feed resulting in the horn patterns (Fig. 1B). The sum of the horn pattern results in the effective antenna gain pattern of the receiver (Fig. 1C). The difference between the two patterns results in the effective antenna gain pattern of the error channel (Fig. 1D).

The received signal is coherently amplitude-detected with the reference generated by the receiver sum channel. The output of the error detector can be represented as

$$v_e(t) = \frac{K_r}{2}\sqrt{2S}\,F(\theta)\cos\phi_e + \frac{K_r}{2}\,n_{ce}(t)\cos\phi_e$$

where

$F(\theta)$ = the effective antenna gain pattern of the error channel

$\theta = \theta_r - \theta_c$ = antenna pointing error, deg

θ_r = the angle location of the object being tracked, deg

θ_c = the angle that the antenna is pointing, deg

K_r = the gain in the error channel including AGC and the multiplier gain, V/V

S = is the average received power

ϕ_e = phase-locked loop error

$n_{ce}(t)$ = gaussian white noise

If the angle error is small, then

$$F(\theta) = K_\theta\,\theta$$

where K_θ is the slope of the error pattern. The linearized error detector output is

$$v_e(t) = \frac{K_r K_\theta}{2}\sqrt{2S}\,\theta\cos\phi_e + \frac{K_r}{2}\,n_{ce}(t)\cos\phi_e$$

This equation represents the input voltage to the servo isolation amplifier whose output drives the position integrator portion of the servo electronics. The overall system model is shown in Fig. 2. In this figure $G(s)$ represents the dynamics and gains of the antenna servo system.

B. Angle Tracking Control System Model

A detailed model of the 26-m diameter angle tracking control system was developed. This model was used to define the important constants of the system, i.e., gain constants and time constants.

Shown in Fig. 3 is a functional block diagram showing the transfer gains throughout the system. Each block has associated with it a gain and a transfer function. The model is based on the assumption that the dynamics of the electronic circuitry is dominated by the integrator network and the integration of the motor. Such factors as receiver AGC, servo component dynamics, and antenna dynamics are assumed to be negligible.

The servo electronics characterize the dynamics of the antenna tracking system. A simplified schematic of the servo electronics is presented in Fig. 4. Note that this schematic represents both the high and low speed electronics which differ only in the compensation network of the preamplifier. The different networks are shown in the lower right of the figure. The resistor R_I and the capacitors C_{I1} and C_{I2} are switched to different values, depending on the BW switch position. These values and the values of the remaining components of the schematic are given in Table 1.

The transfer impedance of each amplifier feedback network is as follows:

---

1. Integrator

Off

$$A_I Z_I = A_I \frac{1 + sT_{I2}}{(1 + sT_{I1}) \times (1 + sT_{I3})}$$

$$A_I = R_{I1} + R_{I2}$$

$$T_{I1} = R_{I2}\,C_{I2}$$

$$T_{I2} = \left(\frac{R_{I1}\,R_{I2}}{R_{I1} + R_{I2}}\right)(C_{I1} + C_{I2})$$

$$T_{I3} = R_{I1}\,C_{I1}$$

On, i.e., $R_{I1} \rightarrow \infty$

$$\frac{Z_I}{B_I} = \frac{1}{sB_I}\left[\frac{1 + sT_{I2}}{1 + sT_{I1}}\right]$$

$$B_I = C_{I1}$$
$$T_{I1} = R_{I2}\,C_{I2}$$
$$T_{I2} = R_{I2}\,(C_{I1} + C_{I2})$$
$$T_{I3} \rightarrow \infty$$

2. *Low-Speed Preamplifier*

$$A_pZ_p = A_p\left(\frac{1 + sT_{p1}}{1 + sT_{p1}}\right)$$

$$A_p = 2R_{p2}$$
$$T_{p1} = \left(R_{p4} + \frac{R_{p2}}{2}\right)C_{p4}$$
$$T_{p2} = R_{p4}C_{p4}$$

3. *High-Speed Preamplifier*

$$A_pZ_p = A_p\frac{1 + sT_{p1}}{1 + sT_{p2}}$$

$$A_p = R_{p5}$$
$$T_{p1} = R_{p6}\,C_{p6}$$
$$T_{p2} = (R_{p5} + R_{p6})C_{p6}$$

4. *Final Amplifier*

$$A_A\,Z_A = A_A\frac{(1 + sT_{A1})}{(1 + sT_{A2})}$$

$$A_A = R_{A2}$$
$$T_{A1} = R_{A3}\,C_{A3}$$
$$T_{A2} = (R_{A2} + R_{A3})C_{A3}$$

The values for the transfer function constants are given in Table 2.

The gains throughout the system as shown in Fig. 5 can be defined as follows:

$$K_T = K_RK_gK_IK_p, \qquad \text{volts/sec}$$

where

K_R = gain through the receiver (K_r) and error detector (K_x) including the antenna error pattern gain (K_θ), volts/degree

K_g = signal processor gain, volts/volt

K_RK_g is adjusted to produce an input into the integrator of 5 V/degree

$K_RK_g = 5$ V/deg

The gain of the integrator (K_I) is dependent on the operating mode

Integrator off

$$K_I = \frac{R_{I1} + R_{I2}}{R_I}, \qquad \frac{\text{volts/sec}}{\text{volt}}$$

Integrator on

$$K_I = \frac{1}{R_I\,C_{I1}}, \qquad \frac{\text{volts/sec}}{\text{volt}}$$

The gain K_p accounts for the error signal fed into the preamplifier summing point which is different for the low speed and high speed modes,

Low speed

$$K_p = \frac{2\,R_{p2}}{R_{p1}}, \qquad \frac{\text{volts}}{\text{volt}}$$

High speed

$$K_p = \frac{R_{p5}}{R_{p1}}, \qquad \frac{\text{volts}}{\text{volts}}$$

The summing point is also used to feed back the rate of the output (rate feedback loop). The gain of the rate feedback is a function of the summer gain times the gain of the feedback tachometer.

Low speed

$$K_t = \left(\frac{R_{p5} + R_{p6}}{R_{p7}}\right) \times G_t, \qquad \frac{\text{volts}}{\text{rad/sec}}$$

High speed

$$K_t = \frac{R_{p5}}{R_{p1}} \times G_t, \qquad \frac{\text{volts}}{\text{rad/sec}}$$

where G_t is the tachometer gain in volts/rad/sec.

The gain of the current amplifier input summer is

$$K_A = \frac{R_{A2}}{R_{A1}}, \qquad \frac{\text{volts}}{\text{volt}}$$

The pressure valve has a linearizing feedback loop which is available only in the high-speed mode. The gain of the feedback path is,

High speed only

$$K_f = \frac{R_{A2}}{R_{A4}} \times G_f, \qquad \frac{\text{volts}}{\text{psi}}$$

where G_f is the pressure transducer gain in $\frac{\text{volts}}{\text{psi}}$

The remaining gain constants are

K_c = gain of the current amplifier

$$= \frac{1}{R_{A5}}, \qquad \frac{\text{amps}}{\text{volt}}$$

K_v = the gain of the pressure valve, psi/amp or $\frac{\text{in.}^3}{\text{amp-sec}}$

K_m = gain of the motor, $\frac{\text{rad/sec}}{\text{in.}^3}$

K_{ms} = gear ratios between the motor and the pointing axis, $\frac{\text{system radians}}{\text{motor radians}}$

The constants are important in describing the performance of the system. It was not possible to find these constants in any of the obtainable JPL specifications. But, manufacturer's specifications on the various servo components were available. Listed below are the constants calculated for use in the low-speed mode,

$$K_A = 25.6, \text{ volt/volt}$$

$$G_t = 4.4 \text{ volts/1000 rpm}$$

so that

$$K_t = \frac{2R_{p2}}{R_{p7}} \times G_t = 0.099 \times 10^{-3} \text{ volts/deg/sec}$$

$$K_c = \frac{1}{R_{A2}} = 1 \text{ mA/volt}$$

$$K_v = 0.625 \text{ gpm/mA}$$

The flow through the motor was assumed to be half the total flow due to flow in an identical drag motor. Thus, the motor constant is

$$K_m = 1500 \text{ deg/sec/gpm}$$

The gear gain is

$$K_{ms} = \frac{1}{410{,}000}$$

The constant K_T is dependent on the servo-panel gain setting (GS). For

$$GS = 0 \quad K_T = 1.5 \text{ volts/sec}$$

and

$$GS = 5 \quad K_T = 7.5$$

These values along with the time constants were used to simulate the low-speed mode using the transfer function model shown in Fig. 5.

C. Simulation Results

The transfer function model was used to simulate the response of the antenna servo system to a step input which is similar to the actual test method. Although the model is linear, it can be used to predict the ideal performance of the system.

The simulation is written in CSSL III and was run on the Univac 1108. CSSL III provides transfer functions in La Place transform plane and input functions. A step

function was used as the input. The output response of each simulation run was punched onto cards. This output was then processed by a separate processing program which yields the following:

(1) Plots of the input response, the closed-loop amplitude and phase response, and the open-loop amplitude and phase response.

(2) It prints the percent overshoot, delay time, rise time and settling of the response.

(3) It also prints the noise bandwidth, 3-dB bandwidth, and the gain and phase margins.

The processing program can accept either simulation data or test data taken by station personnel.

The simulation program and the processing program were run for four cases. The first two cases (I and II) used the actual calculated constants while the second two cases (III and IV) used a reduced motor gain in order to yield results nearer to those measured.

Results of the first two cases are presented in Table 3. The simulation shows a fast response for the system denoted by the time measurements and the relatively wide bandwidths. The gain margin and phase margin show that the system is not very stable. Runs were also made for both bandwidths using a gain setting of 10 which resulted in instability of the simulation. In Figs. 6 and 7 plots of the step function response of the system simulation are presented for the cases I and II, respectively. The response is similar to the step function response called out in JPL Spec. DOA-1146-DTL for both the 0.025 and 0.05 bandwidth switch position (the specification does not note the gain setting position). Tests performed on the actual servo control system have shown that the response is actually much slower. It was found that by lowering the motor gain (K_m) by a factor of ten, responses could be obtained which were closer to the actual servo control system responses. The simulated responses with the reduced motor gain are shown in Figs. 8 and 9 for cases III and IV. Table 4 tabulates the results from the processing program. These results are representative of the actual performance parameters which can be expected from the standard 26-m-diameter antenna automatic angle tracking system.

Also shown in Figs. 6 to 9 are the plots of the closed-loop amplitude and phase response, and the open-loop amplitude and phase response. They are presented in order to illustrate the plots which are outputted by the processing program.

IV. Angle Tracking Test Design and Results

A. Test Design and Description

The purpose of this effort was to design a test that would measure the ability of the system to track accurately with a good stability margin. It will be used to determine the angle tracking characteristics during system countdown and maintenance tests. The tests should also aid in the adjustment of the system to meet specifications. The test was designed to be used on-site by station personnel. It is easy to operate, does not require excessive time to perform and produces the results during the test so that immediate corrective action can be taken, if required.

First, parameters were chosen to measure performance which would give a good description of the system performance yet be measurable using existing station equipment. The selected parameters were:

(1) Transient responses: rise time (T_r), time delay (T_d), settling time (T_s), and percent overshoot.

(2) Transfer function: bandwidth (noise and 3 dB), phase margin and gain margin.

The APS (XDS 910) computer is used to perform the test. (Advantages of using the APS are that all stations have a computer of the proper size and that the program developed can also be used to test the computer control mode.) With the APS computer the antenna can be pointed off the collimation tower with the system in the computer control mode. As the system is switched to the automatic track mode the APS is signaled to begin taking data.

The test program samples the step response output from the datex encoders. The sample response data is stored in the computer. The computer then calculates the time domain measurements (T_r, T_d, T_s, and percent overshoot). The step response data is then differentiated and fast Fourier transformed. This results in complex samples of the closed-loop transfer function from which the amplitude response and phase response are plotted. The program then computes the 3 dB and the noise bandwidths. Next, the complex samples of the closed-loop response are used to determine the open-loop complex samples from which open-loop amplitude and phase re-

sponses are plotted. The program then calculates the phase and gain margin of the system.

B. Results of Tests Performed at DSS 12

Tests were performed at DSS 12 with preliminary software. This software contained all the main elements of the test program except the ability to begin sampling at the instantaneous beginning of the test (a minor ECO will make this capability available).

The tests were run for the same system settings that were used in case III (BW setting = 0.025, G.S. = 0) and case IV (BW setting = 0.05, G.S. = 5) of the simulation runs. Since this was a preliminary test, not all of the data was processed, although the program had the capability. Thus, only time response data and closed-loop transfer function data were plotted.

Results from the test are tabulated in Table 5. The rise time, noise bandwidth, and 3-dB bandwidth are close to the values predicted by the simulation. The numbers for percent overshoot, delay time, phase margin and gain margin were not as close. There are two possible reasons for the discrepancy. First, there is an error in detecting the beginning of the test. This error could be as large as five seconds. Second, the antenna exhibits a large amount of friction or sticking. The effect that this has on the system can be seen by studying the time response shown in Fig. 10. The response is flattened and damped greater than the simulation results.

Shown in Fig. 11 is the closed-loop transfer function of the DSS 12 servo system for the two test cases. Both curves have somewhat periodic components on the lower end. These components could be due to the sticking of the antenna or possibly could be caused by quantization errors in the sampling routine or differentiation routine.

V. Summary

A model has been developed which can be used to predict the ideal performance of the automatic angle tracking system. Parameters such as the important time constants and gains have been documented. Test software has been developed and tested at DSS 12. This software is being modified for use in standard 26- and 64-m computer control mode tests and for 26-m mutual site tests. System test procedures are currently being developed.

Future plans are to obtain test data from each station. The test data will be processed, and the results of each station will be compared with each other and with the model. These comparisons will be used to set specifications on the system. They may also be used to detect and fix anomalies between the systems. The capability of measuring angle error variance and the error coefficients will also be available.

Table 1. Servo electronics component values

Integrator network						
	Low speed			High speed		
BW switch	0.025	0.05	0.1	0.2	0.4	0.6
R_I	0.1 MΩ	0.1 MΩ	0.1 MΩ	0.133 MΩ	0.133 MΩ	0.1
R_G	0 → 1 MΩ	0 → 1 MΩ	0 → 1 MΩ	0 → 1 MΩ	0 → 1 MΩ	0 → 1 MΩ
R_{I1}	[a]					
C_{I1}	8 μF	4 μF	2 μF	1.46 μF	0.69 μF	0.47 μF
R_{I2}	2.6 MΩ	2.6 MΩ	2.6 MΩ	2.6 MΩ	2.6 MΩ	2.6 MΩ
C_{I2}	1.76 μF	0.94 μF	0.47 μF	0.72 μF	0.57 μF	0.1 μF
[a] R_{I1} = 10kΩ with integrator off = ∞ with integrator on, series switch open						
Preamplifier compensation						
Low speed R_{p1} = 84 kΩ C_{p4} = 0.45 μF	R_{p2} = 100 kΩ	R_{p3} = 100 kΩ	R_{p4} = 6.2 kΩ	R_{p7} = 1.5 MΩ		
High speed R_{p1} = 144 KΩ C_{p6} = 0.37 μF	R_{p5} = 3.9 MΩ	R_{p6} = 430 KΩ	R_{p7} = 10 MΩ			
Final amplifier						
R_{A1} = 39 kΩ C_{A3} = 1.50 F	R_{A2} = 1 MΩ	R_{A3} = 100 kΩ	R_{A4} = 5 MΩ	R_{A5} = 1		
High-speed pressure feedback (high speed only)						
R_V = 0 → 50 kΩ	R_{V1} = 1 MΩ	R_{V2} = 1 MΩ				

Table 2. Transfer function constants

Integrator (low-speed) constants			
0.025 BW Integrator off $A_I = 2.6 \times 10^6$	$T_{I1} = 4.576$ sec $f_{I1} = 0.0348$ Hz	$T_{I2} = 97.6 \times 10^{-3}$ $f_{I2} = 1.63151$	$T_{I3} = 80 \times 10^{-3}$ $f_{I3} = 1.990$
Integrator on $C_{I1} = 8\ \mu F$	$T_{I1} = 4.576$ sec $f_{I1} = 0.0348$ Hz	$T_{I2} = 25.376$ $f_{I2} = 0.00628$	$T_{J3} \rightarrow \infty$ $f_{J3} \rightarrow 0$
0.05 BW Integrator off $A_I = 2.6 \times 10^6$	$T_{I1} = 2.44$ sec $f_{I1} = 0.06526$ Hz	$T_{I2} = 49.4 \times 10^{-3}$ $f_{I2} = 3.249$	$T_{I3} = 4.0 \times 10^{-3}$ $f_{I3} = 3.98$
Integrator on $C_{I1} = 4\ \mu F$	$T_{I1} = 2.44$ sec $f_{I1} = 0.0653$ Hz	$T_{I2} = 10.4$ $f_{I2} = 0.01531$	$T_{I3} \rightarrow \infty$ $f_{I3} \rightarrow 0$
0.1 BW Integrator off $A_I = 2.6 \times 10^6$	$T_{I1} = 1.222$ sec $f_{I1} = 0.13052$ Hz	$T_{I2} = 24.7 \times 10^{-3}$ $f_{I2} = 6.446$	$T_{I3} = 20 \times 10^{-3}$ $f_{I3} = 7.961$
Integrator on $C_{I1} = 2\ \mu F$	$T_{I1} = 1.222$ $f_{I1} = 0.13031$	$T_{I2} = 6.47$ $f_{I2} = 0.0246$	$T_{I3} \rightarrow \infty$ $f_{I3} \rightarrow 0$
Low-speed preamplifier			
$A_p = 168 \times 10^3$	$T_{p1} = 21.690 \times 10^{-3}$ sec $f_{p1} = 7.338$ Hz		$T_{p2} = 2.79 \times 10^{-3}$ $f_{p2} = 57.$

Table 2 (contd)

Integrator (high speed) constants			
0.2 BW Integrator off $A_I = 2.6 \times 10^6$	$T_{I1} = 1.872$ sec $f_{I1} = 0.08506$ Hz	$T_{I2} = 22.8 \times 10^{-3}$ $f_{I2} = 6.984$	$T_{I3} = 14.6 \times 10^{-3}$ $f_{I3} = 10.91$
Integrator on $C_{I1} = 1.46\ \mu F$	$T_{I1} = 1.872$ $f_{I1} = 0.08506$	$T_{I2} = 5.928$ $f_{I2} = 0.02686$	$T_{I3} \rightarrow \infty$ $f_{I3} \rightarrow 0$
0.4 BW Integrator off $A_I = 2.6 \times 10^6$	$T_{I1} = 1.482$ $f_{I1} = 0.1075$	$T_{I2} = 12.6 \times 10^{-3}$ $f_{I2} = 12.63$	$T_{I3} = 6.9 \times 10^{-3}$ $f_{I3} = 23.07$
Integrator on $C_{I1} = 0.69\ \mu F$	$T_{I1} = 1.482$ $f_{I1} = 1.075$	$T_{I2} = 3.276$ $f_{I2} = 0.04861$	$T_{I3} \rightarrow \infty$ $f_{I3} \rightarrow 0$
0.6 BW Integrator off $A_I = 2.6 \times 10^6$	$T_{I1} = 0.26$ $f_{I1} = 0.612$	$T_{2I} = 5.7 \times 10^{-3}$ $f_{2I} = 27.936$	$T_{3I} = 4.7 \times 10^{-3}$ $f_{3I} = 33.88$
Integrator on $C_{I1} = 0.47\ \mu F$	$T_{I1} = 0.26$ $f_{I1} = 0.612$	$T_{I2} = 1.482$ $f_{I2} = 9.306$	$T_{I3} \rightarrow \infty$ $f_{I3} \rightarrow 0$
High-speed preamplifier			
$A_p = 3.9 \times 10^6$	$T_{p1} = 0.159$ sec $f_{p1} = 1.00$ Hz	$T_{p2} = 1.602$ $f_{p2} = 0.0994$	
Final amplifier (low and high speed)			
$A_A = 1 \times 10^6$	$T_{1A} = 150 \times 10^{-3}$ $f_{1A} = 1.06$	$T_{2A} = 1.67$ $f_{2A} = 0.0965$	

Table 3. Results of simulation with normal motor gain

Case No.	Bandwidth setting	Gain setting	Percent overshoot	Delay time, sec	Rise time, sec	Settling time, sec	Noise bandwidth, Hz	3-dB Bandwidth, Hz	Phase margin, deg	Gain margin, dB
I	0.025	0	52.37	7.0	7.0	62.0	0.089	0.048	31.99	−18.18
II	0.05	5	77.09	4.0	4.0	62.5	0.310	0.089	16.3	−12.9

Table 4. Results of simulation with reduced motor gain

Case No.	Bandwidth setting	Gain setting	Percent overshoot	Delay time, s	Rise time, s	Settling time, s	Noise bandwidth, Hz	3-dB Bandwidth, Hz	Phase margin, deg	Gain margin, dB
III	0.025	0	51.93	24.0	30.0	326	0.021	0.011	31.6	−27.67
IV	0.05	5	63.83	12.0	13.5	191.	0.060	0.023	24.28	−10.80

Table 5. Test results from DSS 12

Bandwidth setting	Gain setting	Percent overshoot	Delay time, s	Rise time, s	Settling time, s	Noise bandwidth, Hz	3-dB Bandwidth, Hz	Phase margin, deg	Gain margin, dB
0.025	0	46	18.5	30.0	460	0.024	0.017	40.8	−16
0.05	5	40	8.6	10.4	91.5	0.05	0.026	39.3	−20.4

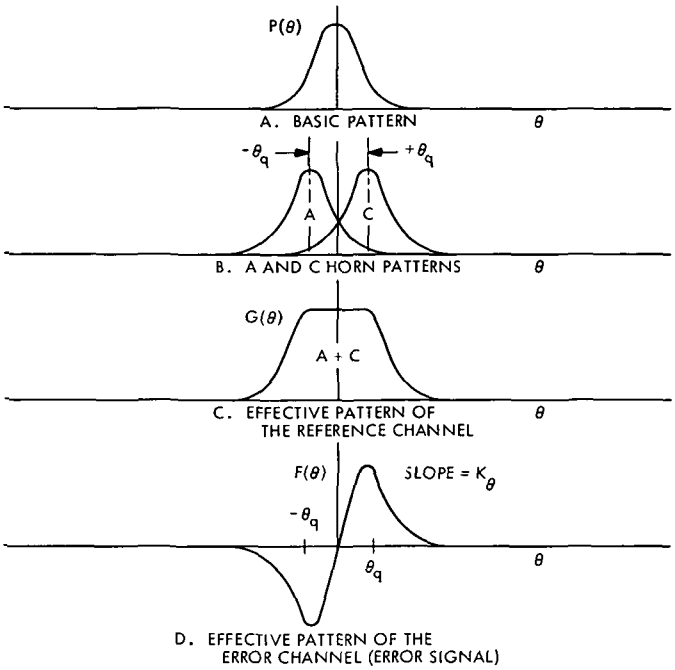

Fig. 1. Antenna and error patterns of the four-horn monopulse feed system

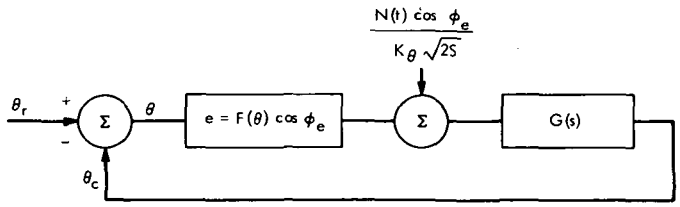

Fig. 2. System model of the automatic angle tracking system

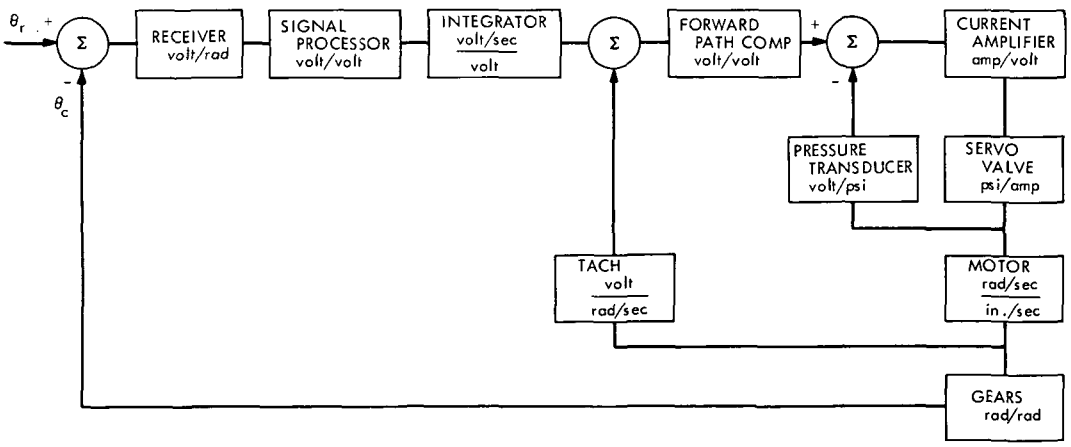

Fig. 3. Functional block diagram of the automatic angle tracking system

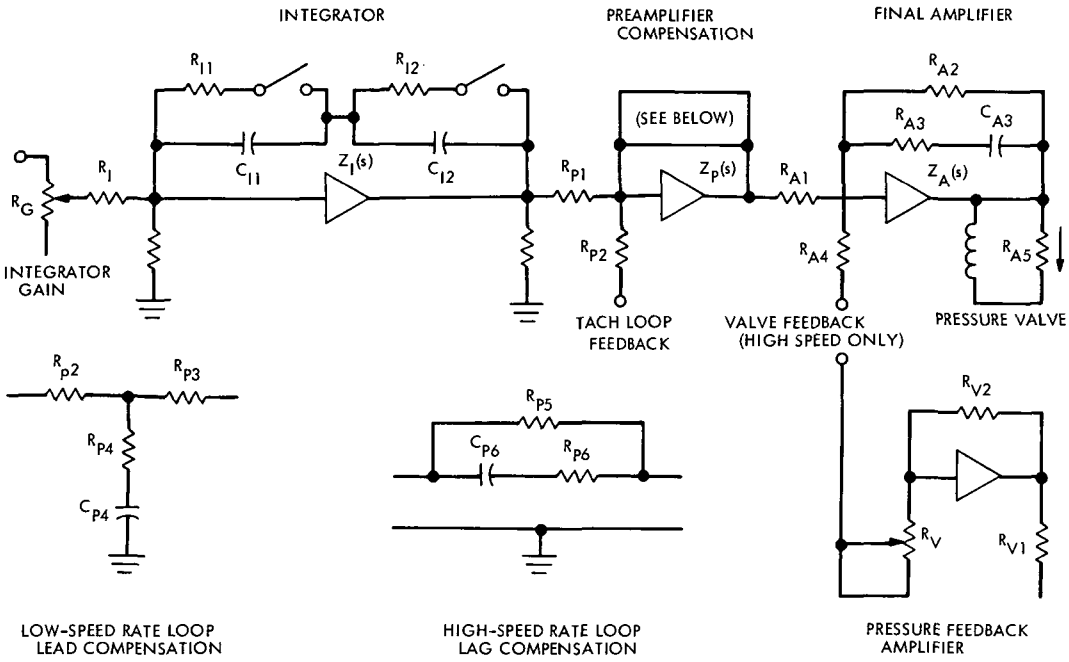

Fig. 4. Simplified schematic of the servo electronics

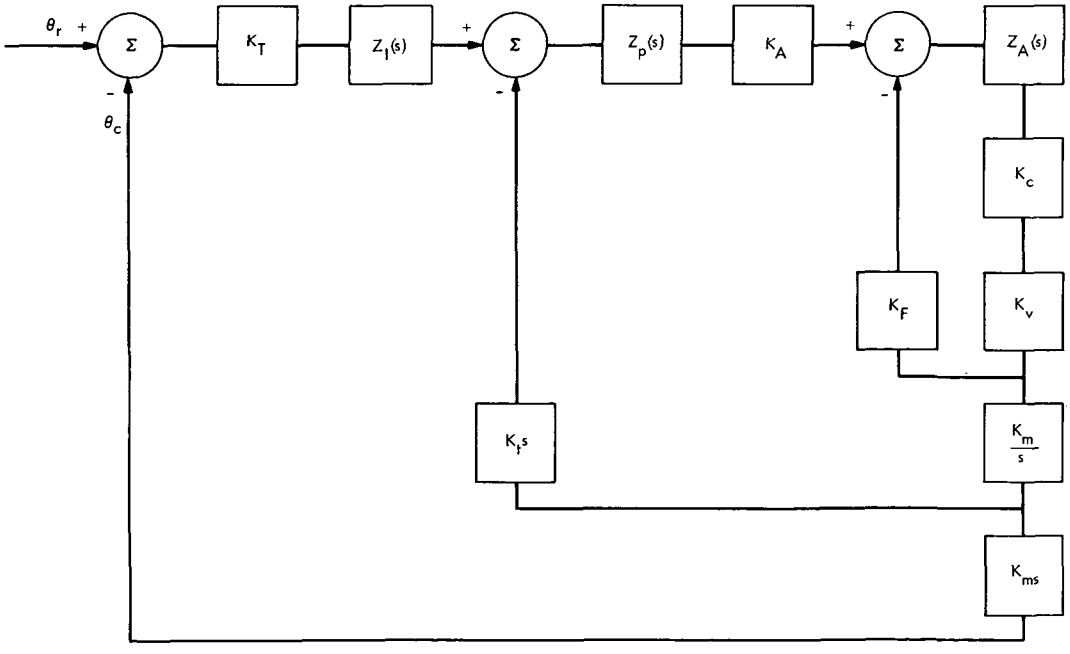

Fig. 5. Transfer function model of the automatic angle tracking system

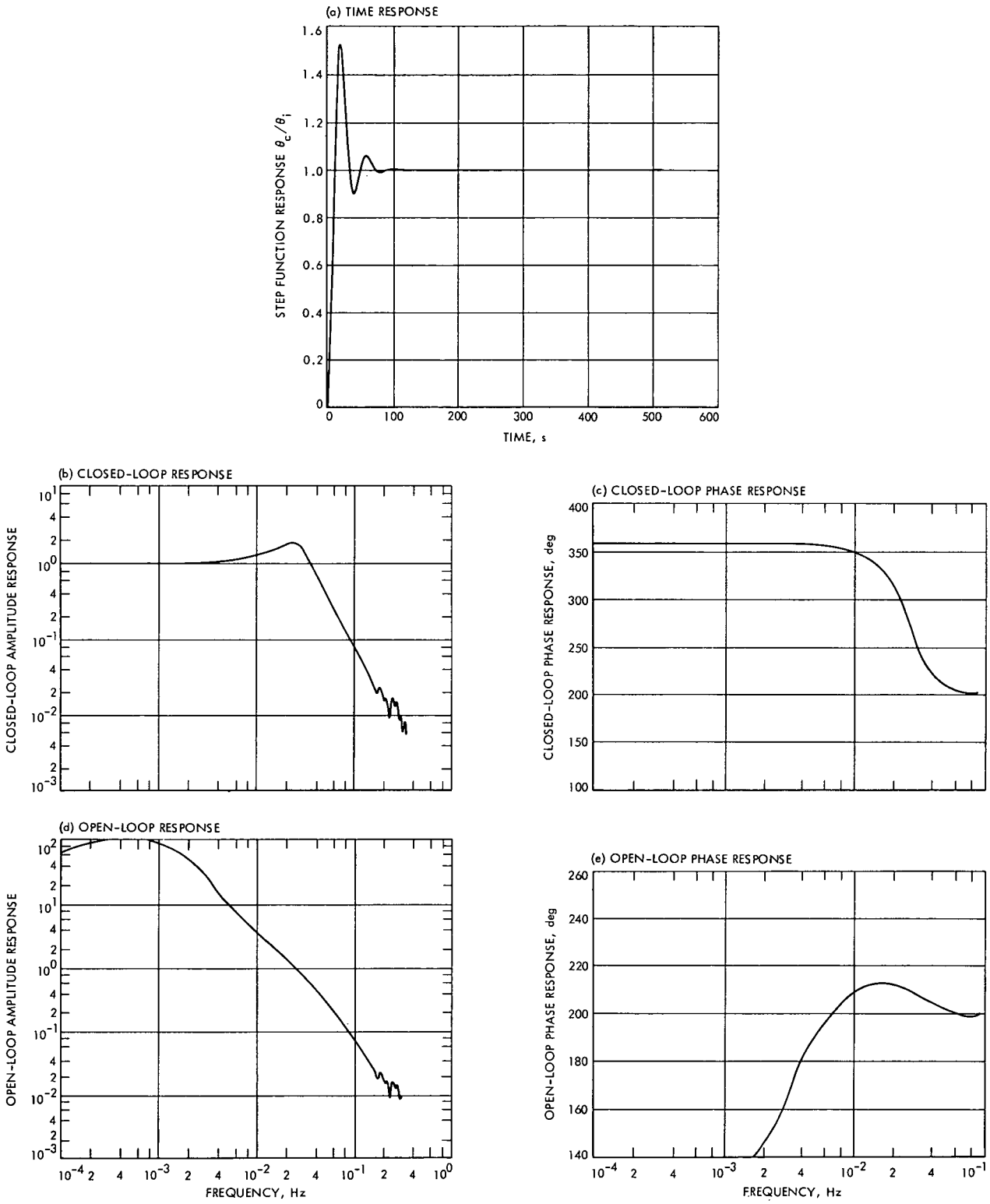

Fig. 6. Simulation results of case I (bandwidth = 0.025, gain setting = 0, normal motor gain): (a) time response, (b) closed-loop response, (c) closed-loop phase response, (d) open-loop response, (e) open-loop phase response

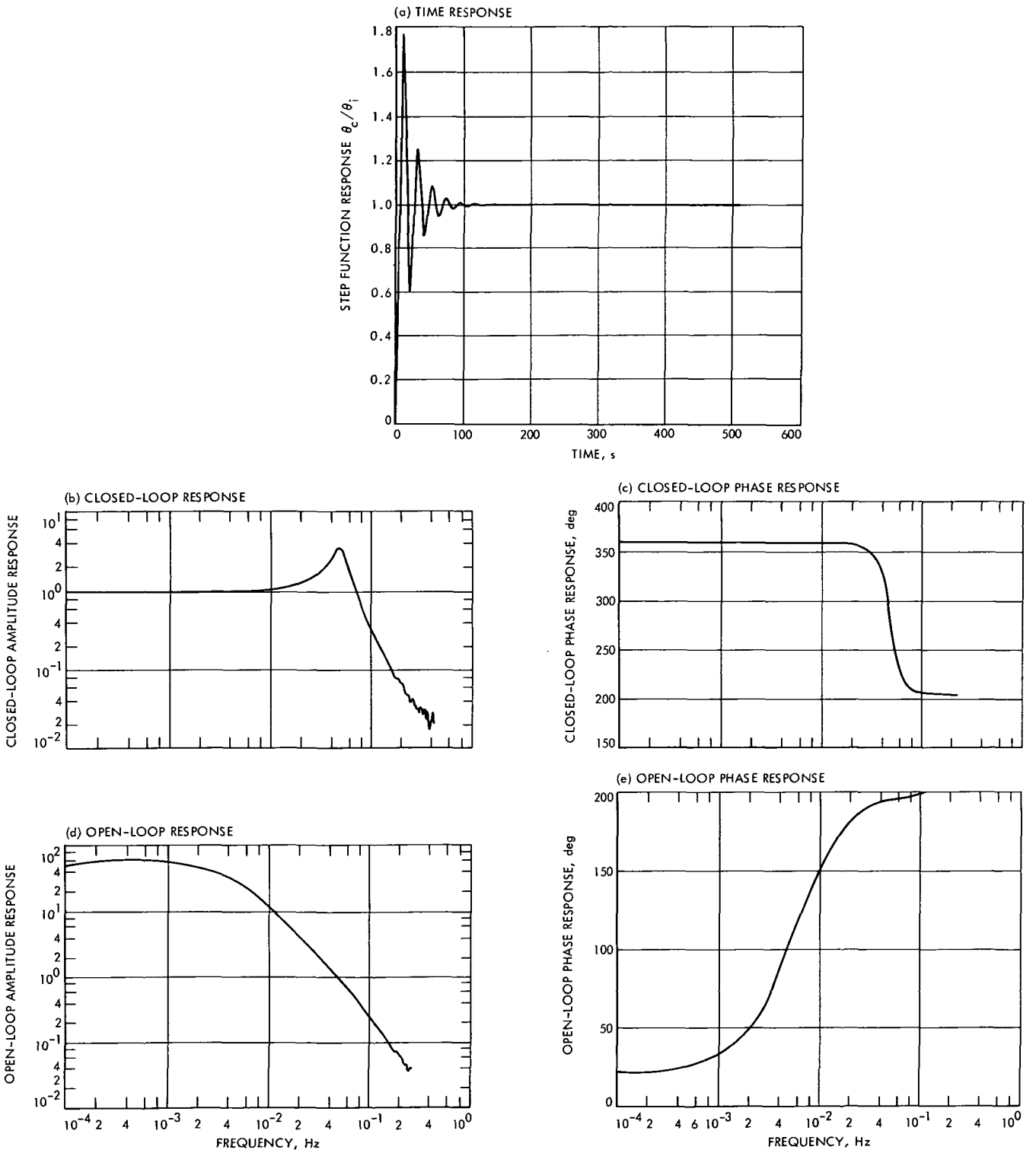

Fig. 7. Simulation results of case II (bandwidth = 0.05, gain setting = 5, normal motor gain): (a) time response, (b) closed-loop response, (c) closed-loop phase response, (d) open-loop response, (e) open-loop phase response

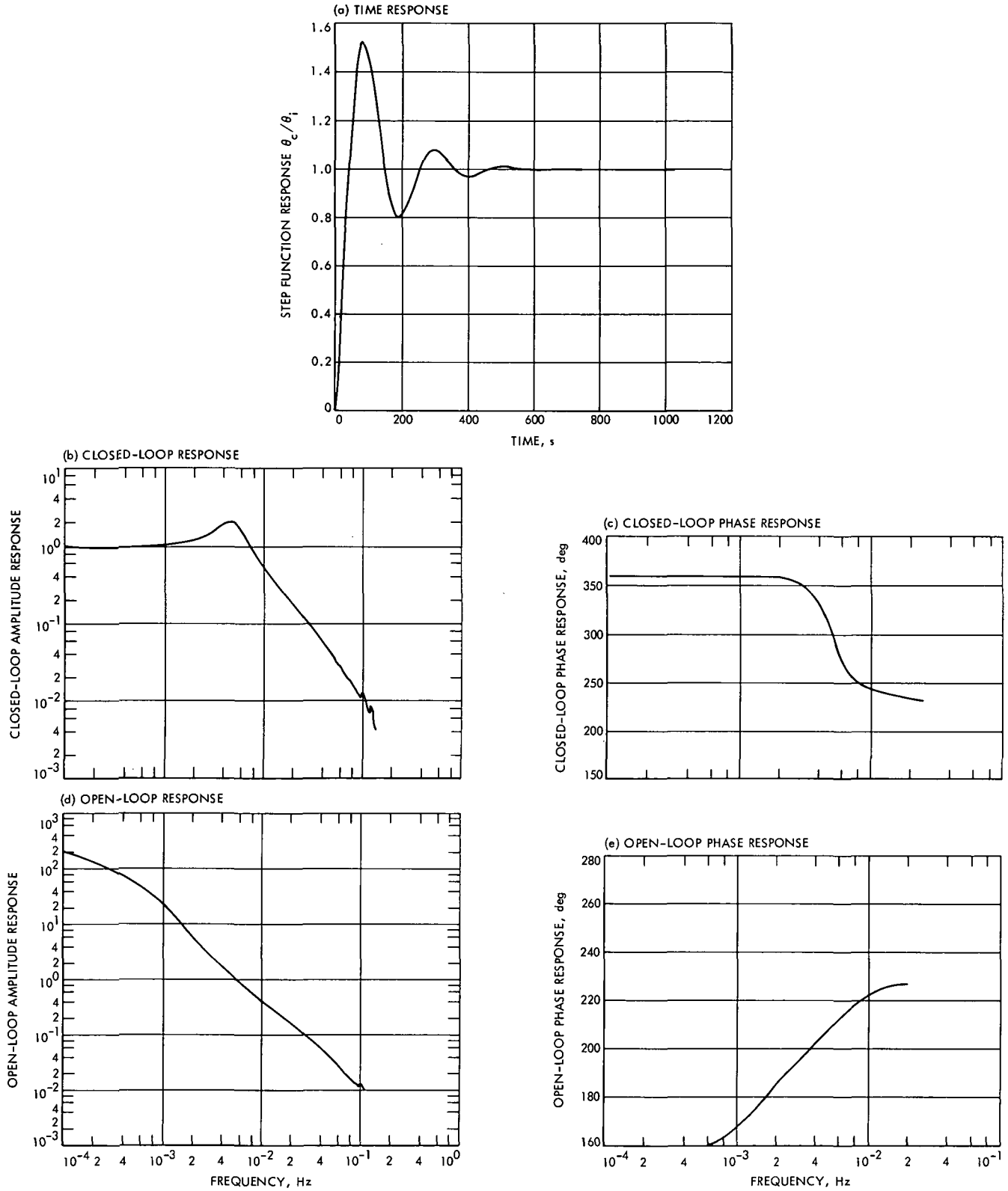

Fig. 8. Simulation results of case III (bandwidth = 0.024, gain setting = 0, reduced motor gain): (a) time response, (b) closed-loop response, (c) closed-loop phase response, (d) open-loop response, (e) open-loop phase response

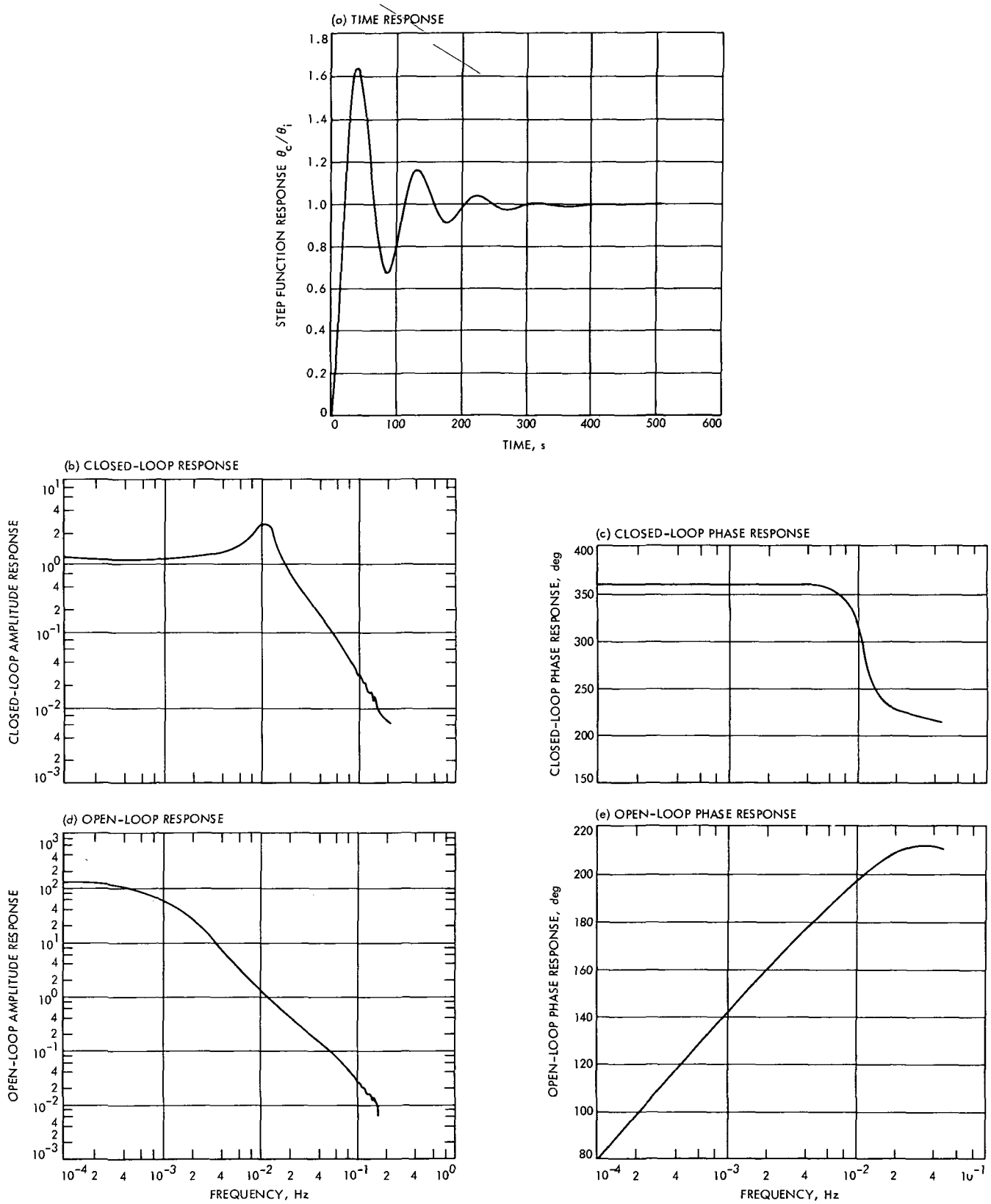

Fig. 9. Simulation results of case IV (bandwidth = 0.05, gainsetting = 5, reduced motor gain): (a) time response, (b) closed-loop response, (c) closed-loop phase response, (d) open-loop response, (e) open-loop phase response

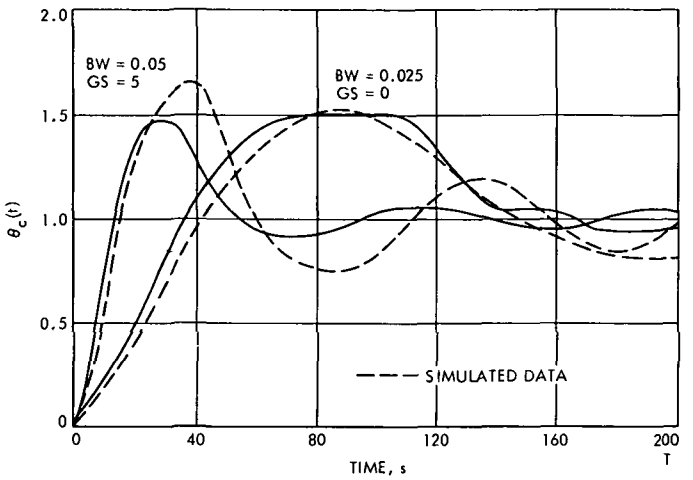

Fig. 10. Time responses measured at DSS 12

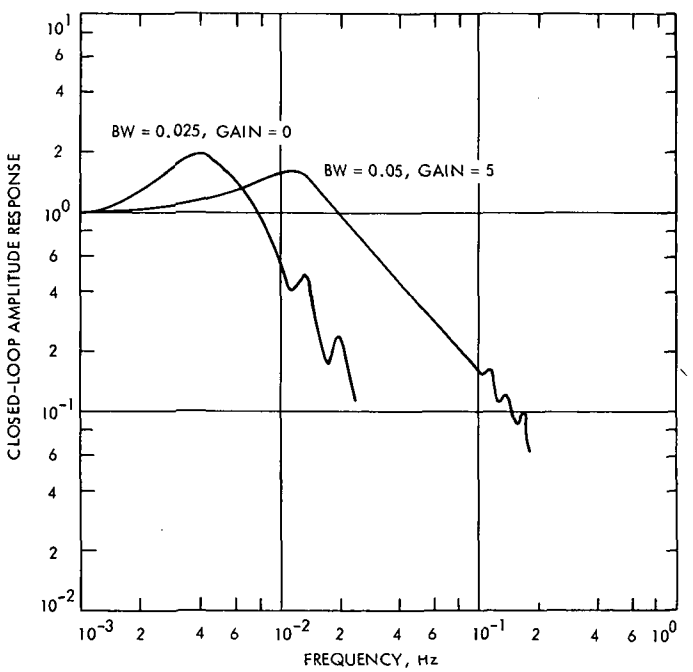

Fig. 11. Closed-loop transfer function measured at DSS 12

Bibliography

Anderson, J. D., *Determination of the Masses of the Moon and Venus and the Astronomical Unit from Radio Tracking Data of the Mariner II Spacecraft.* Technical Report 32-816. Jet Propulsion Laboratory, Pasadena, Calif., July 1, 1967.

Anderson, J. D., et al., "The Radius of Venus as Determined by Planetary Radar and Mariner V Radio Tracking Data," *J. Atmos. Sci.*, pp. 1171–1174, Sept. 25, 1968.

Berman, A. L., *Tracking System Data Analysis Report, Ranger VII Final Report,* Technical Report 32-719, Jet Propulsion Laboratory, Pasadena, Calif., June 1, 1965.

Berman, A. L., *ABTRAJ—On-Site Tracking Prediction Program for Planetary Spacecraft,* Technical Memorandum 33-391. Jet Propulsion Laboratory, Pasadena, Calif., Aug. 15, 1968.

Cain, D. L., and Hamilton, T. W., *Determination of Tracking Station Locations by Doppler and Range Measurements to an Earth Satellite,* Technical Report 32-534. Jet Propulsion Laboratory, Pasadena, Calif., Feb. 1, 1964.

Carey, C. N., and Sjogren, W. L., "Gravitational Inconsistency, in the Lunar Theory: Confirmation by Radio Tracking," *Science,* Vol. 160, pp. 875, 876, Apr.–June 1968.

Curkendall, D. W., and Stephenson, R. R., "Earthbased Tracking and Orbit Determination—Backbone of the Planetary Navigation System," *Astronaut. Aeronaut.*, Vol. 7, May 1970.

Curkendall, D. W., "Planetary Navigation: The New Challenges," *Astronaut. Aeronaut.*, Vol. 7, May 1970.

Efron, L., and Solloway, C. B., *Proceedings of the Conference on Scientific Applications of Radio and Radar Tracking in the Space Program,* Technical Report 32-1475. Jet Propulsion Laboratory, Pasadena, Calif., July 1970.

Flanagan, F. M., et al., *Deep Space Network Support of the Manned Space Flight Network for Apollo: 1962–1968,* Technical Memorandum 33-452, Vol. I. Jet Propulsion Laboratory, Pasadena, Calif., July 1970.

Flanagan, F. M., et al., *Deep Space Network Support of the Manned Space Flight Network for Apollo: 1969–1970,* Technical Memorandum 33-452, Vol. II. Jet Propulsion Laboratory, Pasadena, Calif., May 1, 1971.

Fjeldbo, G., and Eshleman, V. R., "Radio Occultation Measurements and Interpretations," in *The Atmospheres of Venus and Mars,* p. 225. Gordon and Breach, Science Publishers, Inc., New York, N. Y.

Goldstein, R. M., "Radar Time-of-Flight Measurements to Venus," *Astron. J.*, Vol. 73, No. 9, Aug. 1968.

Goldstein, R. M., and Rumsey, H., Jr., "A Radar Snapshot of Venus," *Science,* Vol. 169, Sept. 1970.

Gordon, H. J., et al., *The Mariner 6 and 7 Flight Paths and Their Determination From Tracking Data,* Technical Memorandum 33-469. Jet Propulsion Laboratory, Pasadena, Calif., Dec. 1, 1970.

Bibliography (contd)

Hamilton, T. W., et al., *The Ranger IV Flight Path and Its Determination From Tracking Data,* Technical Report 32-345. Jet Propulsion Laboratory, Pasadena, Calif., Sept. 15, 1962.

Kellermann, K. I., et al., "High Resolution Observations of Compact Radio Sources at 13 Centimeters," *Astrophys. J.,* Vol. 161, pp. 803–809, Sept. 1970.

Kliore, A., "Radio Occultation Measurements of the Atmospheres of Mars and Venus," in *The Atmospheres of Venus and Mars,* p. 205. Gordon and Breach Science Publishers, Inc., New York, N. Y.

Labrum, R. G., Wong, S. K., and Reynolds, G. W., *The Surveyor V, VI, and VII Flight Paths and Their Determination from Tracking Data,* Technical Report 32-1302. Jet Propulsion Laboratory, Pasadena, Calif., Dec. 1, 1968.

Lieske, J. H., and Null, G. W., "Icarus and the Determination of Astronomical Constants," *Astron. J.,* Vol. 74, No. 2, Mar. 1969.

Lorell, J., and Sjogren, W. L., *Lunar Orbiter Data Analysis,* Technical Report 32-1220. Jet Propulsion Laboratory, Pasadena, Calif., Nov. 15, 1967.

Lorell, J., *Lunar Orbiter Gravity Analysis,* Technical Report 32-1387. Jet Propulsion Laboratory, Pasadena, Calif., June 15, 1969.

Lorell, J., et al., "Celestial Mechanics Experiment for *Mariner,*" *Icarus,* Vol. 12, Jan. 1970.

McNeal, C. E., *Ranger V Tracking Systems Data Analysis Final Report,* Technical Report 32-702. Jet Propulsion Laboratory, Pasadena, Calif., Apr. 15, 1965.

Melbourne, W. G., et al., *Constants and Related Information for Astrodynamical Calculations,* Technical Report 32-1306. Jet Propulsion Laboratory, Pasadena, Calif., July 15, 1968.

Melbourne, W. G., "Planetary Ephemerides," *Astronaut. Aeronaut.,* Vol. 7, May 1970.

Miller, L., et al., *The Atlas–Centaur VI Flight Path and Its Determination from Tracking Data,* Technical Report 32-911. Jet Propulsion Laboratory, Pasadena, Calif., Apr. 15, 1966.

Mulhall, B. D., et al., *Tracking System Analytic Calibration Activities for the Mariner Mars 1969 Mission,* Technical Report 32-1499. Jet Propulsion Laboratory, Pasadena, Calif., Nov. 15, 1970.

Mulholland, J. D., and Sjogren, W. L., *Lunar Orbiter Ranging Data,* Technical Report 32-1087. Jet Propulsion Laboratory, Pasadena, Calif., Jan. 6, 1967.

Mulholland, J. D., *Proceedings of the Symposium on Observation, Analysis, and Space Research Applications of the Lunar Motion,* Technical Report 32-1386. Jet Propulsion Laboratory, Pasadena, Calif., Apr. 1969.

Muller, P. M., and Sjogren, W. L., *Consistency of Lunar Orbiter Residuals With Trajectory and Local Gravity Effects,* Technical Report 32-1307. Jet Propulsion Laboratory, Pasadena, Calif., Sept. 1, 1968.

Muller, P. M., and Sjogren, W. L., *Lunar Mass Concentrations,* Technical Report 32-1339. Jet Propulsion Laboratory, Pasadena, Calif., Aug. 16, 1968.

Bibliography (contd)

Null, G. W., Gordon, H. J., and Tito, D. A., *Mariner IV Flight Path and its Determination From Tracking Data,* Technical Report 32-1108. Jet Propulsion Laboratory, Pasadena, Calif., Aug. 1, 1967.

O'Neil, W. J., et al., *The Surveyor III and Surveyor IV Flight Paths and Their Determination From Tracking Data,* Technical Report 32-1292. Jet Propulsion Laboratory, Pasadena, Calif., Aug. 15, 1968.

Pease, G. E., et al., *The Mariner V Flight Path and Its Determination From Tracking Data,* Technical Report 32-1363. Jet Propulsion Laboratory, Pasadena, Calif., July 1, 1969.

Renzetti, N. A., *Tracking and Data Acquisition for Ranger Missions I–V,* Technical Memorandum 33-174. Jet Propulsion Laboratory, Pasadena, Calif., July 1, 1964.

Renzetti, N. A., *Tracking and Data Acquisition for Ranger Missions VI–IX,* Technical Memorandum 33-275. Jet Propulsion Laboratory, Pasadena, Calif., Sept. 15, 1966.

Renzetti, N. A., *Tracking and Data Acquisition Support for the Mariner Venus 1962 Mission,* Technical Memorandum 33-212. Jet Propulsion Laboratory, Pasadena, Calif., July 1, 1965.

Renzetti, N. A., *Tracking and Data Acquisition Report, Mariner Mars 1964 Mission: Near-Earth Trajectory Phase,* Technical Memorandum 33-239, Vol. I. Jet Propulsion Laboratory, Pasadena, Calif., Jan. 1, 1965.

Renzetti, N. A., *Tracking and Data Acquisition Report, Mariner Mars 1964 Mission: Cruise to Post-Encounter Phase,* Technical Memorandum 33-239, Vol. II. Jet Propulsion Laboratory, Pasadena, Calif., Oct. 1, 1967.

Renzetti, N. A., *Tracking and Data Acquisition Report, Mariner Mars 1964 Mission: Extended Mission,* Technical Memorandum 33-239, Vol. III. Jet Propulsion Laboratory, Pasadena, Calif., Dec. 1, 1968.

Renzetti, N. A., *Tracking and Data System Support for Surveyor: Missions I and II,* Technical Memorandum 33-301, Vol. I. Jet Propulsion Laboratory, Pasadena, Calif., July 15, 1969.

Renzetti, N. A., *Tracking and Data System Support for Surveyor: Missions III and IV,* Technical Memorandum 33-301, Vol. II. Jet Propulsion Laboratory, Pasadena, Calif., Sept. 1, 1969.

Renzetti, N. A., *Tracking and Data System Support for Surveyor: Mission V,* Technical Memorandum 33-301, Vol. III. Jet Propulsion Laboratory, Pasadena, Calif., Dec. 1, 1969.

Renzetti, N. A., *Tracking and Data System Support for Surveyor: Mission VI,* Technical Memorandum 33-301, Vol. IV. Jet Propulsion Laboratory, Pasadena, Calif., Dec. 1, 1969.

Renzetti, N. A., *Tracking and Data System Support for Surveyor: Mission VII,* Technical Memorandum 33-301, Vol. V. Jet Propulsion Laboratory, Pasadena, Calif., Dec. 1, 1969.

Bibliography (contd)

Renzetti, N. A., *Tracking and Data System Support for the Mariner Venus 67 Mission: Planning Phase Through Midcourse Maneuver,* Technical Memorandum 33-385, Vol. I. Jet Propulsion Laboratory, Pasadena, Calif., Sept. 1, 1969.

Renzetti, N. A., *Tracking and Data System Support for the Mariner Venus 67 Mission: Midcourse Maneuver Through End of Mission,* Technical Memorandum 33-385, Vol. II. Jet Propulsion Laboratory, Pasadena, Calif., Sept. 1, 1969.

Renzetti, N. A., *Tracking and Data System Support for the Pioneer Project. Pioneer VI. Prelaunch to End of Nominal Mission,* Technical Memorandum 33-426, Vol. I. Jet Propulsion Laboratory, Pasadena, Calif., Feb. 1, 1970.

Renzetti, N. A., *Tracking and Data System Support for the Pioneer Project. Pioneer VII. Prelaunch to End of Nominal Mission,* Technical Memorandum 33-426, Vol. II. Jet Propulsion Laboratory, Pasadena, Calif., Apr. 15, 1970.

Renzetti, N. A., *Tracking and Data System Support for the Pioneer Project. Pioneer VIII. Prelaunch Through May 1968,* Technical Memorandum 33-426, Vol. III. Jet Propulsion Laboratory, Pasadena, Calif., July 15, 1970.

Renzetti, N. A., *Tracking and Data System Support for the Pioneer Project. Pioneer IX. Prelaunch Through June 1969,* Technical Memorandum 33-426, Vol. IV. Jet Propulsion Laboratory, Pasadena, Calif., Nov. 15, 1970.

Renzetti, N. A., *Tracking and Data System Support for the Pioneer Project. Pioneer VI. Extended Mission: July 1, 1966–July 1, 1969,* Technical Memorandum 33-426, Vol. V. Jet Propulsion Laboratory, Pasadena, Calif., Feb. 1, 1971.

Renzetti, N. A., *Tracking and Data System Support for the Pioneer Project. Pioneer VII. Extended Mission: February 24, 1967–July 1, 1968,* Technical Memorandum 33-426, Vol. VI. Jet Propulsion Laboratory, Pasadena, Calif., Apr. 15, 1971.

Renzetti, N. A., *Tracking and Data System Support for the Pioneer Project. Pioneer VII. Extended Mission: July 1, 1968–July 1, 1969,* Technical Memorandum 33-426, Vol. VII. Jet Propulsion Laboratory, Pasadena, Calif., Apr. 15, 1971.

Renzetti, N. A., *Tracking and Data System Support for the Pioneer Project. Pioneer VIII. Extended Mission: June 1, 1968–July 1, 1969,* Technical Memorandum 33-426, Vol. VIII. Jet Propulsion Laboratory, Pasadena, Calif., May 1, 1971.

Renzetti, N. A., *Tracking and Data System Support for the Pioneer Project. Pioneers VI–IX. Extended Missions: July 1, 1969–July 1, 1970,* Technical Memorandum 33-426, Vol. IX. Jet Propulsion Laboratory, Pasadena, Calif., Aug. 15, 1971.

Sjogren, W. L., *The Ranger III Flight Path and Its Determination From Tracking Data,* Technical Report 32-563. Jet Propulsion Laboratory, Pasadena, Calif., Sept. 15, 1965.

Sjogren, W. L., et al., *Physical Constants as Determined From Radio Tracking of the Ranger Lunar Probes,* Technical Report 32-1057. Jet Propulsion Laboratory, Pasadena, Calif., Dec. 30, 1966.

Sjogren, W. L., et al., *The Ranger VI Flight Path and Its Determination From Tracking Data,* Technical Report 32-605. Jet Propulsion Laboratory, Pasadena, Calif., Dec. 15, 1964.

Bibliography (contd)

Sjogren, W. L., et al., *The Ranger V Flight Path and Its Determination From Tracking Data,* Technical Report 32-562. Jet Propulsion Laboratory, Pasadena, Calif., Dec. 6, 1963.

Sjogren, W. L., and Trask, D. W., *Physical Constants as Determined From Radio Tracking of the Ranger Lunar Probes,* Technical Report 32-1057. Jet Propulsion Laboratory, Pasadena, Calif., Dec. 30, 1966.

Sjogren, W. L., *Proceedings of the JPL Seminar on Uncertainties in the Lunar Ephemeris,* Technical Report 32-1247. Jet Propulsion Laboratory, Pasadena, Calif., May 1, 1968.

Stelzried, C. T., *A Faraday Rotation Measurement of a 13-cm Signal in the Solar Corona,* Technical Report 32-1401. Jet Propulsion Laboratory, Pasadena, Calif., July 15, 1970.

Stelzried, C. T., et al., "The Quasi-Stationary Coronal Magnetic Field and Electron Density as Determined From a Faraday Rotation Experiment," *Sol. Phys.*, Vol. 14, No. 2, pp. 440–456, Oct. 1970.

Thornton, J. H., Jr., *The Surveyor I and Surveyor II Flight Paths and Their Determination From Tracking Data,* Technical Report 32-1285. Jet Propulsion Laboratory, Pasadena, Calif., Aug. 1, 1968.

Vegos, C. J., et al., *The Ranger IX Flight Path and Its Determination From Tracking Data,* Technical Report 32-767. Jet Propulsion Laboratory, Pasadena, Calif., Nov. 1, 1968.

Winn, F. B., *Selenographic Location of Surveyor VI, Surveyor VI Mission Report: Part II. Science Results,* Technical Report 32-1262. Jet Propulsion Laboratory, Pasadena, Calif., Jan. 10, 1968.

Winn, F. B., "Post Landing Tracking Data Analysis," in *Surveyor VII Mission Report: Part II. Science Results,* Technical Report 32-1264. Jet Propulsion Laboratory, Pasadena, Calif., Mar. 15, 1968.

Winn, F. B., "Post Lunar Touchdown Tracking Data Analysis," in *Surveyor Project Final Report: Part II. Science Results,* Technical Report 32-1265. Jet Propulsion Laboratory, Pasadena, Calif., June 15, 1968.

Winn, F. B., *Surveyor Posttouchdown Analyses of Tracking Data,* NASA SP-184. National Aeronautics and Space Administration, Washington, D.C., p. 369.

Wollenhaupt, W. R., et al., *The Ranger VII Flight Path and Its Determination From Tracking Data,* Technical Report 32-694. Jet Propulsion Laboratory, Pasadena, Calif., Dec. 15, 1964.

NASA — JPL — Coml., L.A., Calif.